This is to certify that the

dissertation entitled

Response of an Earth Dam to Spatially Varying Earthquake Ground Motion

presented by

Mu-Tsang Chen

has been accepted towards fulfillment
of the requirements for

Ph.D. degree in Civil Engineering

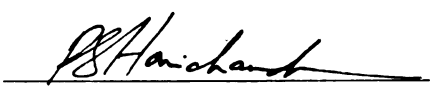

Major professor

Date 8/1/95

RESPONSE OF AN EARTH DAM TO SPATIALLY VARYING EARTHQUAKE GROUND MOTION

By

Mu-Tsang Chen

A DISSERTATION

Submitted to
Michigan State University
in partial fulfillment of the requirements
for the degree of

DOCTOR OF PHILOSOPHY

Department of Civil and Environmental Engineering

1995

ABSTRACT

RESPONSE OF AN EARTH DAM TO SPATIALLY VARYING EARTHQUAKE GROUND MOTION

By

Mu-Tsang Chen

The stochastic responses of the Santa Felicia earth dam to spatially varying earthquake ground motion (SVEGM) are analyzed. A space-time earthquake ground motion model that accounts for both coherency decay and seismic wave propagation is used to specify the support motions, and the results are compared with those for various simplified excitations. In addition, a preliminary reliability analysis using the Mohr-Coulomb strength criterion is performed. The effects of propagation speed and direction for SV/P and SH waves and different coherency models on the responses of the dam are also investigated. Finally, techniques to simplify the excitation for use with simplified mechanical models of the dam are presented.

The Santa Felicia dam is represented as a three-dimensional inhomogeneous finite element model using the I-DEAS VI.i computer program. The variation of shear modulus with depth from the crest due to confining pressure is taken into account. Finite element-based random vibration analysis is performed and the statistical moments of the displacement, strain and stress responses are computed. Statistical moments of the maximum shear stress, which is non-linearly related to the Cartesian stresses, are computed using Monte Carol simulation as well as an approximate first order second moment method.

The results of the study indicate that the effect of SVEGM is significant, especially on the stress response of stiff material near the base of the dam. The assumption of fully coherent support motions is found to slightly over-estimate the displacement and strain responses but significantly under-estimate the stress response near the base. The wave passage effect is not as significant as the coherency decay when the ground displacements are not highly coherent. The sensitivity of the stress response to different coherency functions at the base can be dramatic. For simplified analysis, a 2-D shear beam model should be capable of yielding good results at locations distant from the base with a suitably modified seismic excitation. For computing the stress response in stiff material near the base, a 3-D finite element model is required, but costly dynamic analysis can be avoided if the ground displacements are not highly coherent; a pseudo-static analysis suffices in this case.

To My Family

ACKNOWLEDGEMENTS

I would like to express my sincere appreciation to Professor Ronald Harichandran for his insight, encouragement and assistance throughout this research. It is certain that this work would not have been possible without him.

I would also like to thank my guidance committee members Professor Frank Hatfield, Professor Thomas Wolff and Professor Chi Lo for their generous support and constructive suggestions during the period of this study.

Loving thanks is offered to my parents and my wife for their sacrifice and patience.

Finally, I gratefully acknowledge the financial support provided by the National Science Foundation under Grant No. BCS 9121292.

TABLE OF CONTENTS

LIST OF TABLES

LIST OF FIGURES

1. INTRODUCTION

Earth dams have been used in various parts of the world for many centuries. However, the behavior of earth dams under earthquake excitation has been investigated only during the past six decades. Because the failure of earth dams can result in large property damage and loss of life, design, analysis and construction efforts to build safe and economic structures are very important. Over the years considerable research has been directed towards the development of analytical and numerical techniques for evaluating the response of earth dams subjected to earthquake ground motions. While the developments have enabled the estimation of deformations, strains, accelerations and stresses generated in earth dams in response to earthquake excitation, the limitations of the models used and the assumptions made in the analysis should be carefully considered when evaluating the predicted performance or type of damage.

In many earth-dam studies, the analysis techniques used are quite simplistic. For example, one of the most commonly used analytical model, known as the "shear beam" model, characterizes the dam as a uniform one-dimensional elastic beam, with the dynamic response restricted to horizontal shear deformation in the upstream-downstream direction. Although some of the more restrictive assumptions of the shear beam model have now been relaxed, it still remains somewhat unsatisfactory. More realistic and sophisticated models based on the finite element method have found increasing use since the mid-1960s. For the most part these have been restricted to two-dimensional plane strain model which assumes that the dam is infinitely long. With advances in computer performance and storage, three-dimensional models can now be used in order to model the dam more realistically and to obtain more accurate predictions of the responses to earthquake excitation.

Finite element models are successful in accounting for geometry irregularity and material inhomogeneity. However, in most studies to date, the ground motion acting at the base of a dam has been assumed to be identical at all location, or at best due to a simple

propagating wave. Recent research has shown (Harichandran and Vanmarcke 1986, Loh 1985, Abrahamson et al. 1990, Schneider et al. 1990) that significant variation of earthquake ground motion exists over the base dimensions of large structures such as dams. This spatially varying earthquake ground motion (SVEGM) is characterized by wave propagation as well as by coherency loss. Studies on certain classes of structures have shown that the coherency loss aspect of SVEGM is very significant (Harichandran and Wang 1990, Novak and Suen 1987, Sweidan 1990, Zerva 1988).

The Santa Felicia earth dam located in southern California has been selected for assessing the effect of SVEGM since it has been studied extensively (Abdel-Ghaffar and Scott 1979a, Abdel-Ghaffar and Scott 1979b, Abdel-Ghaffar and Scott 1981a, Abdel-Ghaffar and Scott 1981b, Gazetas 1981, Abdel-Ghaffar and Koh 1982, Prevost et al. 1985, Abdel-Ghaffar and Elgamal 1987, Elgamal and Abdel-Ghaffar 1987). The dam is analyzed using a three-dimensional finite element model using Integrated Design Engineering Analysis Software (I-DEAS) developed by SDRC (1987). Some structural properties such as natural frequencies, mode shapes, modal masses, and stiffness and mass matrices are obtained using I-DEAS.

In contrast to traditional dynamic analysis, which is based on deterministic concepts, the theory of random vibration accounts explicitly for uncertainties that almost always exist in the dynamic loads or inputs that act on the system, especially seismic ground motions. Further, SVEGM is usually characterized as a random field and hence the responses of structures subjected to this are most effectively computed using random vibration analysis. Therefore, the responses of the Santa Felicia dam to SVEGM are computed in this study using random vibration and probabilistic analysis.

Chapter 2 contains a review of conventional methods used to model earth dams and techniques for earth-dam analysis and design. In general, there are two different approaches, theoretical methods and numerical methods. The former is developed on the

basis of the shear beam theory by which the dynamic behavior of earth dams can be solved analytically. The latter is based upon the finite element method which is a widely accepted numerical procedure for solving the partial differential equations of motion governing the system.

Traditionally, earthquake-resistant design of earth dams is performed with slope stability analysis using the "limiting equilibrium" method. The method is described at the beginning of the chapter. Following this, the applications of the shear beam model and the finite element model are briefly reviewed. The limitations and disadvantages of each method are also discussed. In addition, some sophisticated deterministic analyses treating soil as viscoelastic material are reviewed. Finally, recent studies on the applications of probabilistic methods to the seismic analysis of earth dams are outlined.

In Chapter 3, the deterministic response of the Santa Felicia dam to a simulated earthquake excitation is computed. The constituent material properties and site conditions of the dam are specified here. Some assumptions in the model such as geometry, soil properties, hydrodynamic effect, dam-foundation interaction and radiation damping effect are also elucidated.

A three-dimensional finite element model is used throughout this study. The modeling and analysis processes using I-DEAS are discussed briefly and further details are given in the Appendix. The number of modes required to obtain accurate responses is determined by assessing convergence of deterministic dynamics analysis results. The types of vibration modes are shown and classified. In addition, the types of damage sustained by earth dams due to earthquake motions, such as sliding, liquefaction, cracking and piping failure, are also described.

Chapter 4 presents the background of the theories employed in this study. The characteristics of earthquake ground motions and engineering interpretation of stochastic responses are described in the beginning. A ground motion model which accounts for wave

travel and coherency loss is used (Harichandran and Vanmarcke 1986). In the second part, finite element discretization and modal analysis are introduced. The theory of random vibration is presented. An expression for the displacement response is obtained using stationary random vibration analysis.

In addition to the displacement response, stress and strain are also of interest in the analysis. The covariances of Cartesian stress and strain responses to SVEGM are formulated using random vibration analysis. The maximum shear stress and strain indicate where local yielding of dam material will occur. Since principal stresses (strains) are related non-linearly to the Cartesian stresses (strains), the first-order second-moment method (FOSM) is employed to approximately estimate the mean and variance of the maximum shear stress from those of the Cartesian stresses. The accuracy of the FOSM approach results is assessed by comparing them with results obtained using Monte Carlo simulation. Another important factor which significantly affects the dynamic characteristics of earth dams is damping. The effect of two types of damping, hysteretic damping and viscous damping, are assessed using a one-dimensional shear beam model.

In Chapter 5, the parameters of the ground motion model used are given. The computational steps of the stochastic response analysis are summarized. The computed responses due to simplified excitations, such as identical and delayed excitations, as well as due to general excitation are presented in this chapter. The results for the maximum shear stress responses using the FOSM method and simulation are compared. Correction factors are proposed for the mean and standard deviation of the maximum shear stress estimated by the FOSM approximation.

Details of the responses such as the significance of the various modal responses and the contributions of the three response components (the variance of the pseudo-static response, the variance of the dynamic response, and the covariance between the static and

dynamic response) to the total response are examined. Finally, reliability against local yielding under gravity and earthquake loads is assessed in this chapter.

Chapter 6 considers a series of parametric studies. The effect of seismic waves travelling with a lower velocity or at a shallow incident angle is evaluated. The effect of having SH waves rather than P/SV waves is assessed. Sensitivity of the responses to the different coherency models proposed by Abrahamson (1993), Novak (1987), Luco and Wong (1986) and Hao (1989) are studied in addition to the model proposed by Harichandran and Vanmarcke (1986). The discrepancies among these models are presented and discussed and comparisons between the effects of different coherency models are made.

In Chapter 7, a technique of simplifying the excitation in order to enable the use of a 2-D shear beam model is presented. The boundary of the dam where the ground motion excitation is applied is divided into several strips. Each strip is considered to have a single degree of freedom and hence fully-correlated excitation is assumed within each strip. However, ground motion incoherence is still allowed between each pair of strips. The displacement, maximum shear strain and maximum shear stress responses using this simplified excitation model are compared with those using the general model. In addition, the effect of using different numbers of strips on the boundary are evaluated and the adequacy of this simplified model is discussed.

In the final chapter, Chapter 8, the conclusions of the research and recommendations for future work in this area are presented.

2. Literature Review

2.1 General

In the past six decades or so, engineers have attempted to better understand the dynamic behavior of dam structures under earthquake conditions. Theoretical analysis as a shear beam, numerical analysis as a two-dimensional (2-D) or three-dimensional (3-D) body using the finite element method (FEM), and full-scale or model tests are the principal methods of analyzing the vibrations of earth dams.

The one-dimensional (1-D) shear beam model considers the dam as a plate obtained by slicing it with two cross sections perpendicular to the dam axis and analyzing the in-plane response of the plate as a wedge-shaped shear beam. The effect of both banks of the valley is neglected, but it is said to be small when the length of the dam exceeds four times the height (Hatanaka 1955). However, this limitation has been improved by using a 2-D shear beam theory which accounts for the variation of deformation along the longitudinal direction of the dam. The problem is therefore handled in a more realistic manner, but a precise analysis in this case is rather difficult, especially for modeling a dam with inhomogeneous material.

The FEM was initially used to analyze the plate model described above as a 2-D plane-strain model (Clough and Chopra 1966). A dam with an infinite length is assumed in the analysis. The popularity of the finite-element method stemmed mainly from three factors: (a) its capability for handling any number of zones with different materials; (b) its capability of rationally reproducing the 2-D dynamic stress and displacement field during ground motion; and (c) its capability to account for the effects of excitation by horizontally travelling waves. Nevertheless, the assumption of plane-strain conditions is inappropriate for dams built in narrow valleys. In such cases, the stiffening effect due to the short length may not be neglected. Recent advances in computer hardwares have facilitated the use of 3-D models (Martinez and Bielak 1980).

In experimental approaches, a scaled model of the dam is typically placed on a shaking table and vibrated. The test includes an elastic vibration test for investigating the vibration characteristics of the dam and a dynamic failure test for studying the conditions of failure due to vibration. The most important consideration in a model test is for a similarity to exist between the real structure and the model, but with a complex structure, such as an earth dam, it is difficult to obtain similarities for all characteristics. Therefore, the model is usually made so that the property being tested is similar to that of the actual earth dam. Instead of model tests, full-scale forced-vibration tests (Petrovski et al. 1974, Abdel-Ghaffar and Scott 1981a) were performed to overcome the drawback in modeling. Furthermore, field measurement and observation (Seed et al. 1978) of earth dam responses during earthquakes can yield direct information for purposes of analysis and design.

2.2 Conventional Approaches

2.2.1 Seismic design criteria

2.2.1.1 Pseudo-static method

For a long time the standard method of evaluating the safety of earth dams against sliding during earthquakes has been the so called "pseudo-static" method. This method is based on the assumption that dams are absolutely rigid bodies fixed on their foundations, and experience a uniform horizontal base acceleration equal to the underlying ground acceleration. The horizontal ground acceleration was obtained from seismic codes in terms of a single peak value, giving a horizontal inertia force on a potential sliding mass in the upstream-downstream direction. The force is determined as the product of a seismic coefficient and the weight of the potential sliding mass. The stability of slopes can be analyzed on a trial failure surface, considering the equilibrium of the weight, the inertia force and the resisting force of the sliding block.

According to this method, a trial failure surface ABC shown in Fig. 2.1 is an arc of a circle with its center at O and a radius of R. Considering the unit length of the embankment

perpendicular to the cross section shown, the forces acting on the trial failure surface are as follows:

1. Weight of the wedge, W.
2. Inertia force on the wedge, $k_h W$, which accounts for the effect of an earthquake on the trial wedge. The factor k_h is the average coefficient of horizontal acceleration.
3. Resisting force per unit area, F_R, which is the shear strength of the soil acting along the trial failure surface, ABC.

The factor of safety with respect to strength, F_s, is determined by

$$F_s = \frac{\text{Resisting moment about } O}{\text{Overturning moment about } O} = \frac{F_R\left(A\widehat{BC}\right)R}{WL_1 + k_h W L_2}. \tag{2.1}$$

This procedure is repeated with several trial failure surfaces to determine the minimum value of F_s. The slope is considered to be stable if the minimum value of F_s is greater than or equal to 1. The magnitude of k_h used for the design of many dams in the past ranged from 0.05 to 0.15 in the United States (Das 1993).

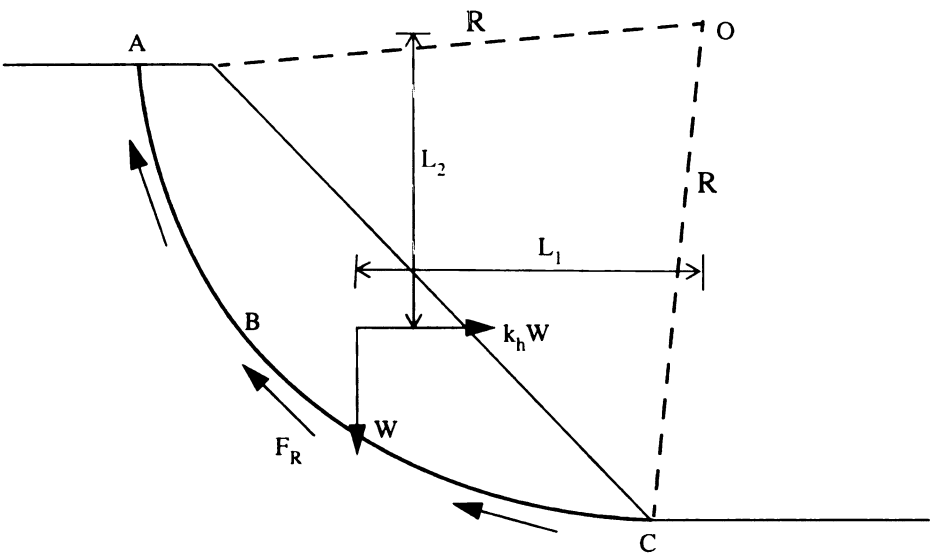

Figure 2.1 Stability analysis for slope of an earth dam

Nevertheless, it is now clearly understood that earth dams behave as deformable rather than rigid bodies, and their response to seismic base excitation is influenced by the properties of the constituent materials, the geometry, and the nature of the base motion. Early convincing evidence of such behavior has come from forced-vibration tests (Keightley 1966), and from observations of response during earthquakes (Okamoto et al. 1969), although it had been theoretically anticipated much earlier (Mononobe 1936). Other serious drawbacks of the pseudo-static procedure have been thorough discussed by Seed et al. (1973) as follows:

1. The design method considers classical slope instability as the only potential mode of failure. In fact, over the years, several types of seismic damage have been observed in earth dams and embankments over the world, such as liquefaction flow failure, longitudinal cracks, differential crest settlement, loss of free board, transverse cracks, and piping failure.
2. The horizontal inertia forces do not remain at a constant level for a significant time duration or act along a single direction, but rather fluctuate rapidly in both magnitude and direction. Thus, even if the factor of safety dropped momentarily below unity the slope would not necessarily experience a gross instability but might merely undergo some permanent deformation. This idea of performance controlled by magnitude of deformations rather than by limiting value of pseudo-static factors of safety has been exploited and evolved into a full-fledged standard practical procedure of assessing the seismic safety of earth dams consisting of nonliquefiable soils, which will be introduced in the next section.

2.2.1.2 Sliding displacement method

The sliding displacement method is primarily based on the original concept proposed by Newmark (1965). It is assumed that sliding of an earth mass will begin during an earthquake when the moment due to extraneous forces exceeds the resisting moment. The earth mass which has begun to slide will be subject to gravitational force, seismic force and

resistance, but the sliding will progress. However, resistance will continue to act while the seismic force reduces and reverses, so that the sliding of the earth mass is decelerated and then stopped. When earthquake acceleration is again increased the sliding starts once more and the same behavior is repeated. With each repetition, the total quantity of sliding is increased, and when the earthquake is over there will be a certain degree of displacement remaining. If the amount of sliding does not endanger the dam, the dam will be stable after the earthquake.

To clarify this phenomenon, consider a slope, as shown in Fig. 2.1, subjected to an earthquake, the stability of the slope will depend on the shear strength of the soil and the average coefficient of horizontal acceleration. The factor of safety of the soil mass located above the most critical surface ABC will become equal to 1 when k_h is equal to k_y. This value of k_y is defined as the coefficient of yield acceleration. If the soil wedge ABC is subjected to given earthquake accelerograph, the velocity of the sliding wedge can be determined by integration of the area under the acceleration versus time plot, in which the acceleration exceeds k_y. Similarly, the displacement can be derived from the velocity. With time, the displacement of the wedge gradually increases. In most cases of embankment stability, it can be shown (Seed, 1979) that when the crest acceleration does not exceed 0.75g, deformation of such embankments will usually be acceptably small if the dam has $F_s = 1.15$ as determined by the pseudo-static analysis.

The sliding displacement method has gained acceptance more recently in the determination of the displacement of slopes (Sarma 1975, Makdisi and Seed 1978). And it was proved to be useful in cases where the yield resistance of the soil can be reliably determined and does not significantly decrease with time during an earthquake. Compacted cohesive clays, dry sands and very dense saturated sand may belong in this category of soils since no significant pore water pressure builds up during cyclic loading.

2.2.1.3 Liquefaction criterion

When dams are constructed of loose or medium dense saturated sands, severe damage and failures due to build-up of pore water pressure may occur. To evaluate the seismic stability of such embankments, Seed (1979) developed an analysis procedure which involves the following essential steps:

1. Estimate the initial static stresses in the dam by means of finite element analysis.
2. Determine the dynamic soil properties such as shear modulus, Poisson ratio and damping characteristics as functions of the strain level.
3. Compute the stresses induced in the dam by the design ground excitation, using plane-strain finite element analysis and the dynamic soil characteristics determined in step 2.
4. Subject representative samples of the embankment materials to the combined effects of the initial static stresses and the superimposed dynamic stresses, and determine their effects in terms of the generation of pore water pressures and the ensuing reduction in strength and development of strains.
5. Perform slope stability analyses and semi-empirically convert the strain potentials to a set of "compatible" deformations. The stability and performance of the dam are judged from the results of these stability analyses and/or the size and distribution within the dam of the "compatible" deformations.

This procedure has been employed to explain several cases of liquefaction failures, most notably those of the Sheffield and Lower San Fernando Dams. However, some potential limitations of the liquefaction evaluation procedure have been criticized in recent years. Regarding the definition of liquefaction as that stage in a cyclic laboratory test when a peak pore pressure ratio reach 100%, it has been argued that development of a 100% pore pressure ratio does not necessarily lead to zero shear strength. Second, the associated undrained cyclic triaxial stress-controlled testing of anisotropically consolidated specimens

is used for evaluating the liquefaction potential. A particular limitation of the cyclic triaxial test stems from the fact that the orientation of the major principal stress may rotate intermittently by 90° during each cycle. In reality, it is more likely that the principal stress directions rotate randomly during shaking, and only momentarily could the planes of maximum static and dynamic shear stress coincide.

From a practical point of view, these methods are acceptable as preliminary design criteria. However, for rigorous seismic design of earth dams, more comprehensive investigations are required. Shear beam and finite element models have been developed to estimate earthquake induced deformations and stresses in dams, and to be able to predict various types of damage and failure.

2.2.2 Shear beam model

The shear beam model for earth dams was first introduced by Mononobe (1936). This model was rigorously exploited in the 1960's and 1970's to conduct parametric studies, to interpret the results of full-scale tests, and to obtain seismic coefficients for use in design. The following major assumptions are made in the shear beam theory:

1. The dam is a beam with a variable wedge-shaped cross section. Only horizontal lateral displacements and simple shearing deformations take place, and are uniformly distributed along horizontal planes across the dam.
2. The dam consists of homogeneous material which can be described by a constant shear modulus, or a modulus that varies along the height of the dam.
3. The dam is built in a rectangular canyon and is subjected to identical lateral base motions.

2.2.2.1 One-dimensional shear beam theory

Based on the assumptions of the shear beam theory, closed-form solutions to the vibration of the dam can be derived as summarized below. Fig. 2.2 shows a typical 1-D

shear beam model. Considering the equilibrium of the inertia force and shearing force acting on the shaded element in Fig. 2.2,

$$\rho b dy \frac{\partial^2 u}{\partial t^2} = \frac{\partial Q_{yx}}{\partial y} dy = \frac{\partial (b\tau)}{\partial y} dy \tag{2.2}$$

where

u = displacement along the x axis;

ρ = density of material;

Q = shearing force; and

τ = shearing stress.

At any y location,

$$\frac{\partial (b\tau)}{\partial y} = \frac{\partial b}{\partial y}\tau + b\frac{\partial \tau}{\partial y} = \frac{b}{y}\tau + b\frac{\partial \tau}{\partial y} \tag{2.3}$$

Thus, equation (2.2) becomes

$$\rho \frac{\partial^2 u}{\partial t^2} - \frac{\partial \tau}{\partial y} - \frac{\tau}{y} = 0 \tag{2.4}$$

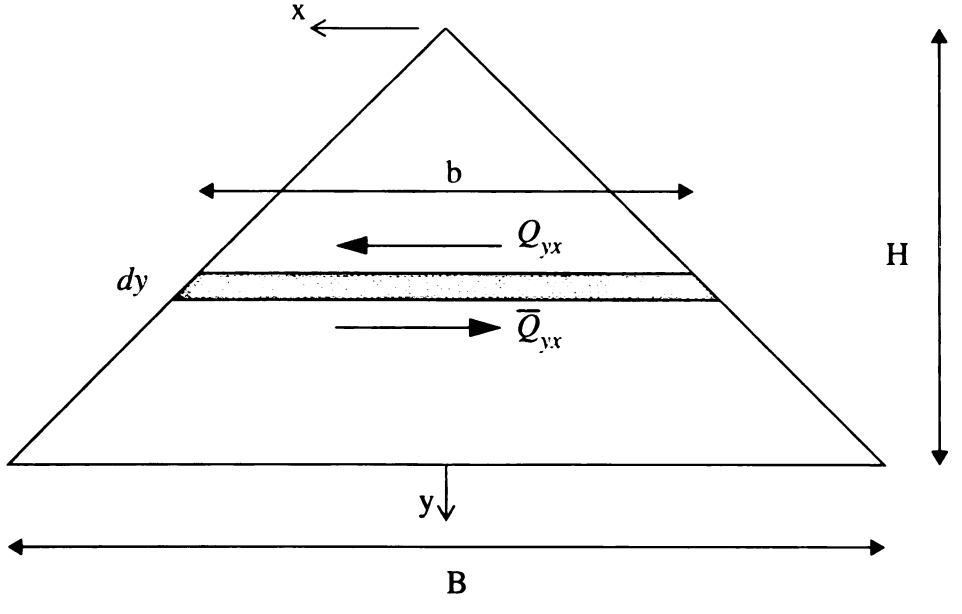

Figure 2.2 One-dimensional shear beam model

Assuming the relation between shear stress and shear deformation to be

$$\tau = G\frac{\partial u}{\partial y} \tag{2.5}$$

where G = shear modulus, and substituting equation (2.4),

$$\frac{\rho}{G}\frac{\partial^2 u}{\partial t^2} - \frac{\partial^2 u}{\partial y^2} - \frac{1}{y}\frac{\partial u}{\partial y} = 0 \tag{2.6}$$

This is the differential equation governing the vibration of the dam.

Let the natural frequency and the mode of vibration be ω and $\Phi(y)$, respectively. Then assuming u to be $u = \Phi e^{i\omega t}$ and substituting in equation (2.4),

$$\frac{d^2\Phi}{dy^2} + \frac{1}{y}\frac{d\Phi}{dy} + \frac{\rho\omega^2}{G}\Phi = 0 \tag{2.7}$$

which is a typical Bessel's equation.

Let $V_s = \sqrt{G/\rho}$ denote the velocity of shear waves. The general solution of equation (2.7) with arbitrary constants C_1 and C_2 is:

$$\Phi(y) = C_1 J_o\left(\frac{\omega y}{V_s}\right) + C_2 Y_o\left(\frac{\omega y}{V_s}\right) \tag{2.8}$$

where J_n and Y_n are Bessel functions of the first and second kind of order n, respectively. Using the boundary conditions:

$$\tau = 0 \text{ at } y = 0 \;\Rightarrow\; \left.\frac{\partial\Phi}{\partial y}\right|_{y=0} = 0 \;\Rightarrow\; C_2 = 0;$$

$$u = 0 \text{ at } y = H \;\Rightarrow\; \Phi(H) = 0 \;\Rightarrow\; J_o\left(\frac{\omega H}{V_s}\right) = 0.$$

Therefore, the characteristic equation becomes $\frac{\omega H}{V_s} = Z_i$ where Z_i are the roots of $J_o(Z) = 0$.

From this the undamped natural frequencies of vibration are

$$\omega_i = \frac{V_s}{H} Z_i \tag{2.9}$$

and the vibration modes are

$$\Phi_i(y) = J_o\left(\frac{Z_i y}{H}\right) \tag{2.10}$$

The shearing stress will be

$$\tau_i = -\frac{GH}{Z_i} J_1\left(\frac{Z_i y}{H}\right) e^{i\omega t} \tag{2.11}$$

Modal analysis can now be used to compute the response of the dam to an earthquake. In modal analysis, the earthquake excitation is distributed to the various normal modes, and the sum of the modal responses is the total response. The proportion of excitation distributed to each normal mode, i.e. participation factor, is given by

$$\Gamma_i = \frac{\int_0^H \rho \frac{B}{H} y \Phi_i(y)\, dy}{\int_0^H \rho \frac{B}{H} y (\Phi_i(y))^2 dy} = \frac{\int_0^H y J_o\left(\frac{Z_i y}{H}\right) dy}{\int_0^H y \left(J_o\left(\frac{Z_i y}{H}\right)\right)^2 dy} = \frac{2}{Z_i J_1(Z_i)} \tag{2.12}$$

Assuming H = 275 ft and V_s = 1,000 ft/sec, the values of frequency, participation factor, and vibrational shape function for the first four modes are listed in Table 2.1. Their mode shapes are shown in Fig. 2.3.

2.2.2.2 Shear beam with variable rigidity

In the above theory the shear modulus is assumed to be constant over the entire dam, but in most cases it is greater in the interior of the dam than near the surface because of the

TABLE 2.1 Response of 1-D shear beam model

i	Z_i	ω_i (Hz)	Γ_i	$\Phi_i(y)$
1	2.4048	1.39	1.602	$J_o(0.00874y)$
2	5.5201	3.19	-1.065	$J_o(0.02007y)$
3	8.6537	5.01	0.851	$J_o(0.03147y)$
4	11.7915	6.82	-0.730	$J_o(0.04288y)$

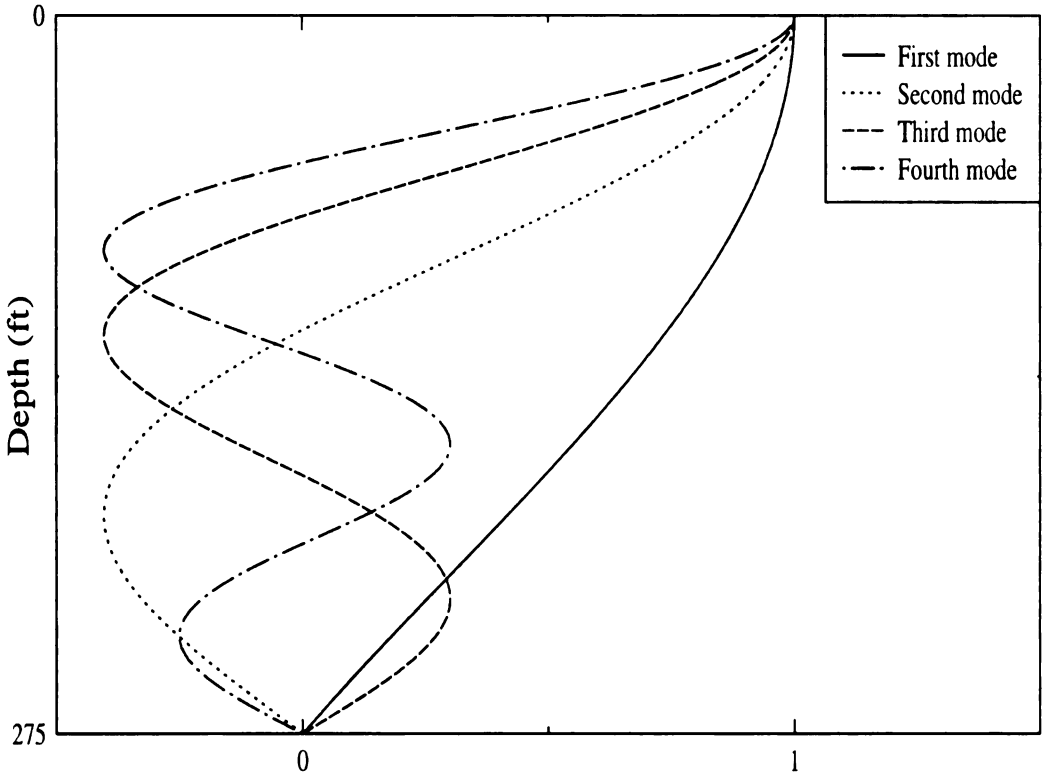

Figure 2.3 One-dimensional shear beam vibration modes

high confining pressure. As a result, the upper portion of the dam is considerably more flexible, and the vibration modes can be rather different from those shown in Fig. 2.3.

Sawada and Takahashi (1975) investigated the velocity of seismic waves in the bodies of existing rockfill dams and obtained important data on the distribution of the rigidity in dam bodies. According to their tests, the velocity of transverse wave at any depth can be represented by the formula

$$V_s = \alpha y^{\beta} \tag{2.13}$$

where V_s = velocity of the shear wave, y = depth from the surface of the dam, and the two parameters α and β are determined by the geometry and material properties of the dam. Table 2.2 shows the typical velocity of a transverse wave and the Poisson's ratio.

Further refinement can be performed by adjusting the shear modulus based on the level of stresses and strains during the response to earthquake motions. This would lead to an iterative analysis. A simpler method of obtaining equivalent dynamic shear modulus that accounts for stresses and strains due to the first mode only, has been proposed for 1-D and 2-D shear beam models by Abdel-Ghaffar and Scott (1979a). In their studies, a formula for the variable shear modulus used in the analysis of the Santa Felicia dam response to earthquakes was

$$G(y) = \rho v_{so}\left(\frac{\gamma y}{2}\right)^{\frac{1}{3}} \tag{2.14}$$

where ρ = mass density; γ = specific weight; and v_{so} = parameter defined by Price (1956) to determine G as a function of depth y. Furthermore, Abdel-Ghaffar and Koh (1982) used the shear modulus as functions of position within the dam to investigate 3-D dynamic behaviors. It has the form

$$G(x, y) = G_0\left(\frac{y}{H}\right)^{\frac{1}{3}}\left(1 - \left(\frac{x}{\frac{B}{2} - 2.2(H-y)}\right)^2\right) \tag{2.15}$$

where G_0 is a constant parameter.

It should be noted that the damping ratio increases with increasing shear strain while the shear modulus decreases with increasing shear strain. More comprehensive investigations from laboratory and field tests suggest that the main factors affecting shear moduli and damping factors for soils are strain amplitude, confining pressure, void ratio,

TABLE 2.2 Velocity of Transverse Wave (m/sec)

Zone Depth (m)	Shell	Core
0-5 5-30 30 <	$V_s = 245$ $V_s = 250y^{0.20}$ $V_s = 200y^{0.315}$	$V_s = 210$ $V_s = 180y^{0.35}$ $V_s = 180y^{0.35}$
Poisson's ratio	$\nu = 0.49\text{-}0.001y^{0.95}$	$\nu = 0.45\text{-}0.006y^{0.60}$

number of cycles of loading, and the degree of saturation for cohesive soils. For sand, the modulus values are strongly influenced by the confining pressure, the strain amplitude, and the relative density but not significantly by variation in grain-size characteristics. In case a dam is constructed mainly of cohesionless soils, the shear modulus G (at low strain) and confining pressure p' are related by

$$G = 1,000K_2 (p')^{1/2} \ lb/ft^2 \tag{2.16}$$

so that the influence of void ratio and strain amplitude can be expressed through their influence on the soil parameter K_2.

2.2.2.3 Forced vibration analysis

Supposing the dam shown in Fig. 2.2 is subjected to a horizontal upstream-downstream ground motion, $u_g(t)$, the equation (2.6) will become

$$\frac{\rho}{G}\frac{\partial^2 u}{\partial t^2} - \frac{\partial^2 u}{\partial y^2} - \frac{1}{y}\frac{\partial u}{\partial y} = -\frac{\partial^2 u_g}{\partial t^2} \tag{2.17}$$

The solution to equation (2.17) can be expressed

$$u(y, t) = \sum_{n=1}^{\infty} \frac{2J_0[Z_n(y/H)]}{\omega_n Z_n J_1(Z_n)} \int_0^t \ddot{u}_g \sin[\omega_n (t - t')] \, dt' \tag{2.18}$$

If viscous damping is included, then equation (2.18) will be modified to the form

$$u(y, t) = \sum_{n=1}^{\infty} \frac{2J_0[Z_n(y/H)]}{\omega_n Z_n J_1(Z_n)} \int_0^t \ddot{u}_g e^{-\zeta_n \omega_n (t - t')} \sin[\omega_{dn} (t - t')] \, dt' \tag{2.19}$$

where ζ_n = damping factor in the nth mode; and

$\omega_{dn} = \omega_n \sqrt{(1 - \zeta_n^2)}$ = damped natural angular frequency in the nth mode.

For small values of damping, $\omega_{dn} \approx \omega_n$. Thus, from equation (2.19), the absolute acceleration response is

$$\ddot{u}_a(y,t) = \sum_{n=1}^{\infty} 2\omega_n \left[\frac{J_0(Z_n y/H)}{Z_n J_1(Z_n)}\right] \int_0^t \ddot{u}_g e^{-\zeta_n \omega_n (t-t')} \sin[\omega_n (t-t')]\, dt' \qquad (2.20)$$

Equation (2.20) can be rewritten as

$$\ddot{u}_a(y,t) = \sum_{n=1}^{\infty} \omega_n \psi_n(y)\, V_n(t) \qquad (2.21)$$

where

$$\psi_n(y) = \frac{2J_0(Z_n y/H)}{Z_n J_1(Z_n)} \quad \text{and} \qquad (2.22)$$

$$V_n(t) = \int_0^t \ddot{u}_g e^{-\zeta_n \omega_n (t-t')} \sin[\omega_n (t-t')]\, dt' \qquad (2.23)$$

For a given ground acceleration record, $\ddot{u}_g(t)$, and dam, equation (2.20) can be evaluated numerically to obtain the absolute acceleration with depth.

Regarding the average value of k_h in the Section 2.2.1, it is worth noting that a theoretical derivation has been recommended by Seed and Martin (1966). Using equation (2.19), the distribution of shear stress, $\tau(y,t) = G\frac{\partial u(y,t)}{\partial y}$, can be derived. Considering the shear force, $F(y,t)$, induced by inertia force at the base of an arbitrary soil wedge, i.e.

$$F(y,t) = \tau(y,t)\, b = \left(\frac{1}{2}\rho b y\right)\ddot{u}_{av}(t) \qquad (2.24)$$

the average lateral acceleration $\ddot{u}_{av}(t)$ is

$$\ddot{u}_{av}(t) = \sum_{n=1}^{\infty} \frac{4GJ_1(Z_n y/H)}{\rho\omega_n H y J_1(Z_n)} V_n(t) \qquad (2.25)$$

$$\therefore k_h = \frac{1}{g}\ddot{u}_a(t)_{av} = \sum_{n=1}^{\infty} \frac{4GJ_1(Z_n y/H)}{g\rho\omega_n H y J_1(Z_n)} V_n(t) \qquad (2.26)$$

Note that the value of k_h is a function of time. Since the average acceleration varies with the depth y, the magnitude of k_h also varies with y.

2.2.2.4 Two-dimensional shear beam theory

The schematic of a typical dam is shown in Fig. 2.4(a). Fig. 2.4(b) shows the shear forces on the four internal faces of an infinitesimal element of a dam with sides *dy* and *dz* and width *b*. The forces acting on the element during free vibrations include the inertia force, and the shear forces, Q_{yx} and Q_{zx}. Equilibrium of the forces acting on the element in the x-direction yields the following equation of motion for a constant shear modulus (Martin 1965):

$$\frac{\rho}{G}\frac{\partial^2 u}{\partial t^2} = \frac{\partial^2 u}{\partial y^2} + \frac{1}{y}\frac{\partial u}{\partial y} + \frac{\partial^2 u}{\partial z^2} \tag{2.27}$$

For earth dams consisting mainly of cohesive materials, it is acceptable as a first approximation to assume a constant shear modulus. However, for dams constructed with

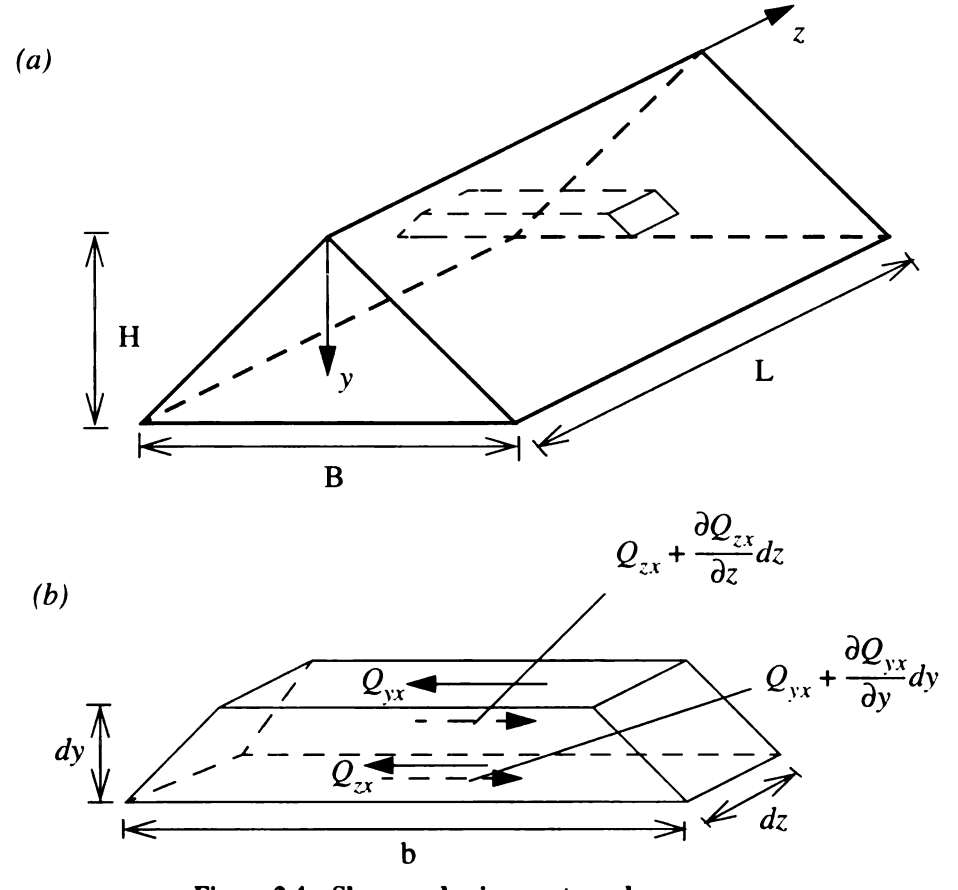

Figure 2.4 Shear wedge in a rectangular canyon

non-cohesive materials, it is more appropriate to assume that the average shear modulus varies with the depth from the crest in the form (Abdel-Ghaffar and Scott 1978, Gazetas 1980)

$$G_v = G\left(\frac{y}{H}\right)^{\beta} \tag{2.28}$$

where G is a nominal shear modulus equal to the shear modulus at the base. Substitution of equation (2.28) into equation (2.27) yields

$$\frac{\partial^2 u}{\partial t^2} = \frac{G(y/H)^{\beta}}{\rho}\left(\frac{\partial^2 u}{\partial y^2} + \frac{(\beta+1)}{y}\frac{\partial u}{\partial y} + \frac{\partial^2 u}{\partial z^2}\right) \tag{2.29}$$

where u is the lateral displacement of the dam and ρ is the mass density of the dam material. It is assumed that the displacements of the dam at its base and at its banks are zero, whereas at the crest the lateral shear force vanishes.

Using the separation of variables method, equation (2.27) can be uncoupled. By enforcing the boundary conditions, the dynamic characteristics of the dam model can be obtained (Ambraseys and Sarma 1967, Abdel-Ghaffar and Scott 1978, Martinez and Bielak 1980). The natural frequencies of vibrations are given by

$$\omega_{mn} = \frac{V_s}{H}\left(Z_m^2 + \left(\frac{n\pi H}{L}\right)^2\right)^{1/2} \tag{2.30}$$

where ω_{mn} is the frequencies of vibration modes, $V_s = \sqrt{G/\rho}$ = is the nominal velocity of propagation of shear waves within the dam, and Z_m are roots of the characteristic equation $J_0(Z_m)=0$. The corresponding modes of vibrations are expressed as

$$\Phi_{mn}(y, z) = J_0\left(\frac{Z_m y}{H}\right)\sin\left(\frac{n\pi z}{L}\right) \tag{2.31}$$

Fig. 2.5, Fig. 2.6 and Fig. 2.7 show the vibration modes for m=1 and n=1, m=1 and n=2, and m=2 and n=2, respectively.

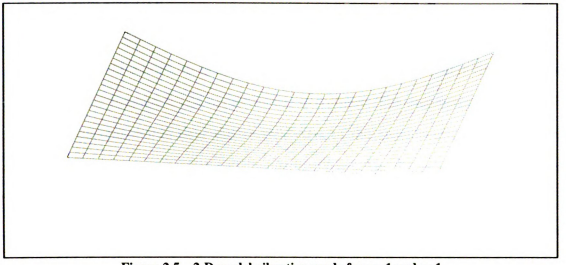

Figure 2.5 2-D model vibration mode for m=1 and n=1

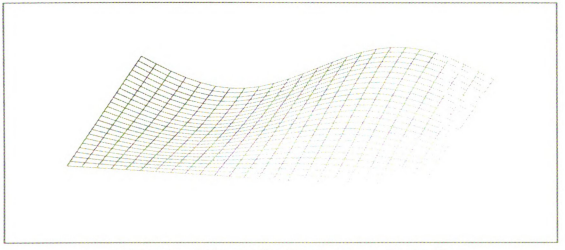

Figure 2.6 2-D model vibration mode for m=1 and n=2

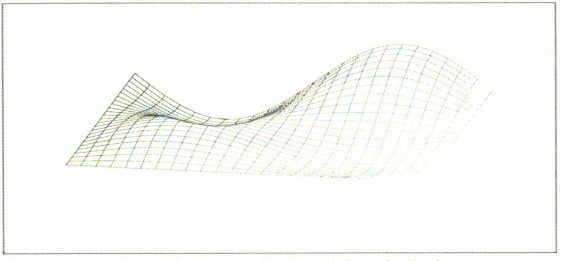

Figure 2.7 2-D model vibration mode for m=2 and n=2

2.2.2.5 Relevant research

Although the shear beam model treats earth dams as deformable structures, the analysis of the 1-D model, in general, overestimates the fundamental frequency and overestimates the frequencies of higher modes even more. The assumption of pure shear deformation is reasonable near the vertical axis of the cross section, but results in significant error near the upstream and downstream faces. The displacement near the faces of the dam may be significantly different form the center-line displacement, which is neglected in the theory. Apparently, the analysis does not give an adequate prediction of the dam behavior because the design criteria for earth dams are based on slope stability which is controlled by conditions near the free surfaces. Consequently, further work has been done in order to overcome the shortcomings. A summary of the most significant developments and studies is presented here.

- Hatanaka (1952) performed a 2-D shear beam analysis for dams in rectangular canyons and showed that shearing deformations are predominant. In addition, a rational design procedure using response spectra was developed.
- Martin (1965) conducted parametric studies using the 1-D shear beam model, and proposed a non-linear variation of the shear modulus due to confining pressure, in which the modulus was assumed to be proportional to the cube root of depth from the crest. The results differ from those using homogeneous shear beam models which was shown to be inadequate when dealing with the vibrations of earth dams.
- Ambraseys and Sarma (1967) summarized that the magnitude and time distribution of inertia force, geometric configuration, damping and strain-rate are the principal factors that control response characteristics. They used the 1-D shear beam model to obtain seismic coefficients by performing stability analysis on potential sliding blocks.

- Gazetas (1981) studied the response of embankment dams to longitudinal vibrations using a triangular elastic wedge model. Transverse cracks that can induce uncontrolled seepage through the dam and thereby result in piping failure, are mainly due to tensile stresses created by longitudinal vibrations of the dam. The numerical results indicate that, for a narrow dam ($L/H \leq 1.5$), the fundamental natural period is independent of the dam height and is only a function of the length and shear wave velocity. In contrast, the period depends only on the height for long dams. It was also found that axial deformations are more significant than shear deformations in narrow dams, while shear deformations are more important than axial deformations in relatively long dams.
- Oner (1984) studied the shear vibration of inhomogeneous earth dams in rectangular canyons using a shear wedge model. The effect of the restraint provided by lateral valley was considered in the analysis. The solutions indicated that the effect of the valley width to depth ratio and the modulus inhomogeneity are coupled. This coupling affects the mode shapes, frequencies, and modal participation factors. The fundamental period can be predicted, within 6-9% error, by using an average modulus value in the homogeneous shear wedge solution.
- Prato and Delmastro (1987) used a 1-D shear beam model coupled with an equivalent linear method for approximating the dynamic soil properties to analyze a gravel shell dam. The results compared favorably the more precise 2-D analyses. Crest accelerations were predicted within 5% of those given by 2-D analyses. Shear stress patterns and values within shells exhibited differences between 5 and 12%.
- Ernesto-Motta and Zeng (1993) studied the effect of travelling seismic waves on the dynamic response of earth dams, using a truncated 2-D elastic wedge. For comparison, 1-D and 2-D wedge models were also used without considering the travelling wave effect. The results showed that: (1) for the longitudinal mode of vibration, the greater the ratio of the height to the length of the complete wedge, the

more the natural transverse period of vibration of the 2-D wedge is less than that of the 1-D wedge; (2) when the phase difference of ground motion at both ends of the dam equals π, the amplification for a 2-D wedge is less than that for a 1-D wedge; and (3) in general, the displacement caused by an earthquake is greater for a 1-D model than for a 2-D model when considering travelling waves, but the acceleration response of a long 2-D wedge to travelling waves with a long dominant wave length is greater than that of a 1-D wedge.

2.2.3 Plane strain finite element model

The FEM for 2-D plane-strain analysis in earth dams was first presented by Clough and Chopra (1966). The structure was assumed to be of infinite length and loaded uniformly along the length so as to produced plane strain behavior of the cross section. The method can account for any arbitrary geometry and material property variations and can be applicable to the analysis of any elastic system subjected to any type of dynamic loading. Another significant advantage is that the method can be adapted to take account of non-uniform base motions in the width direction; that is, of the effects of seismic waves passing under the dam in which the wave lengths are short compared to the cross-section width of the dam base.

Concerning the finite element (FE) plane strain analysis procedure in general, it may be noted that: (1) compatibility is satisfied everywhere in the system; (2) equilibrium is satisfied within each element; and (3) equilibrium of stresses is not satisfied along the element boundaries, in general, but the nodal force resultants are in equilibrium. This local discrepancy in stress equilibrium represents the type and extent of the approximation involved in the FEM.

It has been the limitations of computer storage capacity and high costs that have generally restricted the use of FE models to the plane-strain case. The following lists the evolution of developments related to the 2-D FE model.

- Chopra (1967) compared the response of a shear wedge model with that of the 2-D FE model to a prescribed horizontal base acceleration (El Centro earthquake 1940). The important conclusion from this comparison was that the natural mode shapes obtained by the FEM differed significantly from those obtained with the shear wedge model. Only the fundamental mode resembles the shear wedge behavior, but even in this case the 2-D deformations are much more complex than those assumed in the shear wedge analysis. On the other hand, stresses near the faces of the dam computed by the FEM were found to depend significantly on the slope of the sides, with steeper side slopes resulting in greater stresses; this is in contrast to the shear wedge approach which yields stresses independent of the side slopes.
- Dibaj and Penzien (1967) studied the response of a 2-D FE model of a dam to horizontally travelling waves. It was concluded that the time variation of the ground motion must be taken into account especially for seismic waves with low velocity. They also concluded that the spatial variation of ground motion was negligible only when the ratio of base width to wave velocity is less than 0.1 second.
- Ghaboussi and Wilson (1973) modeled the soil as a porous elastic medium and studied the dam-reservoir interaction. The upstream shell and the central core were considered as a coupled two-phase fluid-solid zone. This was the first attempt determining the pore pressures and the intergranular stresses under earthquake loading conditions. It should be noted that, while in a local shear failure the soil regains its strength when the load reverses, once local liquefaction develops, the soil in that zone is likely to remain liquefied for the rest of the duration of the earthquake. It was also concluded that an important source of the pore pressure built up in the earth dams is due to the dilatancy of soil under shear deformation, which cannot be simulated by linearly elastic material models. Therefore, it was concluded that nonlinear material properties should be adopted.

- Martinez and Bielak (1980) combined a 2-D FE discretization of a dam's cross section with Fourier expansion in the longitudinal direction to obtain the response of dams in symmetric canyons.
- Mansuri et al. (1983) studied the liquefaction of earth dams due to shear straining, using a 2-D FE model with soil treated as a poroelastic material. The effect of elastic wave propagation and the volumetric strain resulting from an applied shear strain were considered. The results of an analysis of a hypothetical dam were observed to agree well with the observed liquefaction in the lower San Fernando Dam during the San Fernando Earthquake of February 8, 1971.

Comprehensive comparative studies of the linear viscoelastic predictions by the shear beam model and plane strain model has been reported by Tsiatas and Gazetas (1982) and Dakoulas and Gazetas (1985). The following are the main conclusion from these studies:

1. The two models yield very similar fundamental natural frequencies and fundamental mode shape. Specifically, the shear beam invariably under-predicts the natural period by about 10% in most cases.
2. The significant higher lateral modes computed with finite elements exhibit an increasingly stronger component of vertical deformation. The shear beam neglects this component and thereby leads to higher natural frequencies.
3. Peak values and time histories of horizontal relative displacements computed with the two models are in very close agreement, the discrepancies being within 10% for all dams and all seismic excitations studied.
4. The most significant disagreement of the two models involves absolute accelerations of relatively flexible dams, for which the shear-beam frequently overestimates the crest peak acceleration by as much as 50%.
5. In general, the shear beam also tends to overestimate slightly the largest peak values of strain, which usually occur within the upper third of the dam. On the other hand,

shear stresses are in very good accord; the shear beam predictions are approximately equal to the average-across-the-width shear stress computed using the FEM.

2.2.4 Three-dimensional model

It has been conventional practice in the past to evaluate the dynamic response of an earth dam by making plane-strain analyses of several representative sections through the dam. The assumption of plane-strain conditions is valid for infinitely long dams subjected to synchronous lateral motion on longitudinal lines along the base. However, for dams built in narrow valleys, which is the frequent case in mountainous regions, plane strain analyses can give grossly misleading results. The presence of relatively rigid abutments creates a 3-D stiffening effect. As the canyon becomes narrower, natural frequencies increase and displacement mode shapes tend to become sharper. Thus while much effort is always directed towards simplification of the evaluation procedure, it is sometimes necessary to use more sophisticated analyses in the interest of improved understanding and accuracy.

A number of studies using 3-D model have been performed in the 1980s. For earth dams with a plane of symmetry perpendicular to the longitudinal axis, Martinez and Bielak (1980) developed a numerical procedure for 3-D FE analysis, and concluded that the 3-D deformation behavior yields higher stiffness characteristics than does the 2-D idealization. Ohmachi (1981) extended the shear wedge model into a simplified finite element model, and concluded that three dimensionality has an important effect on the earthquake response of dams located in narrow canyons. Abdel-Ghaffar and Koh (1982) presented a more rigorous although computationally quite efficient 3-D semi-analytical solution for dams built in canyons of any shape but having a plane of symmetry. This solution is based on the Rayleigh-Ritz method with the shear-beam shapes or even simple sinusoids as "basis function", and involves an appropriate transformation of the dam geometry into a cuboid. An attempt was made to reproduce the recorded seismic response of the Santa Felicia dam

during the 1971 San Fernando earthquake. Of particular significance is the versatility of the method which has been extended to formulate a realistic approximate solution for the non-linear inelastic response of dams in non-rectangular canyons (Elgamal et al. 1984). Makdisi et al. (1982), Mejia et al. (1982) and Mejia and Seed (1983) developed relatively efficient 3-D FE formulations to obtain the steady state and transient responses of homogeneous dams in triangular canyons. The results show that the presence of the rigid triangular boundary increases the fundamental frequencies, and seems to substantially increase the seismic acceleration while decreasing the seismic strains.

More sophisticated deterministic analyses including non-linear effects and differential ground motion are summarized below:

- Prevost et al. (1985) performed 2-D and 3-D non-linear finite element analyses of the Santa Felicia earth dam utilizing a multi-surface plasticity theory. In the study, all three orthogonal components of the input ground motions were considered, rather than only base excitation in the upstream-downstream direction. The results are more reliable because all possible vibration modes of the dam were taken into account. Comparing the responses from the 2-D model with that of the 3-D model, it was found that the 2-D model predicted the permanent shear strain to be 30% lower when the dam was subjected to strong shaking. The three-dimensionality of the dynamic earthquake responses of earth dams was shown to be important.
- Abdel-Ghaffar and Elgamal (1987) developed a simplified analytical-numerical procedure based on a Galerkin formulation of the 3-D equations of motion. A simplified elastic-plastic technique was applied to compute the non-linear seismic 3-D response of the Santa Felicia dam. The linear mode shapes were obtained using low-strain elastic moduli and a variational energy approach utilizing both Hamilton's principle and the Rayleigh-Ritz method. The results of the simplified analysis were found to compare favorably with those of an elaborate 3-D FE model.

- Lacy and Prevost (1987) modeled soil as a non-linear two-phase system, and used FE discretization of the field equations followed by time integration to obtain the resulting non-linear semi-discrete FE equations. Since earth dams are susceptible to liquefaction failure, an integrated, coupled treatment of the dynamic interaction between the soil skeleton and the water fluid phase was used in the analysis. The results of the numerical calculations were in good agreement with the recorded response of the dam.
- Haroun and Abdel-Hafiz (1987) performed a deterministic study of the effect of differential ground motion on the displacement response of earth dams using a 2-D shear beam model and the FE model. The effective force vector was varied at each time step to reflect both the temporal and spatial variations of the input ground motion. The results for spatially uniform ground motion was shown to be conservative.

2.2.5 Model testing

2.2.5.1 Elastic vibration test

The purpose of performing elastic vibration tests on a model dam is to experimentally determine the natural period and mode shape. The similarity between the prototype and the model is determined by the law of similitude. According to elastic vibration theory of the shear beam model presented in Section 2.2.2.1, the natural period is proportional to $H\sqrt{\rho/G}$. Therefore, if subscript p and m are added to express the quantities relating to the prototype and the model, respectively,

$$\frac{T_p}{T_m} = \frac{H_p}{H_m}\sqrt{\frac{\rho_p G_m}{\rho_m G_p}} \tag{2.32}$$

If the natural period T_m of the model is measured in the model test, the natural period T_p of the prototype may be calculated from equation (2.32). The elastic modulus of a real dam will vary depending on the soil, construction process and the length of time which has

elapsed since construction. However, its average value ranges from 50 to 270 kg/cm^2. This was calculated from measurements of propagation velocities of elastic waves in several existing earth dams (Severn, 1979). The propagation velocity of transverse waves and the Poisson's ratio for rockfill dams are given in Table 2.2.

2.2.5.2 Dynamic failure test

In an earth dam failure test, a valid similarity between the displacements, the major external forces and resisting forces of the prototype and the model is required. In this case major external forces consist of the weight of the dam and the earthquake-induced inertia force, and the major resistance force comes from the frictional and cohesive forces. The following symbols are used: (Okamoto 1984)

L = length; λ = length scale factor; u = displacement; f = force; τ = stress;

s = strength of materials; and θ = angle of internal friction.

The similitude of displacement is the same as the similarity of length. Thus,

$$\frac{u_m}{u_p} = \frac{L_m}{L_p} = \lambda \tag{2.33}$$

The ratio between the weight of the model and that of the prototype will be

$$\frac{\rho_m g L_m^3}{\rho_p g L_p^3} = \frac{\rho_m}{\rho_p}\lambda^3 \tag{2.34}$$

The same ratio must be valid for force f. As stress is force per unit area,

$$\frac{\tau_m}{\tau_p} = \frac{f_m/L_m^2}{f_p/L_p^2} = \frac{\rho_m}{\rho_p}\lambda \tag{2.35}$$

Since the strength of the material is of the same order as stresses,

$$\frac{s_m}{s_p} = \frac{\rho_m}{\rho_p}\lambda \tag{2.36}$$

The strength of granular material is given by the product of the normal stress and coefficient of friction. However, since the similitude of normal stress satisfies equation (2.35), the coefficient of friction must be identical for the prototype and model. Namely,

$$\tan\theta_m = \tan\theta_p \tag{2.37}$$

The objective of a vibration test is to determine the displacement and surface strain of the dam during earthquakes taking the detailed configuration of the valley into consideration. The type of damage may be observed during the dynamic failure test. Regarding the material modeling, plaster or dense gelatin is generally used for the valley and gelatin for the dams, since these materials are convenient for reproduction of the shapes of valleys and dams.

2.2.6 Field measurement

The seismic behavior of earth dams can be learned by installing instruments to carry out observations during earthquakes. Measurements have been made on and within dams, including dynamic earth pressures, dynamic pore-water pressures and residual deformations after an earthquake. There is no difficulty when instruments are installed on the dam or on the ground, but when they are set up within the dam, there is liable to be problems with moisture entering the instruments, tilting of instruments, and breaking of lead wires due to dam settlement or heavy equipment used during construction. Therefore, care must be taken on the installation of instruments.

Abdel-Ghaffar and Scott (1981a) performed full-scale dynamic tests, including ambient vibration tests, forced vibration tests and popper tests, which were carried out on the Santa Felicia dam. The measuring equipment consisted of: (1) motion sensing transducers (SS-1 seismometer by Kinemetrics, Inc.); (2) recording instruments including signal conditioners (SS-1 also by Kinemetrics, Inc.), and an oscillograph recorder (7418A by Hewlett-Packard), and tape recorders (3460A by Hewlett-Packard); (3) force generating systems or shaking machines capable of producing a force up to 44,500 N (10,000 lbs); and

(4) data processing instruments including an electronic analog-digital converter (DDS-1103 by Kinemetrics) and a digital signal processor (SD360 manufactured by Spectral Dynamics Corp.).

According to the test results, it was found that existing shear-beam theories do not predict all the upstream-downstream modes, indicating the inadequacy of these theories for comprehensive earthquake response computation. The correspondence between resonant frequencies from full-scale tests and those estimated from the spectral analysis of two earthquake records (San Fernando earthquake 1971 and Southern California earthquake 1976) is reasonably good over the first few frequencies, but higher modes could not be reliably matched. It should be noted that full-scale tests at levels of excitation much lower than those experienced during the earthquakes produced substantial changes in the dynamic properties of the dam. Thus it was concluded that the behavior under real earthquakes was significantly non-linear.

Several actual measurements of earth dam responses during earthquakes has been conducted in the past. Attention has generally been paid to three major concerns: (1) earthquake acceleration; (2) magnification of the maximum acceleration at the tops of dams; and (3) stresses developed in the embankment. The accelerations of dams induced by earthquakes is important in determining the earthquake inertia forces acting on the dam. The ratio of the maximum acceleration at the ground surface and the maximum acceleration at the crest of a dam is also of interest because most failures occur near the crest. In addition, the stresses developed in the embankment are mainly due to earth pressure and pore water pressure. Their magnitude has a significant effect on the seismic stability of dams. Although the measured responses can give direct information for design, the cost of testing prohibits its widespread use.

2.3 Recent Studies

Since most structures are quite sensitive to the details of ground excitation, which are of an unpredictable nature, little confidence can be achieved form the results of a single deterministic dynamic analysis using a recorded or artificially generated ground motion. To avoid the expense and effort required for multiple deterministic analyses, random vibration methods have been developed. In the 1980s, the application of probabilistic methods to the seismic analysis of earth dams increased notably:

- Gazetas, DebChaudhury and Gasparini (1981 & 1982) used the random vibration technique to study the seismic response of earth dams. The Kanai-Tajimi spectral density function was used to characterize the ground motion, and a shear beam model with a variable cross section was used to characterize the dam. However, due to the limitations of the idealized model of the dam, wave passage effects were neglected.
- Gasparini and Sun (1982) used the FEM in conjunction with random vibration analysis. They studied the effect of correlation between vertical and horizontal ground motion components, but did not account for spatially varying earthquake ground motions (SVEGM).
- Luco and Wong (1986), and Harichandran (1987) studied the response of rigid mat foundations to SVEGM. However, it is rather unreasonable to consider an earth dam as being located on a rigid mat foundation. If the base of a dam is considered as rigid, then the averaging effect over its large base dimension would reduce the earthquake excitation drastically, severely under-predicting the dam response.
- Novak and Suen (1987) are the first to include SVEGM in the random vibration analysis of dams. Their study was a preliminary one, in which the dam was modeled as a prismatic beam, wave propagation effects were neglected, and only vertical excitation was considered. They did include dam-foundation interaction effects,

and found that while this was important for concrete dams, it may be neglected for earth dams. In spite of the rather simplistic model used, their study confirmed that bending distortions produced by spatially correlated ground motion substantially increased the stresses within the dams.

- Dakoulas and Hashmi (1992) presented an analytical model for the steady-state lateral response of earthfill and rockfill dams in canyons subjected to a steady train of harmonic SH waves incident at an arbitrary angle. The dam was modeled as a 2-D shear beam with a triangular cross-section, while the canyon was considered to be rectangular and consisting of elastic rock. The result showed that obliquely incident waves traveling at an angle of about 55^{o}-60^{o} to the horizontal yielded the maximum response.
- Ramadan and Novak (1992) addressed dam-reservoir-foundation interaction on a long gravity dam under SVEGM. A simplified mathematical model which accounts for spatial coherence effects as well as wave passage effects was formulated in the study. However, the analysis is adequate only for long gravity dams and may not be suitable for the analyzing the behavior of earth dams under earthquake conditions.

Based on the above review, it is apparent that although a substantial body of work exists on the seismic response of earth dams, only marginal attention has been paid to include the effects of SVEGM. This is due to the fact that spatial variation of strong ground motion has been quantified only very recently, based on actual observations from dense seismograph arrays (Loh 1985, Harichandran and Vanmarcke 1986, Harichandran 1987, Abrahamson et al. 1990, Schneider et al. 1990). A new thrust is therefore necessary to include the effect of SVEGM on the seismic analysis of earth dams.

3. DETERMINISTIC RESPONSE OF THE SANTA FELICIA EARTH DAM

3.1 Description of Santa Felicia Dam

The Santa Felicia earth dam is a modern rolled-fill earth embankment located on Piru Creek, 65 km northwest of Los Angeles. It is owned by the United Water Conservation District of Ventura County and was completed in December 1955. The dam, shown in Fig. 3.1, is 83.8 m (275 ft) high above its rock foundation and 137.2 m (450 ft) long across the valley at the base. The crest has a width of 9.14 m (30 ft) and a maximum length of 388.6 m (1,275 ft). The dam is made of a central impervious core and pervious shell upstream and downstream. The core and shell materials are basically alluvial, consisting of clay, sand, gravel and boulders. The core rises from bedrock with a slope of 0.33:1. The shells rest on existing stream gravel, 22.9 m (75 ft) in height. Upstream and downstream slopes have slopes of 2.25:1 and 2:1, respectively.

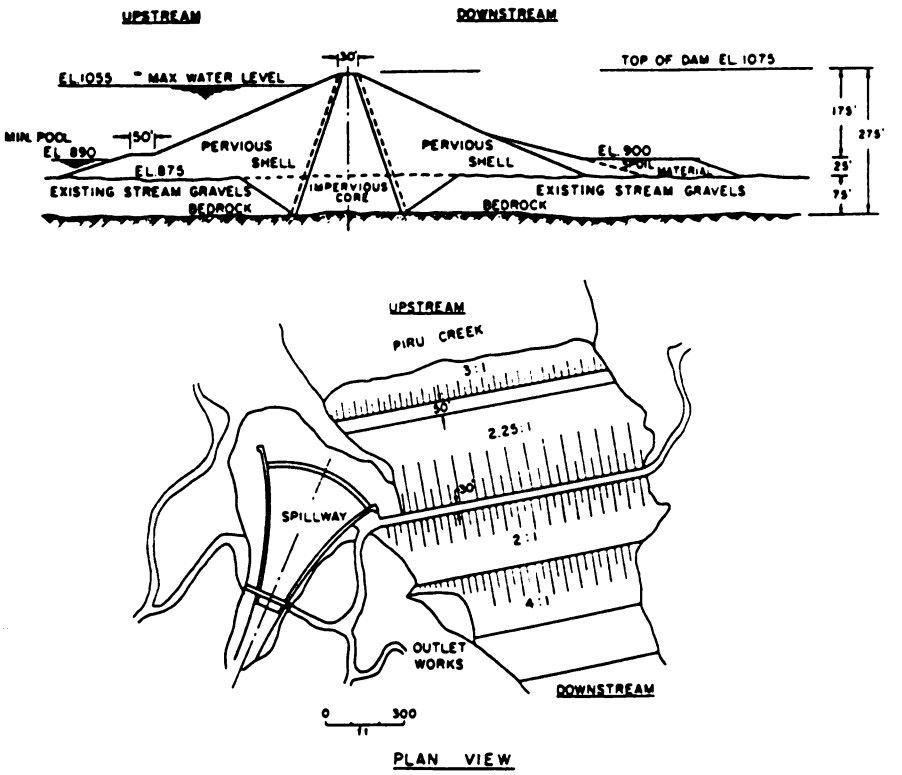

Figure 3.1 Structural Details of Santa Felicia Earth Dam

Fig. 3.2 is the side view of the Santa Felicia dam model, which shows an impervious clay core covered by a sand and gravel shell resting on a stiff layer of gravel and sand down to bedrock. Due to confining pressure, the elastic moduli of the soil varies with the depth from the crest of the dam. The low strain elastic moduli for each material at each depth were computed from the results of both shear wave velocity measurements and full-scale dynamic tests performed at the site and have been reported by Abdel-Ghaffar and Scott (1981). The elastic shear moduli back-calculated from those measurements and used in the analysis are listed in Table 3.1 (adopted from Prevost et al., 1985). The material zones listed in Table 3.1 are shown in Fig. 3.3. Poisson's ratio is assumed equal to 0.45 for the clay core and 0.30 for the remaining materials. Saturated unit weights of 20.59 kN/m^3 (134 pcf) and 22.17 kN/m^3 (141 pcf) are used for the clay and the remains, respectively.

Prevost et al. (1985) simplified the model and assumed zone 5S to be stream gravel. This simplification on author's model (Case I) causes an error in the fundamental natural frequency of about 3% compared with the model with pervious shell material at zone 5S (Case II). The first ten natural frequencies of the model (Case II) used in the study and of the simplified model (Case I) are compared in Table 3.2.

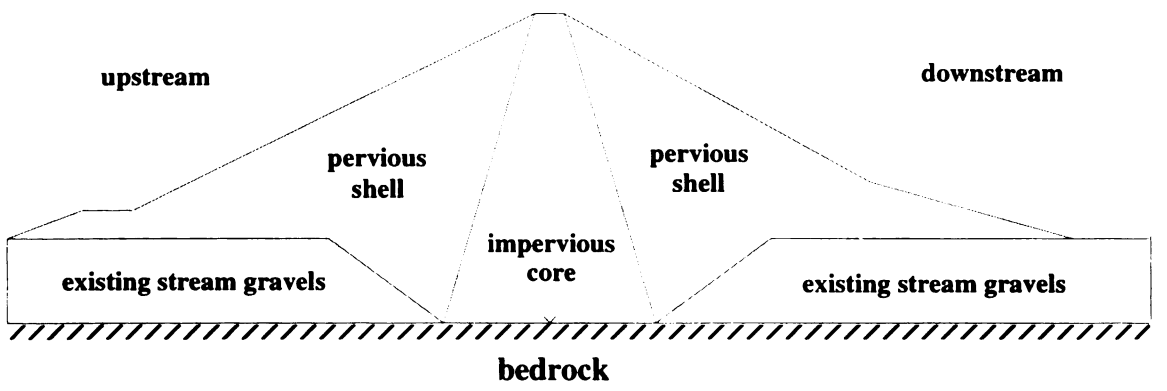

Figure 3.2 Santa Felicia earth dam model side view

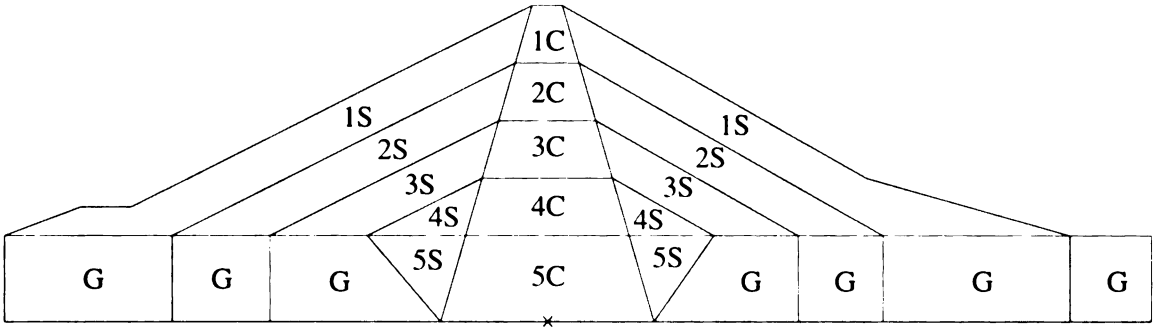

Figure 3.3 Illustration for different material zones

TABLE 3.1 Low strain shear moduli for Santa Felicia earth dam

Depth below crest (ft)	Zone number	Core (lb/ft^2)	Zone number	Shell (lb/ft^2)	Zone number	Gravel (lb/ft^2)
0-50	1C	2,441,492	1S	1,725,423		
50-100	2C	3,755,302	2S	2,939,447		
100-150	3C	4,414,405	3S	3,781,540		
150-200	4C	4,763,929	4S	3,972,660		
200-275	5C	4,763,929	5S	4,062,370	G	39,726,600

TABLE 3.2 Natural frequencies (Hz) compared with simplified model

Mode	Case II (the model used)	Case I (simplified Model)	Mode	Case II (the model used)	Case I (simplified Model)
1	1.392	1.427	6	1.859	1.873
2	1.466	1.510	7	1.965	1.982
3	1.582	1.609	8	2.138	2.154
4	1.812	1.812	9	2.244	2.259
5	1.820	1.820	10	2.303	2.338

3.2 Model Assumptions

3.2.1 Geometry

The Santa Felicia earth dam is located on Piru Creek whose banks on both sides do not exactly have the same shape. However, in this study it is assumed to be symmetric about the middle of the dam axis. This simplification does not have a significant effect on the response, which was found by Elgamal and Abdel-Ghaffar (1987). Another simplification made was to terminate the very long dimension of the existing stream gravel in the upstream-downstream direction shortly after the extent of the pervious shell.

3.2.2 Soil properties

Soil is, in reality, an inhomogeneous, anisotropic, nonlinear and hysteretic material. During an earthquake, its dynamic shear modulus decreases with increasing shear strain, while its damping ratio increases with increasing shear strain. However, in this study the emphasis was on obtaining better insight into the effect of SVEGM rather than on complex material models and so linearly elastic, isotropic dam materials were assumed in the analysis. In addition, low strain viscous damping is adopted to facilitate a simple finite element dynamic analysis. In this study, the increase in the pore water pressure of the soil during seismic response is neglected.

3.2.3 Hydrodynamic effect

It has been reported that the hydrodynamic effect on earth dams is not significant compared to the response due to earthquakes. Assuming that water is incompressible and that the ground motion is horizontal, Zangar (1955) reported that the water pressure acting against an inclined upstream face decreases with decreasing angle of inclination. For the case of the Santa Felicia dam, the water pressure is only one-fifth of that acting on a vertical upstream face. As a result, the hydrodynamic effect may be important for concrete gravity dams with a steep upstream surface (Chopra and Gupta 1981, Hall and Chopra 1982), but it is negligible on earth dams.

3.2.4 Dam-foundation interaction

It has been concluded that soil-structure interaction is important for concrete gravity dams but insignificant for earth dams built on rigid foundations (Chopra and Perumalswami 1969, Idriss et. al 1974, Novak, 1987). Because the material properties of concrete gravity dams are close to those of rock foundations, resonant vibration is very likely to occur during earthquake excitation. For the Santa Felicia dam, since the magnitudes of the earth dam stiffnesses are much smaller than those of the foundation stiffness, the vibration characteristics of the dam differ greatly from that of the bedrock. Therefore, dam-foundation interaction can be neglected so that the free-field bedrock motions may be applied at the base of the dam and the responses analyzed directly.

3.2.5 Radiation damping

When an earth dam subjected to ground motion vibrations, energy dissipation may take place through feedback into the ground soil. Radiation damping is considered as the energy loss through partial refraction of the waves in the soil back into bedrock. Finite element methods have inherent difficulties in modeling the radiation damping effects (Seed et al. 1975). Dakoulas and Hashmi (1992) related the radiation damping of the dam-foundation system to the effect of the impedance ratio. By observing acceleration amplification corresponding to different impedance ratios between canyon and dam, they concluded that the flexibility of the canyon rock has a dramatic effect on the response of earth dams, as it affects the amount of energy radiated back to the canyon. However, for a dam built in a rigid canyon, the effect of radiation damping is not significant, and hence it is neglected in this study.

3.3 Modeling and Analysis using I-DEAS VI.i

3.3.1 Introduction

Deterministic analysis of the Santa Felicia dam was performed using I-DEAS VI.i finite element program. The simultaneous vector iteration technique was used to obtain the dynamic modes of the dam. The I-DEAS computer software was developed and marketed

by Structural Dynamics Research Corporation of Milford, Ohio. I-DEAS provides a broad array of analysis and pre- and post-processing tools that are suited for this study. The main features of I-DEAS families used in modeling and analysis are briefly presented in Appendix A.1.

3.3.2 Finite element model

The three-dimensional finite element model, shown in Fig. 3.4, was used for all analyses in this study. The model consists of 1,004 nodes and 4,140 tetrahedral elements. Since the dam is located on a rigid rock base, 288 nodes on the boundary surface between the dam and the valley are completely restrained. A brief description of the modeling procedures used in I-DEAS VI.i is presented in Appendix A.2.

3.3.3 Free vibration analysis

The free vibration characteristics of a dam is fundamental to understanding the behavior of the dam during an earthquake. The free vibration characteristics are represented by natural frequencies and vibration modes and can be computed by performing modal analysis in I-DEAS. The steps for free vibration analysis are described in Appendix A.3.

In the FE method, there is a trade-off between computational effort and numerical accuracy. Progressively finer meshes were used to determine the number of elements required for acceptable accuracy. Four cases using coarser to finer finite element meshes

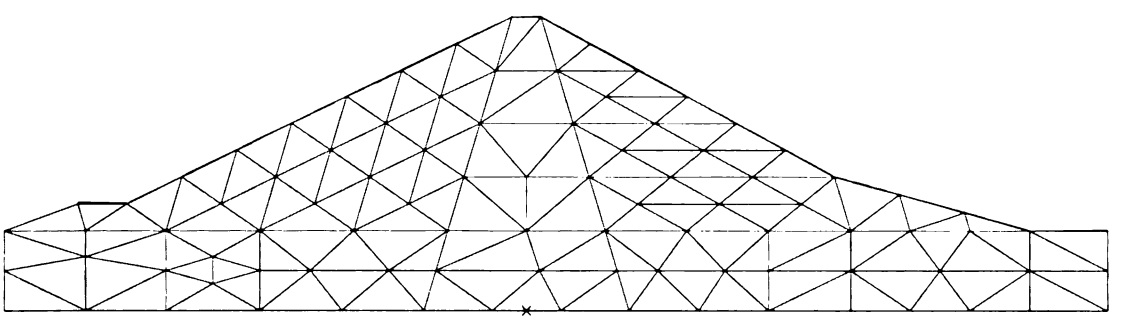

Figure 3.4 Finite Element Mesh

are compared in Table 3.3. The elapsed time for the analyses listed in the table is for an HP model 715/50 UNIX workstation. Ten modal frequencies are solved for in each case. The results are listed in Table 3.4. Based on the convergence of the first ten modal frequencies, the third case was selected as being sufficiently accurate. The first eighty natural frequencies for the third case are listed in Table 3.6, and these agree well with values reported in previous studies (Abdel-Ghaffar and Scott 1979, Prevost et al. 1985). The vibration modes may be either symmetric or antisymmetric about the mid-plane of the dam

TABLE 3.3 Comparison of elapsed time for solving ten vibration modes

Case	Average element size (ft)	Total number of elements	Total number of nodes	CPU time (sec)
I	100	1916	491	196
II	85	2626	666	363
III	70	4140	1004	810
IV	55	5952	1446	874

TABLE 3.4 Comparison of natural frequencies (Hz) using different mesh sizes

Mode	Case I	Case II	Case III	Case IV
Mode 1	1.414	1.400	1.391	1.385
Mode 2	1.491	1.474	1.466	1.458
Mode 3	1.631	1.604	1.582	1.568
Mode 4	1.951	1.802	1.812	1.634
Mode 5	1.993	1.973	1.820	1.648
Mode 6	2.235	2.163	1.859	1.825
Mode 7	2.338	2.261	1.965	1.937
Mode 8	2.355	2.296	2.138	2.088
Mode 9	2.441	2.362	2.244	2.110
Mode 10	2.593	2.464	2.303	2.195

axis. The types of the first 20 vibration modes are shown in Table 3.5. And the first eight mode shapes are shown in Figs. 3.5 and 3.6.

3.3.4 Response to ground motion

A convergence analysis indicated that about 80 vibration modes were required in order to obtained an adequately accurate response to the earthquake excitation shown in Fig. 3.7 which is similar to the El Centro accelerogram. The excitation was applied at all nodes on the boundary in the upstream-downstream direction. A viscous damping ratio of 0.06 corresponding to low strain deformation was adopted for all modes. The steps used in I-DEAS to perform deterministic dynamic analysis are briefly described in Appendix A.4.

The ground acceleration, velocity and displacement in the upstream-downstream direction was specified at nodes along the dam and rock interface. Figs. 3.8 and 3.9 show the velocity and displacement time histories obtained by integrating the acceleration time history in Fig. 3.7. Fig. 3.8 shows that the final ground velocity is not zero as expected.

TABLE 3.5 Types of mode for the first 20 modes

Mode no.	Type of Mode	Mode no.	Type of Mode
1	Symmetric	11	Anti-symmetric
2	Anti-symmetric	12	Anti-symmetric
3	Anti-symmetric	13	Symmetric
4	Anti-symmetric	14	Anti-symmetric
5	Symmetric	15	Symmetric
6	Symmetric	16	Symmetric
7	Symmetric	17	Symmetric
8	Anti-symmetric	18	Anti-symmetric
9	Anti-symmetric	19	Symmetric
10	Symmetric	20	Symmetric

TABLE 3.6 Natural Frequencies

Mode	Natural Freq. (Hz)	Mode	Natural Freq. (Hz)	Mode	Natural Freq. (Hz)	Mode	Natural Freq. (Hz)
1	1.392	21	2.807	41	3.356	61	3.876
2	1.466	22	2.814	42	3.371	62	3.880
3	1.582	23	2.837	43	3.384	63	3.937
4	1.812	24	2.889	44	3.411	64	3.940
5	1.820	25	2.911	45	3.446	65	3.958
6	1.859	26	2.929	46	3.499	66	3.974
7	1.965	27	2.950	47	3.507	67	4.008
8	2.138	28	2.964	48	3.590	68	4.029
9	2.244	29	2.966	49	3.597	69	4.065
10	2.303	30	2.980	50	3.659	70	4.081
11	2.341	31	3.041	51	3.694	71	4.099
12	2.430	32	3.069	52	3.709	72	4.105
13	2.455	33	3.093	53	3.724	73	4.142
14	2.461	34	3.143	54	3.745	74	4.167
15	2.493	35	3.167	55	3.752	75	4.179
16	2.511	36	3.184	56	3.802	76	4.192
17	2.587	37	3.251	57	3.803	77	4.210
18	2.609	38	3.258	58	3.814	78	4.212
19	2.640	39	3.298	59	3.831	79	4.247
20	2.756	40	3.325	60	3.849	80	4.292

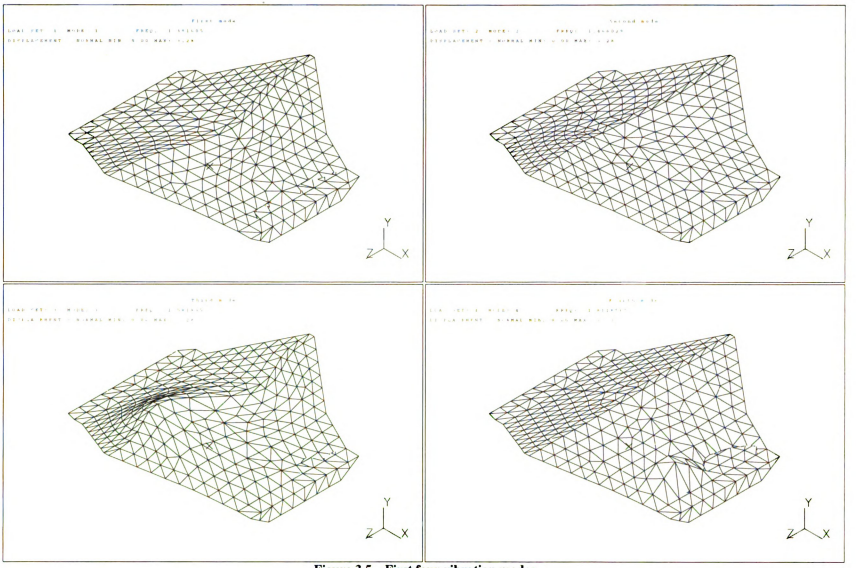

Figure 3.5 First four vibration modes

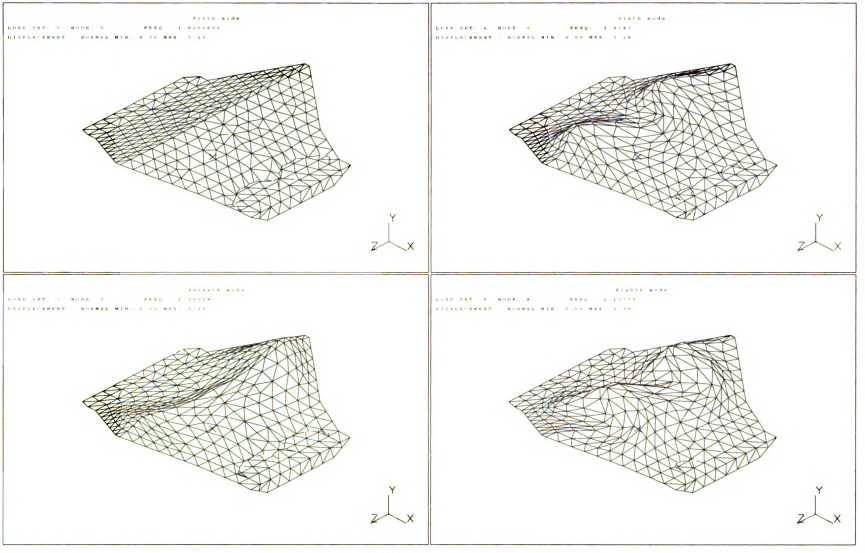

Figure 3.6 Vibration modes 5, 6, 7 and 8.

Typically, baseline correction procedures are employed to correct the acceleration time history so that the final ground velocity is zero. However, for the convergence analysis performed here, base line correction is not necessary and hence it was not performed.

Table 3.7 lists some nodal responses computed with an increasing number of vibration modes. The maximum acceleration responses at four different locations were computed in order to study the sensitivity of the response to the number of vibration modes included in the analysis. The table indicates that using the first eighty modes yields sufficient accuracy in the computations.

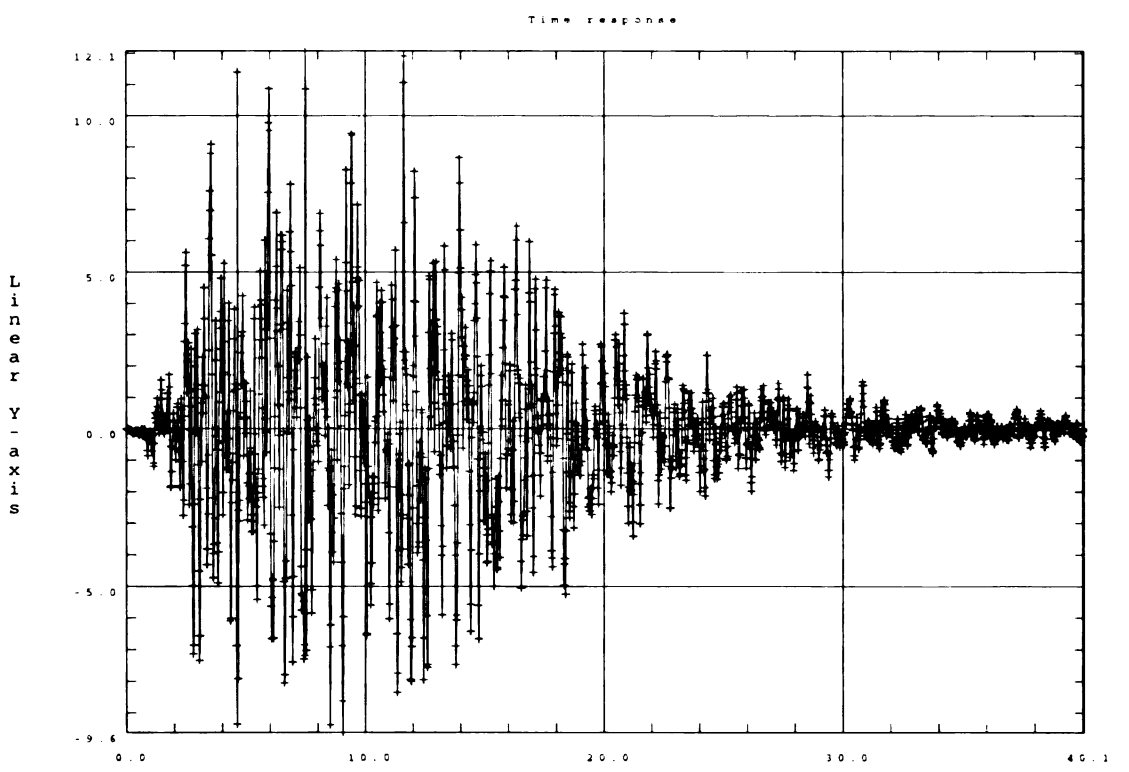

Figure 3.7 Accelerogram similar to the E1 Centro, California, earthquake of May 18, 1940

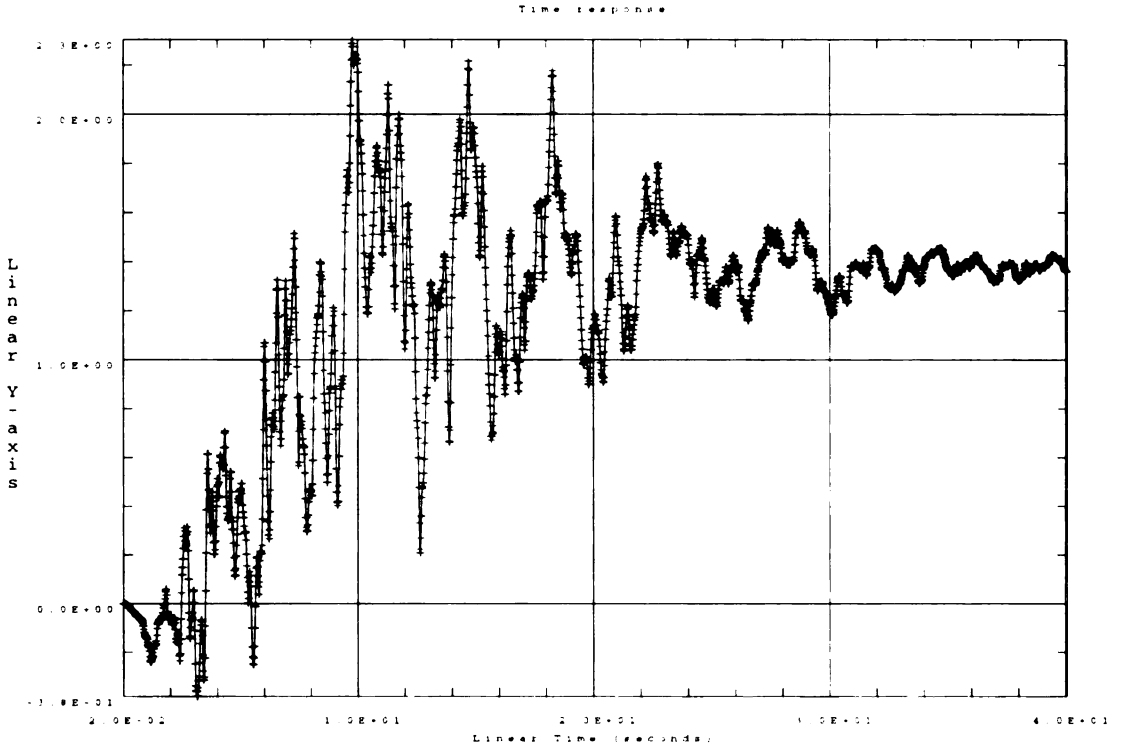

Figure 3.8 Velocity excitation

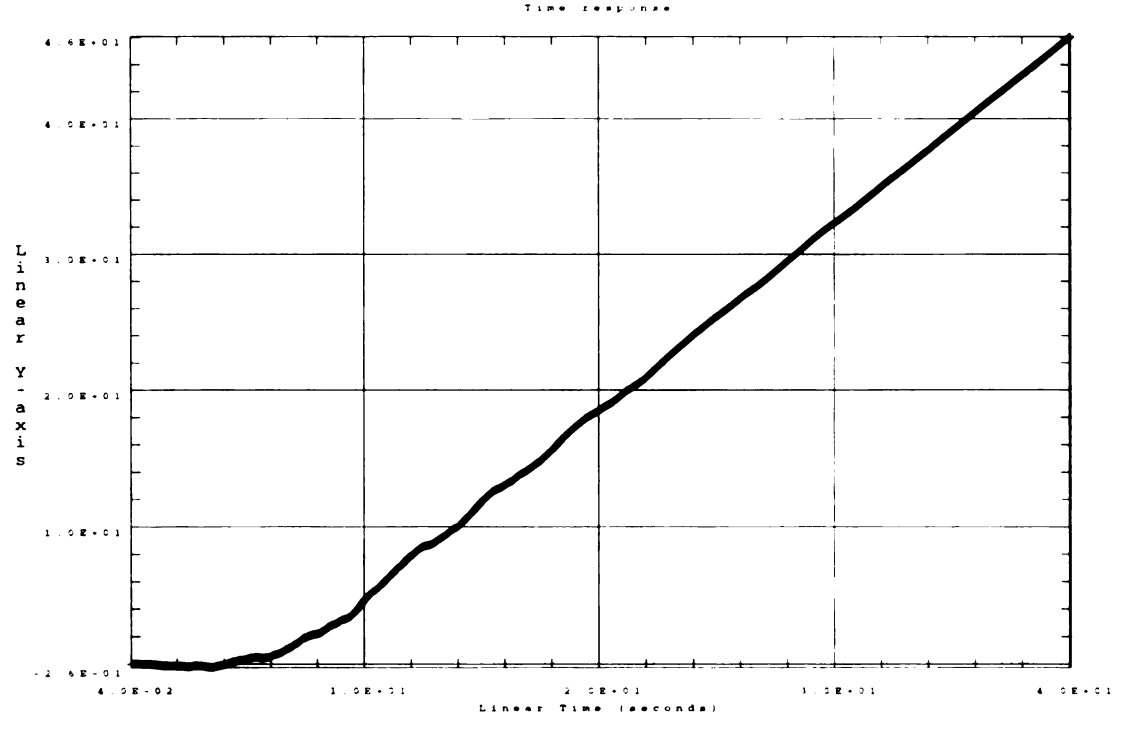

Figure 3.9 Displacement excitation

TABLE 3.7 Maximum acceleration (ft/sec^2) response to different number of modes

Number of activated modes	Middle point at the crest	Side point at the crest	point on the upstream side	Point on the downstream side
20	45.1	42.3	11.0	12.0
40	45.0	38.6	11.0	12.0
60	46.0	41.0	11.3	12.3
70	48.1	41.4	11.3	12.0
80	47.1	40.7	11.0	12.0
90	48.1	41.8	11.0	11.7
100	47.6	40.6	11.0	12.0

3.4 Types of Failures in Earth Dams

Over the years several types of earthquake damage have been observed in earth dams and embankments (Seed et al. 1978). Three major factors affect the stability and performance of an embankment during an earthquake: (a) section geometry (upstream and downstream slopes); (b) construction method and compaction procedure; and (c) type of embankment and foundation material. The possible ways in which an earth dam might fail during an earthquake include (Sherard et al. 1963):

1. Failure due to disruption of the dam by major fault movement in the foundation.
2. Slope failures induced by ground motions.
3. Loss of freeboard due to differential crest settlement.
4. Piping failure through cracks induced by the ground movements.
5. Overtopping of the dam due to failure of the spillway or outlet works.

In general, the principal types of damage can be classified as sliding failure, liquefaction failure, longitudinal cracks, transverse cracks, and piping failure.

3.4.1 Sliding failure

Sliding, as shown in Fig. 3.10, is a major type of damage that can occur in earth dams subjected to earthquake ground motions. Sliding initially causes settlement and subsequently leads to dam failure. The slope stability of earth dams is usually evaluated in terms of the shear strength of soils and the Mohr-Coulomb strength criterion is often used to characterize local failure. According to the Mohr-Coulomb criterion, the shear strength of the soil, τ_f, is expressed as

$$\tau_f = c + \tau' \tan\phi \tag{3.1}$$

where τ' = effective normal stress on the failure surface, and c and ϕ are the cohesion and angle of internal friction, respectively. When earthquake-induced maximum shear stress exceeds the shear strength of soils, local yielding is expected to occur. Consequently, if the shear strength along a trial sliding surface cannot resist destabilizing seismic forces, sliding failure may occur.

3.4.2 Liquefaction failure

Under earthquake conditions, due to rapid cyclic straining, gravity loading is transferred from soil solids to the pore water. This results in an increase of pore water pressure with a reduction in the capacity of the soil to resist loading. This process by which

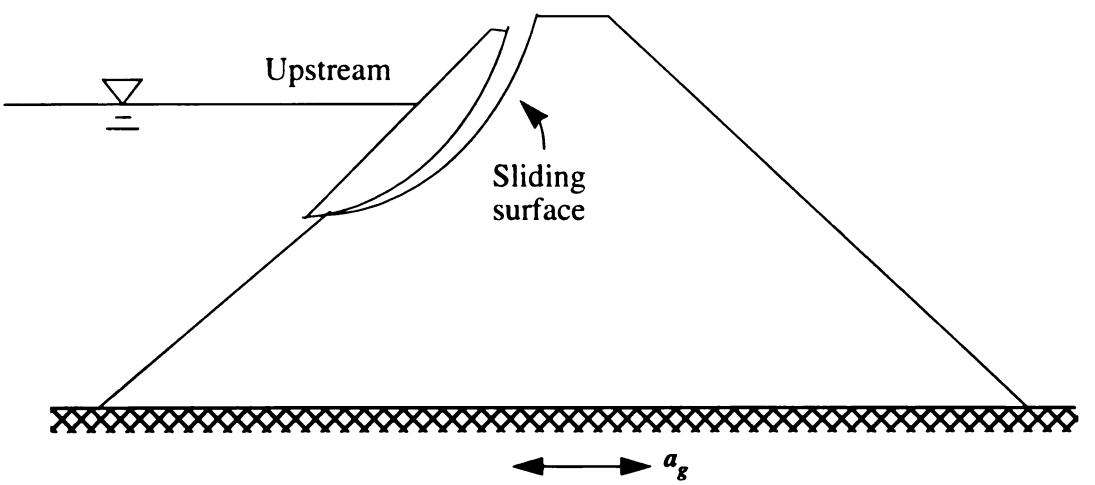

Figure 3.10 Sliding failure of earth dam subjected to earthquake motions

loss of strength occurs in soil is called liquefaction. The phenomenon of soil liquefaction is primarily associated with medium- to fine-grained saturated cohesionless soils. Sliding of a slope is attributed to the dam losing stability due to variation in stress, and the soil losing resistance due to vibration and the rise of pore-water pressure. Such damage induced by ground motions occurs most often at the upstream slope as shown in Fig. 3.11. If the earth dam is saturated at the upstream side, it may liquefy when subjected to vibration exceeding a certain limit.

The occurrence of liquefaction failure is usually related to the volumetric strain in the soil which is given by

$$\varepsilon_v = \varepsilon_1 + \varepsilon_2 + \varepsilon_3 \tag{3.2}$$

where ε_1, ε_2 and ε_3 are the principal strains for 3-D problems.

Another method to evaluate possible liquefaction is the use of a threshold strain. If the cyclic shear strain in soil as a result of an earthquake does not exceed a certain threshold level, liquefaction should not occur. The peak shear strain caused by an earthquake ground motion can be estimated by (Commission on Engineering and Technical Systems 1985)

$$\gamma_{max} = \frac{1.2 a_{max} h}{v_s^2} \tag{3.3}$$

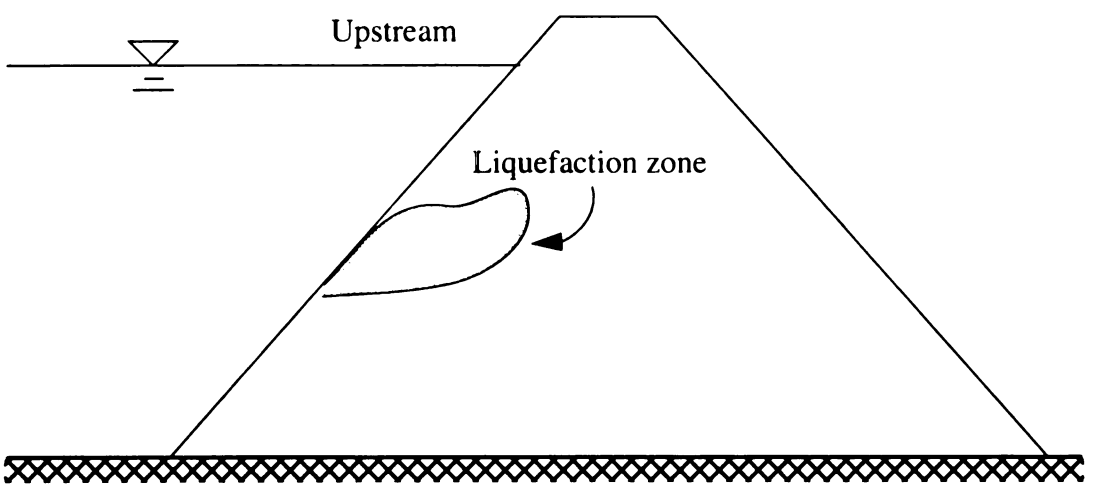

Figure 3.11 Liquefaction at the upstream side

in which a_m = peak acceleration of earthquake motions, h = depth from the crest and v_s = shear wave velocity in the soil.

3.4.3 Longitudinal cracks

Longitudinal cracks take place mostly in the crest area as shown in Fig. 3.12. The formation of wide longitudinal cracks is considered to be due to tensile stresses produced at the surface. Shear sliding deformation may also contribute to such failure. Another cause of longitudinal cracks is the uneven settlement of the core or foundation. Uneven settlement usually occurs when the strength of the foundation is not uniform or when loose river deposits are left unexcavated. It should be noted that longitudinal cracks are sometimes concealed. The internal cracks formed in the Hachi Dam in Niigata, Japan were discovered when the dam was excavated to repair sluiceways damaged in the Niigata earthquake. Therefore, careful investigation is necessary even when no damage is visible (Okamoto 1984).

3.4.4 Transverse cracks

Transverse cracks consists of four types: (a) those formed due to violent vibration in the direction parallel to dam axis, (b) those formed near both ends of an embankment

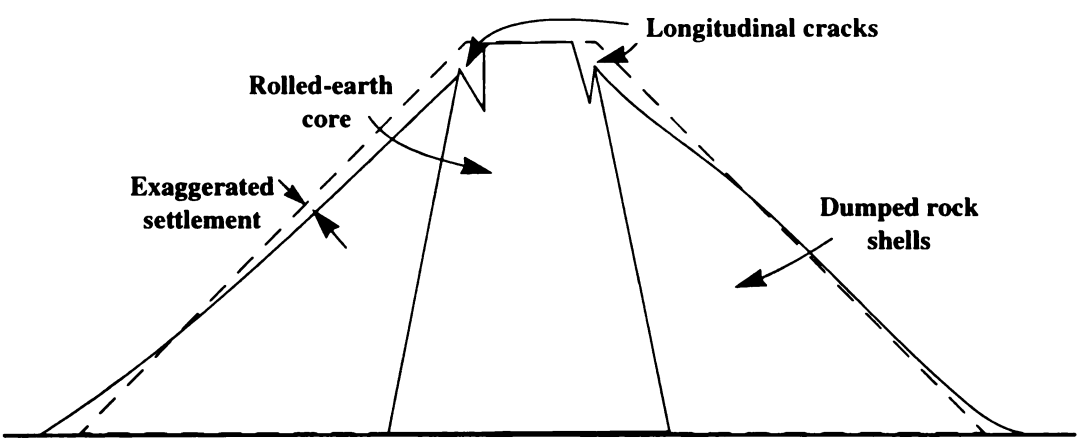

Figure 3.12 Cracking caused by differential settlement between embankment sections of dumped rock and rolled earth

because of the difference in the vibration characteristics of the embankment and the banks, (c) those formed due to nonuniformity of consolidation within the dam when repairs were made on sluiceways, and (d) those due to uneven settlement of the foundation. Typical transverse cracks due to differential settlement are shown in Fig. 3.13. Generally, transverse cracks are fewer than the number of longitudinal cracks, but these can serve as water channels, causing breaking, so early repair is necessary.

3.4.5 Embankment and foundation piping

Piping, or progressive erosion of concentrated leaks, has caused a number of catastrophic failures. As water seeps through the compacted soil of an embankment or the natural soil of a foundation, the pressure head is dissipated in overcoming the viscous drag forces which resist the flow through the small soil pores. Conversely, the seeping water generates erosive forces which tend to pull the soil particles with it in its travel through and under the dam. If the forces resisting erosion are less than those which tend to cause it, the soil particles are washed away and piping occurs. The resisting forces depend on the cohesion and the weight of the soil particles, as well as on the action of the downstream filter.

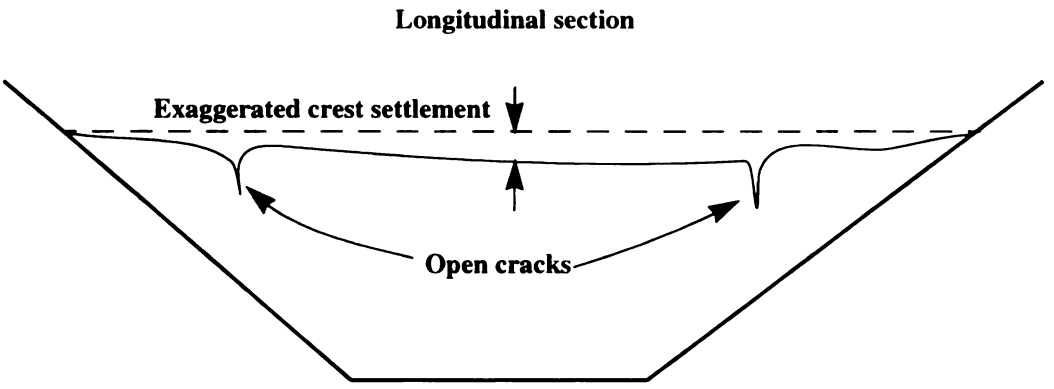

Figure 3.13 Typical transverse differential settlement cracks

4. STOCHASTIC RESPONSE ANALYSIS USING A FINITE ELEMENT MODEL — THEORY

4.1 Characteristics of Earthquakes

An earthquake is a phenomenon of strong vibration occurring on the ground due to the release of a large amount of energy within a short period of time through a sudden disturbance in the earth's crust or in the upper part of the mantle. Energy released underground moves through the earth in the form of wave motions to reach the surface. Two types of wave motion of different nature, longitudinal waves (P waves) and transverse waves (S waves), may be transmitted through the ground. In the case of P waves, the direction of motion of particles of matter coincides with the direction of advance of the waves. For S waves, the direction of motion of particles of matter is orthogonal to the direction of advance. In particular, the transverse wave is called an SV wave when it is vertically polarized or an SH wave when it is horizontally polarized.

For any specified ground motion, the responses of any structure can be computed deterministically. However, earthquake motions are irregular and each one differs from another in the fine details. It is not possible to predict the precise details of a future earthquake ground motion. Owing to the variation in ground motion details, stochastic modeling of strong ground motions is more appropriate and is finding increasing use. In addition, recent studies of seismograms recorded by the SMART-1 array in Lotung, Taiwan and other arrays indicate that earthquake ground motions exhibit travelling wave effects as well as spatial correlation effects. Spatially varying earthquake ground motion (SVEGM) can only be effectively characterized in terms of stochastic models. Therefore, the effect of SVEGM on the Santa Felicia dam is studied using random vibration analysis.

4.2 Engineering Interpretation of Stochastic Responses

The trend in civil engineering today, more than ever before, is toward providing economical designs at specified levels of safety. Earthquake ground motion is one of the

main factors which significantly affects the safety of structures. Current earthquake-resistant design procedures, which generally have been determined only from a specific earthquake record, often fall short of expectations in future situations. Little confidence can be achieved from the results of a single deterministic dynamic analysis. Therefore, to avoid the expense and effort required for multiple deterministic analyses, probabilistic methods are employed.

In the simplest case, the time history of earthquake-induced ground motion can be assumed to be ergodic random process. The ergodic process is characterized by: (a) all the ensemble averages being stationary with respect to the time scale; and (b) the averages taken along any single sample function being the same as the ensemble averages. In practical terms, each sample function is completely representative of the ensemble that constitutes the random process. Based on this assumption, some statistical properties of interest, as described in the following sections, can be obtained from a single earthquake record.

Random vibration is rooted in the theory of probability and random variables. The behavior of a random variable is characterized by its probability distribution. The most important probability distribution in theory as well as in application is the Gaussian distribution. The earthquake acceleration excitation is assumed to be a zero-mean Gaussian process throughout this study. It follows that most stochastic responses must be zero-mean Gaussian random processes for a linear system. Two of the most important moments of the response process are the mean and the variance. The first moment, i.e., the mean, is the average value of the response. The second moment, i.e., the variance, measures the dispersion of the response about its mean. The positive square root of the variance is called the standard deviation which has the same unit as the mean and for a zero-mean, this is identical to the root-mean-square (r.m.s.). The standard deviation measures the spread of the distribution.

As mentioned in the beginning, economics as well as safety is the goal of structural design. Usually, a structure designed to be almost 100% safe over a certain period of time will be uneconomical. In general, the expected reliability of most civil engineering systems is in the range of 0.95 to 0.999. The reliability varies depending on the importance of the structure. For earth dam structures, a reliability of more than 0.997 is typically required. Typically, responses such as displacement, maximum shear stress and maximum shear strain are of primary interest. Mean plus three standard deviation ($\mu+3\sigma$) values of the responses are computed in this study.

Fig. 4.1 shows a typical sample of a random response. In deterministic problems, one is usually interested in designing for the peak response. However, for stochastic loading, the peak response is itself a random variable. For a stationary response duration T, the response threshold that will not be exceeded the probability P can be expressed as

$$y_{peak} = \mu + \Upsilon_{T,P}\sigma \tag{4.1}$$

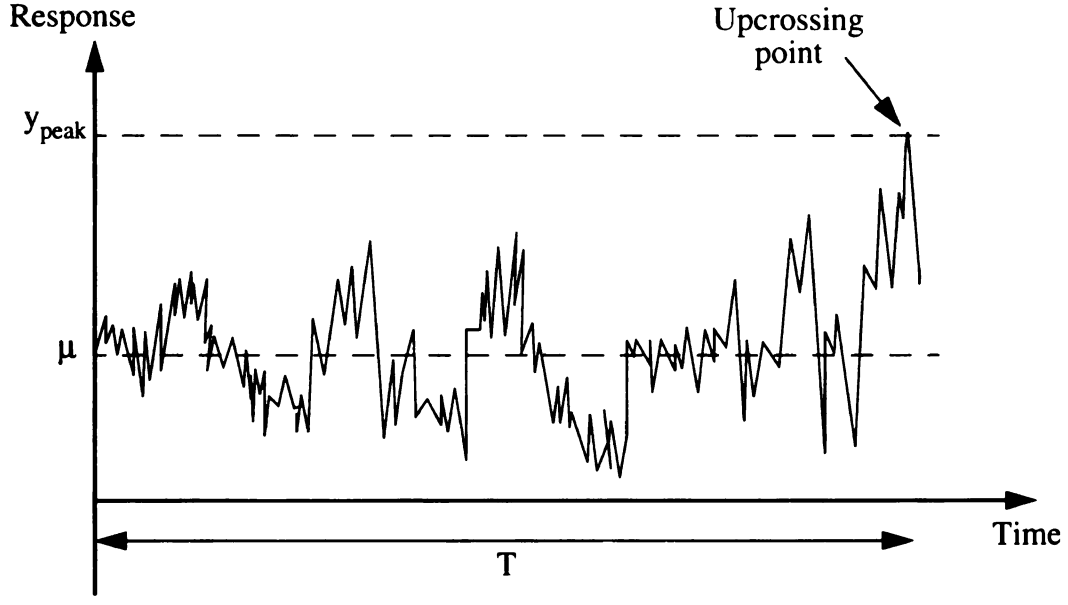

Figure 4.1 First upcrossing of the level y_{peak} in time history of response

where μ and σ are the mean and standard deviation of the response and $\Upsilon_{T,P}$ is a peak factor that is dependent on the duration T and probability of non-exceedance P. Expression for $\Upsilon_{T,P}$ have been proposed for Gaussian process (Der Kiureghian 1980). In order to compare peak responses due to different excitations, a value of $\Upsilon_{T,P} = 3$ should suffice, and this is used herein.

4.3 Ground Motion Model

In order to study the response of the Santa Felicia earth dam to SVEGM, the ground motion model proposed by Harichandran and Vanmarcke (1986) is adopted. The model which accounts for both spatial correlation and wave passage effects is used to specify the base motions in the upstream-downstream direction of the dam. In the model the ground accelerations are assumed to constitute a homogeneous random field. The auto spectral density function (SDF) of the ground acceleration, $S_{\ddot{u}_g}(\omega)$, is therefore assumed to be the same at all spatial locations. The correlation between the accelerations at two different points is characterized by a coherency function, $|\gamma(v,\omega)|$, and all waves are assumed to have a constant apparent propagation velocity V. The cross SDF between the accelerations at two locations A and B is then expressed as the product of the point SDF, coherency function and phase delay

$$S_{\ddot{u}_A \ddot{u}_B}(\omega) = S_{\ddot{u}_g}(\omega)\,|\gamma(v,\omega)|\,e^{-i\omega v/V} \tag{4.2}$$

Based on the analysis of some events recorded by the SMART-1 array, Harichandran and Vanmarcke (1986) proposed the following empirical coherency function:

$$|\gamma(v,\omega)| = A\exp\left[-\frac{2v}{\alpha\theta(\omega)}(1-A+\alpha A)\right] + (1-A)\exp\left[-\frac{2v}{\theta(\omega)}(1-A+\alpha A)\right] \tag{4.3}$$

where

$$\theta(\omega) = k\left[1+(\omega/\omega_o)^b\right]^{-1/2} \tag{4.4}$$

and A, α, k, ω_o and b are empirical model parameters; v = separation between locations A and B; V = apparent wave propagation velocity from A to B; and $S_{\ddot{u}_g}(\omega)$ = auto SDF of the ground acceleration.

A commonly-used form of the auto SDF is (Clough and Penzien, 1975)

$$S_{\ddot{u}_g}(\omega) = \left[\frac{\omega_g^4 + 4\omega^2\omega_g^2\zeta_g^2}{(\omega_g^2 - \omega^2)^2 + 4\omega^2\omega_g^2\zeta_g^2}\right]\left[\frac{\omega^4}{(\omega_f^2 - \omega^2)^2 + 4\omega^2\omega_f^2\zeta_f^2}\right]S_o \qquad (4.5)$$

in which the five parameters ω_g, ζ_g, ω_f, ζ_f and S_0 can be estimated by fitting the above function to observed acceleration spectra. This ground acceleration spectrum, is a modified version of the popular Kanai-Tajimi spectrum.

4.4 Finite Element Formulation of the Equations of Motion

The finite element method has been widely used in many applications. For analyzing the vibration of earth dams, the finite element method successfully overcomes geometric irregularity and material inhomogeneity. It is therefore expedient to resort to the finite element technique for the analysis of the Santa Felicia dam. Tetrahedral elements in which each node has three translation components, x, y and z, were used in the analysis. The equation of motion of the nodal points in the finite element system may be expressed in matrix form as

$$[M]\{\ddot{u}\} + [C]\{\dot{u}\} + [K]\{u\} = 0 \qquad (4.6)$$

in which $[M]$ = the mass matrix, $[C]$ = a viscous damping matrix, and $[K]$ = the stiffness matrix. The vector {u} represents the nodal displacements, and $\{\dot{u}\}$ and $\{\ddot{u}\}$ are the nodal velocity and acceleration vectors, respectively.

4.4.1 Finite element discretization

From equation (4.6), by reordering and partitioning $[M]$, $[C]$ and $[K]$, to correspond to the partitioning of the nodal displacements $\{u\}$ into free and restrained displacements $\{u_F\}$ and $\{u_R\}$, the dynamic equations of motion become

$$\begin{bmatrix} [M_{FF}] & [M_{FR}] \\ [M_{RF}] & [M_{RR}] \end{bmatrix} \begin{pmatrix} \{\ddot{u}_F\} \\ \{\ddot{u}_R\} \end{pmatrix} + \begin{bmatrix} [C_{FF}] & [C_{FR}] \\ [C_{RF}] & [C_{RR}] \end{bmatrix} \begin{pmatrix} \{\dot{u}_F\} \\ \{\dot{u}_R\} \end{pmatrix} + \begin{bmatrix} [K_{FF}] & [K_{FR}] \\ [K_{RF}] & [K_{RR}] \end{bmatrix} \begin{pmatrix} \{u_F\} \\ \{u_R\} \end{pmatrix} = \begin{pmatrix} \{0\} \\ \{0\} \end{pmatrix} \tag{4.7}$$

in which $\{u_F\}$ are the free (unrestrained) degrees-of-freedom (DOF) and $\{u_R\}$ are the restrained (support) DOF.

The free nodal displacements $\{u_F\}$ can be decomposed into pseudo-static and dynamic parts, $\{u_s\}$ and $\{u_d\}$, respectively:

$$\{u_F\} = \{u_s\} + \{u_d\} \tag{4.8}$$

The pseudo-static displacements are obtained from the support displacements, $\{u_R\}$, using the static equilibrium equations (with no external loading)

$$[K_{FF}]\{u_s\} + [K_{FR}]\{u_R\} = \{0\}$$

yielding

$$\{u_s\} = -[K_{FF}]^{-1}[K_{FR}]\{u_R\} = [A]\{u_R\} \tag{4.9}$$

in which $[A] = -[K_{FF}]^{-1}[K_{FR}]$. These displacements are the instantaneous free displacements of the structure due to support movement $\{u_R\}$ at a given time t. Substituting equation (4.8) and equation (4.9) into equation (4.7) yields

$$\begin{aligned} &[M_{FF}]\{\ddot{u}_d\} + [C_{FF}]\{\dot{u}_d\} + [K_{FF}]\{u_d\} \\ &= -([M_{FF}][A] + [M_{FR}])\{\ddot{u}_R\} - ([C_{FF}][A] + [C_{FR}])\{\dot{u}_R\} \end{aligned} \tag{4.10}$$

For light damping, the second term on the right-hand-side of the above equation may be neglected. Thus the final equations of motion for the free DOF become

$$[M_{FF}]\{\ddot{u}_d\} + [C_{FF}]\{\dot{u}_d\} + [K_{FF}]\{u_d\} \approx -([M_{FF}][A] + [M_{FR}])\{\ddot{u}_R\} \quad (4.11)$$

4.4.2 Modal analysis

In order to simplify the damped equations of motion of the multi-DOF system, the orthogonality properties of the normal coordinates may be used to decouple equation (4.11). For undamped free vibration

$$[M_{FF}]\{\ddot{u}_d\} + [K_{FF}]\{u_d\} = 0 \quad (4.12)$$

Assuming harmonic vibration in the form

$$\{u_d\} = \{\phi_j\} e^{i\omega_j t} \quad (4.13)$$

results in the generalized eigenvalue problem

$$\left[[K_{FF}] - \omega_j^2 [M_{FF}]\right]\{\phi_j\} = 0 \quad (4.14)$$

The solutions of these equations yield the natural frequencies of vibration ω_j, and the mode shapes, $\{\phi_j\}$, of the structure. For general vibration, the nodal displacements may be expanded in terms of the mode shapes as

$$\{u_d\} = \sum_{k=1}^{n} \{\phi_k\} U_k(t) \quad (4.15)$$

where $U_k(t)$ are generalized modal responses. Substituting equation (4.15) into equation (4.11), premultiplying by the transpose of mode-shape vector $\{\phi_j\}^T$ and assuming that the mode shapes are orthogonal to the damping matrix, i.e.

$$\{\phi_j\}^T [C]\{\phi_k\} = 0, j \neq k$$

results in the uncoupled modal equations

$$\ddot{U}_j + 2\zeta_j \omega_j \dot{U}_j + \omega_j^2 U_j = G_j, \quad j = 1, ..., n \tag{4.16}$$

where

$$G_j = \frac{-1}{M_j} \{\phi_j\}^T ([M_{FF}] [A] + [M_{FR}]) \{\ddot{u}_R\} = \{\Gamma_j\}^T \{\ddot{u}_R\} \tag{4.17}$$

$$\{\Gamma_j\} = \frac{-1}{M_j} [[M_{FF}] [A] + [M_{FR}]]^T \{\phi_j\} \tag{4.18}$$

$$\text{and} \qquad M_j = \{\phi_j\}^T [M_{FF}] \{\phi_j\} \tag{4.19}$$

in which $\{\Gamma_j\}$ is the modal participation factor, M_j is the normal-coordinate generalized mass (modal mass), and ζ_j represents the modal damping ratio. In practice, it is common to assume the damping ratio for each mode than it is to try to evaluate the coefficients of the damping matrix [*C*]. It is convenient to collect the excitations $G_j(t)$ into a vector $\{G(t)\}$ and the modal participation factors $\{\Gamma_j\}$ into a matrix

$$[\Gamma] = \left[\{\Gamma_1\} \{\Gamma_2\} \dots \{\Gamma_n\} \right]$$

in which case equation (4.17) may be written as

$$\{G\} = [\Gamma]^T \{\ddot{u}_R\} \tag{4.20}$$

In addition, the mode shapes may be collected into a matrix

$$[\Phi] = \left[\{\phi_1\} \{\phi_2\} \dots \{\phi_n\} \right]$$

and equation (4.15) may be written as

$$\{u_d\} = [\Phi] \{U(t)\} \tag{4.21}$$

4.5 Random Vibration Analysis

4.5.1 Introduction

Assuming that the earthquake-induced ground acceleration is a stationary random process, it can be shown that the displacement response is also a stationary process. Consequently, the autocorrelation matrix of the random process $\{u_F\}$ will be independent of time t and is defined as

$$[R_{u_F}(\tau)] = E\left[\{u_F(t)\}\{u_F(t+\tau)\}^T\right] \tag{4.22}$$

where $E[\ ]$ denotes the expectation of the random variable. Substituting equation (4.8) into equation (4.22),

$$\begin{aligned}[R_{u_F}(\tau)] &= E\left[\{u_s(t)+u_d(t)\}\{\{u_s(t+\tau)\}^T+\{u_d(t+\tau)\}^T\}\right] \\ &= [R_{u_s}(\tau)]+[R_{u_d}(\tau)]+[R_{u_s u_d}(\tau)]+[R_{u_d u_s}(\tau)]\end{aligned} \tag{4.23}$$

in which $[R_{u_s}(\tau)]$ and $[R_{u_d}(\tau)]$ are the autocorrelation matrices of the pseudo-static and dynamic displacements, respectively, and $[R_{u_s u_d}(\tau)]$ and $[R_{u_d u_s}(\tau)]$ are the cross correlation matrices. For stationary response

$$[R_{u_s u_d}(\tau)] = [R_{u_d u_s}(-\tau)]$$

The Fourier Transform of equation (4.23) yields the spectral density matrix of the free displacements:

$$[S_{u_F}(\omega)] = [S_{u_s}(\omega)]+[S_{u_d}(\omega)]+[S_{u_s u_d}(\omega)]+[S_{u_d u_s}(\omega)] \tag{4.24}$$

For stationary response, the cross spectral density matrices are related through

$$[S_{u_s u_d}(\omega)] = \left[\overline{S_{u_d u_s}(\omega)}\right] \tag{4.25}$$

where the overbar denotes the complex conjugate.

The variance of the ith free displacement can be obtained from the ith diagonal terms of the spectral density matrices

$$\sigma^2_{u_{F_i}} = \int_{-\infty}^{\infty} S_{u_{s_i}}(\omega)\, d\omega + \int_{-\infty}^{\infty} S_{u_{d_i}}(\omega)\, d\omega + 2\mathrm{Re}\left[\int_{-\infty}^{\infty} S_{u_{s_i}u_{d_i}}(\omega)\, d\omega\right]$$
$$= \sigma^2_{u_{s_i}} + \sigma^2_{u_{d_i}} + 2\mathrm{Cov}\,(u_{s_i}, u_{d_i}) \qquad (4.26)$$

where Re [ ] denotes the real part of the argument. $\sigma^2_{u_{s_i}}$ and $\sigma^2_{u_{d_i}}$ are the variances of the pseudo-static and dynamic *i*th free displacement, and $\mathrm{Cov}\,(u_{s_i}, u_{d_i})$ is the covariance between the static and dynamic displacements.

4.5.2 Variance of dynamic displacements

Let $h_j(t)$ be the impulse response function of the *j*th mode corresponding to equation (4.16), i.e. the response to $G_j(t) = \delta(t)$ is $U_j(t)=h_j(t)$. For linear response, applying superposition for any general excitation, the response can be expressed by

$$U_j(t) = \int_{-\infty}^{\infty} h_j(\theta)\, G_j(t-\theta)\, d\theta \qquad (4.27)$$

In matrix notation, the modal response vector may be expressed as

$$\{U_j(t)\} = \int_{-\infty}^{\infty} [h_j(\theta)]\, \{G_j(t-\theta)\}\, d\theta \qquad (4.28)$$

in which the diagonal n x n modal impulse response matrix is

$$[h(\theta)] = [diag\,(h_j(\theta))]$$

The autocorrelation matrix of the dynamic displacements $\{u_d\}$ is

$$[R_{u_d}(\tau)] = E\left[\{u_d(t)\}\,\{u_d(t+\tau)\}^T\right]$$
$$= E\left[[\Phi]\,\{U(t)\}\,\{U(t+\tau)\}^T[\Phi]^T\right] \qquad (4.29)$$
$$= [\Phi]\,E\left[\{U(t)\}\,\{U(t+\tau)\}^T\right][\Phi]^T = [\Phi]\,[R_U(\tau)]\,[\Phi]^T$$

Using equation (4.28)

$$
\begin{aligned}
[R_U(\tau)] &= E\left[\{U(t)\}\{U(t+\tau)\}^T\right] \\
&= \int_{-\infty}^{\infty}\int_{-\infty}^{\infty}[h(\theta_1)]E\left[\{G(t-\theta_1)\}\{G(t+\tau-\theta_2)\}^T\right][h(\theta_2)]^T d\theta_1 d\theta_2 \\
&= \int_{-\infty}^{\infty}\int_{-\infty}^{\infty}[h(\theta_1)][R_G(\tau+\theta_1-\theta_2)][h(\theta_2)]^T d\theta_1 d\theta_2
\end{aligned}
\tag{4.30}
$$

Since $\{G\} = [\Gamma]^T\{\ddot{u}_R\}$,

$$
\begin{aligned}
[R_G(\tau+\theta_1-\theta_2)] &= E\left[\{G(t-\theta_1)\}\{G(t+\tau-\theta_2)\}^T\right] \\
&= E\left[[\Gamma]^T\{\ddot{u}_R(t-\theta_1)\}\{\ddot{u}_R(t+\tau-\theta_2)\}^T[\Gamma]\right] \\
&= [\Gamma]^T[R_{\ddot{u}_R}(\tau+\theta_1-\theta_2)][\Gamma]
\end{aligned}
\tag{4.31}
$$

Finally, combining equation (4.29), equation (4.30) and equation (4.31),

$$
[R_{u_d}(\tau)] = [\Phi]\left[\int_{-\infty}^{\infty}\int_{-\infty}^{\infty}[h(\theta_1)][\Gamma]^T R_{\ddot{u}_R}(\tau+\theta_1-\theta_2)[\Gamma][h(\theta_2)]^T d\theta_1 d\theta_2\right][\Phi]^T \tag{4.32}
$$

The Fourier Transform of the above equation yields the spectral density matrix of the dynamic displacements:

$$
S_{u_d}(\omega) = [\Phi][H(-\omega)][\Gamma]^T[S_{\ddot{u}_R}(\omega)][\Gamma][H(\omega)]^T[\Phi]^T \tag{4.33}
$$

where the diagonal modal frequency response matrix $[H(\omega)]$ is

$$
[H(\omega)] = \int_{-\infty}^{\infty}[h(t)]e^{-i\omega t}dt = [diag(H_j(\omega))] \tag{4.34}
$$

and $S_{\ddot{u}_R}(\omega)$ is the spectral density matrix of the support accelerations.

The diagonal terms of $[S_{u_d}(\omega)]$ may be written in scalar form as

$$S_{u_{d_i}}(\omega) = \sum_{j=1}^{n}\sum_{k=1}^{n}\sum_{l=1}^{r}\sum_{m=1}^{r} \phi_{ij}\phi_{ik}\Gamma_{lj}\Gamma_{mk} H_j(-\omega)\, H_k(\omega)\, S_{\ddot{u}_{R_l}\ddot{u}_{R_m}}(\omega) \tag{4.35}$$

where n is the number of free degree-of-freedom and r is the number of restrained degree-of-freedom. The modal frequency response function has the form

$$H_j(\omega) = \frac{1}{\omega_j^2 - \omega^2 + 2i\zeta_j\omega_j\omega} \tag{4.36}$$

The variance of the ith free dynamic displacement is

$$\sigma^2_{u_{d_i}} = \int_{-\infty}^{\infty} S_{u_{d_i}}(\omega)\, d\omega = \sum_{j=1}^{n}\sum_{k=1}^{n} \phi_{ij}\phi_{ik} I_{jk} \tag{4.37}$$

where

$$I_{jk} = \sum_{l=1}^{r}\sum_{m=1}^{r} \Gamma_{lj}\Gamma_{mk} \int_{-\infty}^{\infty} H_j(-\omega)\, H_k(\omega)\, S_{\ddot{u}_{R_l}\ddot{u}_{R_m}}(\omega)\, d\omega \tag{4.38}$$

4.5.3 Variances of pseudo-static displacements

From equation (4.9), $\{u_s\} = [A]\{u_R\}$, thus the autocorrelation matrix of the pseudo-static free displacements $\{u_s\}$ is

$$\begin{aligned} [R_{u_s}(\tau)] &= E\left[\{u_s(t)\} \{u_s(t+\tau)\}^T \right] \\ &= E\left[[A] \{u_R(t)\} \{u_R(t+\tau)\}^T [A]^T \right] \\ &= [A]\, [R_{u_R}(\tau)]\, [A]^T \end{aligned} \tag{4.39}$$

The Fourier Transform of the above equation yields the spectral density matrix

$$[S_{u_s}(\omega)] = [A]\, [S_{u_R}(\omega)]\, [A]^T = \frac{1}{\omega^4}\left([A]\, [S_{\ddot{u}_R}(\omega)]\, [A]^T \right) \tag{4.40}$$

The diagonal elements of this matrix may be written in scalar form as

$$S_{u_{s_i}}(\omega) = \frac{1}{\omega^4} \sum_{l=1}^{r} \sum_{m=1}^{r} A_{il} A_{im} S_{\ddot{u}_{R_l} \ddot{u}_{R_m}}(\omega) \tag{4.41}$$

The variances of the pseudo-static displacements are therefore

$$\sigma^2_{u_{s_i}} = \sum_{l=1}^{r} \sum_{m=1}^{r} A_{il} A_{im} \int_{-\infty}^{\infty} \frac{1}{\omega^4} S_{\ddot{u}_{R_l} \ddot{u}_{R_m}}(\omega)\, d\omega \tag{4.42}$$

4.5.4 Covariance of pseudo-static and dynamic displacements

The cross correlation matrix of the pseudo-static and dynamic displacement is defined as

$$\begin{aligned}
[R_{u_s u_d}(\tau)] &= E\left[\{u_s(t)\} \{u_d(t+\tau)\}^T \right] \\
&= E\left[[A] \{u_R(t)\} \{U(t+\tau)\}^T [\Phi]^T \right] \\
&= E\left[[A] \{u_R(t)\} \left\{ \int_{-\infty}^{\infty} \{\ddot{u}_R(t+\tau-\theta)\}^T [\Gamma] [h(\theta)]^T d\theta \right\} [\Phi]^T \right] \\
&= [A] \left\{ \int_{-\infty}^{\infty} \{R_{u_R \ddot{u}_R}(\tau-\theta)\} [\Gamma] [h(\theta)]^T d\theta \right\} [\Phi]^T
\end{aligned} \tag{4.43}$$

Again, the Fourier Transform of the above equation yields the cross spectral density matrix

$$[S_{u_s u_d}(\omega)] = [A] [S_{u_R \ddot{u}_R}(\omega)] [\Gamma] [H(\theta)]^T [\Phi]^T \tag{4.44}$$

There exists a direct relationship between $[S_{u_R \ddot{u}_R}(\omega)]$ and $[S_{\ddot{u}_R}(\omega)]$. Consider

$$\begin{aligned}
[R''_{u_R}(\tau)] &= \frac{d^2}{d\tau^2} E\left[\{u_R(t)\} \{u_R(t+\tau)\}^T \right] \\
&= E\left[\{u_R(t)\} \{\ddot{u}_R(t+\tau)\}^T \right] = [R_{u_R \ddot{u}_R}(\tau)]
\end{aligned} \tag{4.45}$$

The Fourier Transform of $[R''_{u_R}(\tau)]$ is $-\omega^2 [S_{u_R}(\omega)]$, and therefore, the Fourier Transform of the equation (4.45) becomes

$$[S_{u_R \ddot{u}_R}(\omega)] = -\omega^2 [S_{u_R}(\omega)] = -\frac{1}{\omega^2}[S_{\ddot{u}_R}(\omega)] \tag{4.46}$$

As a result, equation (4.44) may also be written as

$$[S_{u_s u_d}(\omega)] = -\frac{1}{\omega^2}[A]\,[S_{\ddot{u}_R}(\omega)]\,[\Gamma]\,[H(\theta)]^T[\Phi]^T \tag{4.47}$$

The diagonal elements of $[S_{u_s u_d}(\omega)]$ in scalar form are

$$S_{u_{s_i} u_{d_i}}(\omega) = -\frac{1}{\omega^2}\sum_{j=1}^{n}\sum_{l=1}^{r}\sum_{m=1}^{r}\phi_{ij}A_{il}\Gamma_{mj}H_j(\omega)\,S_{\ddot{u}_{R_l}\ddot{u}_{R_m}}(\omega) \tag{4.48}$$

The covariance of the ith free pseudo-static and dynamic displacements is therefore

$$\mathrm{Cov}(u_{s_i}, u_{d_i}) = Re\left[\int_{-\infty}^{\infty} S_{u_{s_i} u_{d_i}}(\omega)\, d\omega\right] \tag{4.49}$$

4.5.5 Calculation of covariance matrix of nodal stresses

As with the displacement response, any Cartesian stress can also be decomposed into pseudo-static and dynamic parts, $\{\tau_s\}$ and $\{\tau_d\}$, respectively. Consider two Cartesian stresses, τ_1 and τ_2, which can be expressed as $\tau_1 = \tau_{1s} + \tau_{1d}$ and $\tau_2 = \tau_{2s} + \tau_{2d}$, respectively. Thus,

$$\begin{aligned} E[\tau_1\tau_2] &= E[(\tau_{1s} + \tau_{1d})(\tau_{2s} + \tau_{2d})] \\ &= E[\tau_{1d}\tau_{2d} + \tau_{1s}\tau_{2s} + \tau_{1d}\tau_{2s} + \tau_{1s}\tau_{2d}] \end{aligned} \tag{4.50}$$

Since all Cartesian stresses are zero-mean Gaussian processes, equation (4.50) becomes

$$\mathrm{Cov}(\tau_1, \tau_2) = \mathrm{Cov}(\tau_{1d}, \tau_{2d}) + \mathrm{Cov}(\tau_{1s}, \tau_{2s}) + \mathrm{Cov}(\tau_{1d}, \tau_{2s}) + \mathrm{Cov}(\tau_{1s}, \tau_{2d}) \tag{4.51}$$

Therefore, the total covariance matrix of the six Cartesian stresses at the ith node may be expressed as

$$\begin{aligned} [\mathrm{Cov}(\tau_p, \tau_q)]_i &= [\mathrm{Cov}(\tau_{pd}, \tau_{qd})]_i + [\mathrm{Cov}(\tau_{ps}, \tau_{qs})]_i \\ &\quad + [\mathrm{Cov}(\tau_{pd}, \tau_{qs})]_i + [\mathrm{Cov}(\tau_{ps}, \tau_{qd})]_i \end{aligned} \tag{4.52}$$

where $[\mathrm{Cov}(\tau_{ps}, \tau_{qs})]_i$ and $[\mathrm{Cov}(\tau_{pd}, \tau_{qd})]_i$ are the covariances matrix of the pseudo-static and dynamic stresses at the ith node; $[\mathrm{Cov}(\tau_{pd}, \tau_{qs})]_i$ and $[\mathrm{Cov}(\tau_{ps}, \tau_{qd})]_i$ are the covariance matrix between the static and dynamic stresses; and p=1, ..., 6 and q=1, ..., 6 are subscripts denoting the stress components, in which the six stress components τ_x, τ_y, τ_z, τ_{xy}, τ_{xz} and τ_{yz} are denoted by τ_1, τ_2, τ_3, τ_4, τ_5 and τ_6, respectively. In expanded form, the covariance matrix is

$$[\mathrm{Cov}(\tau_p, \tau_q)]_i = \begin{bmatrix} \mathrm{Cov}(\tau_1, \tau_1) & \mathrm{Cov}(\tau_1, \tau_2) & \cdots & \mathrm{Cov}(\tau_1, \tau_6) \\ & \mathrm{Cov}(\tau_2, \tau_2) & \cdots & \mathrm{Cov}(\tau_2, \tau_6) \\ & & \cdots & \cdots \\ \text{Symmetric} & & & \mathrm{Cov}(\tau_6, \tau_6) \end{bmatrix}_i \tag{4.53}$$

4.5.5.1 Dynamic response

As with the dynamic displacement response in equation (4.15), the nodal stresses may also be expanded in terms of the stress mode shapes, $[\Psi]$, as

$$\{\tau_d\} = [\Psi]\{U(t)\} \tag{4.54}$$

Consequently, following the procedures in Section 4.5.2, the covariance matrix of the dynamic stresses at each node can be obtained as

$$[\mathrm{Cov}(\tau_{pd}, \tau_{qd})]_i = \sum_{k=1}^{n}\sum_{j=1}^{n}\sum_{p=1}^{6}\sum_{q=1}^{6}\frac{1}{2}(\psi_{uj}\psi_{vk} + \psi_{vj}\psi_{uk})I_{jk} \quad i = 1, ..., N_n \tag{4.55}$$

where subscripts $u = 6(i-1) + p$ and $v = 6(i-1) + q$, N_n is the total number of nodes, n is the number of modes used and I_{jk} was defined in equation (4.38).

4.5.5.2 Pseudo-static response

The pseudo-static stresses may be expressed as

$$\{\tau_s\} = [\eta]\{u_R\} \tag{4.56}$$

where the *j*th column of [η] are the stresses due to a unit displacement along the *j*th restrained DOF. Equation (4.56) is similar to the pseudo-static displacement representation in equation (4.9). Following the procedures in Section 4.5.3, the covariance matrix can be obtained as

$$[\mathrm{Cov}(\tau_{ps}, \tau_{qs})]_i = \sum_{l=1}^{r}\sum_{m=1}^{r}\sum_{p=1}^{6}\sum_{q=1}^{6}\frac{1}{2}(\eta_{ul}\eta_{vm} + \eta_{vl}\eta_{um})\int_{-\infty}^{\infty}\frac{1}{\omega^4}S_{\ddot{u}_{R_l}\ddot{u}_{R_m}}(\omega)\,d\omega \qquad i = 1, \ldots, N_n \qquad (4.57)$$

4.5.5.3 Covariance of pseudo-static and dynamic responses

The calculations of the covariance matrix between the pseudo-static and dynamic stress responses are similar to those presented in Section 4.5.4. It can be shown that the covariance matrix of the stresses at the *i*th node may be expressed as

$$[\mathrm{Cov}(\tau_{pd}, \tau_{qs}) + \mathrm{Cov}(\tau_{ps}, \tau_{qd})]_i = \mathrm{Re}\left[\sum_{j=1}^{n}\sum_{l=1}^{r}\sum_{m=1}^{r}\sum_{p=1}^{6}\sum_{q=1}^{6}(\psi_{uj}\eta_{vl} + \psi_{vj}\eta_{ul})\int_{-\infty}^{\infty}\Gamma_{mj}\frac{-1}{\omega^2}S_{\ddot{u}_{R_l}\ddot{u}_{R_m}}(\omega)\,d\omega\right] \qquad (4.58)$$

The covariance matrices of the three strain response components can be obtained using equations (4.55), (4.57) and (4.58) by replacing ψ and η with strain mode shapes and strain responses due to a unit displacement at each restrained DOF, respectively. Finally, the total covariance matrix of Cartesian strains at *i*th node can be obtained analogous to equation (4.52).

4.6 Viscous Damping vs. Hysteretic Damping

It is customary in dynamic analysis to use viscous damping to account for the loss of energy during vibration. The main shortcoming of viscous damping is that the energy dissipated is frequency dependent, with more energy being dissipated at higher frequencies. Experimental results indicate that earth dams exhibit frequency-independent energy dissipation due to hysteretic damping. However, the equation of motion with exact hysteretic damping is non-linear. The most common method of accounting for hysteretic

damping is to linearize the equations of motion by replacing the stiffness of the system, k, by the complex-valued stiffness $\bar{k} = k(1 + 2i\zeta)$ where ζ is the hysteretic damping parameter. The effect of viscous and hysteretic damping on the response of earth dams is examined in the next sections using a simple one-dimensional shear beam model.

4.6.1 Shear beam with viscous damping

The one-dimensional shear beam model was reviewed in Section 2.2.2.1. It is known that stress can be expressed as a function of strain and rate of change of strain with time for viscous behavior. Therefore (Okamoto 1984),

$$\tau = \left(G + G_1 \frac{\partial}{\partial t}\right)\left(\frac{\partial u}{\partial y}\right) \tag{4.59}$$

where G and G_1 are material constants. Substituting this into equation (2.4),

$$\rho \frac{\partial^2 u}{\partial t^2} - \left(G + G_1 \frac{\partial}{\partial t}\right)\left(\frac{\partial^2 u}{\partial y^2} + \frac{1}{y}\frac{\partial u}{\partial y}\right) = 0 \tag{4.60}$$

For each mode of vibration, letting $u = \Phi_j U_j$, the above equation becomes

$$\rho \Phi_j \frac{d^2 U_j}{dt^2} - \left(G U_j + G_1 \frac{dU_j}{dt}\right)\left(\frac{d^2 \Phi_j}{dy^2} + \frac{1}{y}\frac{d\Phi_j}{dt}\right) = 0, \; j = 1, ..., n \tag{4.61}$$

Substituting equation (2.7) into equation (4.61),

$$\frac{d^2 U_j}{dt^2} + \frac{G_1}{G}\omega_j^2 \frac{dU_j}{dt} + \omega_j^2 U_j = 0, \; j = 1, ..., n \tag{4.62}$$

Letting $\zeta_j = \frac{G_1}{2G}\omega_j$, the familiar 1-D modal equation of motion is obtained:

$$\frac{d^2 U_j}{dt^2} + 2\zeta_j \omega_j \frac{dU_j}{dt} + \omega_j^2 U_j = 0 \tag{4.63}$$

For a base acceleration of $\ddot{x}_g$, the modal equation of motion becomes

$$\ddot{U}_j + 2\zeta_j \omega_j \dot{U}_j + \omega_j^2 U_j = -\Gamma_j \ddot{x}_g \tag{4.64}$$

where Γ_j is given in equation (2.12). The frequency response function is therefore

$$H_j(\omega) = \frac{1}{\omega_j^2 - \omega^2 + 2i\zeta_j\omega_j\omega} \tag{4.65}$$

so that

$$|H_j(\omega)|^2 = \frac{1}{\left(\omega_j^2 - \omega^2\right)^2 + 4\zeta_j^2\omega_j^2\omega^2} \tag{4.66}$$

Using the Kanai-Tajimi spectrum for $\ddot{x}_g$,

$$S_{\ddot{x}_g}(\omega) = \left[\frac{\omega_g^4 + 4\omega^2\omega_g^2\zeta_g^2}{(\omega_g^2 - \omega^2)^2 + 4\omega^2\omega_g^2\zeta_g^2}\right] S_o \tag{4.67}$$

The two parameters ω_g and ζ_g are taken to be 15.0 rad/s and 0.55, respectively. The intensity parameter S_o is adjusted such that the standard deviation of the ground acceleration is $0.09g$.

4.6.1.1 Displacement response

Using random vibration analysis with n vibration modes (i.e., $u = \sum_{j=1}^{n} \Phi_j U_j$), the displacement variance for widely separated modes can be approximated by

$$\sigma_u^2 \approx \sum_{j=1}^{n} \Phi_j^2 \Gamma_j^2 \int_{-\infty}^{\infty} |H_j(\omega)|^2 S_{\ddot{x}_g}(\omega)\, d\omega \tag{4.68}$$

in which modal cross correlation have been neglected. The mode shape of the 1-D shear beam model was shown to be a Bessel's function in Section 2.2.2.1. Therefore, the displacement response at the top (y = 0) is

$$\sigma_{u(0)}^2 \approx \sum_{j=1}^{n} J_0^2(0)\, \Gamma_j^2 \int_{-\infty}^{\infty} |H_j(\omega)|^2 S_{\ddot{x}_g}(\omega)\, d\omega \tag{4.69}$$

4.6.1.2 Shear force

For the generalized single-degree-of-freedom system, using the principle of virtual work, the elastic forces f_s for each mode developed during an earthquake response can be estimated by

$$f_s(y,t) = \omega^2 m(y)\, u(y,t) = \omega^2 m(y)\, \Phi_j(y)\, U_j(t)\ ,\ j = 1, ..., n \tag{4.70}$$

where $m(y) = \rho y B/H$ for a unit width of the dam. The same notation was used in the 1-D shear beam theory in Section 2.2.2.1. Consequently, the base shear f_B for each mode is given by

$$f_B(t) = \int_0^H \rho y \frac{B}{H} \Phi_j(y)\, dy \omega^2 U_j(t)\ ,\ j = 1, ..., n \tag{4.71}$$

Taking the Fourier Transform, the spectral density function of the base shear is then

$$S_{f_B}(\omega) = \sum_{j=1}^{n} \left(\int_0^H \rho y \frac{B}{H} \Phi(y)\, dy \right)^2 \omega_j^4 \Gamma_j^2 \left| H_j(\omega) \right|^2 S_{\ddot{x}_g}(\omega) \tag{4.72}$$

Therefore, the variance of the shear force at the base ($y = H$) is

$$\sigma_{f_B}^2 = \sum_{j=1}^{n} \left(\int_0^H \rho y \frac{B}{H} J_0\left(\frac{Z_j y}{H} \right) dy \right)^2 \omega_j^4 \Gamma_j^2 \int_{-\infty}^{\infty} \left| H_j(\omega) \right|^2 S_{\ddot{x}_g}(\omega)\, d\omega \tag{4.73}$$

4.6.1.3 Bending moment

Similarly, from the above result, the base moment for each mode can be expressed by

$$M_B(t) = \int_0^H f_s(y,t)\, y dy = \int_0^H \rho y^2 \frac{B}{H} \Phi_j(y)\, dy \omega^2 U_j(t)\ ,\ j = 1, ..., n \tag{4.74}$$

The spectral density function of the base moment is then

$$S_{M_B}(\omega) = \sum_{j=1}^{n} \left(\int_0^H \rho y^2 \frac{B}{H} \Phi(y)\, dy \right)^2 \omega_j^4 \Gamma_j^2 \left| H_j(\omega) \right|^2 S_{\ddot{x}_g}(\omega) \tag{4.75}$$

Therefore, the variance of the bending moment at the base of the dam is given by

$$\sigma_{M_B}^2 = \sum_{j=1}^{n} \left(\int_0^H \rho y^2 \frac{B}{H} J_0\left(\frac{Z_j y}{H} \right) dy \right)^2 \omega_j^4 \Gamma_j^2 \int_{-\infty}^{\infty} \left| H_j(\omega) \right|^2 S_{\ddot{x}_g}(\omega)\, d\omega \tag{4.76}$$

4.6.2 Shear beam with hysteretic damping

For an analysis with hysteretic damping, a complex modulus is used instead of an elastic modulus. For mathematical convenience, a complex-valued stress $\bar{\tau}$ and a complex-

valued displacement $\bar{u}$ are used. The stress and the corresponding displacement must satisfy an equation similar in form to equation (2.4), i.e.

$$\rho\frac{\partial^2}{\partial t^2}\bar{u} - \frac{\partial}{\partial y}\bar{\tau} - \frac{\bar{\tau}}{y} = 0 \tag{4.77}$$

Substituting $\bar{\tau} = (G + iG_2)\frac{\partial}{\partial y}\bar{u}$ into the above equation,

$$\rho\frac{\partial^2}{\partial t^2}\bar{u} - (G + iG_2)\left(\frac{\partial^2}{\partial y^2}\bar{u} + \frac{1}{y}\frac{\partial}{\partial y}\bar{u}\right) = 0 \tag{4.78}$$

For each mode of vibration, letting $\bar{u} = \Phi_k \bar{U}_k$, the above equation becomes

$$\frac{d^2\bar{U}_k}{dt^2} + \left(1 + i\frac{G_2}{G}\right)\omega_k^2\bar{U}_k = 0, \quad k = 1, ..., n \tag{4.79}$$

Letting $\zeta = G_2/G$, equation (4.79) becomes

$$\ddot{\bar{U}}_k + (1 + 2i\zeta)\,\omega_k^2\bar{U}_k = 0, \quad k = 1, ..., n \tag{4.80}$$

and the modal equation for base excitation becomes,

$$\ddot{\bar{U}}_k + (1 + 2i\zeta)\,\omega_k^2\bar{U}_k = -\Gamma_k\ddot{x}_g \tag{4.81}$$

Therefore, the frequency response function is

$$H_k(\omega) = \frac{1}{(1 + 2i\zeta)\,\omega_k^2 - \omega^2} \tag{4.82}$$

so that

$$\left|H_k(\omega)\right|^2 = \frac{1}{\left(\omega_k^2 - \omega^2\right)^2 + 4\zeta^2\omega_k^2} \tag{4.83}$$

The variance of the displacement, base shear and base moment are obtained by using these frequency response functions in equations (4.69), (4.73) and (4.76).

4.6.3 Discussion

The following values were used for the dimension and material properties of the Santa Felicia dam: dam height H = 275 ft, dam width B = 1,050 ft, soil mass density ρ = 4.02 lb-s^2/ft^4 and damping ratio ζ = 0.06. Four vibration modes were used in the analysis. The results of three cases: constant modal viscous damping ratios, modal viscous damping ratios varying with frequency and hysteretic damping, are compared in Table 4.1 and Table 4.2. For the case with varying modal viscous damping ratios, the damping ratio of the first mode was set at 0.06 and the ratios for higher modes increased with the natural frequency so that they were consistent with a constant damping c. The values listed in the Tables are

TABLE 4.1 Comparison of responses using hysteretic damping and varying viscous damping

Case	R.m.s. displacement at the top (ft)	R.m.s. shear force at the base (kips/ft)	R.m.s. bending moment at the base (kips-ft/ft)
Hysteretic damping	0.19111	7.41576×10^8	1.86148×10^{11}
Varying viscous damping	0.18993	4.80325×10^8	1.20568×10^{11}
Difference	-0.6%	-35.2%	-35.2%

TABLE 4.2 Comparison of responses using hysteretic damping and constant viscous damping

Case	R.m.s. displacement at the top (ft)	R.m.s. shear force at the base (kips/ft)	R.m.s. bending moment at the base (kips-ft/ft)
Hysteretic damping	0.19111	7.41576×10^8	1.86148×10^{11}
Constant viscous damping	0.19143	7.46685×10^8	1.87431×10^{11}
Difference	0.17%	0.69%	0.69%

the root-mean-square (r.m.s.) values of the responses. Table 4.1 indicates that for the case of varying viscous damping the r.m.s. values of the base shear and base moment are significantly lower than those for the case of hysteretic damping due to frequency-dependent energy dissipation. At higher frequencies, the loss of energy is higher.

On the other hand, if the viscous damping ratio for each mode is kept constant, as was done in the 3-D finite element model Table 4.2 indicates that the responses are very similar to those obtained from a hysteretic damping model. This indicates that although soil displays hysteretic behavior, the simpler viscous damping model with constant modal damping ratios is adequate for evaluating the seismic responses.

4.7 Statistical Moments of Maximum Shear Stress

4.7.1 Introduction

The random vibration analysis described in Section 4.5.5 yields the statistical moments of Cartesian stress components. However, an important quantity of interest in the seismic analysis of earth dams is the maximum shear stress τ_{max}. Several approximate methods have been developed to estimate the moments of functions of random variables. The first-order second-moment (FOSM) method is one of the simplest and most popular. This method is based on truncating the Taylor series expansion of a function to retain only linear terms. Since the relationship between maximum shear stress τ_{max} and Cartesian stresses is nonlinear, the FOSM method may be employed to approximately estimate the mean and variance of τ_{max}.

As an example, consider a function of two variable $F(x,y)$. Its Taylor series expansion about the point $(\bar{x},\bar{y})$, retaining only linear terms, is

$$F(x, y) \approx F(\bar{x}, \bar{y}) + \frac{\partial F}{\partial x}(x - \bar{x}) + \frac{\partial F}{\partial y}(y - \bar{y}) \tag{4.84}$$

Commonly, $\bar{x}$ and $\bar{y}$ are taken to be the mean values (in which case the method is called the mean-value FOSM method). As a result, the mean and variance of function $F(x,y)$ can be expressed as

$$E[F(x, y)] \approx F(\bar{x}, \bar{y}) \tag{4.85}$$

and

$$\begin{aligned} \mathrm{Var}[F(x, y)] \approx & \left(\left.\frac{\partial F}{\partial x}\right|_{\bar{x}, \bar{y}}\right)^2 \mathrm{Var}[x] + \left(\left.\frac{\partial F}{\partial y}\right|_{\bar{x}, \bar{y}}\right)^2 \mathrm{Var}[y] \\ & + 2\left(\left.\frac{\partial F}{\partial x}\right|_{\bar{x}, \bar{y}}\right)\left(\left.\frac{\partial F}{\partial y}\right|_{\bar{x}, \bar{y}}\right)\mathrm{Cov}[x, y] \end{aligned} \tag{4.86}$$

where all derivatives are evaluated at the expected values of the variates.

4.7.2 Calculation of maximum shear stress for special cases

It is well known that for 2-D case τ_{max} can be determined by

$$\tau_{max} = \sqrt{\left(\frac{\tau_x - \tau_y}{2}\right)^2 + \tau_{xy}^2} \tag{4.87}$$

The exact moments of τ_{max} can be computed for certain specified cases, and these cases are first used to gain insight into the adequacy of the FOSM method.

4.7.2.1 Uniaxial loading τ_x

In this case,

$$\tau_{max} = F(\tau_x) = \sqrt{\left(\frac{\tau_x}{2}\right)^2} = \frac{|\tau_x|}{2} \tag{4.88}$$

Assuming that τ_x is a zero-mean Gaussian random variable with a probability density function $f_{\tau_x} = \frac{1}{\sqrt{2\pi}\sigma_{\tau_x}} \exp\left(-\frac{\tau_x^2}{2\sigma_{\tau_x}^2}\right)$, the exact first two moments of τ_{max} are

$$\begin{aligned} E[\tau_{max}] &= E\left[\frac{|\tau_x|}{2}\right] = \int_{-\infty}^{\infty} \frac{|\tau_x|}{2} f_{\tau_x} d\tau_x \\ &= \frac{1}{2}\left(\int_0^{\infty} \tau_x f_{\tau_x} d\tau_x + \int_{-\infty}^{0} -\tau_x f_{\tau_x} d\tau_x\right) = \frac{\sigma_{\tau_x}}{\sqrt{2\pi}} \end{aligned} \tag{4.89}$$

and

$$\begin{aligned} \mathrm{Var}[\tau_{max}] &= E\left[\tau_{max}^2\right] - (E[\tau_{max}])^2 = \int_{-\infty}^{\infty} \frac{\tau_x^2}{4} f_{\tau_x} d\tau_x - \left(\frac{\sigma_{\tau_x}}{\sqrt{2\pi}}\right)^2 \\ &= \frac{1}{4}\sigma_{\tau_x}^2 - \frac{1}{2\pi}\sigma_{\tau_x}^2 = 0.090845\sigma_{\tau_x}^2 \end{aligned} \tag{4.90}$$

Therefore, the standard deviation of the maximum shear stress is $0.3014\sigma_{\tau_x}$.

Using τ_x as the basic variable, the mean-value FOSM method yields

$$E[\tau_{max}] \approx F\left(\overline{\tau_x}\right) = \frac{|E[\tau_x]|}{2} = 0 \tag{4.91}$$

and the variance of τ_{max} unable to obtain because $\left.\frac{\partial F(\tau_x)}{\partial \tau_x}\right|_{\overline{\tau_x}} = \frac{1}{2}\left.\frac{\partial |\tau_x|}{\partial \tau_x}\right|_0$ is undefined. These are clearly not good approximation. However, if $|\tau_x|$ is used as the basic variable, then the mean-value FOSM method yields

$$E[\tau_{max}] \approx F\left(\overline{|\tau_x|}\right) = \frac{E[|\tau_x|]}{2} = \frac{\sigma_{\tau_x}}{\sqrt{2\pi}} \tag{4.92}$$

$$\begin{aligned} \mathrm{Var}[\tau_{max}] &\approx \left(\left.\frac{\partial F(|\tau_x|)}{\partial |\tau_x|}\right|_{\overline{|\tau_x|}}\right)^2 \mathrm{Var}[|\tau_x|] = \left(\frac{1}{2}\right)^2 \times \left(E\left[\tau_x^2\right] - (E[|\tau_x|])^2\right) \\ &= \frac{1}{4}\left(\sigma_{\tau_x}^2 - \frac{2}{\pi}\sigma_{\tau_x}^2\right) = 0.090845\sigma_{\tau_x}^2 \end{aligned} \tag{4.93}$$

which are exact results for $E[\tau_{max}]$ and $\sigma_{\tau_{max}}$. The reason for this is as follow:

- With τ_x as the basic variable, $F(\tau_x)$ is bilinear as shown in Fig. 4.2(a). Linearization of $F(\tau_x)$ at any value of τ_x yields a poor approximation for half the range that τ_x can assume.
- With $|\tau_x|$ as the basic variable, $F(|\tau_x|)$ is linear as shown in Fig. 4.2(b), and hence the FOSM method yields exact results.

If consider τ_x^2 as the basic variable, $\tau_{max} = F\left(\tau_x^2\right) = \frac{1}{2}\sqrt{\tau_x^2}$. Using the FOSM method,

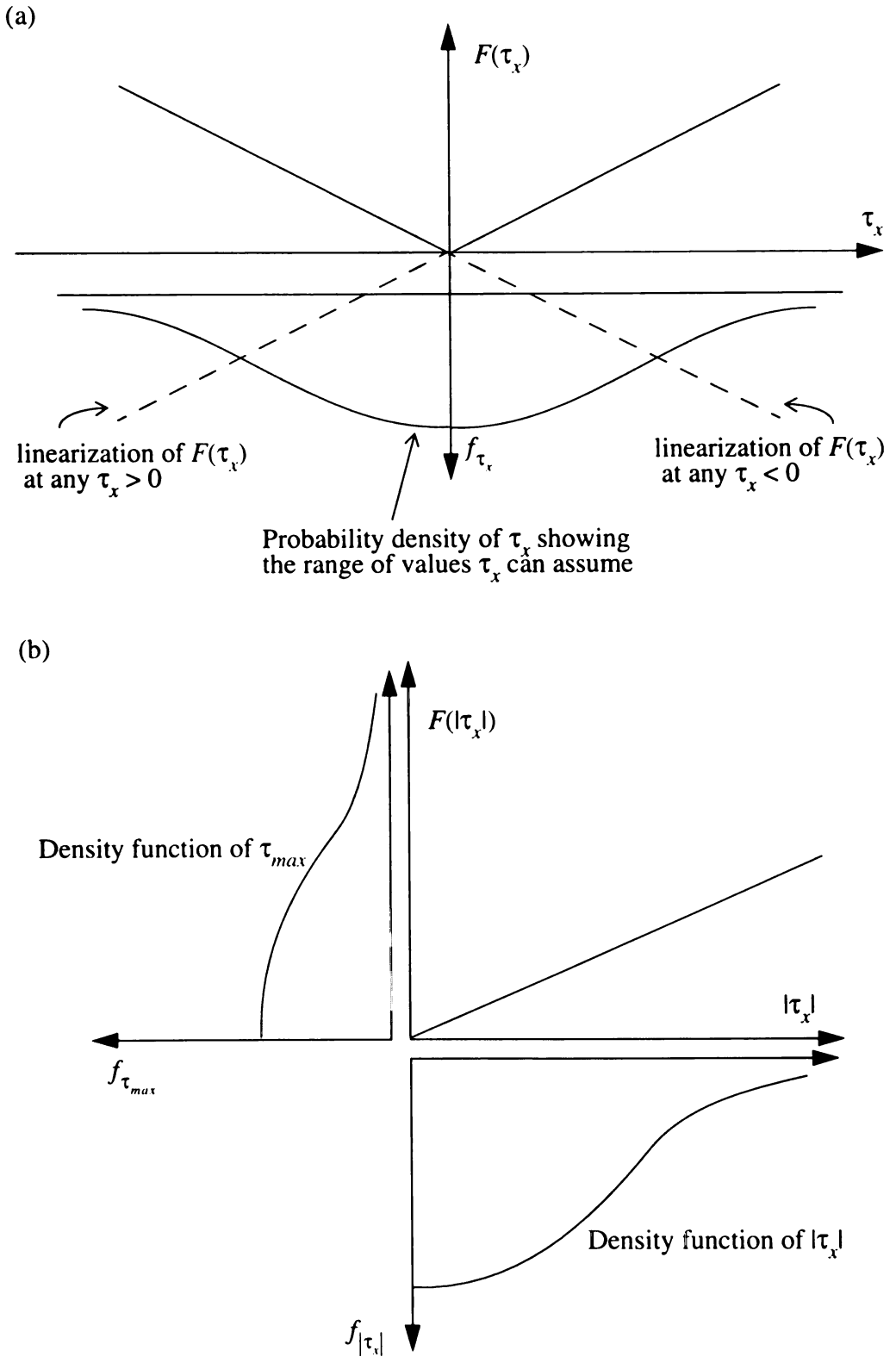

Figure 4.2 Illustration of probability distribution of maximum shear stress for 1-D case

$$E[\tau_{max}] \approx F\left(\overline{\tau_x^2}\right) = \frac{1}{2}\sqrt{E\left[\tau_x^{\,2}\right]} = \frac{1}{2}\sigma_{\tau_x} \tag{4.94}$$

$$\mathrm{Var}[\tau_{max}] \approx \left(\left.\frac{\partial F\left(\tau_x^{\,2}\right)}{\partial \tau_x^{\,2}}\right|_{\overline{\tau_x^2}}\right)^2 \mathrm{Var}\left[\tau_x^{\,2}\right] = \left(\left.\frac{1}{4\sqrt{\tau_x^{\,2}}}\right|_{\overline{\tau_x^2}=\sigma_{\tau_x}^2}\right)^2 \times 2\left(\mathrm{Var}[\tau_x]\right)^2 \tag{4.95}$$

$$= \frac{1}{16\sigma_{\tau_x}^2} \times 2\sigma_{\tau_x}^4 = 0.125\sigma_{\tau_x}^2$$

Consequently, the standard deviation of τ_{max} is $0.3536\sigma_{\tau_x}$. Table 4.3 shows the differences of the results using different basic variables, and indicates that using FOSM method with τ_x^2 as the basic variable has 25.3% error for the mean value and 17.3% error for the standard deviation of τ_{max}. Note that the correction factors (CF) defined as the ratio of the exact mean and standard deviation to the approximate mean and standard deviation are CF_μ = 0.80 and CF_σ = 0.85, respectively.

4.7.2.2 Pure shear loading τ_{xy}

For this case, $\tau_{max} = F(\tau_{xy}) = \sqrt{\tau_{xy}^2} = |\tau_{xy}|$. As in the previous section, if $|\tau_{xy}|$ is taken as the basic variable, then τ_{max} is linearly related to $|\tau_{xy}|$ and the FOSM method yields exact results. If τ_{xy}^2 is used as the basic variable, the FOSM method yields the same percentage error percentage as for uniaxial loading.

4.7.2.3 2-D beam bending problem with stresses τ_x and τ_{xy}

For this case, since $\tau_y = 0$, equation (4.87) reduces to

TABLE 4.3 Comparison of statistical moments of τ_{max} using different approaches

Maximum shear stress	Exact value	Basic variable used in FOSM method		
		τ_x	$\lvert\tau_x\rvert$	τ_x^2
Mean Value	$\sigma_{\tau_x}/\sqrt{2\pi}$	0	$\sigma_{\tau_x}/\sqrt{2\pi}$	$\sigma_{\tau_x}/2$ (CF_μ = 0.80)
Standard deviation	$0.3014\sigma_{\tau_x}$	undefined	$0.3014\sigma_{\tau_x}$	$0.3536\sigma_{\tau_x}$ (CF_σ = 0.85)

$$\tau_{max} = F(\tau_x, \tau_{xy}) = \sqrt{\frac{\tau_x^2}{4} + \tau_{xy}^2} \tag{4.96}$$

If τ_x and τ_{xy} are used as the basic variables, the FOSM method yields zero for the mean value of τ_{max} and an undefined variance for τ_{max} since $F(\tau_x, \tau_{xy})$ is not differentiable at the origin. Fig. 4.3 shows $F(\tau_x, \tau_{xy})$ with the cusp at the origin.

Alternatively, if $|\tau_x|$ and $|\tau_{xy}|$ are used as the basic variables, for all positive values, the function F can be rewritten as

$$\tau_{max} = F(|\tau_x|, |\tau_{xy}|) = \sqrt{\frac{|\tau_x|^2}{4} + |\tau_{xy}|^2} \tag{4.97}$$

and the FOSM method yields

$$\begin{aligned} E[\tau_{max}] \approx F\left(\overline{|\tau_x|}, \overline{|\tau_{xy}|}\right) &= \sqrt{\frac{1}{4}\left(\sqrt{\frac{2}{\pi}}\sigma_{\tau_x}\right)^2 + \left(\sqrt{\frac{2}{\pi}}\sigma_{\tau_{xy}}\right)^2} \\ &= \sqrt{\frac{2}{\pi}}\sqrt{\frac{\sigma_{\tau_x}^2}{4} + \sigma_{\tau_{xy}}^2} \end{aligned} \tag{4.98}$$

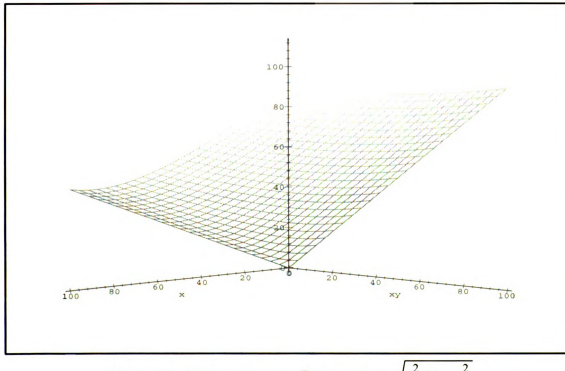

Figure 4.3 Display of function $F(\tau_x, \tau_{xy}) = \sqrt{\tau_x^2/4 + \tau_{xy}^2}$

$$\mathrm{Var}[\tau_{max}] \approx \left(\frac{\partial F}{\partial|\tau_x|}\bigg|_{\overline{|\tau_x|},\,\overline{|\tau_{xy}|}}\right)^2 \mathrm{Var}[|\tau_x|] + \left(\frac{\partial F}{\partial|\tau_{xy}|}\bigg|_{\overline{|\tau_x|},\,\overline{|\tau_{xy}|}}\right)^2 \mathrm{Var}[|\tau_{xy}|] + 2\left(\frac{\partial F}{\partial|\tau_x|}\bigg|_{\overline{|\tau_x|},\,\overline{|\tau_{xy}|}}\right)\left(\frac{\partial F}{\partial|\tau_{xy}|}\bigg|_{\overline{|\tau_x|},\,\overline{|\tau_{xy}|}}\right)\mathrm{Cov}[|\tau_x|, |\tau_{xy}|] \tag{4.99}$$

in which the variances of $|\tau_x|$ and $|\tau_{xy}|$ are

$$\begin{aligned}\mathrm{Var}[|\tau_x|] &= E\left[\tau_x^2\right] - (E[|\tau_x|])^2 \\ &= \sigma_{\tau_x}^2 - \frac{2}{\pi}\sigma_{\tau_x}^2 = 0.3634\sigma_{\tau_x}^2\end{aligned} \tag{4.100}$$

and $\mathrm{Var}[|\tau_{xy}|] = 0.3634\sigma_{\tau_{xy}}^2$, respectively; the covariance is (Papoulis 1991, p. 179)

$$\begin{aligned}&\mathrm{Cov}[|\tau_x|, |\tau_{xy}|] = E[|\tau_x||\tau_{xy}|] - E[|\tau_x|]\,E[|\tau_{xy}|] \\ &= 2\sigma_{\tau_x}\sigma_{\tau_{xy}}\left(\cos\left(\sin^{-1}(\rho)\right) + \rho\sin^{-1}(\rho)\right)/\pi - \sqrt{\frac{2}{\pi}}\sigma_{\tau_x}\sqrt{\frac{2}{\pi}}\sigma_{\tau_{xy}} \\ &= \frac{2\sigma_{\tau_x}\sigma_{\tau_{xy}}}{\pi}\left(\cos\left(\sin^{-1}(\rho)\right) + \rho\sin^{-1}(\rho) - 1\right)\end{aligned} \tag{4.101}$$

where ρ is the correlation coefficient between τ_x and τ_{xy}; and the derivative terms are

$$\frac{\partial F}{\partial|\tau_x|}\bigg|_{\overline{|\tau_x|},\,\overline{|\tau_{xy}|}} = \frac{1}{2}\frac{\overline{|\tau_x|}/2}{\sqrt{\left(\overline{|\tau_x|}\right)^2/4 + \left(\overline{|\tau_{xy}|}\right)^2}}\bigg|_{\overline{|\tau_x|},\,\overline{|\tau_{xy}|}} = \frac{1}{4}\frac{\sigma_{\tau_x}}{\sqrt{\sigma_{\tau_x}^2/4 + \sigma_{\tau_{xy}}^2}} \tag{4.102}$$

and

$$\frac{\partial F}{\partial|\tau_{xy}|}\bigg|_{\overline{|\tau_x|},\,\overline{|\tau_{xy}|}} = \frac{\sigma_{\tau_{xy}}}{\sqrt{\sigma_{\tau_x}^2/4 + \sigma_{\tau_{xy}}^2}} \tag{4.103}$$

Finally, if τ_x^2 and τ_{xy}^2 are used as the basic variables,

$$\tau_{max} = F\left(\tau_x^2, \tau_{xy}^2\right) = \sqrt{\tau_x^2/4 + \tau_{xy}^2} \tag{4.104}$$

and the FOSM method yields

$$E[\tau_{max}] \approx F\left(\overline{\tau_x^2}, \overline{\tau_{xy}^2}\right) = \sqrt{\sigma_{\tau_x}^2/4 + \sigma_{\tau_{xy}}^2} \tag{4.105}$$

$$\mathrm{Var}[\tau_{max}] \approx \left(\left.\frac{\partial F}{\partial \tau_x^2}\right|_{\overline{\tau_x^2},\,\overline{\tau_{xy}^2}}\right)^2 \mathrm{Var}\left[\tau_x^2\right] + \left(\left.\frac{\partial F}{\partial \tau_{xy}^2}\right|_{\overline{\tau_x^2},\,\overline{\tau_{xy}^2}}\right)^2 \mathrm{Var}\left[\tau_{xy}^2\right] + 2\left(\left.\frac{\partial F}{\partial \tau_x^2}\right|_{\overline{\tau_x^2},\,\overline{\tau_{xy}^2}}\right)\left(\left.\frac{\partial F}{\partial \tau_{xy}^2}\right|_{\overline{\tau_x^2},\,\overline{\tau_{xy}^2}}\right)\mathrm{Cov}\left[\tau_x^2, \tau_{xy}^2\right] \tag{4.106}$$

in which

$$\begin{aligned}\mathrm{Var}\left[\tau_x^2\right] &= E\left[\tau_x^4\right] - \left(E\left[\tau_x^2\right]\right)^2 \\ &= 3\times\left(\mathrm{Var}\left[\tau_x\right]\right)^2 - \left(\mathrm{Var}\left[\tau_x\right]\right)^2 = 2\times\left(\mathrm{Var}\left[\tau_x\right]\right)^2\end{aligned} \tag{4.107}$$

$$\begin{aligned}\mathrm{Cov}\left[\tau_x^2, \tau_{xy}^2\right] &= E\left[\left(\tau_x^2 - \overline{\tau_x^2}\right)\left(\tau_{xy}^2 - \overline{\tau_{xy}^2}\right)\right] = E\left[\tau_x^2\tau_{xy}^2\right] - \sigma_{\tau_x}^2\sigma_{\tau_{xy}}^2 \\ &= \sigma_{\tau_x}^2\sigma_{\tau_{xy}}^2 + 2\left(E\left[\tau_x\tau_{xy}\right]\right)^2 - \sigma_{\tau_x}^2\sigma_{\tau_{xy}}^2 = 2\times\left(\mathrm{Cov}\left[\tau_x, \tau_{xy}\right]\right)^2\end{aligned} \tag{4.108}$$

$$\left.\frac{\partial F}{\partial \tau_x^2}\right|_{\overline{\tau_x^2},\,\overline{\tau_{xy}^2}} = \frac{1}{8}\frac{1}{\sqrt{\sigma_{\tau_x}^2/4 + \sigma_{\tau_{xy}}^2}} \tag{4.109}$$

and

$$\left.\frac{\partial F}{\partial \tau_{xy}^2}\right|_{\overline{\tau_x^2},\,\overline{\tau_{xy}^2}} = \frac{1}{2}\frac{1}{\sqrt{\sigma_{\tau_x}^2/4 + \sigma_{\tau_{xy}}^2}} \tag{4.110}$$

As an example, consider a cantilever beam supporting a concentrated load P at its free end. Distributions of the normal stress τ_x and shear stress τ_{xy} along the depth of the beam are illustrated in Fig. 4.4. The normal stress τ_x at any distance y from the neutral axis is determined by

$$\tau_x = \frac{My}{I} \tag{4.111}$$

where M is the bending moment at the cross section under consideration, and I is the moment of inertia of the cross section with respect to the neutral axis. The shear stress τ_{xy} is determined by

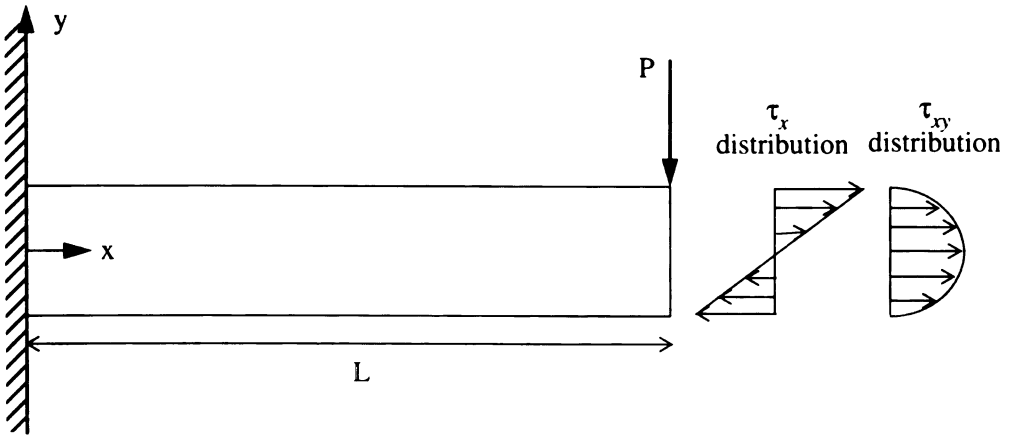

Figure 4.4 Illustration for stress distributions of beam bending problem

$$\tau_{xy} = \frac{VQ}{It} \tag{4.112}$$

in which t is the width of the beam and Q is the first moment with respect to the neutral axis.

For this problem, Fig. 4.4 shows that the sign of the shear stress may be the same as or opposite to that of the normal stress depending on whether the point under consideration is above or below the neutral axis. This implies that the correlation coefficient between τ_x and τ_{xy} could be positive or negative. For some specified cases given in Tables 4.4, the mean and standard deviation of τ_{max} were computed using the FOSM method with τ_x^2 and τ_{xy}^2 as well as $|\tau_x|$ and $|\tau_{xy}|$ as the basic variables. These results are compared with those computed by using a sufficient number of simulated samples. The details for simulation are described in Section 4.8. Two correction factors CF_μ and CF_σ for the mean and standard deviation of τ_{max}, respectively, are defined by

$$CF_\mu = \frac{\mu \text{ based on simulation}}{\mu \text{ based on FOSM}} \tag{4.113}$$

and

$$CF_\sigma = \frac{\sigma \text{ based on simulation}}{\sigma \text{ based on FOSM}} \tag{4.114}$$

which can be used to improve the accuracy of the FOSM method.

Table 4.4 shows that using $|\tau_x|$ and $|\tau_{xy}|$ as the basic variables in the FOSM method yields estimates for $E[\tau_{max}]$ that are quite close to the simulation results for all cases (i.e., $CF_\mu \approx 1$), but estimates of $\sigma_{\tau_{max}}$ fluctuate and are not uniformly accurate. On the other hand, if τ_x^2 and τ_{xy}^2 are used as the basic variables, then the FOSM method yields estimates of $\sigma_{\tau_{max}}$ and $E[\tau_{max}]$ that are consistently on the low side. Therefore, correction factors of 0.82 and 0.85 for the mean and standard deviation of τ_{max}, respectively, may be used for this case to correct the FOSM estimates so that they are close to the simulation results. The

TABLE 4.4 Simulation results and correction factors (CF) for the mean and standard deviation of τ_{max} estimated by FOSM methods using different basic variables

Case	$\sigma^2_{\tau_x}$	$\sigma^2_{\tau_y}$	ρ	Simulation results		Basic variables: $\lvert\tau_x\rvert$ and $\lvert\tau_{xy}\rvert$		Basic variables: τ_x^2 and τ_{xy}^2	
				$E[\tau_{max}]$	$\sigma_{\tau_{max}}$	CF_μ	CF_σ	CF_μ	CF_σ
1	1	1	1.0	0.8896	0.6725	0.9972	0.9979	0.7957	0.8508
2	1	1	0.5	0.9469	0.5818	1.0615	0.9957	0.8470	0.8441
3	1	1	0.0	0.9735	0.5621	1.0913	1.0114	0.8707	0.8600
4	1	1	0.5	0.9577	0.5904	1.0736	1.0103	0.8566	0.8533
5	1	1	-1.0	0.8924	0.6690	1.0004	0.9928	0.7982	0.8507
6	10	1	1.0	1.4905	1.1253	0.9985	0.6168	0.7967	0.8479
7	10	1	0.5	1.6200	0.9493	1.0853	0.6623	0.8659	0.8599
8	10	1	0.0	1.6237	0.8904	1.0878	0.6855	0.8679	0.8829
9	10	1	0.5	1.6125	0.9436	1.0803	0.6583	0.8619	0.8573
10	10	1	-1.0	1.4843	1.1231	0.9944	0.6156	0.7934	0.8549
11	1	10	1.0	2.5489	1.9195	0.9978	2.9877	0.7961	0.8476
12	1	10	0.5	2.5953	1.8582	1.0160	3.0578	0.8106	0.8466
13	1	10	0.0	2.6137	1.8520	1.0232	3.1008	0.8163	0.8353
14	1	10	0.5	2.5946	1.8682	1.0157	3.0743	0.8104	0.8322
15	1	10	-1.0	2.5558	1.9276	1.0005	3.0002	0.7983	0.8589

reason that the use of τ_x^2 and τ_{xy}^2 as the base variables produces good results is that the relationship between τ_{max} and these variables is flatter than when $|\tau_x|$ and $|\tau_{xy}|$ are used as the basic variables.

To sum up, using τ_i^2 as basic variables in the FOSM method does not yield exact results for 1-D problems while the use of $|\tau_i|$ does yield exact results. However, for 1-D and 2-D problems, the use of τ_i^2 as basic variables yields estimates that are under-predicted by consistent factors.

4.7.3 FOSM method for 3-D problems

For 3-D problems, the maximum shear stress, τ_{max}, is a function of all six Cartesian stresses. The six stress components τ_x, τ_y, τ_z, τ_{xy}, τ_{xz} and τ_{yz} are denoted by τ_1, τ_2, τ_3, τ_4, τ_5 and τ_6, respectively. The closed-form solution for τ_{max} is too complicated to work with. However, τ_{max} may be expressed as

$$\tau_{max} = \frac{\tau_{p1} - \tau_{p3}}{2} \tag{4.115}$$

where τ_{p1} and τ_{p3} are the major and minor principal stresses, respectively, and are the largest and smallest eigenvalues of the matrix

$$\begin{bmatrix} \tau_1 & \tau_4 & \tau_5 \\ \tau_4 & \tau_2 & \tau_6 \\ \tau_5 & \tau_6 & \tau_3 \end{bmatrix} \tag{4.116}$$

It should be noted that since the input earthquake excitation is assumed to be a zero-mean Gaussian process, the expected values of all Cartesian stresses are zero. However, as with the 1-D and 2-D cases, the expected value of τ_{max} is not zero.

4.7.3.1 Using $|\tau_i|$ as basic variables

For this case, the maximum shear stress is expressed as

$$\tau_{max} = F(|\tau_1|, |\tau_2|, |\tau_3|, |\tau_4|, |\tau_5|, |\tau_6|) = \frac{\tau_{p1} - \tau_{p3}}{2} \tag{4.117}$$

The FOSM method yields the expected value of τ_{max} as

$$E[\tau_{max}] \approx F\left(\overline{|\tau_1|}, \overline{|\tau_2|}, \overline{|\tau_3|}, \overline{|\tau_4|}, \overline{|\tau_5|}, \overline{|\tau_6|}\right) = \frac{\overline{\tau_{p1}} - \overline{\tau_{p3}}}{2} \tag{4.118}$$

where $\overline{\tau_{p1}}$ and $\overline{\tau_{p3}}$ are the largest and smallest eigenvalues of

$$\begin{bmatrix} \overline{|\tau_1|} & \overline{|\tau_4|} & \overline{|\tau_5|} \\ \overline{|\tau_4|} & \overline{|\tau_2|} & \overline{|\tau_6|} \\ \overline{|\tau_5|} & \overline{|\tau_6|} & \overline{|\tau_3|} \end{bmatrix} \tag{4.119}$$

The FOSM estimate of the variance of τ_{max} is

$$\begin{aligned} \mathrm{Var}[\tau_{max}] \approx & \sum_{i=1}^{6} \left(\frac{\partial F}{\partial |\tau_i|}\bigg|_{\overline{|\tau_i|}} \right)^2 \mathrm{Var}[|\tau_i|] \\ & + \sum_{\substack{i=1 \\ i \neq j}}^{6} \sum_{j=1}^{6} \frac{\partial F}{\partial |\tau_i|}\bigg|_{\overline{|\tau_i|}} \frac{\partial F}{\partial |\tau_j|}\bigg|_{\overline{|\tau_j|}} \mathrm{Cov}[|\tau_i|, |\tau_j|] \end{aligned} \tag{4.120}$$

in which the variance is (see Section 4.7.2.3)

$$\mathrm{Var}[|\tau_i|] = E\left[\tau_i^2\right] - (E[|\tau_i|])^2 = \sigma_{\tau_i}^2 - \frac{2}{\pi}\sigma_{\tau_i}^2 = 0.3634\sigma_{\tau_i}^2 \tag{4.121}$$

and the covariance is (see equation (4.101))

$$\begin{aligned} \mathrm{Cov}[|\tau_i|, |\tau_j|] &= E[|\tau_i||\tau_j|] - E[|\tau_i|]E[|\tau_j|] \\ &= 2\sigma_{\tau_i}\sigma_{\tau_j}\left(\cos\left(\sin^{-1}(\rho_{ij}) \right) + \rho_{ij}\sin^{-1}(\rho_{ij}) \right)/\pi - \sqrt{\frac{2}{\pi}}\sigma_{\tau_i}\sqrt{\frac{2}{\pi}}\sigma_{\tau_j} \\ &= \frac{2\sigma_{\tau_i}\sigma_{\tau_j}}{\pi}\left(\cos\left(\sin^{-1}(\rho_{ij}) \right) + \rho_{ij}\sin^{-1}(\rho_{ij}) - 1 \right) \end{aligned} \tag{4.122}$$

where ρ_{ij} is the correlation coefficient between τ_i and τ_j; and the derivative terms can be determined by

$$\frac{\partial F}{\partial |\tau_i|} = \frac{1}{2}\left(\frac{\partial \tau_{p1}}{\partial |\tau_i|} - \frac{\partial \tau_{p3}}{\partial |\tau_i|} \right) \quad \text{for } i=1, \ldots, 6 \tag{4.123}$$

The derivatives of τ_{p1} and τ_{p3} with respect to $|\tau_i|$ can be determined from the characteristic equation governing the eigenvalue problem. τ_{p1} and τ_{p3} are the largest and smallest roots of

$$\left|\begin{bmatrix} \tau_1-\lambda & \tau_4 & \tau_5 \\ \tau_4 & \tau_2-\lambda & \tau_6 \\ \tau_5 & \tau_6 & \tau_3-\lambda \end{bmatrix}\right| = (\tau_1-\lambda)(\tau_2-\lambda)(\tau_3-\lambda) + 2\tau_4\tau_5\tau_6 \\ -\tau_5^2(\tau_2-\lambda) - \tau_6^2(\tau_1-\lambda) - \tau_4^2(\tau_3-\lambda) = 0 \tag{4.124}$$

Denoting $|\tau_i|$ by α_i, $i = 1, ..., 6$, for all $\tau_i \geq 0$, equation (4.124) becomes

$$g(\lambda, \alpha_1, \alpha_2, \alpha_3, \alpha_4, \alpha_5, \alpha_6) = \lambda^3 - (\alpha_1+\alpha_2+\alpha_3)\lambda^2 \\ +\left(\alpha_1\alpha_2 + \alpha_1\alpha_3 + \alpha_2\alpha_3 - \alpha_5^2 - \alpha_6^2 - \alpha_4^2\right)\lambda \\ -\alpha_1\alpha_2\alpha_3 - 2\alpha_4\alpha_5\alpha_6 + \alpha_5^2\alpha_2 + \alpha_6^2\alpha_1 + \alpha_4^2\alpha_3 = 0 \tag{4.125}$$

Equations (4.124) and (4.125) are equivalent only for all $\tau_i \geq 0$, but this is sufficient since the partial derivative in equation (4.120) are always evaluated at positive values of the variables. $\frac{\partial \tau_{p1}}{\partial \alpha_i}$ and $\frac{\partial \tau_{p3}}{\partial \alpha_i}$ required in equation (4.123) can be computed by treating λ as a function of $\alpha_1, \alpha_2, ..., \alpha_6$, taking the derivative of equation (4.125) with respect to α_i, solving for $\frac{\partial \lambda}{\partial \alpha_i}$ and evaluating it at $\lambda = \tau_{p1}$ and $\lambda = \tau_{p3}$, respectively.

The total derivative of equation (4.125) is

$$dg = \sum_{i=1}^{6}\left(\frac{\partial g}{\partial \lambda}\frac{\partial \lambda}{\partial \alpha_i} + \frac{\partial g}{\partial \alpha_i}\right)\partial\alpha_i = 0 \tag{4.126}$$

Since equation (4.126) must be true for arbitrary $\partial\alpha_i$, this yields

$$\frac{\partial g}{\partial \lambda}\frac{\partial \lambda}{\partial \alpha_i} + \frac{\partial g}{\partial \alpha_i} = 0, \quad i = 1, ..., 6 \tag{4.127}$$

$$\Rightarrow \quad \frac{\partial \lambda}{\partial \alpha_i} = -\frac{\partial g/\partial \alpha_i}{\partial g/\partial \lambda}, \quad i = 1, ..., 6 \tag{4.128}$$

Thus,

$$\frac{\partial \tau_{p1}}{\partial \alpha_i} = -\left.\frac{\partial g/\partial \alpha_i}{\partial g/\partial \lambda}\right|_{\lambda = \tau_{p1}}, \quad i = 1, \ldots, 6 \tag{4.129}$$

and

$$\frac{\partial \tau_{p3}}{\partial \alpha_i} = -\left.\frac{\partial g/\partial \alpha_i}{\partial g/\partial \lambda}\right|_{\lambda = \tau_{p3}}, \quad i = 1, \ldots, 6 \tag{4.130}$$

The partial derivatives in equations (4.129) and (4.130) are:

$$\frac{\partial g}{\partial \lambda} = 3\lambda^2 - 2\lambda(\alpha_1 + \alpha_2 + \alpha_3) + \left(\alpha_1\alpha_2 + \alpha_1\alpha_3 + \alpha_2\alpha_3 - \alpha_5^2 - \alpha_6^2 - \alpha_4^2\right) \tag{4.131}$$

$$\frac{\partial g}{\partial \alpha_1} = -\left(\lambda^2 - (\alpha_2 + \alpha_3)\lambda + \alpha_2\alpha_3 - \alpha_6^2\right) \tag{4.132}$$

$$\frac{\partial g}{\partial \alpha_2} = -\left(\lambda^2 - (\alpha_1 + \alpha_3)\lambda + \alpha_1\alpha_3 - \alpha_5^2\right) \tag{4.133}$$

$$\frac{\partial g}{\partial \alpha_3} = -\left(\lambda^2 - (\alpha_1 + \alpha_2)\lambda + \alpha_1\alpha_2 - \alpha_4^2\right) \tag{4.134}$$

$$\frac{\partial g}{\partial \alpha_4} = -2(\alpha_4\lambda + \alpha_5\alpha_6 - \alpha_4\alpha_3) \tag{4.135}$$

$$\frac{\partial g}{\partial \alpha_5} = -2(\alpha_5\lambda + \alpha_4\alpha_6 - \alpha_5\alpha_2) \tag{4.136}$$

and

$$\frac{\partial g}{\partial \alpha_6} = -2(\alpha_6\lambda + \alpha_4\alpha_5 - \alpha_6\alpha_1) \tag{4.137}$$

4.7.3.2 Using τ_i^2 as basic variables

For this case, τ_{max} can be expressed as

$$\tau_{max} = F\left(\tau_1^2, \tau_2^2, \tau_3^2, \tau_4^2, \tau_5^2, \tau_6^2\right) \tag{4.138}$$

The FOSM method yields the expected value of τ_{max} as

$$E[\tau_{max}] \approx F\left(\overline{\tau_1^2}, \overline{\tau_2^2}, \overline{\tau_3^2}, \overline{\tau_4^2}, \overline{\tau_5^2}, \overline{\tau_6^2}\right) = \frac{\overline{\tau_{p1}} - \overline{\tau_{p3}}}{2} \tag{4.139}$$

where $\overline{\tau_{p1}}$ and $\overline{\tau_{p3}}$ are the largest and smallest eigenvalues of

$$\begin{bmatrix} \sqrt{\overline{\tau_1^2}} & \sqrt{\overline{\tau_4^2}} & \sqrt{\overline{\tau_5^2}} \\ \sqrt{\overline{\tau_4^2}} & \sqrt{\overline{\tau_2^2}} & \sqrt{\overline{\tau_6^2}} \\ \sqrt{\overline{\tau_5^2}} & \sqrt{\overline{\tau_6^2}} & \sqrt{\overline{\tau_3^2}} \end{bmatrix} \tag{4.140}$$

The FOSM estimate of the variance of τ_{max} is

$$\mathrm{Var}[\tau_{max}] \approx \sum_{i=1}^{6} \left(\left. \frac{\partial F}{\partial \tau_i^2} \right|_{\overline{\tau_i^2}} \right)^2 \mathrm{Var}\left[\tau_i^2\right] + \sum_{\substack{i=1 \\ i \neq j}}^{6} \sum_{j=1}^{6} \left. \frac{\partial F}{\partial \tau_i^2} \right|_{\overline{\tau_i^2}} \left. \frac{\partial F}{\partial \tau_j^2} \right|_{\overline{\tau_j^2}} \mathrm{Cov}\left[\tau_i^2, \tau_j^2\right] \tag{4.141}$$

where $\mathrm{Var}\left[\tau_i^2\right]$ and $\mathrm{Cov}\left[\tau_i^2, \tau_j^2\right]$ were shown in equations (4.107) and (4.108), respectively, and the derivative terms can be determined by

$$\frac{\partial F}{\partial \tau_i^2} = \frac{1}{2}\left(\frac{\partial \tau_{p1}}{\partial \tau_i^2} - \frac{\partial \tau_{p3}}{\partial \tau_i^2} \right) \quad \text{for } i=1, \ldots, 6 \tag{4.142}$$

The derivatives of τ_{p1} and τ_{p3} with respect to τ_i^2 can be determined from the characteristic equation governing the eigenvalue problem. τ_{p1} and τ_{p3} are the largest and smallest roots of equation (4.124). Denoting τ_i^2 by β_i, $i = 1, \ldots, 6$, for all $\tau_i \geq 0$, equation (4.124) becomes

$$\begin{aligned} h(\lambda, \beta_1, \beta_2, \beta_3, \beta_4, \beta_5, \beta_6) &= \lambda^3 - \left(\sqrt{\beta_1} + \sqrt{\beta_2} + \sqrt{\beta_3} \right)\lambda^2 \\ &+ \left(\sqrt{\beta_1\beta_2} + \sqrt{\beta_1\beta_3} + \sqrt{\beta_2\beta_3} - \beta_5 - \beta_6 - \beta_4 \right)\lambda \\ &- \sqrt{\beta_1\beta_2\beta_3} - 2\sqrt{\beta_4\beta_5\beta_6} + \beta_5\sqrt{\beta_2} + \beta_6\sqrt{\beta_1} + \beta_4\sqrt{\beta_3} = 0 \end{aligned} \tag{4.143}$$

Again, equations (4.143) and (4.124) are equivalent since the partial derivatives in equation (4.141) are always evaluated at positive values of the variables. $\frac{\partial \tau_{p1}}{\partial \beta_i}$ and $\frac{\partial \tau_{p3}}{\partial \beta_i}$ required in equation (4.142) can be computed by treating λ as a function of $\beta_1, \beta_2, \ldots, \beta_6$, taking the derivative of equation (4.143) with respect to β_i, solving for $\frac{\partial \lambda}{\partial \beta_i}$ and evaluating it at $\lambda = \tau_{p1}$ and $\lambda = \tau_{p3}$, respectively.

The total derivative of equation (4.143) is

$$dh = \sum_{i=1}^{6}\left(\frac{\partial h}{\partial \lambda}\frac{\partial \lambda}{\partial \beta_i} + \frac{\partial h}{\partial \beta_i}\right)\partial\beta_i = 0 \tag{4.144}$$

Since equation (4.144) must be true for arbitrary $\partial\beta_i$, this yields

$$\frac{\partial h}{\partial \lambda}\frac{\partial \lambda}{\partial \beta_i} + \frac{\partial h}{\partial \beta_i} = 0,\ i = 1, \ldots, 6 \tag{4.145}$$

$$\Rightarrow \quad \frac{\partial \lambda}{\partial \beta_i} = -\frac{\partial h/\partial \beta_i}{\partial h/\partial \lambda},\ i = 1, \ldots, 6 \tag{4.146}$$

Thus,

$$\frac{\partial \tau_{p1}}{\partial \beta_i} = -\left.\frac{\partial h/\partial \beta_i}{\partial h/\partial \lambda}\right|_{\lambda = \tau_{p1}},\ i = 1, \ldots, 6 \tag{4.147}$$

and

$$\frac{\partial \tau_{p3}}{\partial \beta_i} = -\left.\frac{\partial h/\partial \beta_i}{\partial h/\partial \lambda}\right|_{\lambda = \tau_{p3}},\ i = 1, \ldots, 6 \tag{4.148}$$

The partial derivatives in equations (4.147) and (4.148) are:

$$\begin{aligned}\frac{\partial h}{\partial \lambda} &= 3\lambda^2 - 2\lambda\left(\sqrt{\beta_1} + \sqrt{\beta_2} + \sqrt{\beta_3}\right) \\ &+\left(\sqrt{\beta_1\beta_2} + \sqrt{\beta_1\beta_3} + \sqrt{\beta_2\beta_3} - \beta_5 - \beta_6 - \beta_4\right)\end{aligned} \tag{4.149}$$

$$\frac{\partial h}{\partial \beta_1} = -\frac{1}{2\sqrt{\beta_1}}\left(\lambda^2 - \left(\sqrt{\beta_2} + \sqrt{\beta_3}\right)\lambda + \sqrt{\beta_2\beta_3} - \beta_6\right) \tag{4.150}$$

$$\frac{\partial h}{\partial \beta_2} = -\frac{1}{2\sqrt{\beta_2}}\left(\lambda^2 - \left(\sqrt{\beta_1} + \sqrt{\beta_3}\right)\lambda + \sqrt{\beta_1\beta_3} - \beta_5\right) \tag{4.151}$$

$$\frac{\partial h}{\partial \beta_3} = -\frac{1}{2\sqrt{\beta_3}}\left(\lambda^2 - \left(\sqrt{\beta_1} + \sqrt{\beta_2}\right)\lambda + \sqrt{\beta_1\beta_2} - \beta_4\right) \tag{4.152}$$

$$\frac{\partial h}{\partial \beta_4} = -\lambda - \frac{\sqrt{\beta_5}\sqrt{\beta_6}}{\sqrt{\beta_4}} + \sqrt{\beta_3} \tag{4.153}$$

$$\frac{\partial h}{\partial \beta_5} = -\lambda - \frac{\sqrt{\beta_4}\sqrt{\beta_6}}{\sqrt{\beta_5}} + \sqrt{\beta_2} \tag{4.154}$$

and

$$\frac{\partial h}{\partial \beta_6} = -\lambda - \frac{\sqrt{\beta_4}\sqrt{\beta_5}}{\sqrt{\beta_6}} + \sqrt{\beta_1} \tag{4.155}$$

4.8 Simulation

The use of higher order terms in the Taylor series expansion in equation (4.84) would be expected to increase the accuracy in the moment estimates of τ_{max} for the 3-D case. However, such an analysis becomes intractable in practice. An alternative and more reliable approach is to use Monte Carlo simulation. Numerous samples of Gaussian Cartesian stresses consistent with a specified covariance matrix can be simulated, samples of τ_{max} can be computed for each Cartesian sample set, and the mean and variance of the τ_{max} samples can be computed. The Naval Surface Warfare Center mathematics subroutines library (NSWC 1993) provides a routine to generate multivariate normal random samples with a specified mean and covariance matrix. The density function of the multivariate Gaussian distribution for $\{x\} = [x_1, ..., x_m]^T$ is given by

$$f(x) = \frac{1}{\sqrt{(2\pi)^m det([A])}} \exp\left(-\frac{1}{2}(\{x\} - \{\mu\})[A]^{-1}(\{x\} - \{\mu\})^T\right) \tag{4.156}$$

in which $[A]$ is the covariance matrix of the variates $\{x\}$ and $\{\mu\}$ is the mean vector. In the case studied, $\{\mu\}=\{0\}$.

A sufficient number of samples must be generated to obtain sufficient accuracy in the moment estimates. Figs. 4.5 and 4.6 show typical estimates of the mean and standard deviation of τ_{max}, respectively, as the number of samples is increased. The figures indicate that 8,000–10,000 samples are required to accurately estimate the first two moments of τ_{max}.

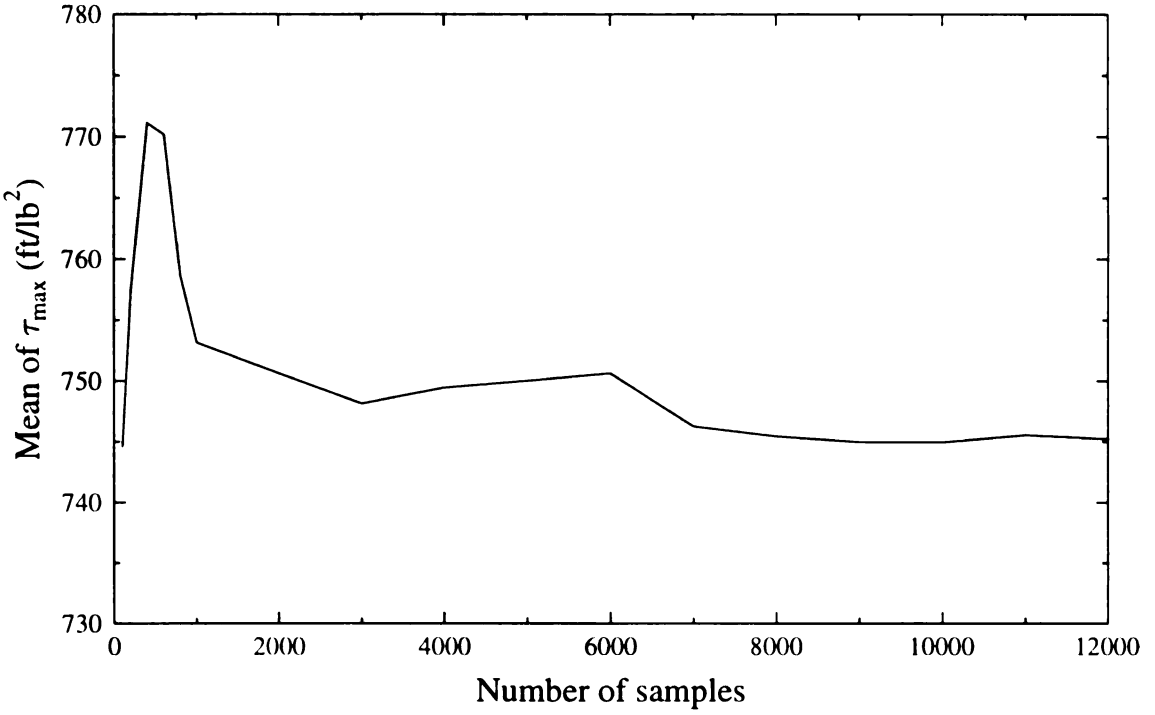

Figure 4.5 Estimate of mean of τ_{max} for different number of samples

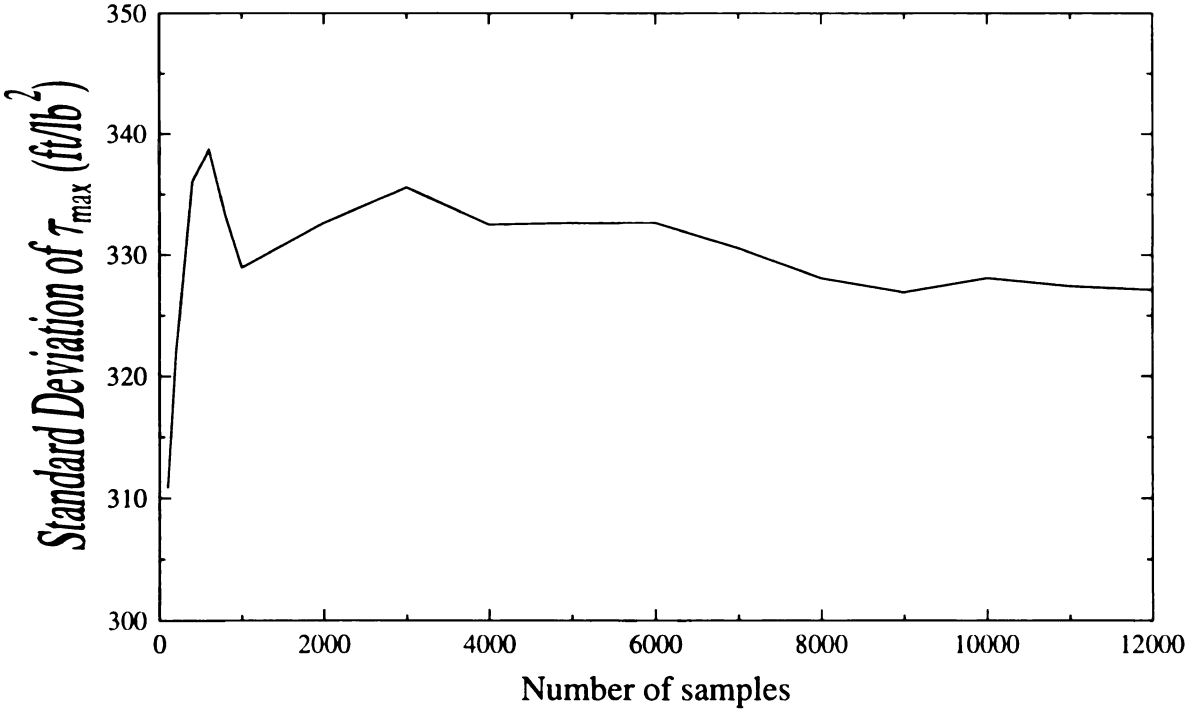

Figure 4.6 Estimate of standard deviation of τ_{max} for different number of samples

A typical histogram of τ_{max} based on 10,000 sample is shown in Fig. 4.7. Although the probability density function of τ_{max} is a function of the covariance matrix of the Cartesian stresses τ_i at the point under consideration, typically about 99.55% of the samples lie below the mean plus three standard deviations of τ_{max}.

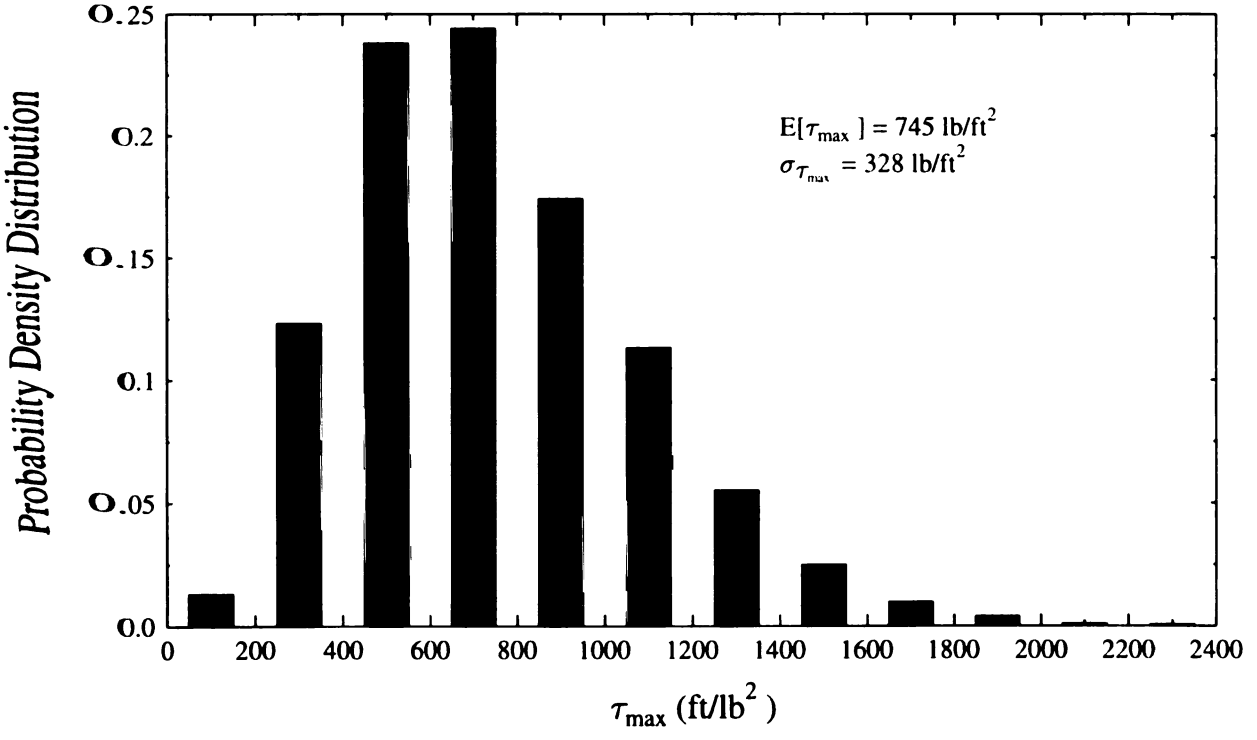

Figure 4.7 Probability density distribution of maximum shear stress

5. STOCHASTIC RESPONSE OF THE SANTA FELICIA DAM — CASE STUDY

5.1 Ground Motion Model

The ground motion model shown in equation (4.2) is based on the analysis of recordings made by the SMART-1 seismograph array in Lotung, Taiwan. The model which considers the spatial as well as the temporal variation of earthquake ground motion is used in this study. The parameters of the auto spectral density function (SDF) $S_{\ddot{u}_g}$ were estimated from the El Centro earthquake record by fitting the function expressed in equation (4.5) to observed acceleration spectra. Fig. 5.1 shows the normalized autospectrum and the fitted model. The parameters ω_g, ζ_g, ω_f and ζ_f which control the shape

TABLE 5.1 **Double-filter Autospectrum Parameters**

ω_g(rad/s)	ζ_g	ω_f(rad/s)	ζ_f
15.0	0.55	3.0	0.60

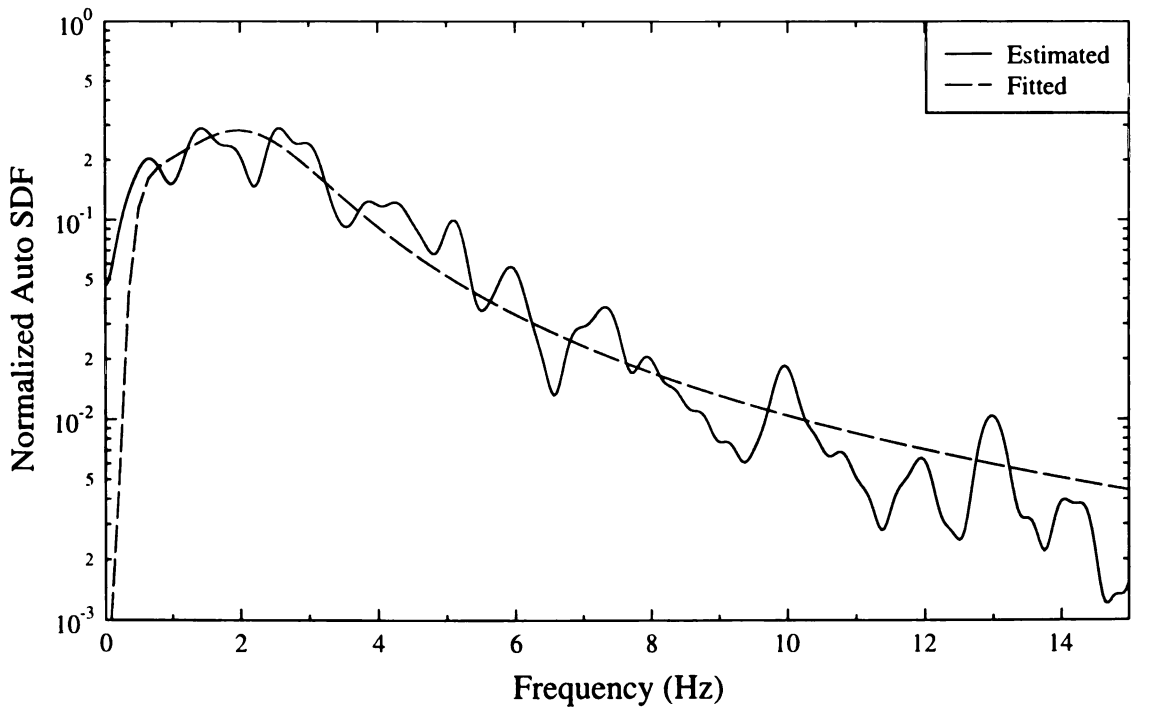

Figure 5.1 **Fitted Autospectra for Ground Motion Accelerogram**

of the spectra are listed in Table 5.1. In the auto SDF, the intensity parameter S_0 was adjusted such that the standard deviation of the ground acceleration is $0.09g$ corresponding to a peak acceleration of about $0.27g$.

For the coherency function $|\gamma(\nu,\omega)|$ in equation (4.3), the five parameters used in the analysis are listed in Table 5.2. These parameters correspond to Event 20 recorded by the SMART-1 array. In general, the coherency decreases with increasing separation and increasing frequency, as shown in Fig. 5.2 and Fig. 5.3. To account for the wave passage effect, an exponential function, $\exp(-i\omega\nu/V)$, is used, in which ν is the separation distance and V is the apparent wave velocity. Since the Santa Felicia dam is located on bedrock, an apparent wave velocity of 4,267 m/s corresponding to waves in the bedrock propagating at 2,134 m/s with an incident angle of 60° to the horizontal was assumed. An incident angle of 60° was found to be critical by Dakoulas and Hashmi (1992). This angle is used to determine the delay due to wave propagation for the nodes along inclined base surfaces. Unless noted otherwise, the waves are assumed to propagate in the upstream/downstream direction (x-direction). Consequently, the delay time between two locations was computed as $(\nu_x \cos\theta + \nu_y \sin\theta)/V_e$, in which V_e is the actual wave propagation velocity in the bedrock, θ is the incident angle to the horizontal, and ν_x and ν_y are separations between two nodes in the x and y directions, respectively.

In order to obtain a physical feel for accelerograms that are consistent with the prescribed SDF, coherency function and propagation velocity, stationary accelerogram segments at the extreme downstream and upstream corners and the middle of the base along the axis of symmetry were simulated. These three accelerograms are shown in Fig. 5.4.

TABLE 5.2 Coherency Function Parameters

A	α	*k (m)*	ω_0 (rad/s)	*b*
0.636	0.0186	31,200	9.49	2.95

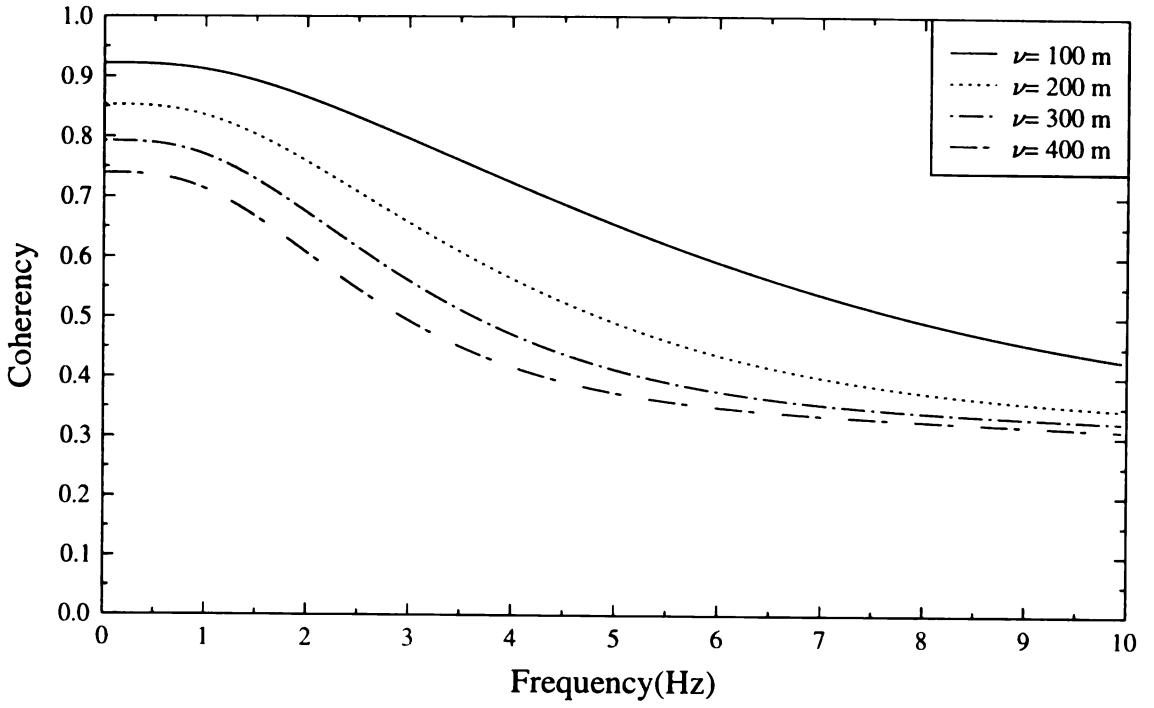

Figure 5.2 **Coherency vs. frequency**

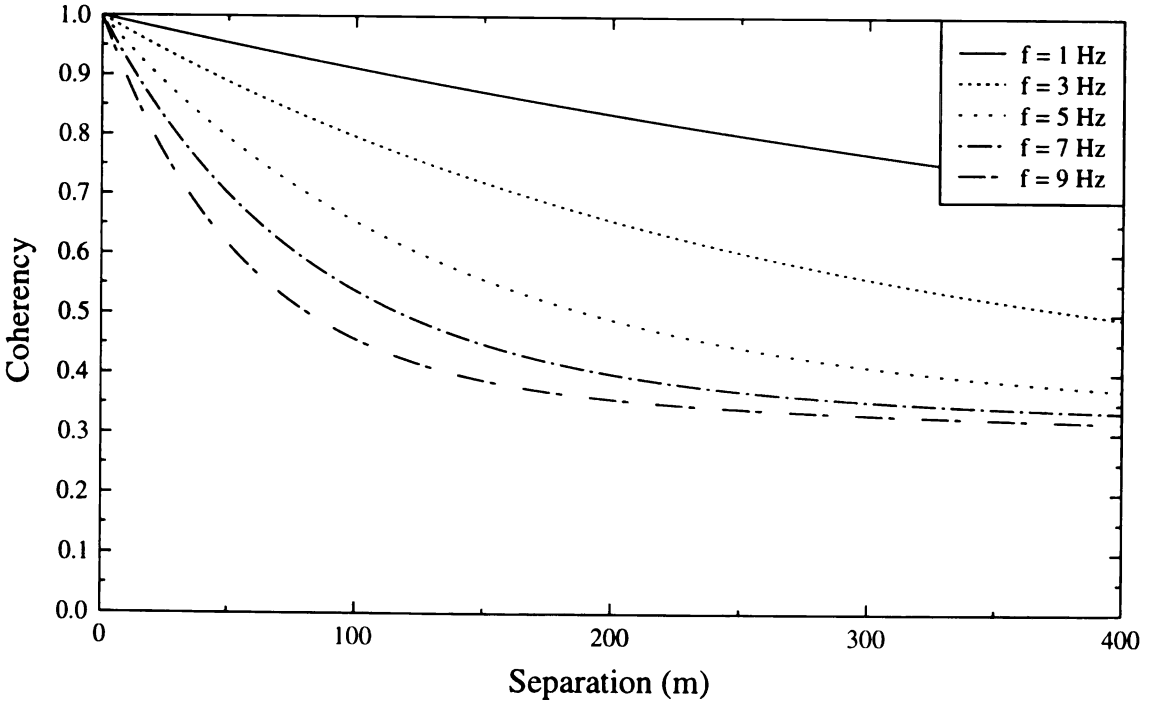

Figure 5.3 **Coherency vs. separation**

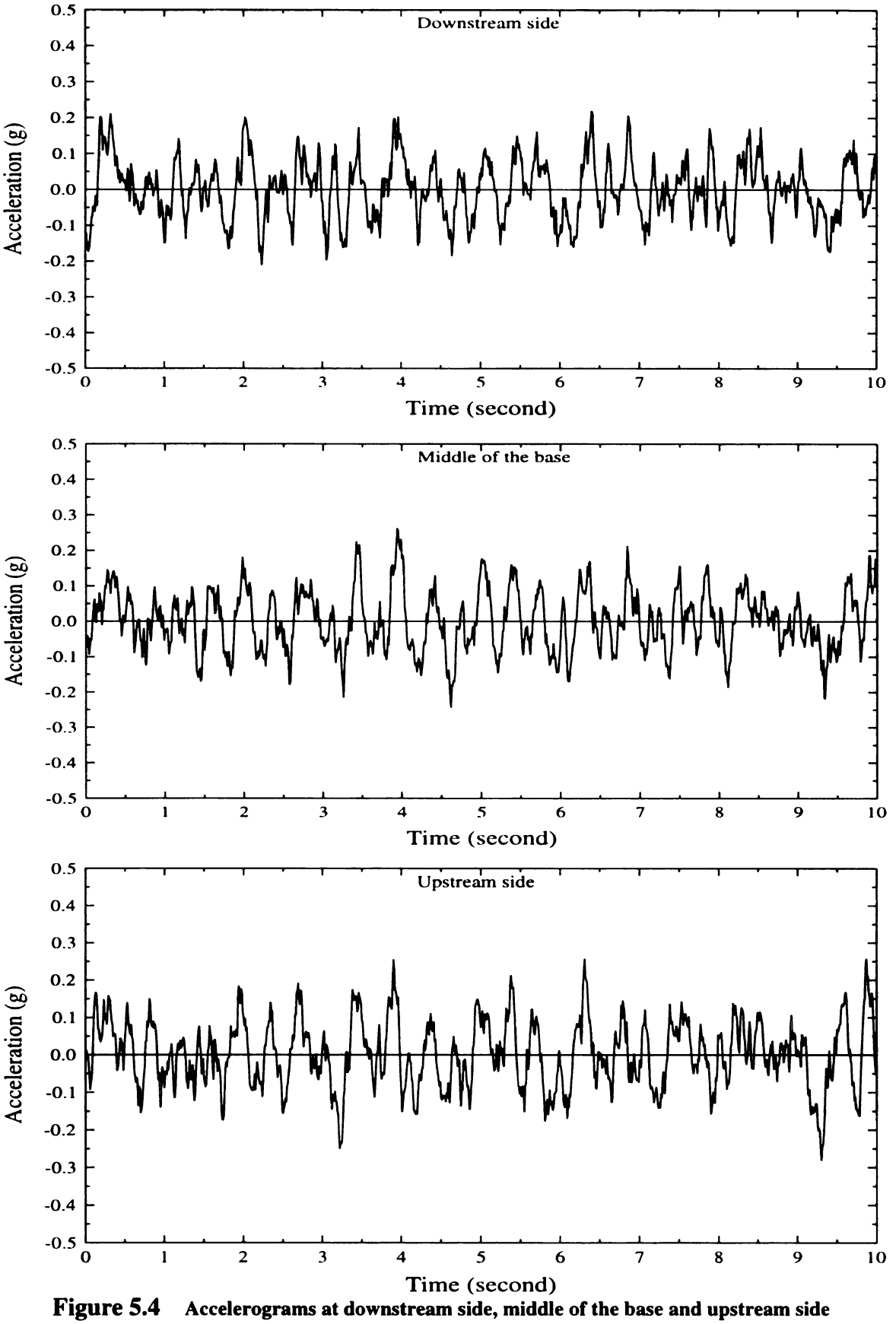

Figure 5.4 **Accelerograms at downstream side, middle of the base and upstream side**

5.2 Computation Steps

A series of computer programs were written to perform the stochastic response analysis of the earth dam. The basic steps of the analysis are summarized below:

1. In equation (4.17), mode shapes $\{\Phi\}$ and modal mass M_j as well as the mass matrix [M] and the static constraint matrix [A] are required in computing the participation factor matrix $[\Gamma]$. $\{\Phi\}$ and M_j can be obtained directly from regular output in I-DEAS, but [M] and [A] need to be generated by special techniques which are described in Appendix A.5.

2. Using equation (4.18), the participation factor matrix $[\Gamma]$ was computed. $[\Gamma]$ is of order $r \times n$, where r = number of restrained DOFs with excitation and n = number of modes (for the model used, $r = 288$ and $n = 80$). The static constraint matrix [A] has a size of $N \times r$, in which each column represents the deformation shape due to unit displacement at a restrained node, and N = total number of DOFs in the model (for the model used, $N = 3012$ and r = 288).

3. The lower triangular part of the integration matrix of equation (4.38) was computed by using the numerical subroutine DQAGI in the NSWC mathematics library, and stored in a 1-D array of order $n(n+1)/2$.

4. The integrals $\int_{-\infty}^{\infty} \frac{1}{\omega^4} S_{\ddot{u}_{R_l}\ddot{u}_{R_m}}(\omega)\, d\omega$ were computed and stored in an array of size $r(r+1)/2$. The integrals $\int_{-\infty}^{\infty} \frac{1}{\omega^2} H_j(\omega)\, S_{\ddot{u}_{R_l}\ddot{u}_{R_m}}(\omega)\, d\omega$ were computed and stored in an array of size $n \times r$. It should be mentioned that the calculations of the integrations using the adaptive algorithms in DQAGI are extremely time-consuming. The approximate elapsed time using an HP Model 715/50 workstation is shown in Table 5.3.

TABLE 5.3 Approximate elapsed time for calculation of integration

Static	Dynamic	Static-Dynamic
15 minutes	21 days	16 hours

5. The variance of the total displacement responses were computed using equations (4.37), (4.42) and (4.49) for each degree of freedom. The three displacement components in the x, y and z directions were computed at each node.
6. For 3-D problem, six Cartesian stresses and strains were computed and the covariance matrix for each node is of order 6 by 6. Because of symmetry, only 21 components in the matrix were calculated. The total covariance matrix of stresses (strains) was computed using equations (4.55), (4.57) and (4.58) for each node, in which the integration values are identical to the results computed in step 4. The stress mode shape $[\Psi]$ is of order $N \times n$ (for the model used, $N = 6024$ and $n = 80$). The static constraint matrix $[\eta]$ has a size of $N \times r$ (for the model used, $N = 6024$ and $r = 288$).
7. Using the covariance matrices for stresses and strains computed in step 6, 10,000 normal random samples were simulated for the six Cartesian stresses and strains at each node. 10,000 values of the maximum shear stress and strain were computed at each node using the Cartesian stresses and strains, and the $\mu+3\sigma$ values were estimated from the simulated data.
8. The $\mu+3\sigma$ of maximum shear stress were also estimated using the FOSM method with τ_i^2 in addition to with $|\tau_i|$ as the basic variables (see Section 4.7.3).
9. Mohr-Coulomb strength criterion is employed to determine the shear strength of soils. By considering gravity and earthquake loads, reliability analysis was performed.

5.3 Numerical Results

Finite element analysis yields a vast amount of results, and a good post-processor is essential to suitably display relevant quantities. Fortunately, the excellent post-processor in I-DEAS can be utilized to display response quantities computed with customized programs for random vibration analysis. The techniques to display response contours are described in Appendix A.6. Shaded image contours of the displacement, stress and strain responses are displayed over the entire dam in this section. All responses should be symmetric about the middle axis of the dam and any observable asymmetry is due to the variability in the simulated data on either side of the axis of symmetry. The origin of the coordinate system used in the study is located at the mid-point of the base in the core clay region.

5.3.1 Responses to general excitation

This section shows the dam responses to general SVEGM. Both correlation and wave propagation effects were included for the base excitations.

5.3.1.1 Displacement

Since the excitations are assumed to be zero-mean Gaussian processes, the mean value of the displacement response must be zero. The variance of the total x-, y- and z-displacements at each node was computed using equation (4.26). The standard deviation (σ) is taken to be the positive square root of the variance. Fig. 5.5 shows four different views of the 3σ x-displacement response contours so that the displacements on the dam surface and within the dam can be easily visualized. The scale for the contour is shown on the right edge of each picture. The darker contour shades signify larger response values. The figures show that the maximum x-displacement occurs at the middle of the crest, with a 3σ value of 191.8 mm (0.630 ft). The displacements decrease with increasing distance from the mid-point of the crest.

In 3-D analysis, the total displacement response consists of the x, y and z components. Fig. 5.6 shows the 3σ contours for each displacement component. As expected, the

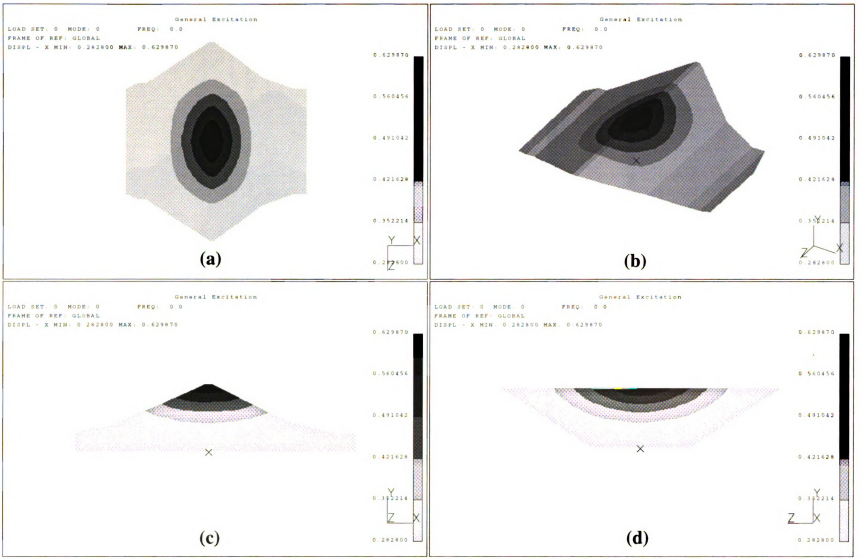

Figure 5.5 3σ x-displacement contours (ft) (a) plan view, (b) isometric view, (c) cutting plane at z = 0, (d) cutting plane at x = 0.

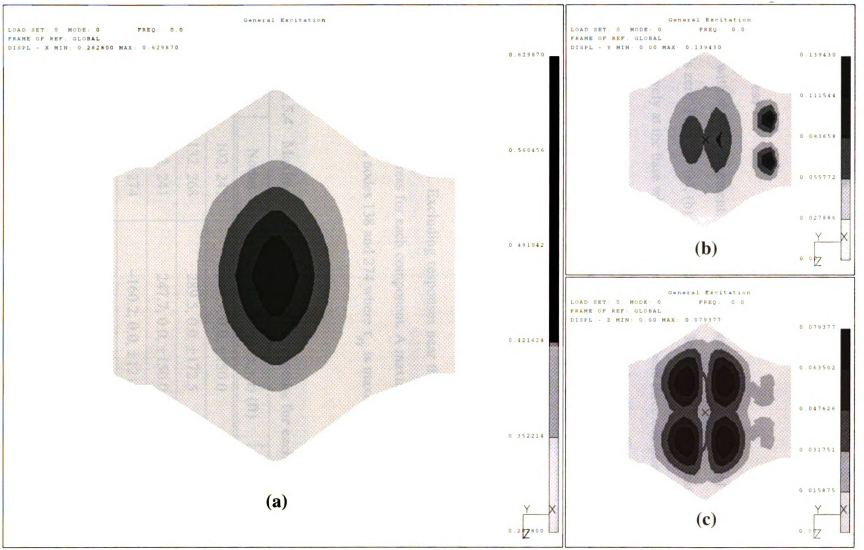

Figure 5.6 3σ x-displacement contours (ft) for general excitation case: (a) x component (b) y component (c) z component.

x-displacement dominates the total displacement response. Since the magnitudes of the y and z components are very small in comparison to the x-displacement, it is reasonable to neglect them.

5.3.1.2 Stress

As with the displacement, for zero-mean excitations, the mean of the Cartesian stresses is zero. Figs. 5.7 (a), (b) and (c) show the 3σ contours of the stresses, τ_x, τ_{xy} and τ_{xz}, respectively at the base where they are critical. These three components are the most significant. The stress component τ_{xy} is mainly caused by bending effects. τ_{xz} at the base is primarily caused by the spatial variation of the base excitation. According to the Mohr-Column failure criterion, the failure of soil material is related to the maximum shear stress, τ_{max}, and the soil properties. The mean plus three standard deviation ($\mu+3\sigma$) contours of τ_{max} at the base are shown in Fig. 5.7(d). It should be noted that the high values of stresses occurring on the upstream and downstream sides are due to the artificial cut-off boundary and should be disregarded. Excluding responses near the boundary, Table 5.4 lists the maximum $\mu+3\sigma$ nodal stress for each component. A maximum shear stress of 1,670 kPa (34,869 lb/ft^2) occurs at nodes 138 and 274 where τ_{xy} is maximum.

TABLE 5.4 Maximum $\mu+3\sigma$ nodal stress response for each component

Component	Nodes	Node Location (x,y,z) (ft)	Stress (kPa)
τ_x	102, 241	247.7, 0.0, ±150.0	3,222
τ_y	132, 268	289.5, 0.0, ±172.5	772
τ_z	102, 241	247.7, 0.0, ±150.0	1,005
τ_{xy}	138, 274	−160.2, 0.0, ±121.8	1,467
τ_{xz}	105, 244	176.3, 0.0, ±225.0	1,187
τ_{yz}	138, 274	−160.2, 0.0, ±121.8	394
τ_{max}	138, 274	−160.2, 0.0, ±121.8	1,670

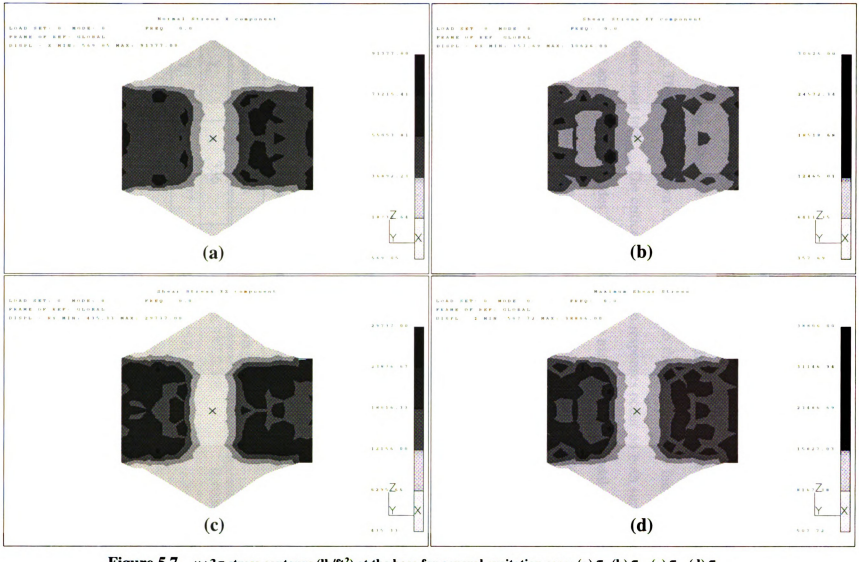

Figure 5.7 $\mu+3\sigma$ stress contours (lb/ft^2) at the base for general excitation case: (a) τ_x (b) τ_{xy} (c) τ_{xz} (d) τ_{max}

5.3.1.3 Strain

Although stresses are critical at the base, strains are critical at the top free surface of the dam because the material at the top is not as stiff as the material of the base. The $\mu+3\sigma$ values of the three dominant strain components, γ_x, γ_{xy} and γ_{xz}, and the maximum shear strain γ_{max} at the top surface of the dam are shown in Figs. 5.8 (a), (b), (c) and (d), respectively. In Fig. 5.8(a), the high values of γ_x along the side boundaries are due to ground straining. The contour pattern of γ_{max} is similar to that of γ_{xy}, which indicates that γ_{xy} contributes most to γ_{max}. The critical shear strain responses occur on both surfaces of the upstream and downstream sides. Table 5.4 lists the maximum $\mu+3\sigma$ nodal strain for each component. It is shown that γ_{xy} dominates the strain response, which gives most contributions to γ_{max}.

5.3.2 Modal contributions

The dynamic response variances consist of individual modal response variances and covariances between pairs of modal responses as indicated in equation (4.37). The relative modal contributions to the x-displacement are examined in detail at the middle of the dam crest (which has the maximum displacement). Table 5.6 shows the percent contribution of

TABLE 5.5 Maximum $\mu+3\sigma$ nodal strain response for each component

Component	Nodes	Node Location (x,y,z) (ft)	Strain
γ_x	336	−212.5, 187.5, 0.0	9.4008×10^{-4}
γ_y	644, 977	147.7, 125.0, ±64.7	4.9636×10^{-4}
γ_z	438	195.0, 185.0, 0.0	5.1313×10^{-4}
γ_{xy}	591, 924	129.1, 176.1, ±39.2	2.2613×10^{-3}
γ_{xz}	504, 837	−125.3, 226.1, ±349.0	9.8622×10^{-4}
γ_{yz}	627,960	−203.3, 180.8, ±187.0	6.2395×10^{-4}
γ_{max}	591, 924	129.1, 176.1, ±39.2	1.9340×10^{-3}

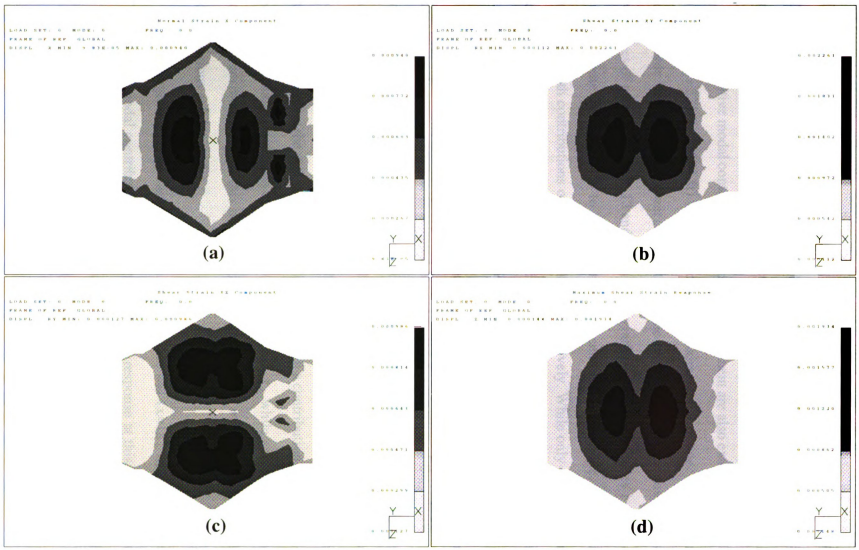

Figure 5.8 $\mu+3\sigma$ **strain contours at the top free surface for general excitation case: (a)** γ_x **(b)** γ_{xy} **(c)** γ_{xz} **(d)** γ_{max}

the model variances (diagonal terms) and covariance (off-diagonal terms). The variances (diagonal elements in Table 5.6) of modes 1, 6 and 16 and the covariances between modes 1 & 6 and 15 & 16 contribute more than 1% to the dynamic displacement. However, the mode 1 variance dominates, with a contribution of 96%.

The relative modal contributions to the x-displacement are also examined at node 329 (x=-15 ft, y=275 ft, z=354 ft) which is located approximately at quarter length along the crest. Table 5.6 shows the percent contribution of the modal variances and covariances. The variances of modes 1, 3, 6, 9, 13 and 19 and the covariances between modes 1 & 6 and 6 & 19 contribute more than 1% to the dynamic displacement. At this node, modes 1 and 6 dominate with contributions of 34% and 40%, respectively. While only symmetric modes contributed to the displacement at the middle of the crest, but symmetric and antisymmetric modes contribute to the displacement at the quarter-length locations.

The τ_{xy} component at node 275 (x=-167 ft, y=0 ft, z=-57.9 ft), which has the maximum dynamic variance, is selected for a detailed examination of the relative modal contributions. Table 5.6 shows the percent contribution of the modal variance and covariance. The variances of modes 1, 6, 10 and 16 and the covariances between modes 1 & 6, 1 & 10 and 10 & 16 contribute more than 1% to the dynamic τ_{xy} at this node. As with the displacement at the mid-crest, mode 1 dominates with a contribution of 94%. Basically, symmetric modes give some contribution to the dynamic τ_{xy} while anti-symmetric modes do not contribute at all at this node. Anti-symmetric modes may of course have larger contributions at other nodes.

The largest dynamic variance of γ_{xy} occurs at node 441 (x=181 ft, y=108 ft, z=0 ft). The percent modal contributions to the total dynamic response at this node are listed in Table 5.6. The variances of modes 1, 6 and 10 and the covariances between modes 1 & 6, 1 & 10 and 6 & 10 contribute more than 1% to the response. Again, mode 1 dominates with

TABLE 5.6 Percent modal contribution to the dynamic x-displacement response at the middle of the dam crest

mode	1	2	3	4	5	6	7	8	9	10	11	12	13	14	15	16	17	18	19	20
1	95.9																			
2	.000	.000																		
3	.000	.000	.000																	
4	.000	.000	.000	.000																
5	-.22	.000	.000	.000	.002															
6	-5.9	.000	.000	.000	.134	4.77														
7	-.08	.000	.000	.000	.001	.047	.001													
8	.000	.000	.000	.000	.000	.000	.000	.000												
9	.000	.000	.000	.000	.000	.000	.000	.000	.000											
10	.106	.000	.000	.000	.000	-.05	.000	.000	.000	.002										
11	.000	.000	.000	.000	.000	.000	.000	.000	.000	.000	.000									
12	.000	.000	.000	.000	.000	.000	.000	.000	.000	.000	.000	.000								
13	.224	.000	.000	.000	.000	-.15	.000	.000	.000	.000	.000	.000	.049							
14	.000	.000	.000	.000	.000	.000	.000	.000	.000	.000	.000	.000	.000	.000						
15	.321	.000	.000	.000	-.01	.012	-.01	.000	.000	.022	.000	.000	-.04	.000	.316					
16	.366	.000	.000	.000	-.01	.186	-.01	.000	.000	.044	.000	.000	-.11	.000	1.37	1.50				
17	.026	.000	.000	.000	.000	-.01	.000	.000	.000	.000	.000	.000	.002	.000	-.01	-.02	.000			
18	.000	.000	.000	.000	.000	.000	.000	.000	.000	.000	.000	.000	.000	.000	.000	.000	.000	.000		
19	.026	.000	.000	.000	.001	-.03	.001	.000	.000	.000	.000	.000	.013	.000	-.09	-.21	.001	.000	.010	
20	.010	.000	.000	.000	.000	-.01	.000	.000	.000	.000	.000	.000	.000	.000	.000	-.01	.000	.000	.001	.000

TABLE 5.7 Percent modal contribution to the dynamic x-displacement response at quarter length along the crest

mode	1	2	3	4	5	6	7	8	9	10	11	12	13	14	15	16	17	18	19	20
1	34.1																			
2	.000	.000																		
3	.000	.003	5.54																	
4	.000	.000	.000	.000																
5	.086	.000	.000	.000	.001															
6	10.1	.000	.000	.000	.259	39.9														
7	.135	.000	.000	.000	.003	.406	.004													
8	.000	.000	.282	.001	.000	.000	.000	.301												
9	.000	.001	.360	.001	.000	.000	.000	.867	1.54											
10	.137	.000	.000	.000	.001	.333	.005	.000	.000	.009										
11	.000	.000	.000	.000	.000	.000	.000	.000	.000	.000	.000									
12	.000	.000	.001	.000	.000	.000	.000	.000	.000	.000	.000	.000								
13	.229	.000	.000	.000	.000	.736	.000	.000	.000	-.01	.000	.000	.146							
14	.000	.000	.000	.000	.000	.000	.000	.000	.002	.000	.000	.000	.000	.000						
15	.101	.000	.000	.000	.003	-.02	.010	.000	.000	.026	.000	.000	-.04	.000	.089					
16	.009	.000	.000	.000	.000	-.02	.000	.000	.000	.004	.000	.000	-.01	.000	.030	.003				
17	.296	.000	.000	.000	.000	.764	.000	.000	.000	.011	.000	.000	.058	.000	-.09	-.02	.083			
18	.000	.000	.000	.000	.000	.000	.000	.000	.000	.000	.000	.000	.000	.000	.000	.000	.000	.000		
19	.188	.000	.000	.000	-.01	1.14	-.03	.000	.000	-.09	.000	.000	.274	.000	-.60	-.11	.285	.000	1.62	
20	.010	.000	.000	.000	.000	-.01	.000	.000	.000	.000	.000	.000	.000	.000	.000	.000	.000	.000	.000	.000

TABLE 5.8 Percent modal contribution to the dynamic τ_{xy} response - Node 275

mode	1	2	3	4	5	6	7	8	9	10	11	12	13	14	15	16	17	18	19	20
1	94.3																			
2	.000	.000																		
3	.000	.002	.305																	
4	.000	.000	.000	.000																
5	-.26	.000	.000	.000	.003															
6	-2.9	.000	.000	.000	.081	1.21														
7	-.76	.000	.000	.000	.015	.238	.051													
8	.000	.000	-.01	.000	.000	.000	.000	.007												
9	.000	.000	-.01	.000	.000	.000	.000	.013	.015											
10	-2.5	.000	.000	.000	.030	.649	.197	.000	.000	1.18										
11	.000	.000	-.01	.000	.000	.000	.000	.003	.002	.000	.015									
12	.000	.000	.000	.000	.000	.000	.000	.000	.000	.000	.001	.000								
13	.032	.000	.000	.000	.000	-.01	.000	.000	.000	.005	.000	.000	.001							
14	.000	.000	.000	.000	.000	.000	.000	.000	.000	.000	.000	.000	.000	.000						
15	-.25	.000	.000	.000	.007	-.01	.053	.000	.000	.433	.000	.000	.004	.000	.203					
16	-.51	.000	.000	.000	.024	-.13	.187	.000	.000	1.49	.000	.000	.022	.000	1.55	3.00				
17	.338	.000	.000	.000	.000	-.09	.000	.000	.000	-.08	.000	.000	.003	.000	.088	.390	.039			
18	.000	.000	.000	.000	.000	.000	.000	.000	.000	.000	.000	.000	.000	.000	.000	.000	.000	.000		
19	.003	.000	.000	.000	.000	.000	.001	.000	.000	.009	.000	.000	.000	.000	.008	.032	.002	.000	.000	
20	-.18	.000	.000	.000	.001	.041	.000	.000	.000	.007	.000	.000	.000	.000	-.05	-.22	-.03	.000	.000	.015

TABLE 5.9 Percent modal contribution to the dynamic γ_{xy} response - Node 441

mode	1	2	3	4	5	6	7	8	9	10	11	12	13	14	15	16	17	18	19	20
1	98.1																			
2	.000	.000																		
3	.000	.000	.000																	
4	.000	.000	.000	.000																
5	.298	.000	.000	.000	.004															
6	-4.4	.000	.000	.000	-.14	2.67														
7	.774	.000	.000	.000	.017	-.35	.051													
8	.000	.000	.000	.000	.000	.000	.000	.000												
9	.000	.000	.000	.000	.000	.000	.000	.000	.000											
10	2.86	.000	.000	.000	.038	-1.1	.217	.000	.000	1.44										
11	.000	.000	.000	.000	.000	.000	.000	.000	.000	.000	.000									
12	.000	.000	.000	.000	.000	.000	.000	.000	.000	.000	.000	.000								
13	.173	.000	.000	.000	.001	-.09	.000	.000	.000	-.03	.000	.000	.029							
14	.000	.000	.000	.000	.000	.000	.000	.000	.000	.000	.000	.000	.000	.000						
15	-.14	.000	.000	.000	.000	.000	-.03	.000	.000	-.25	.000	.000	.013	.000	.056					
16	-.14	.000	.000	.000	-.01	-.05	-.05	.000	.000	-.46	.000	.000	.033	.000	.224	.230				
17	-.48	.000	.000	.000	.000	.189	-.01	.000	.000	-.13	.000	.000	-.02	.000	-.06	-.15	.075			
18	.000	.000	.000	.000	.000	.000	.000	.000	.000	.000	.000	.000	.000	.000	.000	.000	.000	.000		
19	.007	.000	.000	.000	.001	-.01	.000	.000	.000	-.02	.000	.000	.003	.000	.010	.021	-.01	.000	.001	
20	.257	.000	.000	.000	.001	-.09	.000	.000	.000	.011	.000	.000	.007	.000	.039	.084	-.06	.000	.005	.029

a contribution of 98%. Detailed examination of modal contributions indicates that a dynamic analysis using only the first mode should be sufficient in preliminary design.

5.3.3 Responses to simplified excitations

In conventional seismic analysis of earth dams, simplified ground motion models are typically used. In order to assess their adequacy, three simplified ground motion models are considered in addition to general SVEGM model.

- Case I: Propagation only without coherency decay. Correlation effects between support excitations is neglected in the case, i.e. $|\gamma(v, \omega)| = 1$. However, the time delay for seismic waves to propagate from one support to another is considered.
- Case II: Identical ground motion. This case considers the earthquake excitation to be identical at all support points, an assumption often used in practice. For this case, $|\gamma(v, \omega)|e^{-i\omega v/V}$ is equal to one.
- Case III: incoherency only without wave passage effect. For this case the wave propagation effect is neglected and hence $e^{-i\omega v/V} = 1$.

For cases I and II, Harichandran (1991) developed closed-form solutions for the integrals in equations (4.38), (4.42) and (4.49). Use of closed-form solutions instead of numerical integration result in a tremendous saving of computation time, especially for the dynamic response. Computation of the dynamic response using the closed-form solutions took only about 6 hours on a HP 715/50 workstation compared to about 21 days when numerical integration was used.

5.3.3.1 Displacement

Fig. 5.9(a) shows 3σ x-displacement contours for the general SVEGM model, while Figs. 5.9 (b), (c) and (d) show the contours for the simplified excitation cases: propagation only, identical and incoherency only, respectively. The x-displacement contours for the four types of excitation are similar to one another. However, the maximum x-displacement response to identical excitation is 8.1% larger than that due to general SVEGM. The critical

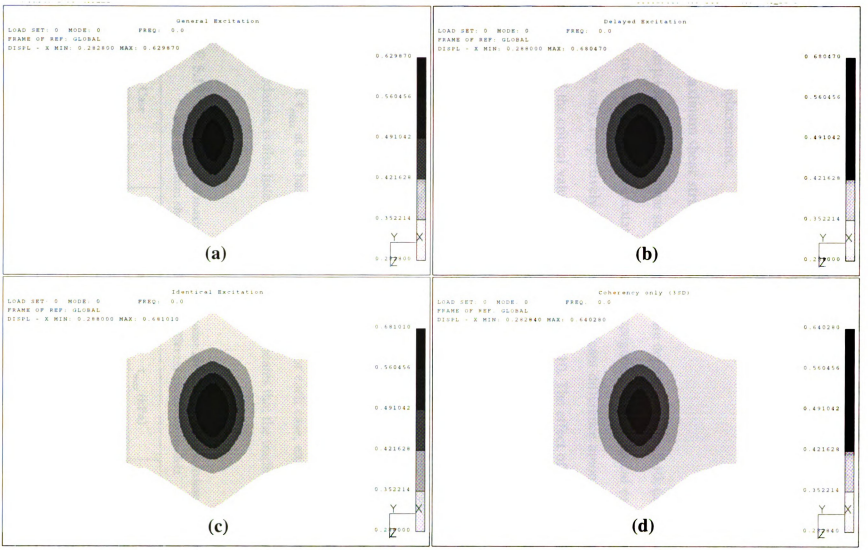

Figure 5.9 3σ x-displacement response (ft) using different excitation models

responses for these four cases are listed in Table 5.10. The figure indicates that for the assumed seismic wave speed, the wave propagation effect is not very significant. The effect of incoherent ground motion slightly decreases the displacement response. The use of identical excitations (typical practice) appears to be adequate and conservative as far as predicting displacements.

5.3.3.2 Maximum shear strain

The $\mu+3\sigma$ maximum shear strain responses are depicted in Figs. 5.10. (a), (b), (c) and (d) due to cases of general excitation, wave propagation only, identical excitation and incoherency only, respectively. There is no significant difference among these contour patterns, and the critical values are listed in Table 5.10. The effect of SVEGM slightly lowers the maximum shear strain response. The wave passage effect does not affect γ_{max} significantly.

5.3.3.3 Maximum shear stress

The $\mu+3\sigma$ contours of τ_{max} response are shown in Fig. 5.11 in which figures (a), (b), (c) and (d) are for the cases of general, propagation only, identical and incoherency only excitations, respectively. A comparison of figures (a) & (d) with (b) & (c) indicates that incoherency of the base excitations has a very significant effect on the magnitude and distribution of τ_{max} at the base. The critical response for each case, excluding that on the cut-off boundaries, is also listed in Table 5.10 and indicates that the traditional assumption

TABLE 5.10 **Comparison of maximum $\mu+3\sigma$ response for displacement, maximum shear stress and maximum shear strain for four different excitation models**

Case	x-displacement (mm)	τ_{max} (kPa)	γ_{max}
General Excitation	191.8	1,670	1.934×10^{-3}
Propagation Only	207.2	511	2.127×10^{-3}
Identical Excitation	207.4	498	2.133×10^{-3}
Incoherency Only	195.0	1669.9	1.975×10^{-3}

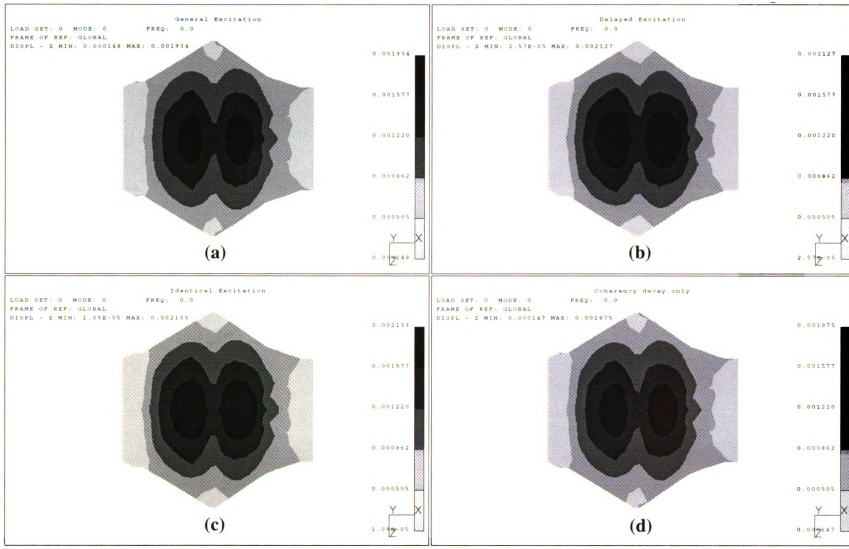

Figure 5.10 $\mu+3\sigma$ contours of γ_{max} at the top free surface for different excitation models

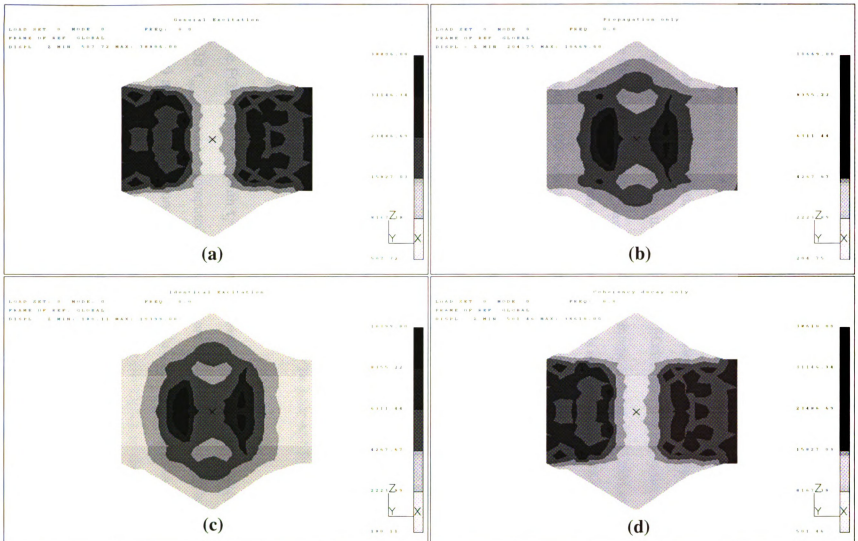

Figure 5.11 $\mu+3\sigma$ contours of τ_{max} (lb/ft^2) at the base for different excitation models using the simulation approach

of uniform earthquake ground motion significantly underestimates the stress response. The response of τ_{max} to general SVEGM is 3.35 times larger than that due to identical excitation. This is because the stress component, τ_{xz}, significantly increases due to the base shearing effect caused by SVEGM.

The contours in Fig. 5.11 were generated using 10,000 simulations of τ_{max} at each node consistent with the covariance matrix of the Cartesian stresses computed by random vibration analysis. In addition, the mean-value FOSM method was also employed to estimate the $\mu+3\sigma$ contours of τ_{max}. The main advantage of using the FOSM method is that the elapsed computing time was only about 4 seconds on a HP Model 715/50 workstation, while simulating 10,000 samples and computing moments required about 21 minutes. The FOSM estimates using $|\tau_i|$ as the basic variables (see Section 4.7.3.1) for the four excitation cases are displayed in Fig. 5.12. A comparison with Fig. 5.11 indicates that the FOSM estimates are clearly unacceptable. The poor estimates are due to the derivative terms evaluated at the mean values of all variables in equation (4.120) being unexpectedly high at some nodes, as a result of which the variances of τ_{max} at these nodes deviate excessively from simulation results. A similar observation was made for the illustrative 2-D beam bending problem in Section 4.7.2.3. Therefore, it may be concluded that the accuracy of the FOSM estimate for the standard deviations of τ_{max} can be poor and fluctuating if $|\tau_i|$ are used as the basic variables.

The FOSM approach with τ_i^2 as the basic variables was presented in Section 4.7.3.2. The $\mu+3\sigma$ τ_{max} responses computed for this case are shown in Fig. 5.13, in which figures (a), (b), (c) and (d) are contours for the general, delayed, identical and incoherency only excitations, respectively. The contour patterns are now closer to those in Fig. 5.11, especially for cases yielding higher stresses. Thus, the use of τ_i^2 as the basic variables in the FOSM approach is better than using $|\tau_i|$ as the basic variables. The differences between critical $\mu+3\sigma$ estimates of τ_{max} using the simulation and FOSM approach with τ_i^2 as the

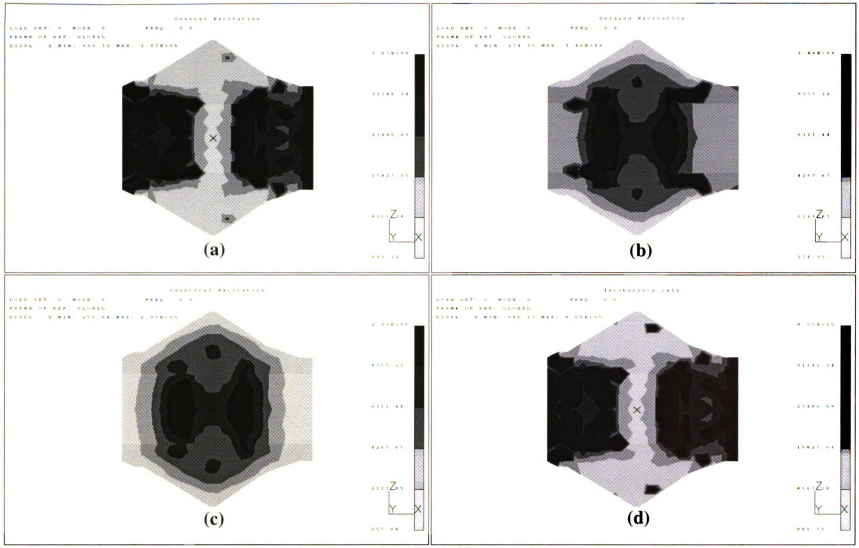

Figure 5.12 $\mu+3\sigma$ contours of τ_{max} (lb/ft^2) at the base for different excitation models using the FOSM approach with $|\tau_i|$ as the basic variables

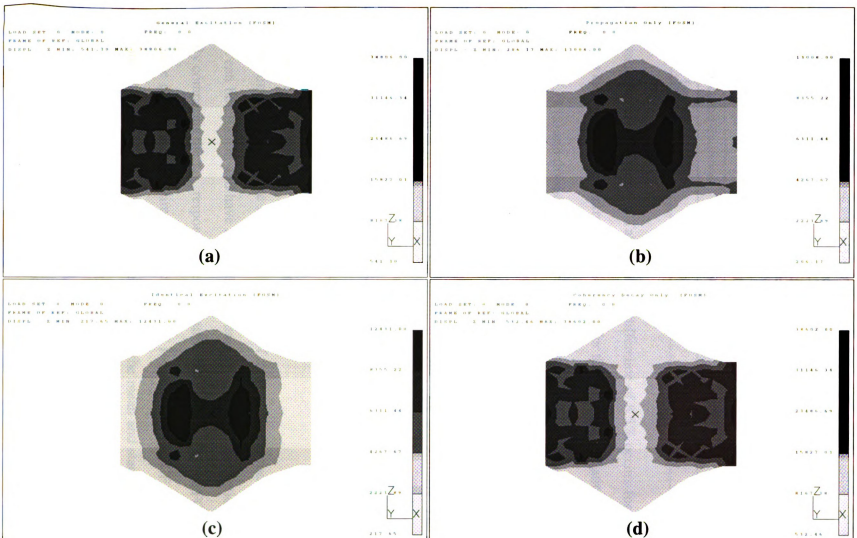

Figure 5.13 $\mu+3\sigma$ contours of τ_{max} (lb/ft^2) at the base for different excitation models using the FOSM approach with τ_i^2 as the basic variables

TABLE 5.11 **Comparison of critical $\mu+3\sigma$ estimates of τ_{max} (kPa) using simulation and FOSM approaches with τ_i^2 as the basic variables**

Case	Simulation	FOSM	Difference
General Excitation	1,670	1,812	8.5%
Propagation Only	511	623	22%
Identical Excitation	498	605	21%
Incoherency Only	1,670	1,812	8.5%

basic variables are compared in Table 5.11. A difference of 8.5% occurs for the general excitation case while a larger error of 21% occurs for the identical excitation case.

Figs. 5.14 (a) and (b) show the $\mu+3\sigma$ contours of γ_{max} at the top free surface using the FOSM approach with $|\tau_i|$ as the basic variables for the general and identical excitations, respectively. As with the τ_{max} response, the FOSM estimates are clearly unacceptable. However, Figs. 5.14 (c) and (d) show the γ_{max} response using the FOSM approach with τ_i^2 as the basic variables for the general and identical excitations, respectively. The contour patterns are quite similar to those using simulation samples as shown in Figs. 5.10 (a) and (c). Therefore, the FOSM method with τ_i^2 as the basic variables can be used to estimate statistical moments of maximum shear stress and strain.

5.3.4 Correction factors for the FOSM method

The linearization of the non-linear function of τ_{max} using the mean-value FOSM method can be efficient and have acceptable accuracy if calibrated correction factors are used. By comparing the τ_{max} responses over the entire dam estimated by the FOSM method with those obtained using simulation, correction factors CF_μ and CF_σ as defined in equations (4.113) and (4.114) can be determined for the mean and standard deviation of τ_{max}, respectively, at each node. The statistics of these correction factors are shown in Table 5.12. The two cases of general and identical excitations are selected to illustrate the accuracy of the FOSM method using $|\tau_i|$ as well as τ_i^2 as the basic variables. In addition to

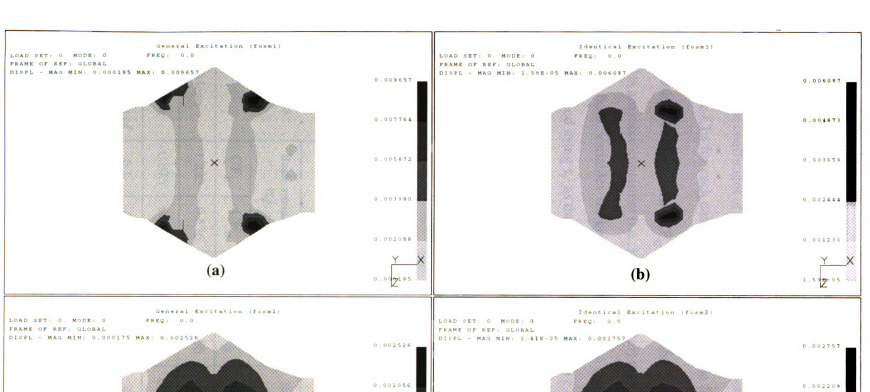

Figure 5.14 $\mu+3\sigma$ contours of γ_{max} at the top free surface using the FOSM approach with $|\tau_i|$ ((a) and (b)) and τ_i^2 ((c) and (d)) as the basic variables; (a) and (c) are for general excitation model. (b) and (d) are for identical excitation model.

the mean and standard deviation of the CFs, the coefficients of variation (c.o.v.) are also shown in Table 5.12. The c.o.v. of a random variable x is defined as

$$\text{c.o.v.} = \frac{\sigma[x]}{E[x]} \times 100 \quad (\%) \tag{5.1}$$

The higher the coefficient of variation, the greater the scatter. The maximum and minimum values of the CFs for each case are also given in Table 5.12.

Table 5.12 shows that CF_σ computed by the FOSM method with τ_i^2 as the basic variables are more consistent (i.e., have less scatter) than those obtained by the method with $|\tau_i|$ as the basic variables for both excitation cases. For the identical excitation case, the FOSM method using τ_i^2 as the basic variables yields a c.o.v. for CF_σ only 3.3%. However, the FOSM method using $|\tau_i|$ as the basic variables yields a c.o.v. as large as 47% for the general excitation case. For CF_μ, however, the two FOSM approaches yield the same c.o.v. for both excitation cases. Therefore, if τ_i^2 are used as the basic variables, then it is possible to arrive at a CF_μ and CF_σ that can be used to correct estimates of the mean and standard deviation, respectively, computed using the FOSM method.

TABLE 5.12 Statistics of the correction factors CF_μ and CF_σ

Statistics of CFs	General Excitation				Identical Excitation			
	Basic variables $\|\tau_i\|$		Basic variables τ_i^2		Basic variables $\|\tau_i\|$		Basic variables τ_i^2	
	CF_μ	CF_σ	CF_μ	CF_σ	CF_μ	CF_σ	CF_μ	CF_σ
Mean	1.223	0.526	0.976	0.856	1.076	0.644	0.858	0.826
Std. Dev.	0.075	0.247	0.060	0.072	0.052	0.191	0.041	0.027
Coefficient of Variation (%)	6.1	47.0	6.1	8.4	4.8	29.7	4.8	3.3
Maximum	1.476	1.337	1.178	1.095	1.408	2.289	1.124	1.158
Minimum	1.059	0.006	0.845	0.757	0.994	0.006	0.793	0.777

Fig. 5.15 show the $\mu+3\sigma$ τ_{max} contours at the base using the corrected FOSM method with τ_i^2 as the basic variables compared with those using simulation results. Figs. 5.15(a) and (b) show the τ_{max} responses due to general excitation for the simulation and corrected FOSM methods, respectively. Correction factors of CF_μ=1.04 and CF_σ=0.91 were used to correct (multiply) the estimated mean and standard deviation of τ_{max} at each node. The difference between the maximum τ_{max} using the corrected FOSM method and simulation samples is only 4%.

Figs. 5.15(c) and (d) show the τ_{max} responses due to identical excitation for the simulation and corrected FOSM methods, respectively. Correction factors of CF_μ=0.86 and CF_σ=0.83 were used. The τ_{max} contours using the corrected FOSM method and simulation results are almost identical, and the difference in the maximum τ_{max} value is less than 0.5%.

In summary, the use of approximate correction factors for the mean and standard deviation estimated by the FOSM method with τ_i^2 as the basic variables can yield fairly accurate results. The corrected results are considerably more accurate for the identical excitation model than for the general excitation model. The correction factors must be arrived at through a calibration process which uses simulation, which partially offsets the computational advantage of using the FOSM method. However, if several analyses are to be performed, then the calibration process and the subsequent use of the corrected FOSM method may be justified. Owing to its better accuracy, the simulation approach was used to generate all contour presented in this study hereafter.

5.3.5 Response details over the dam

Although the critical values of τ_{max} occur at the base and the critical values of γ_{max} occur at the top free surface as shown in previous sections, in order to have global insight on the responses of the dam, τ_{max} at the top free surface and on the cutting plane at z = 0 and γ_{max} at the base are also depicted in this section.

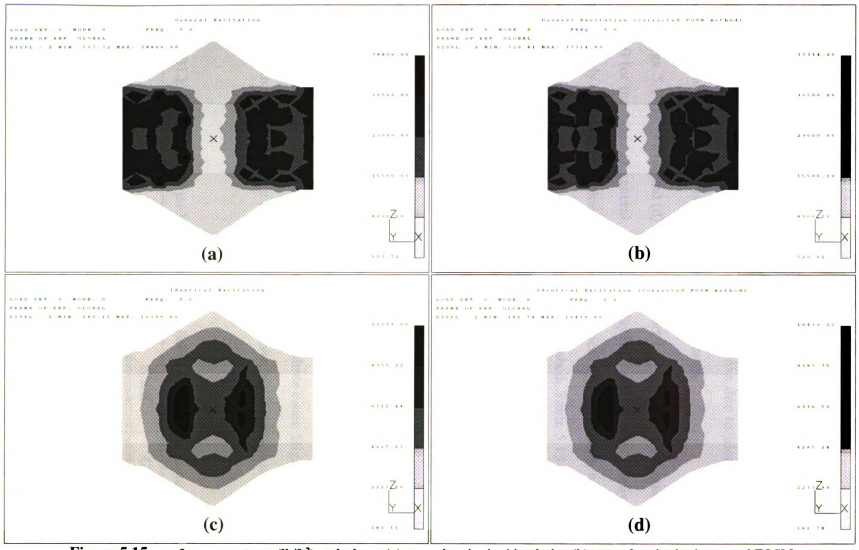

Figure 5.15 $\mu+3\sigma\ \tau_{max}$ **contours (lb/ft^2) at the base: (a) general excitation/simulation,(b) general excitation/corrected FOSM, (c) identical excitation/simulation, (d) identical excitation /corrected FOSM**

Figs. 5.16 (a), (b), (c) and (d) display the $\mu+3\sigma$ contours of τ_{max} at the top free surface for the cases of general, delayed, identical and incoherency only excitations, respectively. All figures are shown on the same scale. The dark regions which signify high τ_{max} on both upstream and downstream sides are due to the artificial cut-off boundaries and should be disregarded. At the top free surface, the τ_{max} response due to identical and delayed excitations are larger than those due to the other two cases.

Figs. 5.17(a), (b), (c) and (d) display the $\mu+3\sigma$ τ_{max} contours on the cutting XY plane at z = 0 for the cases of general, identical, delayed and incoherency only excitations, respectively. Identical excitation case yields the critical τ_{max} in the core, while the general excitation yields the critical τ_{max} in the gravel streambed. Table 5.13 shows the critical $\mu+3\sigma$ values of τ_{max} in the core, shell and gravel material for all these cases and indicates that the traditional assumption of identical earthquake excitation overestimates the τ_{max} response in the core and shells by about 10% and 8%, respectively. The wave passage effect slightly lowers the τ_{max} response in the core, while it does not affect the τ_{max} response in the shell significantly.

Figs. 5.18 (a), (b), (c) and (d) display the $\mu+3\sigma$ contours of γ_{max} at the base for the cases of general, delayed, identical and incoherency only excitations, respectively. The contour patterns have no significant difference among these cases. High γ_{max} values occur in flexible material regions, i.e., core and shell. However, shear stresses are related to shear

TABLE 5.13 Critical $\mu+3\sigma$ values of τ_{max} (kPa) in different material zones

Case	Core	Shell	Gravel
General Excitation	373.8	161.9	1,670
Delayed Excitation	405.5	174.6	511
Identical Excitation	410.6	174.1	498
Incoherency Only	380.5	164.2	1,670

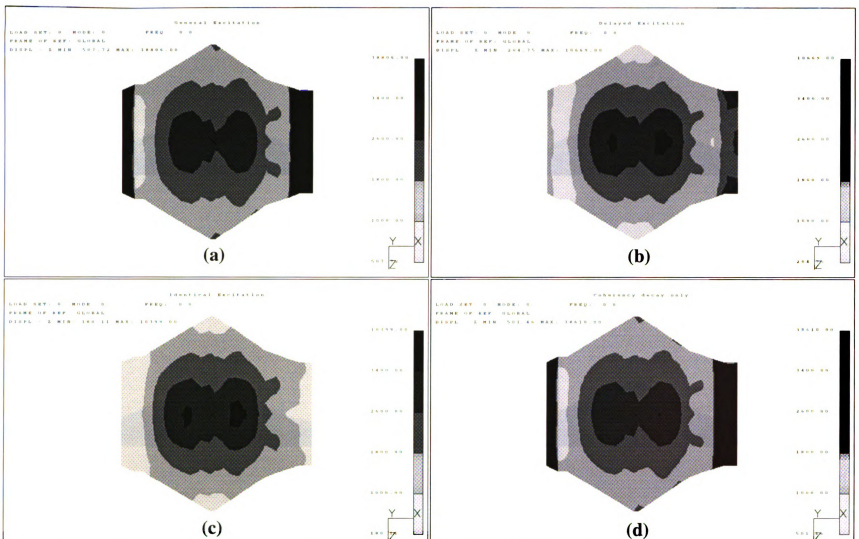

Figure 5.16 $\mu+3\sigma$ contours of τ_{max} (lb/ft^2) at the top free surface due to (a) general, (b) delayed, (c) identical and (d) coherency only excitations

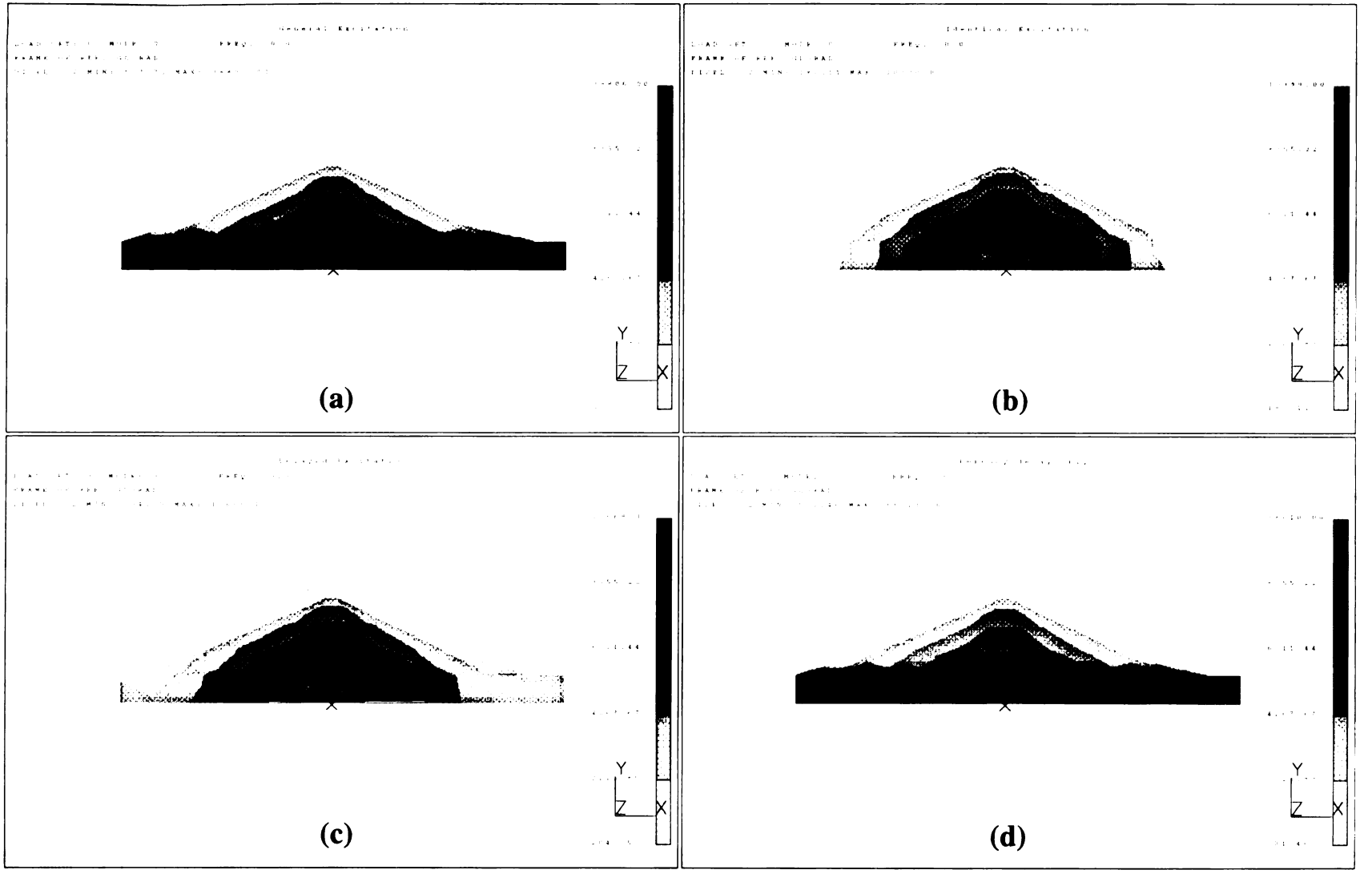

Figure 5.17 $\mu+3\sigma$ contours of τ_{max} (lb/ft^2) on the cutting plane at z = 0 due to (a) general, (b) identical, (c) delayed and (d) coherency only excitations

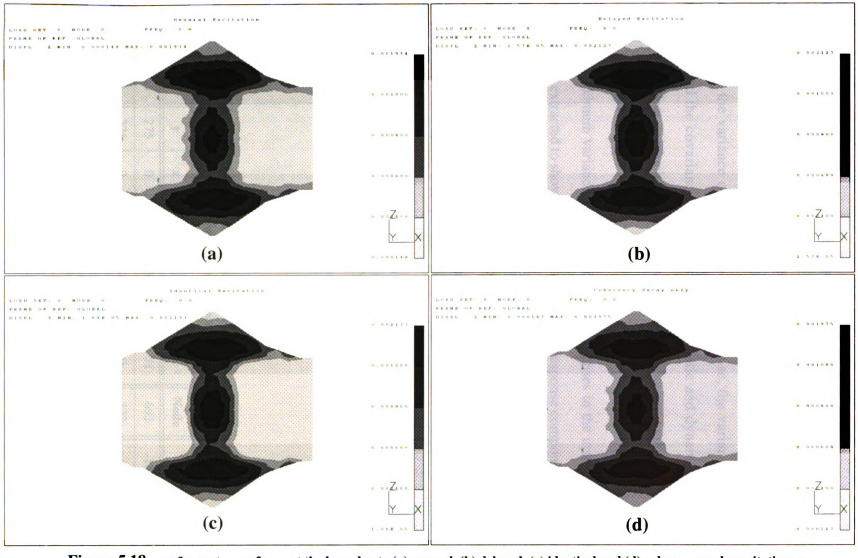

Figure 5.18 $\mu+3\sigma$ contours of γ_{max} at the base due to (a) general, (b) delayed, (c) identical and (d) coherency only excitations

strains through the shear the shear moduli of the materials, and the extremely high values of τ_{max} that occur at the base is due to the very high shear modulus of the gravel.

5.3.6 Contribution of response components to total response

As indicated in equation (4.26), the variance of the total response consists of three components: the variance of the pseudo-static response, the variance of the dynamic response, and the covariance between the pseudo-static and dynamic responses. It is instructive to deduce which component gives most contributions to the total response.

5.3.6.1 Displacement

The maximum variance of 15 displacement responses in the upstream-downstream direction are extracted to show the contributions of the response components. The 15 nodes having the largest responses are the same for the three cases: general excitation, identical excitation and delayed excitation. The coordinates of these nodes are listed in Table 5.14. The percentage contribution of the three response components to the total variance at these nodes are shown in Table 5.15. Clearly, the dynamic response component contributes the most for all the cases but the other components are also significant. It should be noted that for identical excitation, the pseudo-static response consists of a pure rigid body translation of the dam and the static displacement component at all nodes is identical to the ground displacement.

TABLE 5.14 **Coordinates of the nodes (ft) at which the 15 largest x-displacement responses occur**

Node	x	y	z	Node	x	y	z	Node	x	y	z
291	-15	275	0	333	-15	275	71	692	-15	275	-142
299	15	275	0	338	-81	246	0	332	-15	275	142
732	15	275	-71	436	75	245	0	963	67	249	-95
382	15	275	71	731	15	275	-142	630	67	249	95
693	-15	275	-71	381	15	275	142	816	-61	254	-120

TABLE 5.15 Percentage contributions of the response components to the total variance of the x-displacement

Node	General Excitation			Identical Excitation			Delayed Excitation		
	Static	Dynamic	Covariance	Static	Dynamic	Covariance	Static	Dynamic	Covariance
291	19.0	74.7	6.3	17.9	76.3	5.8	17.9	76.3	5.9
299	19.2	74.4	6.4	18.2	76.0	5.9	18.2	75.9	6.0
732	20.6	72.5	6.8	19.7	74.0	6.4	19.7	73.8	6.5
382	20.6	72.5	6.8	19.7	74.0	6.4	19.7	73.8	6.5
693	20.7	72.4	6.9	19.7	73.9	6.4	19.8	73.8	6.5
333	20.7	72.4	6.9	19.7	73.9	6.4	19.8	73.8	6.5
338	23.9	68.5	7.6	22.6	70.4	7.0	22.5	70.5	7.1
436	23.9	68.4	7.7	22.8	70.1	7.1	22.9	69.9	7.3
731	24.2	67.8	8.0	23.5	68.8	7.7	23.9	68.2	7.9
381	24.2	67.8	8.0	23.5	68.8	7.7	23.9	68.2	7.9
692	24.3	67.7	8.1	23.6	68.8	7.7	23.9	68.2	7.9
332	24.3	67.7	8.1	23.6	68.8	7.7	23.9	68.2	7.9
963	25.8	65.8	8.4	24.9	67.2	7.9	25.2	66.7	8.1
630	25.8	65.8	8.4	24.9	67.2	7.9	25.2	66.7	8.1
816	26.2	65.2	8.6	25.3	66.7	8.7	25.4	66.4	8.2

5.3.6.2 Strain

The strain component γ_{xy} is selected to show the contribution of the response components to the total variance. The coordinates of the nodes at which the 15 largest γ_{xy} response occur for the two cases of general and delayed excitations are listed in Table 5.16. The maximum responses occur near the top free surface of the dam for both cases. The percentage contribution of the response components are shown in Table 5.17 and indicate that the dynamic response is dominant for both cases. The pseudo-static and covariance components can be neglected when estimating γ_{xy} at the free surface.

5.3.6.3 Stress

The stress component τ_{xy} is selected to show the contribution of response components to the total variance. Since the largest variance of τ_{xy} occurs at different locations for different excitation models, the nodes at which the 15 largest τ_{xy} responses for the two cases of general and delayed excitations are listed separately in Table 5.18. The percentage contribution of the three response components at these nodes are listed in Table 5.19 for each excitation case. For the general excitation the static component contributes the most to the total response, although the dynamic component is also significant at some nodes. For delayed excitations with an apparent wave speed of 4.27 km/s, the static response is not significant, but the covariance between the static and dynamic responses becomes significant. It should be noted that for identical excitation the static stress component is zero since this consists of a pure rigid body translation of the dam. As a result, the covariance between the static and dynamic components is also zero, and the total stress response consists of only the dynamic component.

In addition, it is of interest to examine the contribution of the response components to the total response at the critical point in the core. Node 396 (0 ft, 125 ft, 0 ft) was found to have the maximum $\mu+3\sigma\ \tau_{max}$ value. Table 5.20 shows the percentage contribution of response components to the total variance of the shear stress τ_{xy} at node 396 and indicates

TABLE 5.16 Nodal coordinates (ft) for the largest 15 variances of γ_{xy}

Sorted Order	General Excitation				Delayed Excitation			
	Node	x	y	z	Node	x	y	z
1	591	129	176	39	352	-104	150	0
2	924	129	176	-39	353	-161	125	0
3	441	181	108	0	441	181	108	0
4	440	114	142	0	440	114	142	0
5	352	-104	150	0	311	-99	195	0
6	353	-161	125	0	295	-48	175	0
7	977	148	125	-65	591	129	176	39
8	644	148	125	65	924	129	176	-39
9	437	135	215	0	857	-185	114	-35
10	446	114	100	0	524	-185	114	35
11	418	91	195	0	446	114	100	0
12	857	-185	114	-35	856	-153	128	-57
13	524	-185	114	35	523	-153	128	57
14	417	151	165	0	977	148	125	-65
15	295	-48	175	0	644	148	125	65

TABLE 5.17 Percentage contribution of response components to the total variance of the shear strain γ_{xy}

Sorted Order	General Excitation			Delayed Excitation		
	Static	Dynamic	Covariance	Static	Dynamic	Covariance
1	0.1	100.0	-0.1	0.0	100.1	-0.1
2	0.1	100.0	-0.1	0.0	100.5	-0.5
3	0.3	100.4	-0.8	0.0	99.4	0.6
4	0.1	100.1	-0.1	0.0	99.9	0.1
5	0.1	99.8	0.1	0.0	100.1	-0.1
6	0.3	99.4	0.3	0.0	100.0	0.0
7	0.2	100.3	-0.5	0.0	99.9	0.1
8	0.2	100.3	-0.5	0.0	99.9	0.1
9	0.1	100.0	-0.1	0.0	100.8	-0.8
10	0.2	100.2	-0.3	0.0	100.8	-0.8
11	0.0	100.0	0.0	0.0	99.8	0.2
12	0.4	99.1	0.5	0.0	100.4	-0.5
13	1.9	97.5	0.6	0.0	100.4	-0.5
14	0.1	100.1	-0.3	0.0	99.7	0.3
15	0.1	99.9	0.0	0.0	99.7	0.3

TABLE 5.18 Nodal coordinates (ft) for the largest 15 variances of τ_{xy}

Sorted order	General Excitation				Delayed Excitation			
	Node	x	y	z	Node	x	y	z
1	274	-160	0	-122	275	-167	0	-58
2	138	-160	0	122	139	-167	0	58
3	176	595	75	-338	274	-160	0	-122
4	26	595	75	338	138	-160	0	122
5	284	-322	25	-263	110	-189	0	0
6	148	-322	25	263	276	-224	0	-47
7	177	595	0	-225	140	-224	0	47
8	28	595	0	225	270	176	0	-44
9	150	-452	0	112.5	134	176	0	44
10	286	-452	0	-112.5	396	0	125	0
11	110	-189	0	0	273	-218	0	-103
12	40	-535	0	0	137	-218	0	103
13	245	-189	0	-225	269	176	0	-113
14	107	-189	0	225	133	176	0	113
15	285	-452	50	-300	662	-228	38	0

TABLE 5.19 Percentage contribution of response components to the total variance of the shear stress τ_{xy}

Sorted Order	General Excitation			Delayed Excitation		
	Static	Dynamic	Covariance	Static	Dynamic	Covariance
1	89.8	12.3	-2.1	1.55	91.44	7.01
2	89.8	12.3	-2.1	1.55	91.44	7.01
3	100.0	0.0	0.0	2.82	87.40	9.78
4	100.0	0.0	0.0	2.82	87.40	9.78
5	98.0	1.9	0.2	1.03	93.51	5.46
6	98.0	1.9	0.2	0.72	94.62	4.66
7	99.9	0.1	0.0	0.72	94.62	4.66
8	99.9	0.1	0.0	1.73	106.20	-7.92
9	98.8	0.7	0.5	1.73	106.20	-7.92
10	98.8	0.7	0.5	0.00	99.92	0.08
11	74.1	28.9	-3.0	0.82	93.92	5.26
12	99.1	0.3	0.6	0.82	93.92	5.26
13	93.5	6.4	0.1	2.09	106.98	-9.08
14	93.5	6.4	0.1	2.09	106.98	-9.08
15	99.5	0.3	0.2	0.61	95.11	4.28

TABLE 5.20 Percentage contribution of response components to the total variance of the shear stress τ_{xy} at the critical node in the core

Node	General Excitation			Delayed Excitation		
	Static	Dynamic	Covariance	Static	Dynamic	Covariance
396	0.4	99.7	-0.1	0.0	100.0	0.0

that for the general excitation the dynamic component contributes the most to the total response, which is in contrast to the response at the base. However, for the delayed excitation, the dynamic component is dominant for the critical response in the core as well as at the base.

It should be noted that the contribution of the stress response components to the total response also depends on the shear modulus of the material. Fig. 5.19 shows $\mu+3\sigma$ contours of τ_{max} at the base. Figures (a) and (c) show the total response and (b) and (d) show the static component, both due to general excitation. The difference between the total response and static component would indicate the contribution of the dynamic component. The contour patterns in figures (a) and (b) are very similar to each other, which indicates the static component dominates the total response in the base gravel region. For figures (c) and (d), the scales were adjusted so that the τ_{max} response in the core can be displayed. The figures show that significantly higher τ_{max} values occur in the clay core and shell for the total response, which indicates the dynamic component is significant for the stress response at the base for flexible material.

In addition, to examine the contribution of the stress response components inside the dam, the τ_{max} contours on the horizontal cutting plane at a height of 21.3 m (70 ft) (i.e., near the top of the gravel streambed) are displayed in Fig. 5.20. Figures (a) and (c) show the total response and (b) and (d) show the static component. Figures (a) and (b) are similar in the gravel region, which indicates that the static component dominates the total response

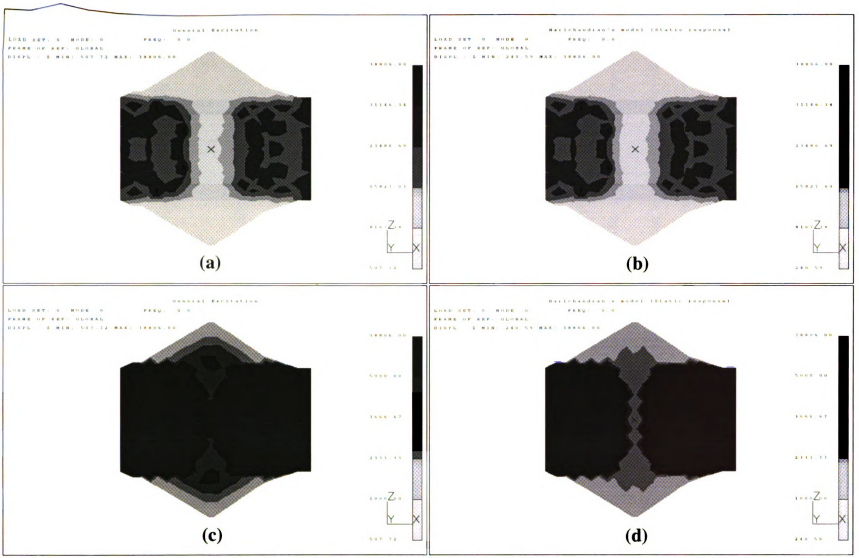

Figure 5.19 $\mu+3\sigma\ \tau_{max}$ **(lb/ft²) contours at the base. (a) and (c) show the total response, (b) and (d) show the static response component**

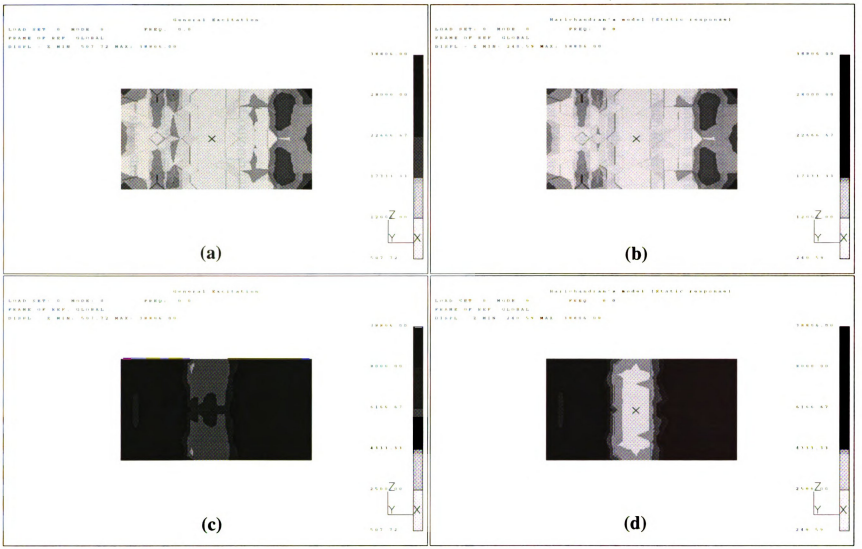

Figure 5.20 $\mu+3\sigma\ \tau_{max}$ **(lb/ft^2) contours at a height of 70 ft. (a) and (c) show the total responses, (b) and (d) show the static response components**

through the gravel layer. However, in the core region the dynamic component is significant since figures (c) and (d) show difference in this region.

The $\mu+3\sigma\ \tau_{max}$ contours at a height of 38.1 m (125 ft) (figures (a) and (b)) and 61 m (200 ft) (figures (c) and (d)) are shown in Fig. 5.21. Figures (a) and (b) are the total responses and (b) and (d) are the static components. Clearly, at these layer heights, the dynamic component is significant in the shell as well as in the core since the static responses are much lower than the total responses.

To sum up, ground straining at the base due to SVEGM causes higher stresses in rigid material like gravel, and the static component is dominant for these material. On the other hand, flexible materials are more sensitive to the ground vibration, and hence the dynamic component is more significant for these material.

5.4 Reliability against Local Failure under Gravity and Earthquake Loads

5.4.1 Introduction

Since the main motivation of this study is to assess the effect of SVEGM, gravity effects are generally neglected and only the seismic response of the dam is considered. This section illustrate how gravity effects can be included in a more complete investigation. Only one failure mode, local yielding governed by the Mohr-Coulomb criterion, is considered in this illustration.

The Mohr-Coulomb failure criterion is usually expressed as

$$\tau_s = c + \tau' \tan\phi \tag{5.2}$$

in which c = cohesion, ϕ = friction angle, τ' = effective normal stress and τ_s = shear strength of the soil. If the shear stress due to loading exceeds the shear strength given by equation (5.2), then the soil would fail locally. In terms of principal stresses, equation (5.2) can be written as

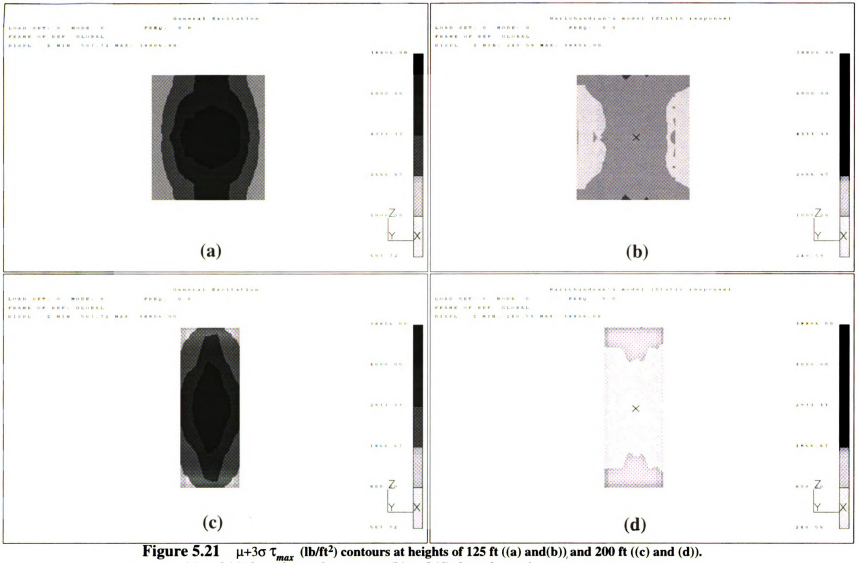

Figure 5.21 $\mu+3\sigma\ \tau_{max}$ **(lb/ft^2) contours at heights of 125 ft ((a) and(b)) and 200 ft ((c) and (d)). (a) and (c) show the total responses, (b) and (d) show the static response components**

$$\frac{\tau_1 - \tau_3}{2} = \frac{\tau_1 + \tau_3}{2}\sin\phi + c\cos\phi \tag{5.3}$$

in which τ_1 and τ_3 are the major and minor principal stresses, respectively. The effect of intermediate principal stress in 3-D problems is neglected by the Mohr-Coulomb criterion.

When the stresses τ_1 and τ_3 and/or the material parameters c and ϕ are random, safety against failure may be expressed by the safety margin failure criterion

$$Y = \frac{\tau_1 + \tau_3}{2}\sin\phi + c\cos\phi - \frac{\tau_1 - \tau_3}{2} \tag{5.4}$$

Failure occurs when $Y < 0$, and hence the probability of failure is $p_f = P[Y < 0]$. Rather than using p_f, a popular measure that is used to assess the reliability of engineering structures is the reliability index defined as

$$\beta = \frac{\bar{Y}}{\sigma_Y} \tag{5.5}$$

where $\bar{Y}$ and σ_Y are the mean and standard deviation of Y, respectively. For a non-linear failure criterion the magnitude of the reliability index is dependent on the form of the failure criterion. For example, a failure criterion written in terms of the factor of safety can yield a different β-value than a criterion written in terms of the safety margin. A comprehensive reliability analysis should use the Hasofer-Lind reliability index (Madsen et al. 1986), which is invariant with respect to different but mechanically equivalent formulations of the failure criterion. However, to keep this illustration simple, the reliability index based on the safety margin is used. For most civil engineering structures, a reliability index of 3 is considered acceptable.

One method of assessing the safety against local failure in a finite element analysis of earth dams is to compute the β-value at each node. The principal stresses τ_1 and τ_3 should include the effects of both gravity and seismic loads. In this illustration, the material parameters c and ϕ are assumed to be deterministic (i.e., constant), and the values used for the three material types are given in Table 5.21.

TABLE 5.21 Physical properties of the core, shell and gravel

Physical property	Core	Shell	Gravel
Friction angle	20	36	42
Cohesion (kN/m^2)	100	0.72	0.72

A high degree of compaction on the dam materials is assumed and thus a small cohesion of 0.72 kN/m^2 for the shell and gravel is used. Typical friction angles of 36° and 42° are adopted for the shell and gravel, respectively. The determination of the consolidated-undrained shear strength of clay is described in Lowe (1967) and Johnson (1975). A typical friction angle of 20° and cohesion of 100 kN/m^2 are used for the clay core. Those nodes at the interface between the core and shell or between the core and gravel were assigned to have the properties of the core, and those nodes between shell and gravel were assigned to have properties of the gravel material. For simplicity, these properties are assumed to be homogeneous for each material region. The excess dynamic pore water pressure induced during earthquakes is neglected.

5.4.2 Gravity load

Soil strength depends on effective stresses. The Santa Felicia dam has a free board of 20 ft as shown in Fig. 3.1. In this study, the situation of full water level is considered so that on the upstream side the effective vertical normal stress due to gravity load is determined by

$$\tau' = (\text{height of the soil column}) \times \gamma' \tag{5.6}$$

where $\gamma' = \gamma_{sat} - \gamma_w$ equals the submerged unit weight of soil.

The gravity-induced stresses can be obtained using I-DEAS by performing a static analysis of the Santa Felicia dam subjected to an acceleration of $1g$ in the vertical direction. The steps of the analysis are described in Appendix A.7. The computed horizontal normal stresses were about 50%~60% of the vertical normal stresses τ'.

The values of the safety margin, Y, due to gravity induced stresses are shown in Fig. 5.22. Figures (a), (b), (c) and (d) are the contours shown at the base, at the top, on the XY cutting plane at z = 0 and on the YZ cutting plane at x = 0, respectively. Note that the lighter contours signify lower safety. The lightest color regions have negative Y values, where local failure is predicted. It is unreasonable that the gravity-induced stresses at some locations near the uppermost layer of elements indicate local failure as shown in Fig. 5.22(c). The reason for this is that the finite element analysis yields tensile principle stresses at these nodes. It is well known that finite element analysis is an approximate procedure, and computed stresses usually have greater error than displacement. The order of the error in nodal stresses arising from finite element analysis is close to the magnitude of the gravity-induced stresses near the top free surface. Yet the Mohr-Coulomb criterion predicts a very small shear strength near the free surface for the cohesionless shell since effective normal stresses are very small. Thus, the results of the analysis in material zone 1S (see Fig. 3.3) is not reliable. For more acceptable and accurate analysis, a finer element mesh near the top free surface should be used.

5.4.3 Results

The reliability analysis was performed considering gravity and earthquake loads for the cases of identical and general excitations. Again, the root-mean-square ground acceleration was set to 0.09g, which corresponds to a peak ground acceleration of about 0.27g. The computed reliability index is shown as shaded image contours over the entire dam. Fig. 5.23 shows the contours for the identical excitation case, in which figures (a), (b), (c) and (d) show the base view, plan view, XY cutting plane at z = 0 and YZ cutting plane at x = 0, respectively. The area in which the reliability index is less than zero is the potential failure zone. It is seen that the material in the bottom half of the dam has high reliability against local failure. However, the soils at about two-thirds the height of the dam in the shell as well as in the core show local failure. When the potential failure zones are narrow and isolated, sliding failure does not develop. However, if the potential failure zones

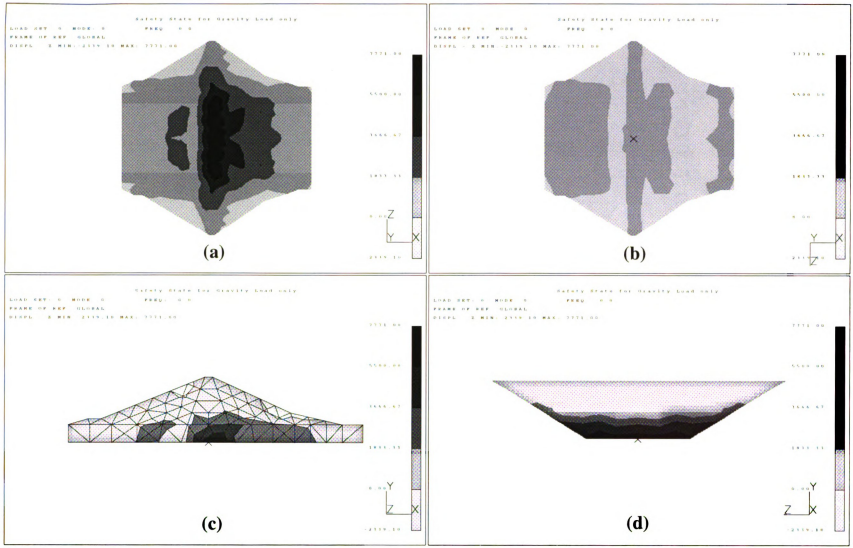

Figure 5.22 Safety State under gravity load (a) base view (b) top view (c) XY cutting plane at z = 0 (d) YZ cutting plane at x = 0.

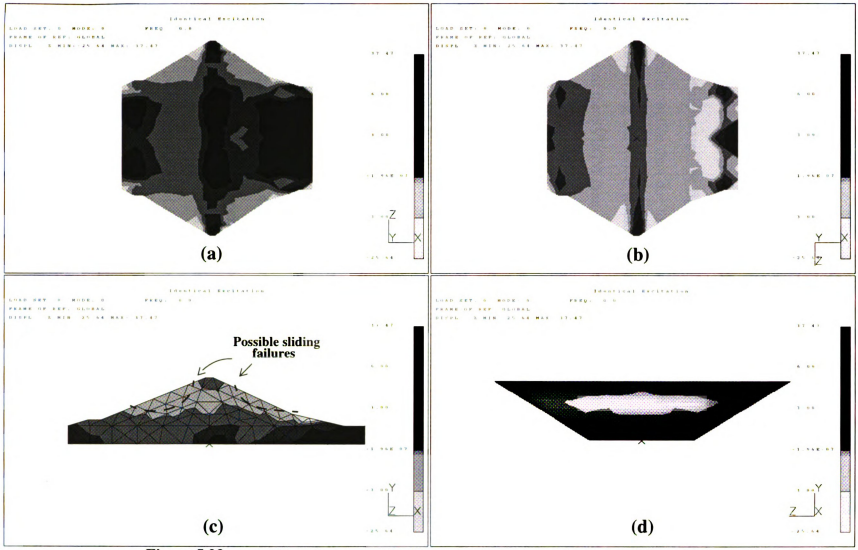

Figure 5.23 Reliability index contours for identical excitation case: (a) plan view, (b) bottom view, (c) XY cutting plane at z = 0 and (d) YZ cutting plane at x = 0.

expand to some extent and are connected with each other, sliding of the slope as shown in Fig. 5.23(c) may occur (Okamato 1984). Note that the zigzag shape of contour boundaries is due to the coarse resolution of the finite element mesh.

Figs. 5.24 (a), (b), (c) and (d) show the reliability index contours at the base, at the top, on the XY cutting plane at $z = 0$ and on the YZ cutting plane, respectively, for the general excitation case. The figures show larger regions of local failure in the dam due to the general excitation than due to identical excitation, especially in the gravel streambed. As shown in Fig. 5.24(c), it would appear that a greater variety of sliding failures could occur due to the SVEGM than due to identical excitation. In particular, sliding masses could include parts of the gravel streambed.

The Santa Felicia earth dam located in southern California experienced the Northridge earthquake of January 17, 1994. The ground acceleration of the Northridge earthquake had a peak value of about 0.27g in the upstream-downstream direction, which is close to the peak acceleration of the simulated El Centro earthquake used in this analysis. However, no severe damage except a 1/8 inch transverse crack in fill placed to connect an access road to the crest of the dam at the abutment was reported due to the Northridge earthquake (Stewart 1994). The analysis results therefore appear to be unrealistic. There are several reasons why the results of the analysis may be over-conservative:

- Linear analysis of the dam was performed by assuming that the entire construction took place in a single operation. In reality, earth dams are constructed in a definite sequence of operations. In embankments, the behavior of soil at a particular stage of loading is dependent upon the state of stress and stress history. Thus the stresses in the final configuration depend on the sequence of intermediate configurations and loadings (Desai and Abel 1972). Nonlinear finite element analysis can be used to compute the stresses in the final configuration of the slope under the effect of gravity (Dunlop and Duncan 1970). The computed horizontal normal stresses in

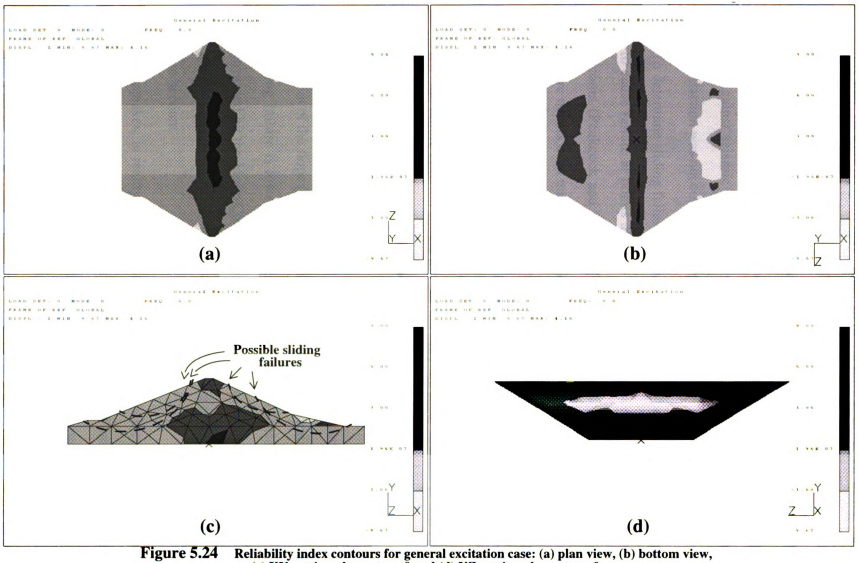

Figure 5.24 Reliability index contours for general excitation case: (a) plan view, (b) bottom view, (c) XY cutting plane at z = 0 and (d) YZ cutting plane at x = 0.

this analysis were typically about one-half of the vertical stress. However, for over-consolidated dam soil, the lateral earth pressure may be larger than the vertical stress, i.e., the lateral earth pressure coefficient can be greater than unity. These under-estimated horizontal stresses could significantly affect the shear strength of soil against seismic force. However, the effect of sequential construction and compaction was not considered in this study.

- To determine sliding failure, the number of cycles of peak shear stresses required to cause failure at points along a potential sliding surface should be taken into account (Peakcock and Seed 1968). The Mohr-Coulomb criterion assumes that failure occurs even under a single excursion of the shear strength during dynamic response. However, in reality, several excursions of the shear strength are required during dynamic response to cause sliding failure; the required number of excursions is a function of confining pressure, void ratio, relative density, etc. Thus, a more realistic failure criterion should include not only the shear strength of soil but also the number of excursions of the shear strength by the dynamic load induced shear stress.
- Earthquake induced sliding failure in the shell has been found to be related to the gradient of the slope (Okamoto 1984). The intensity of vibration necessary to cause sliding failure is lower for steeper slopes. The local yielding failure criterion governed by the Mohr-Coulomb relationship does not account for this effect. For global failure, the effect of slope gradient on the sliding of the slope should be taken into account.
- Earthquakes, in reality, are non-stationary random processes. Fig. 5.25 shows the accelerogram of the Northridge earthquake at the base of the Santa Felicia dam in the upstream-downstream direction. High accelerations occurred only for the short duration from about 3 to 7 seconds. In this study, stationary earthquake excitation (see Fig. 5.4 for a typical stationary accelerogram) and response were assumed.

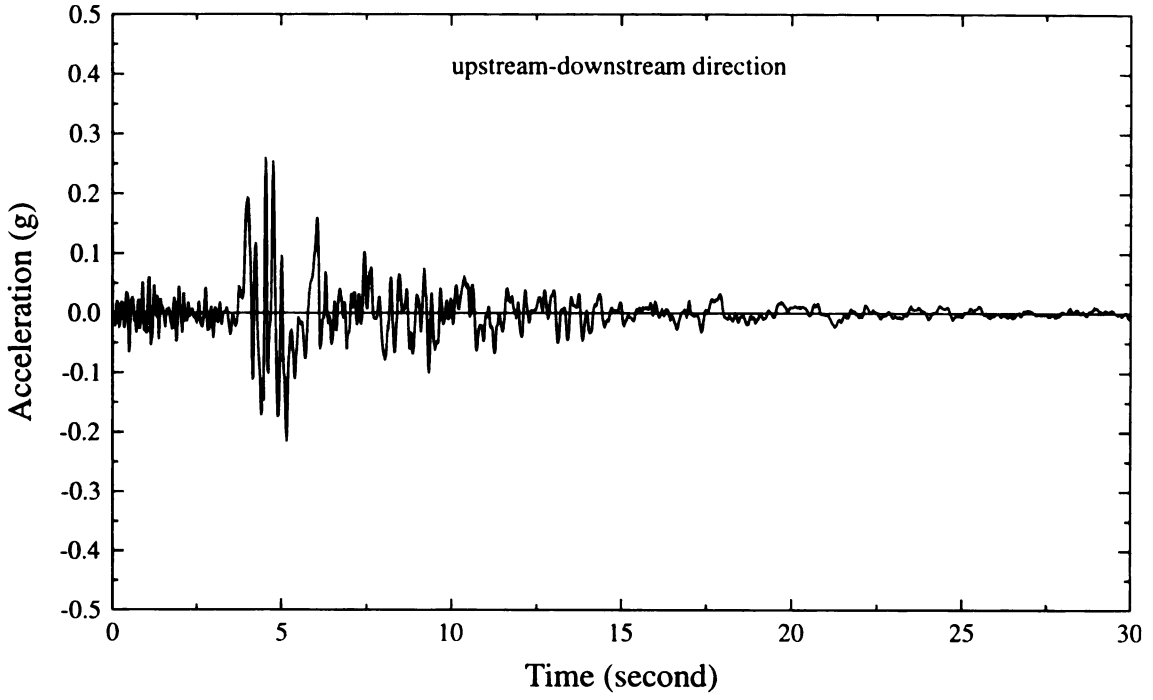

Figure 5.25 **Accelerogram at the base of the Santa Felicia dam in the upstream-downstream direction due to the Northridge earthquake of January 17, 1994**

Clearly, the assumption of stationary response is conservative; a dam that would fail under stationary response may not fail under non-stationary, transient response. Consequently, the reliability analysis based on stationary response is conservative.

- The dynamic analysis of the Santa Felicia dam subjected to the Northridge earthquake is described in Appendix B. Comparison of the computed results with seismograph records indicates that a modal damping ratio as high as 0.45 is appropriate. A higher modal damping ratio would reduce the magnitude of the computed stresses and hence the analysis based on a modal damping ratio of 0.06 is conservative.

This section merely illustrates how the computed earth dam responses can be used to assess reliability against local failure. The reasons given above indicate why the simplistic approach used in this section may yield over-conservative results. Nevertheless, this illustration shows how SVEGM can aggravate sliding failures in earth dams. More accurate

global failure criteria need to be developed in order for a more realistic assessment of reliability against sliding failure.

5.5 Summary

Due to SVEGM, a maximum 3σ displacement of 193 mm occurs at the middle of the crest with the upstream-downstream displacement dominating the total response. A $\mu+3\sigma$ maximum τ_{max} of 1,670 kPa occurs at the base with the τ_{xy} component being dominant. The critical γ_{max} of 0.193% occurs at the top free surface on the downstream side with the γ_{xy} component contributing the most.

The conventional identical ground motion model slightly over-estimates the displacement and γ_{max} responses, and significantly under-estimates the τ_{max} response at the base. However, the critical τ_{max} response in the core as well as in the shell is over-estimated by the identical excitation model. In addition, the contour patterns of the displacement and γ_{max} responses due to identical excitation are similar to those due to general excitation, while the contour patterns for the τ_{max} responses at the base are dissimilar for the two types of excitations.

Modes 1 and 6 contribute most to the dynamic component of the displacement, strain and stress responses. The dynamic component dominates the displacement and strain responses for all types of excitations. However, the pseudo-static component dominates the stress responses in the gravel near the base for general excitation, while the dynamic component dominates for identical and delayed excitations. On the other hand, for the critical stress response in the core, the dynamic component dominates for all cases.

The stochastic moments of the maximum shear stress response were generally computed using Monte Carlo simulation. However, the use of mean-value FOSM methods were also investigated and found to be fast and acceptable if appropriately calibrated correction factors were employed. Finally, reliability against local failure was investigated for the identical and general excitations using the very simple Mohr-Coulomb criterion.

Soils on the upstream side are not as strong as those on the downstream side due to the static pore water pressure. The critical regions susceptible to local failure under identical excitations are typically within the upper one-third height of the dam. However, under SVEGM, the gravel streambed is also susceptible to local failure, and a larger variety of sliding blocks appear feasible.

6. RESPONSE TO DIFFERENT GROUND MOTIONS — PARAMETRIC STUDIES

6.1 Effect of Propagation Speed and Direction for SV/P Waves

Earthquakes, in general, release two types of body waves: P waves and S waves, in which S waves may consist of SV waves and SH waves. P waves are compression waves that cause motions along the direction of wave propagation. S waves are shear waves that cause motions perpendicular to the direction of wave propagation. SV waves are polarized vertically while SH waves are polarized horizontally. P and SV waves are coupled, i.e., one type generates the other upon reflections and refractions. SH waves, on the other hand, remain pure SH waves. For seismic waves propagating in the upstream-downstream direction, SV/P waves would cause critical responses of the earth dam.

According to Abrahamson's investigation (1992), the lowest apparent velocity of S-waves in California is about 2.0 km/s. Therefore, in addition to the apparent speed of 4.3 km/s used in Chapter 5, a wave speed of 1.0 km/s (3,300 ft/s) with an incident angle of 60°, as shown in Fig. 6.1(a), was also used so that the apparent wave velocity (V_a) is close to 2.0 km/s. Further, since the location of earthquake source is usually uncertain and the incident angle of seismic waves approaching the dam will depend on the hypocentral distance and depth, the effect of a shallow incidence angle of 30°, as shown in Fig. 6.1(b), is also investigated. In this case, the apparent velocity is V_a = 2.1 km/s.

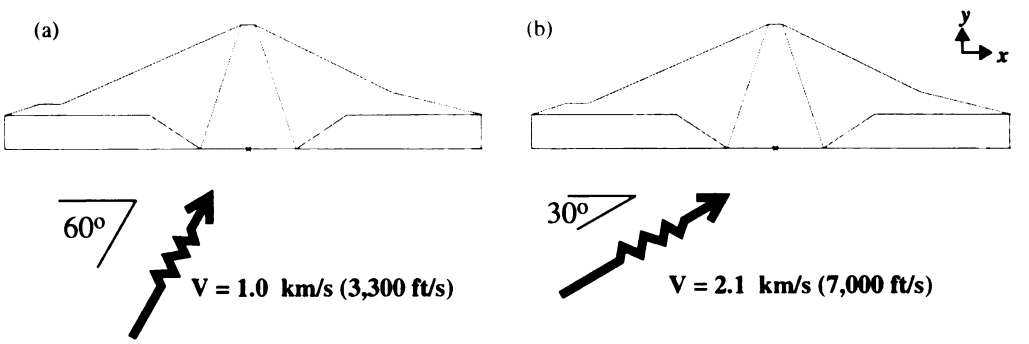

Figure 6.1 **(a) SV/P waves at lower speed, (b) SV/P waves at shallow incident angle**

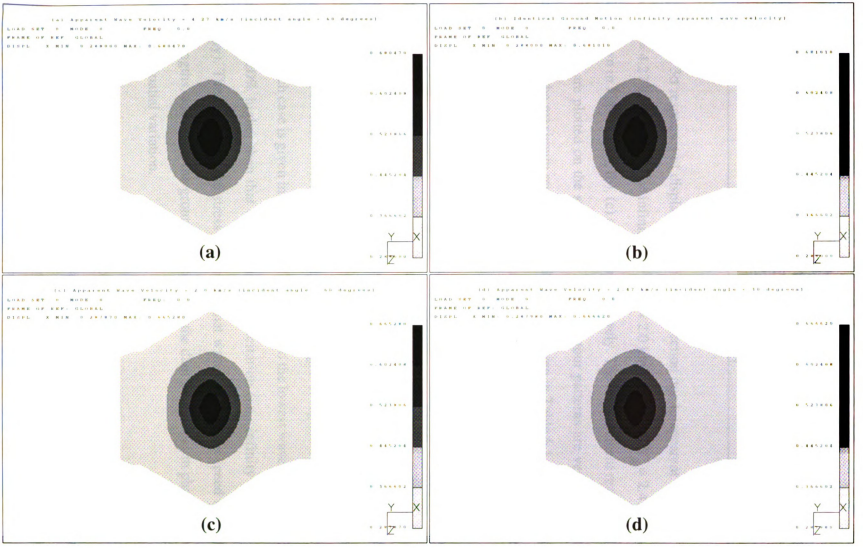

Figure 6.2 **Comparison of contours of 3σ x-displacement response (ft) to seismic waves at different apparent wave velocity**

TABLE 6.1 Maximum $\mu+3\sigma$ responses to different apparent wave velocities

Response	4.27 km/s (60°)	Infinity (90°)	2.0 km/s (60°)	2.47 km/s (30°)
x-displacement (mm)	207.4	207.6	202.8	203.2
τ_{max} (kPa)	511.0	498.0	595.3	567.8

The 3σ responses of displacement in the x direction due to apparent wave velocities of V_a = 4.27 km/s (60°), V_a = infinity (90°), V_a = 2.0 km/s (60°) and V_a = 2.47 km/s (30°) are shown in Figs. 6.2 (a), (b), (c) and (d), respectively. The displacement responses for the four cases are plotted on the same scale. These contour patterns are very similar to one another and the maximum response in each figure is given in Table 6.1. A higher apparent velocity results in a larger x-displacement response, but the increases are not very significant.

In addition, the $\mu+3\sigma$ maximum shear stress responses at the base are also compared for the four wave speeds, and the corresponding contours shown in Fig. 6.3 arranged in the same order as the displacement contours. These patterns of the stress distribution are significantly different from each other and indicate that lower apparent wave speeds can cause significant stress increases, especially in the base gravel region. The critical response value for each case is given in Table 6.1. The τ_{max} due to the lowest wave speed of 2.0 km/s is about 20% higher than that due to identical excitation (i.e., infinity apparent wave velocity). The reason for the stress increase is that waves with lower speed have shorter wave lengths, and hence the ground movement at the dam base is less in phase giving rise to greater spatial variation.

6.2 Effect of Propagation Speed for SH Waves

Since all particle motion for SH waves takes place in a direction horizontally perpendicular to the direction of wave propagation, SH waves traveling in the longitudinal direction of the earth dam, as shown in Fig. 6.4, will give rise to upstream-downstream

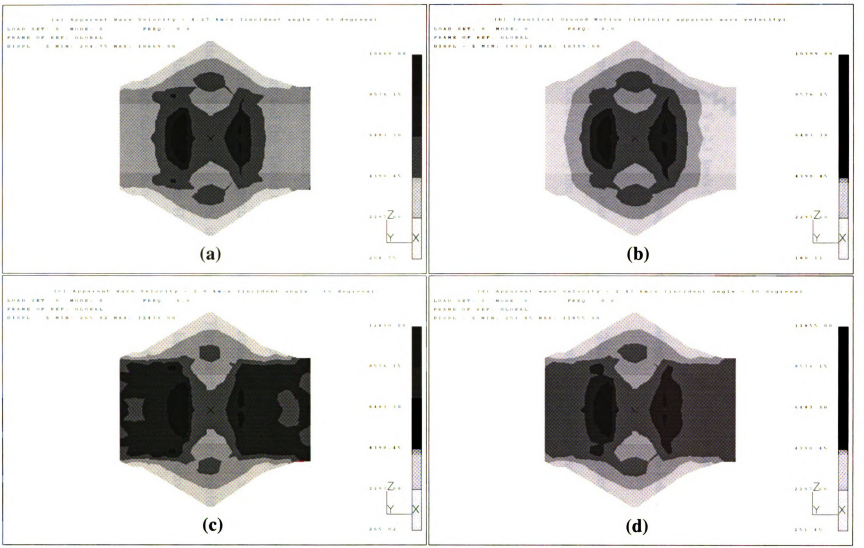

Figure 6.3 Comparison of $\mu+3\sigma$ τ_{max} response (lb/ft^2) at the base to different apparent wave velocity excitation

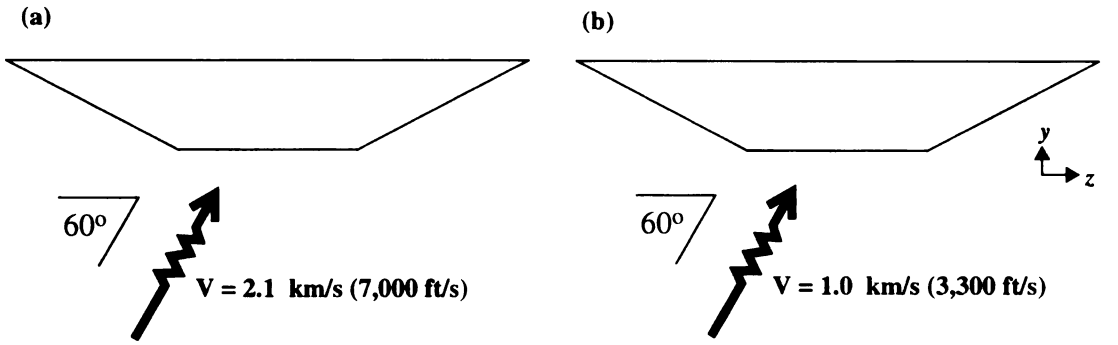

Figure 6.4 **SH waves propagating in the longitudinal direction of Santa Felicia dam**

motion and hence the critical response of the dam. The two cases illustrated in Fig. 6.4(a) and (b) were used to study the effect of SH wave excitations with high and low propagation speed, respectively.

Displacement response due to SV/P and SH waves, both having a high speed of 2.134 km/s and an incident angle of 60° are compared in Fig. 6.5. Figures (a) and (b) show x-displacements at the top free surface for SV/P and SH waves, respectively, while Figures (c) and (d) show x-displacements on the vertical YZ plane at x = 0 for SV/P and SH waves, respectively. The displacement responses are very similar for these two kinds of waves with the same high speed. However, if SH waves propagate at the lower speed of 1.0 km/s, the x-displacement contours have a significant shift in the propagation direction as shown in Fig. 6.7(a) and (b). Table 6.2 lists the critical response values for all these cases and indicates that at the same speed the difference between the maximum x-displacement response to SV/P and SH waves is negligible. The lower wave speed yields a slightly smaller displacement response. However, it should be noted that for SH waves the location of the maximum response is no longer at the middle of the crest.

The comparison of the $\mu+3\sigma$ maximum shear stress responses are shown in Fig. 6.6, in which figures (a) and (b) are τ_{max} responses at the base, and (c) and (d) are τ_{max} on the vertical YZ plane at x = 0 for SV/P and SH waves, respectively. At a wave speed of 2.1 km/s, the distribution of τ_{max} along the YZ plane has a slight shift in the negative

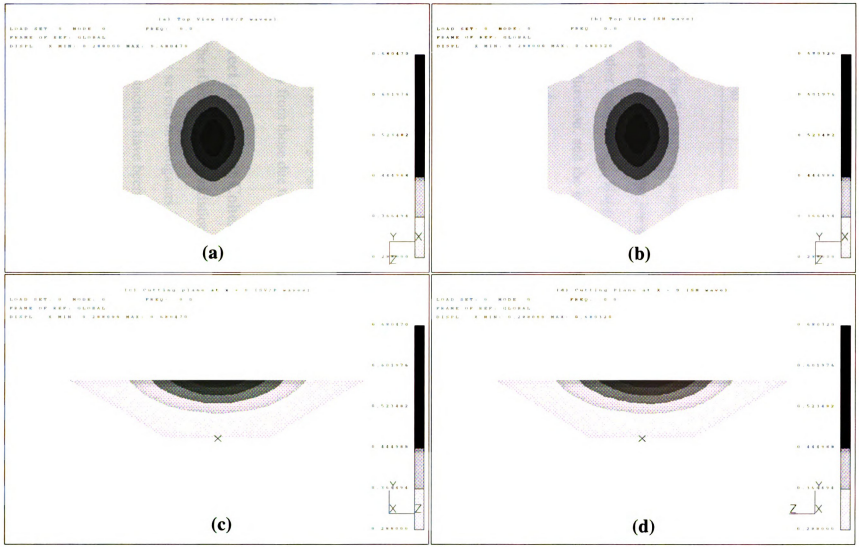

Figure 6.5 Comparison of 3σ x-displacement response (ft) between SV/P wave and SH wave at an apparent wave velocity of 4.27 km/s

TABLE 6.2 Maximum $\mu+3\sigma$ responses due to different wave types and speeds

Response	SV/P waves (2.1 km/s)	SH waves (2.1 km/s)	SH waves (1 km/s)
x-Displacement (mm)	207.41	207.36	204.55
τ_{max} (kPa)	510.97	499.43	519.40

z-direction for SH waves, compared to SV/P waves. The shift is more significant for the response corresponding to the lower SH wave speed of 1.0 km/s as shown in Fig. 6.7(d). On the other hand, for τ_{max} along the base (see Fig. 6.7(c)), the higher stresses shift to the positive z direction, and the critical responses occur at the corner between the base and inclined boundary.

The maximum τ_{max} value for each case is also given in Table 6.2. The critical τ_{max} value due to SH waves is about 2% lower than that due to SV/P waves at the same speed. However, as mentioned earlier, waves with lower speed have smaller wave lengths and cause the stress responses to increase due to out-of-phase motions. The maximum τ_{max} for SH waves with a low velocity of 1.0 km/s is about 4% larger than that for waves with a higher speed of 2.1 km/s. It should be noted that although the magnitude of the stress response does not change significantly, the critical response regions due to SH waves differ considerably from those due to SV/P waves.

6.3 Effect of Different Coherency Models

The effects of spatial variation of seismic ground motion on large structures has been studied by several investigators in the last decade. A number of empirical models for the coherency function have been proposed based on strong motion records obtained at dense seismography arrays. The discrepancy between these models can be quite significant. In general, the ground motions is considered to be a homogeneous random field and the coherency function is assumed to be direction-independent. In this section, the effects of different coherency models on the responses of the Santa Felicia dam are investigated.

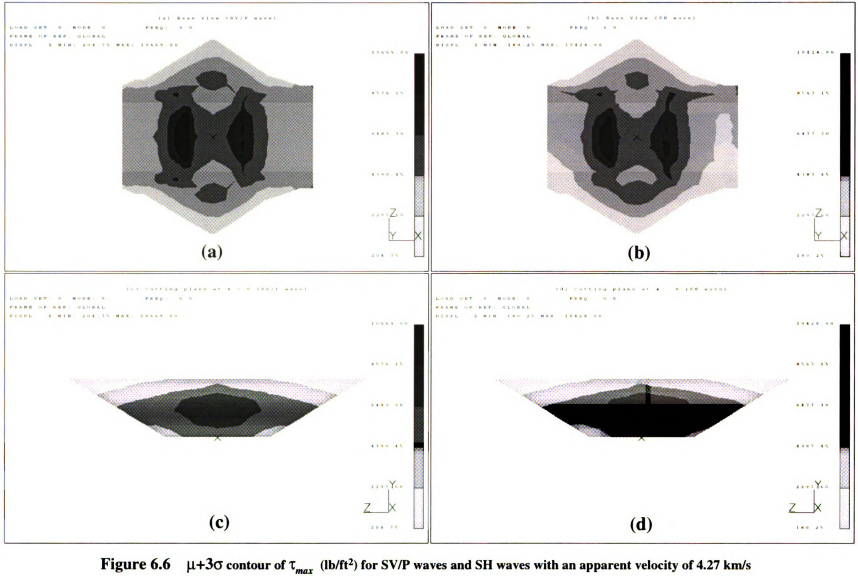

Figure 6.6 $\mu+3\sigma$ contour of τ_{max} (lb/ft^2) for SV/P waves and SH waves with an apparent velocity of 4.27 km/s

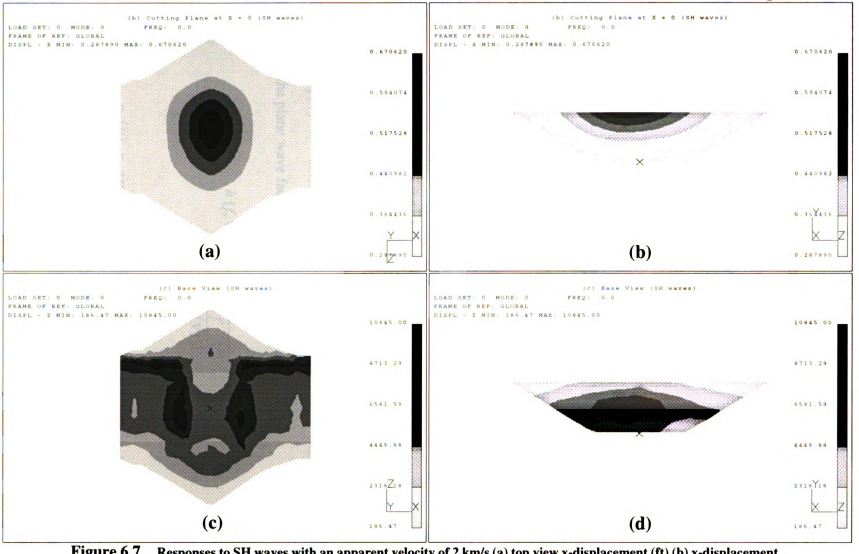

Figure 6.7 **Responses to SH waves with an apparent velocity of 2 km/s (a) top view x-displacement (ft) (b) x-displacement (ft) on YZ cutting plane at x=0 (c) τ_{max} (lb/ft^2) along the base (d) τ_{max} (lb/ft^2) on YZ cutting plane at x=0.**

6.3.1 Coherency models

6.3.1.1 Abrahamson's model

Abrahamson (1993) investigated a number of earthquake events in California and Taiwan. His coherency model was determined empirically based on from several seismography arrays data (Abrahamson 1992), and is

$$|\gamma(f, \nu)| = |\gamma_1(f, \nu)| h(f, \nu) \tag{6.1}$$

where

$$|\gamma_1(f, \nu)| = \tanh\left(\frac{c_3(\nu)}{1 + c_4(\nu) f + c_7(\nu) f^2} + (4.8 - c_3(\nu)) \exp(c_6(\nu) f) + 0.35 \right) \tag{6.2}$$

f is the frequency in Hertz, and ν is the separation distance in meters. The c_i functions in equation (6.2) are given by

$$c_3(\nu) = \frac{3.95}{\left(1 + 0.0077\nu + 0.000023\nu^2\right)} + 0.85\exp(-0.00013\nu)$$

$$c_4(\nu) = \frac{0.4\left[1 - \frac{1}{1 + (\nu/5)^3}\right]}{\left[1 + (\nu/190)^8\right]\left[1 + (\nu/180)^3\right]}$$

$$c_6(\nu) = 3(\exp(-\nu/20) - 1) - 0.0018\nu$$

$$c_7(\nu) = -0.598 + 0.106\ln(\nu + 325) - 0.0151\exp(-0.6\nu)$$

In addition, the plane wave factor $h(f, \nu)$ is

$$h(f, \nu) = \frac{1}{1 + \left(\frac{f}{c_8(\nu)}\right)^6} \tag{6.3}$$

where

$$c_8(\nu) = \exp(8.54 - 1.07\ln(\nu + 200)) + 100\exp(-\nu)$$

This function has smaller coherency loss at lower frequency as shown in Fig. 6.8 compared to Harichandran's model. The relationship between the coherency and separation distance is shown in Fig. 6.9. Abrahamson's model is not based on a single

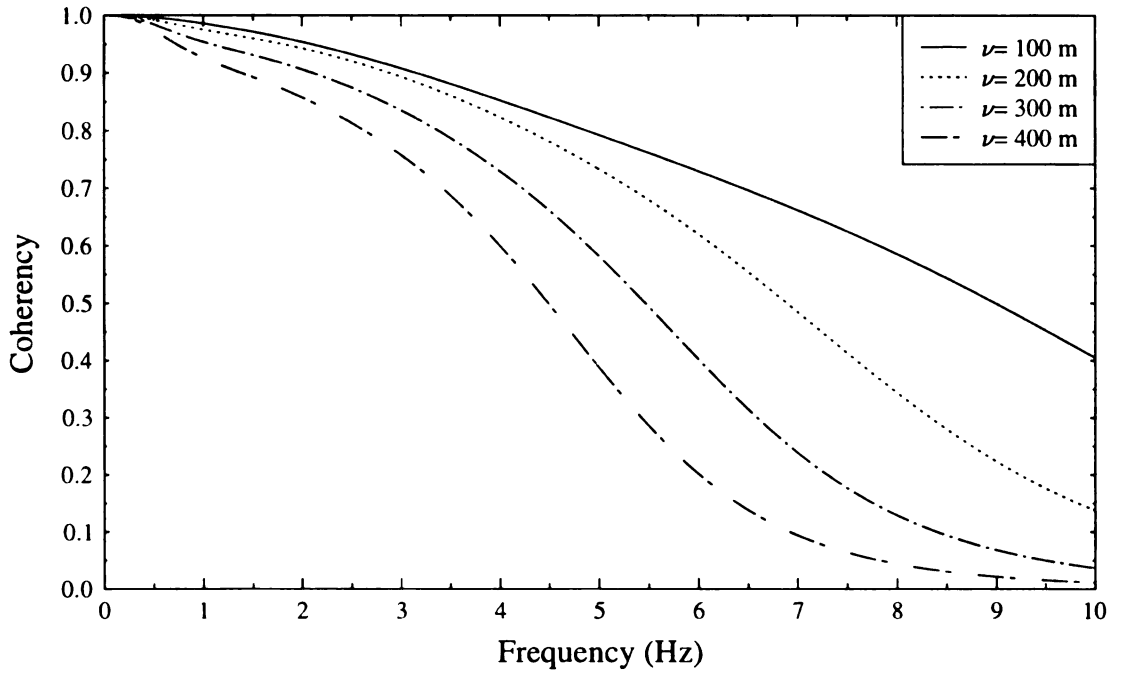

Figure 6.8 Coherency vs. frequency for Abrahamson's model

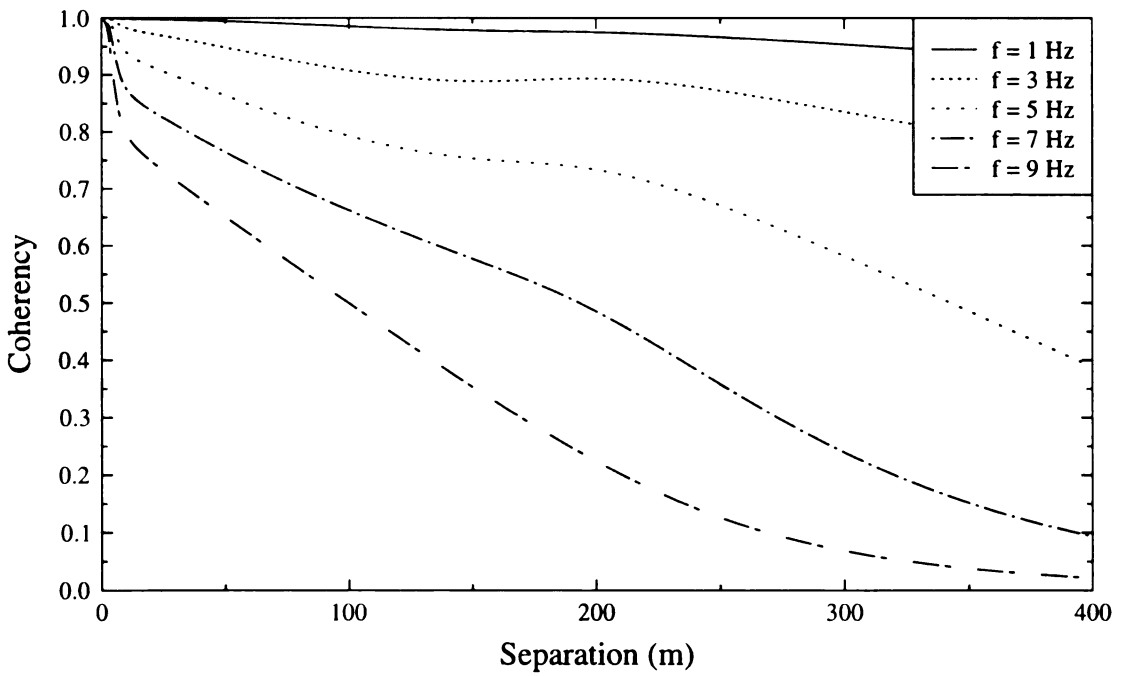

Figure 6.9 Coherency vs. separation for Abrahamson's model

event, but in the average coherency for several events and sites. Abrahamson claimed that the event to event and site to site coherency variations are not statistically significant and hence justified the averaging.

6.3.1.2 Novak's model

Novak (1987) proposed the following single exponential coherency function for SVEGM

$$|\gamma(\omega, \nu)| = \exp\left(-\alpha\left(\frac{2\pi\omega\nu}{V}\right)^{\beta}\right) \tag{6.4}$$

where α and β are empirical constants and V is a wave velocity.

In order to compare Novak's and Harichandran's models, the constants α and β were adjusted so that the two coherency functions matched to some degree. Using the non-dimensional parameter $\chi = c\omega\nu$, where $c = 2\pi/V$, Novak's coherency model becomes $\exp\left(-\alpha\chi^{\beta}\right)$. Since $\nu = \chi/(c\omega)$, Harichandran's model, equation (4.3) can be rewritten as

$$\begin{aligned} |\gamma(\nu, \omega)| = {} & A\exp\left[-\frac{2\chi/(c\omega)}{\alpha\theta(\omega)}(1 - A + \alpha A)\right] \\ & + (1 - A)\exp\left[-\frac{2\chi/(c\omega)}{\theta(\omega)}(1 - A + \alpha A)\right] \end{aligned} \tag{6.5}$$

It is not possible to match the two coherency models closely over all separations. Two types of fits are considered:

Case I – The coherency curves are matched at lower normalized separations as shown in Fig. 6.10. In this case the values of the three parameters, α, β and c, are 1.1, 0.9 and 0.00069, respectively. This coherency function $\exp\left(-0.001572\,(f\nu)^{0.9}\right)$ is shown in Fig. 6.11.

Case II – The coherency curves are matched at higher normalized separations as shown in Fig. 6.12. In this case the values of the three parameters, α, β and c, are 2.0, 0.31 and 0.00002827, respectively. The coherency function $\exp\left(-0.077797\,(f\nu)^{0.31}\right)$ is shown in

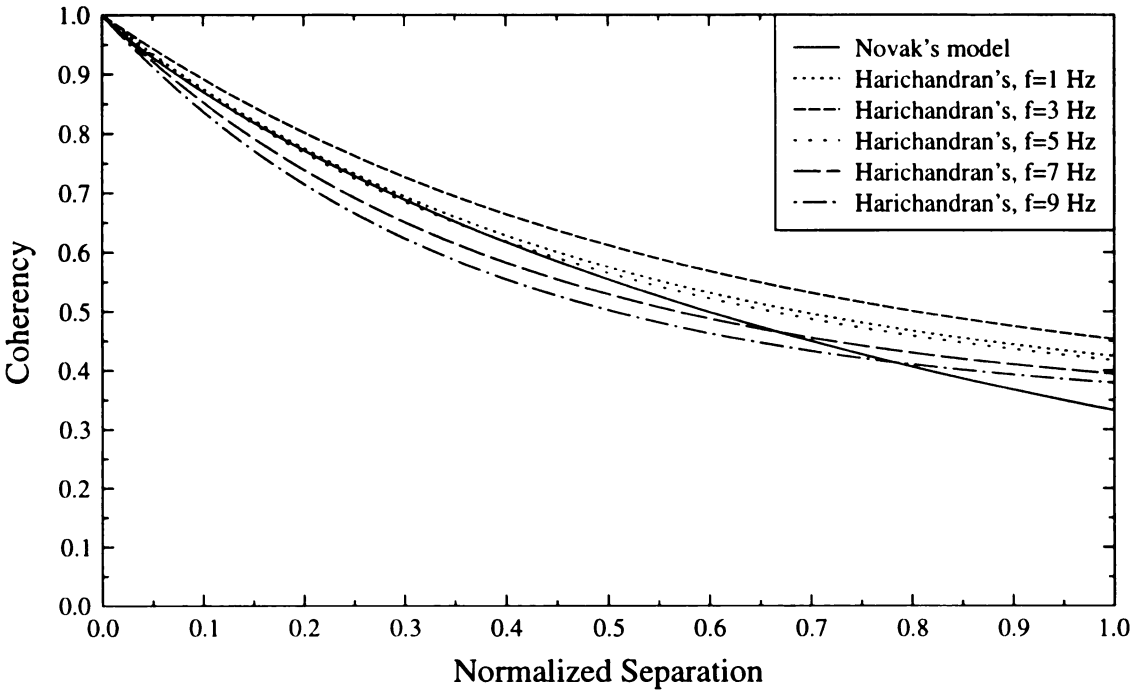

Figure 6.10 **Match of Novak's and Harichandran's models (Case I)**

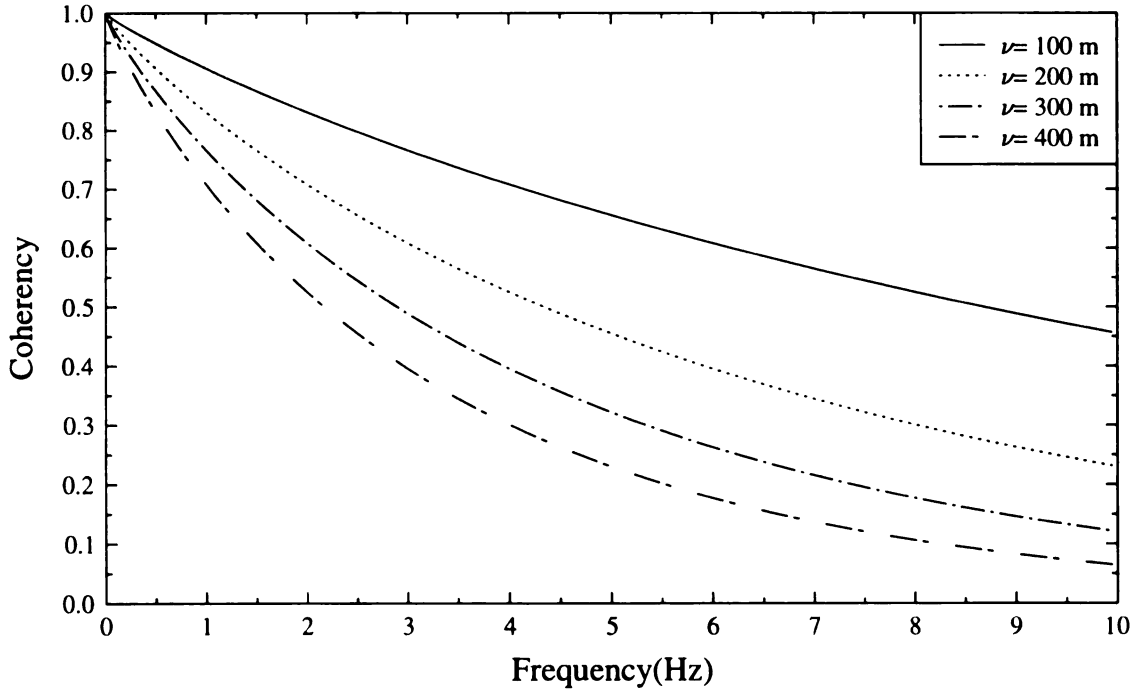

Figure 6.11 **Coherency vs. frequency for Novak's model (Case I)**

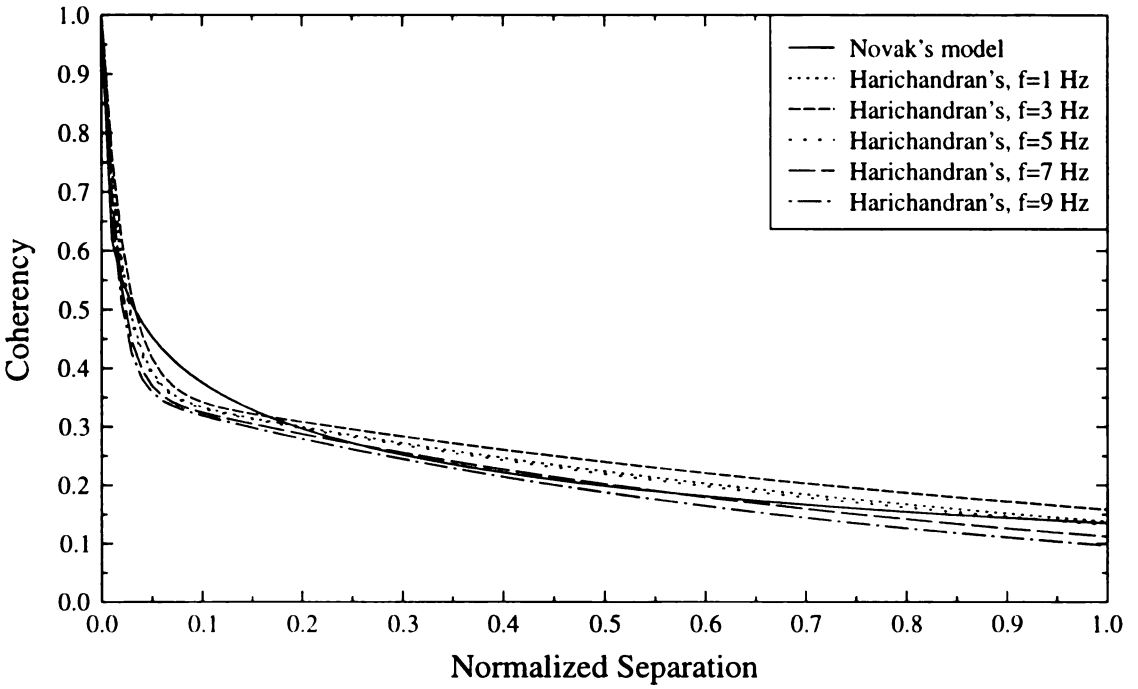

Figure 6.12 **Match of Novak's and Harichandran's model (Case II)**

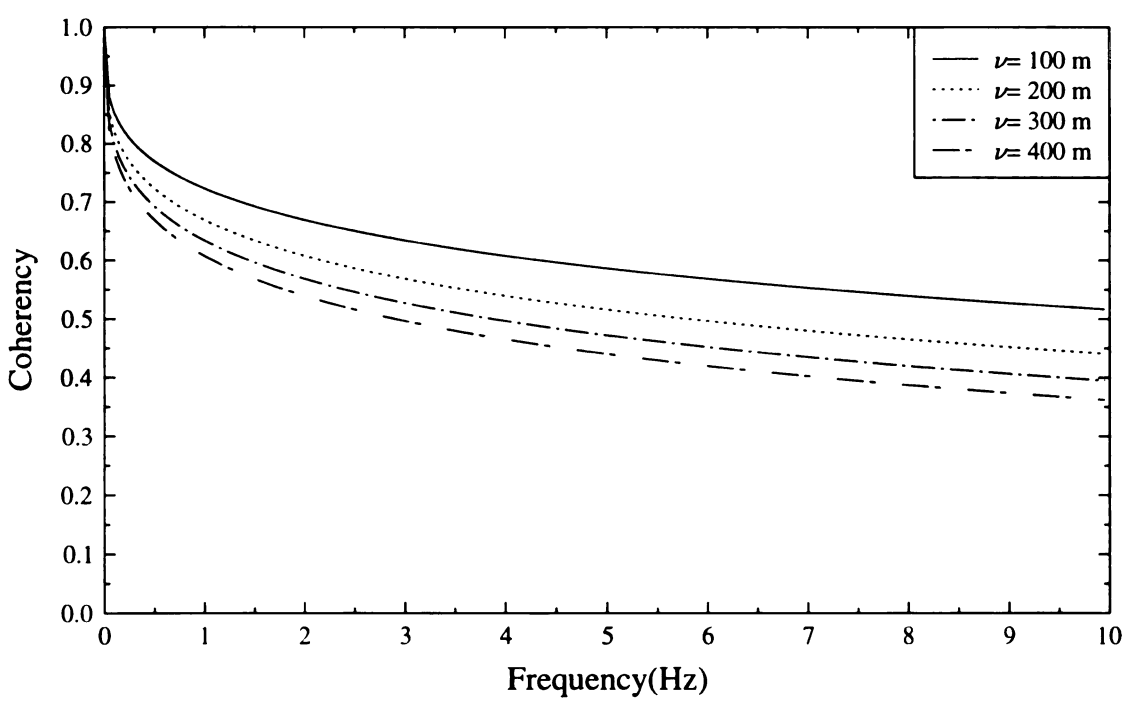

Figure 6.13 **Coherency vs. frequency for Novak's model (Case II)**

Fig. 6.13. Case II has lower coherencies at lower frequencies compared to Case I, while at higher frequencies Case I has lower coherencies.

6.3.1.3 Luco and Wong's model

Luco and Wong (1986) used the coherency function

$$|\gamma(v, \omega)| = \exp\left(-a^2\omega^2 v^2\right) \tag{6.6}$$

where a is an empirical constant, ω is the frequency in rad/s and v is the separation distance between two stations. In order to assess the effects of this coherency function on earth dam responses, two rates of coherency decay are considered:

1. $a = 2 \times 10^{-4}$ s/m is used to represent low coherency decay. $|\gamma(v, \omega)|$ for this value of a is shown in Figs. 6.14 and 6.15, and is somewhat similar to Abrahamson's model. The relatively flat curve at a frequency of 1 Hz indicates nearly fully correlated ground motions at low frequencies.
2. $a = 1 \times 10^{-3}$ s/m is adopted to represent high coherency decay, and the corresponding coherency function is plotted in Figs. 6.16 and 6.17. The abrupt drop of the coherency at low frequencies implies highly incoherent ground movement.

6.3.1.4 Hao's model

Hao et al. (1989) proposed a coherency function based on the study of 17 events recorded by the SMART-1 array. This function is anisotropic and has the form

$$\gamma\left(v^L, v^T, \omega\right) = \exp\left(-\beta_1 v^L - \beta_2 v^T\right) \times \exp\left(-\left(\alpha_1\sqrt{v^L} + \alpha_2\sqrt{v^T}\right)\left(\frac{\omega}{2\pi}\right)^2\right) \tag{6.7}$$

where v^L and v^T are the projected distances between two points in the longitudinal or radial (i.e., wave propagation) and transverse directions, respectively; β_1 and β_2 are empirical constants, and α_1 and α_2 are defined as

$$\alpha_1 = \frac{2\pi a}{\omega} + \frac{b\omega}{2\pi} + c$$
$$\alpha_2 = \frac{2\pi d}{\omega} + \frac{e\omega}{2\pi} + g \qquad 0.314 \le \omega \le 62.83 \text{ (rad/s)}$$

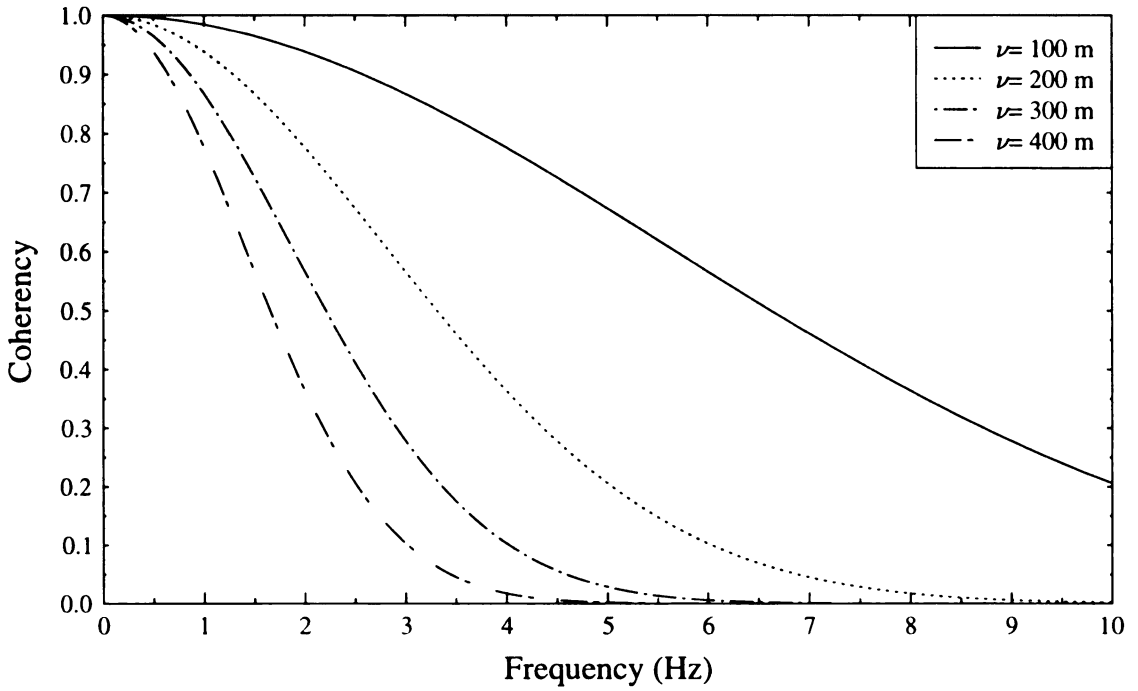

Figure 6.14 **Luco and Wong's low coherency decay model plotted against frequency**

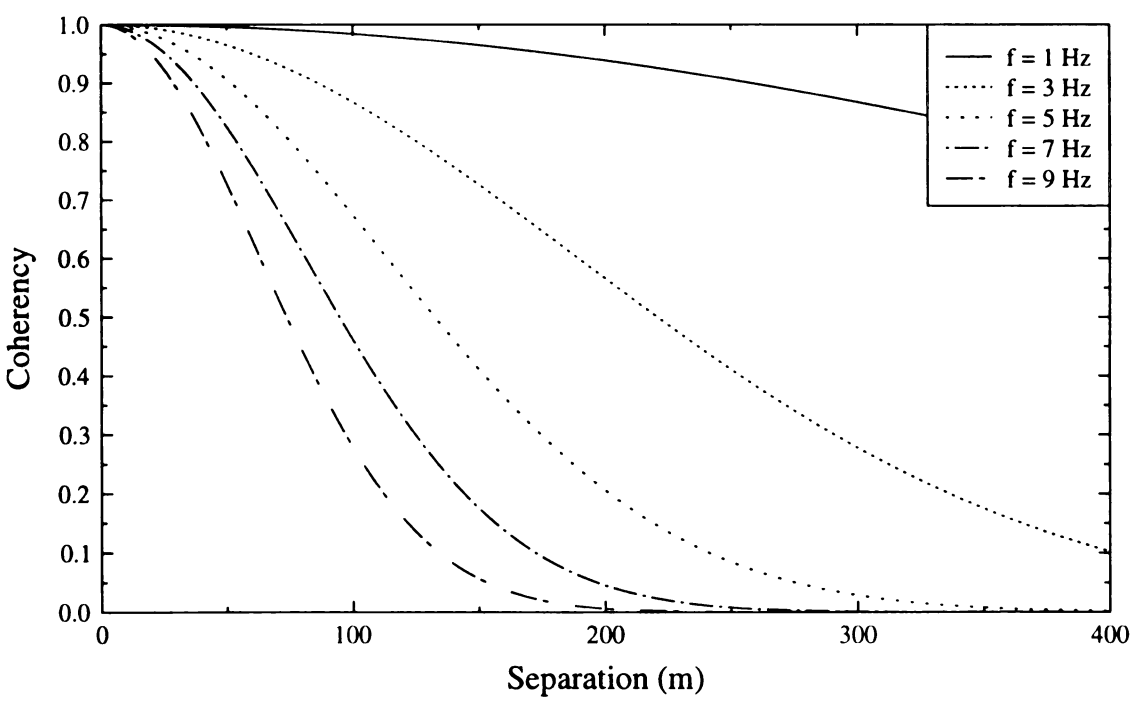

Figure 6.15 **Luco and Wong's low coherency decay model plotted against separation**

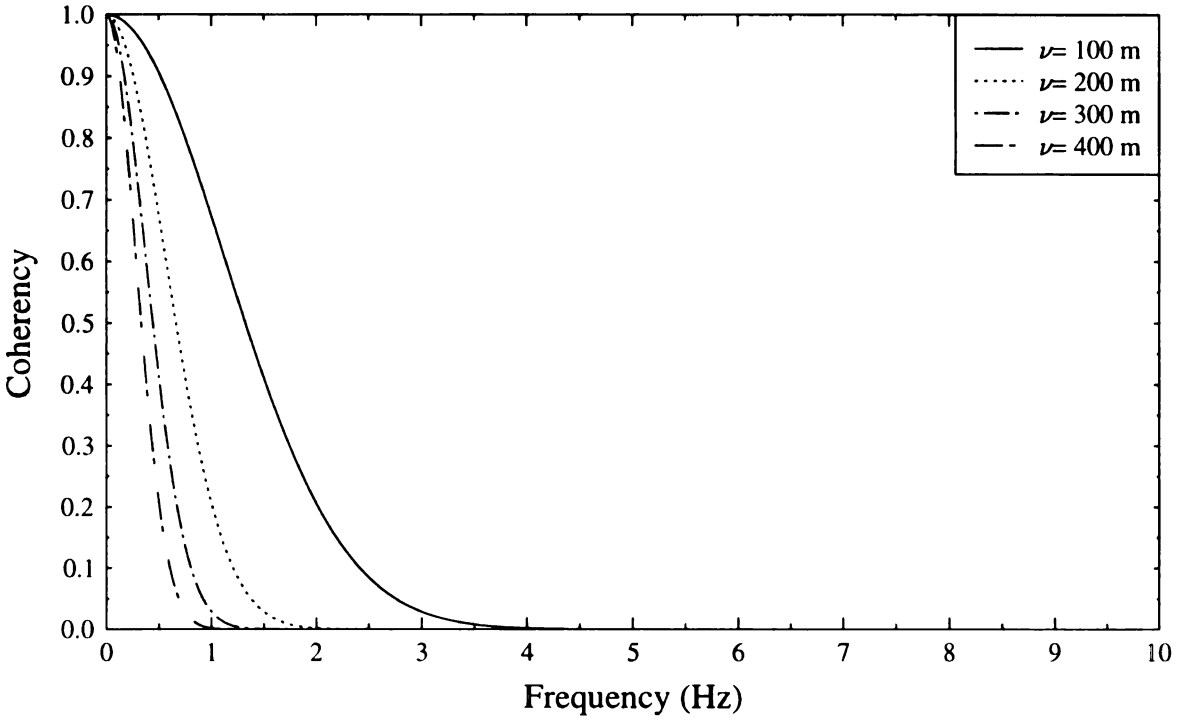

Figure 6.16 **Luco and Wong's high coherency decay model plotted against frequency**

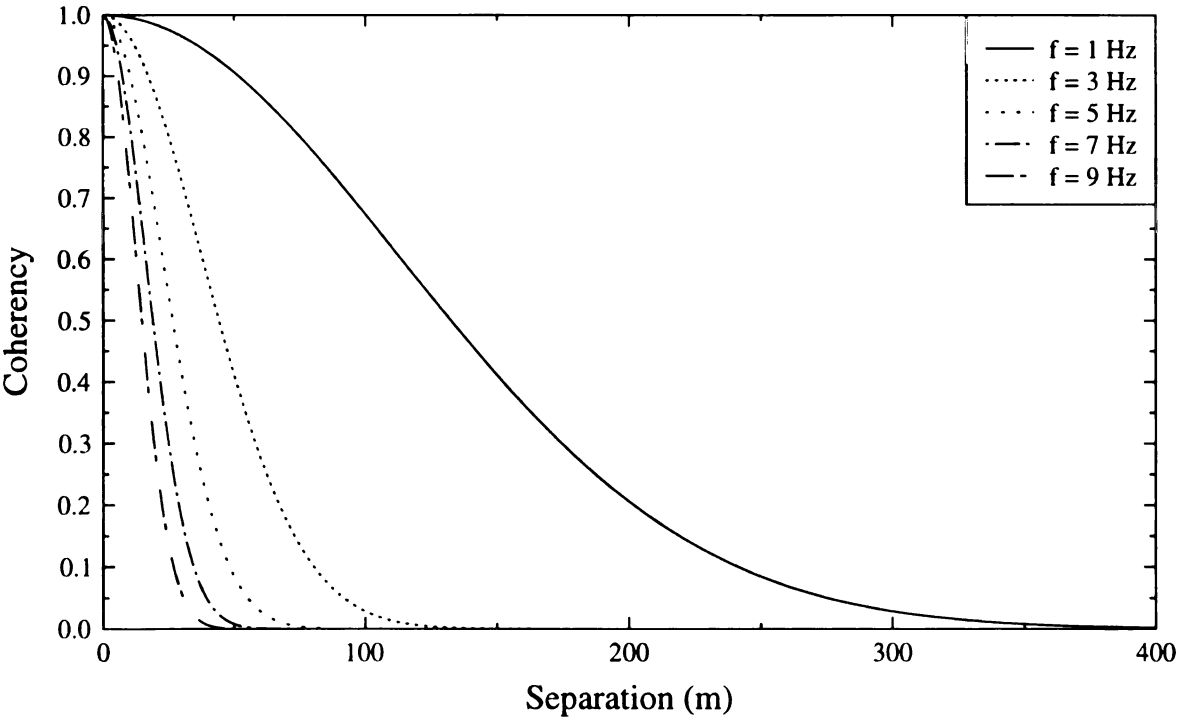

Figure 6.17 **Luco and Wong's high coherency decay model plotted against separation**

TABLE 6.3 **Parameters in coherency function** ($\times 10^{-4}$)

Event	β_1	β_2	*a*	*b*	*c*	*d*	*e*	*g*
45	1.109	0.673	35.83	-0.181	1.177	51.63	-0.076	-1.905
30	2.250	5.100	106.6	0.265	-0.999	66.55	0.588	-11.18

where *a*, *b*, *c*, *d*, *e* and *g* are constants. For $\omega > 62.83$ rad/s, the coherency is assumed to be constant and equal to the value at $\omega = 62.83$ rad/s.

The constants computed by Hao for the SMART-1 Events 45 and 30 are given in Table 6.3 (Hao 1993) and are plotted in Fig. 6.18 to Fig. 6.21. It is apparent that the coherency decay for Event 30 is larger than that for Event 45. Fig. 6.19 indicates that at f = 5 Hz, the coherency decay along the longitudinal and transverse directions is similar for Event 45. However, Fig. 6.21 indicates greater anisotropy for Event 30, with coherency decaying faster in the longitudinal direction than in the transverse direction.

6.3.2 Responses due to different coherency models

6.3.2.1 Displacement and strain

Displacement and strain responses using different coherency functions are presented in this section. The 3σ x-displacement responses due to four coherency models are shown in Fig. 6.22. The four coherency models are: (a) Harichandran's, (b) Abrahamson's, (c) Hao's (Event 30) and (d) Hao's (Event 45) models, respectively. The figures indicate that displacement response is not very sensitive to the coherency model. The maximum 3σ x-displacements are given in Table 6.4 for each coherency model. Basically, higher coherency decay models result in smaller displacements. The largest difference between the critical 3σ x-displacements is about 10.3% (between Abrahamson's and Hoa's Event 30 models).

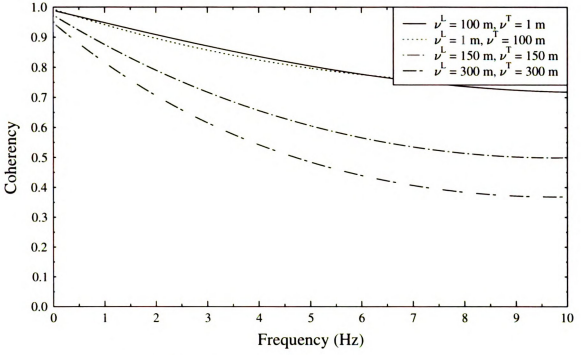

Figure 6.18 Hao's coherency model for SMART-1 Event 45

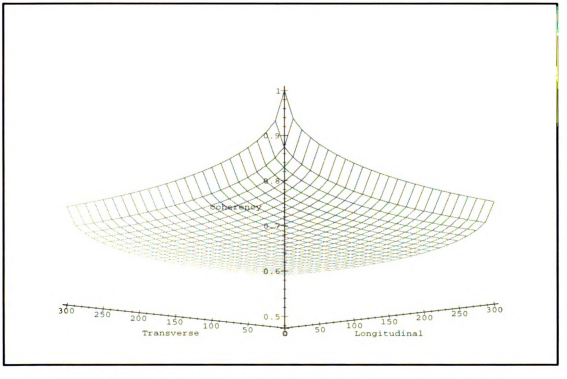

Figure 6.19 Hao's coherency model for SMART-1 Event 45 (at f = 5 Hz)

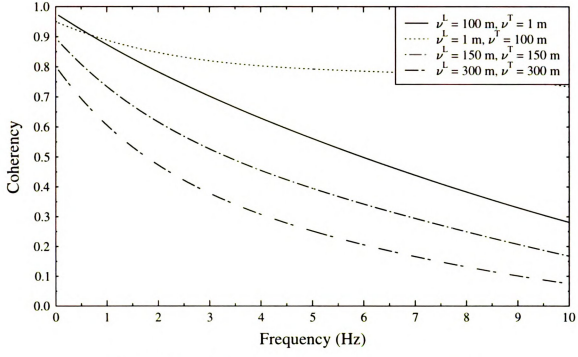

Figure 6.20 **Hao's coherency model for SMART-1 Event 30**

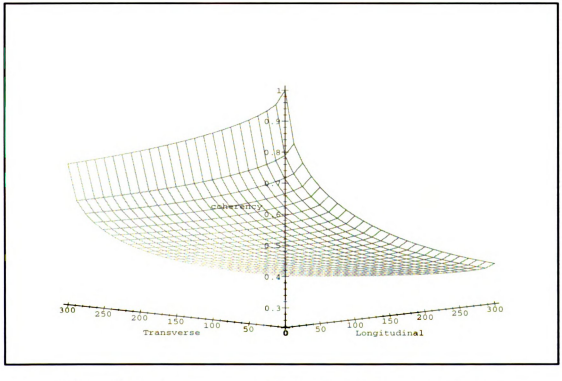

Figure 6.21 **Hao's coherency model for SMART-1 Event 30 (at f = 5 Hz)**

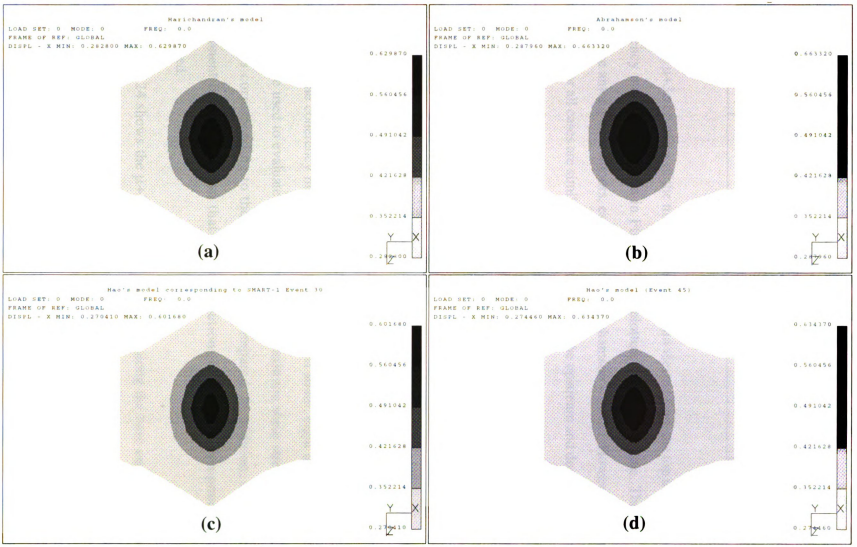

Figure 6.22 3σ x-displacement response (ft) using (a) Harichandran's (b) Abrahamson's (c) Hao's (Event 30) and (d) Hao's (Event 45) models

TABLE 6.4 Maximum responses ($\mu+3\sigma$) corresponding to different coherency models

Response	Harichandran's	Abrahamson's	Hao's (Event 30)	Hao's (Event 45)
x-Displacement	191.8 mm	202.0 mm	183.2 mm	193.2 mm
γ_{max}	0.001934	0.002060	0.001839	0.002050

The $\mu+3\sigma$ contours of the maximum shear strain viewed from the top using these four coherency models are shown in Fig. 6.23, all plotted to the same scale. There is some difference among the contours, especially for Abrahamson's model. However, the critical responses for all cases are similar, occur around both the upstream and downstream surface regions, and are also given in Table 6.4. Basically, higher coherency decay models give rise to lower strain. The largest difference between the critical $\mu+3\sigma$ γ_{max} values is about 12% (between Abrahamson's and Hao's Event 30 models).

6.3.2.2 Maximum shear stress

It was found in Section 5.3.3.3 that stress responses at the base have a significant increase due to SVEGM and that the static response component dominates the total maximum shear stress response for the general excitation case. Since τ_{max} is much more sensitive to the coherency model than displacement and strain, eight different coherency functions are used to evaluate their impacts on the maximum shear stress. The total τ_{max} responses corresponding to these models are compared. In addition, the static τ_{max} component is also shown so that the contributions of response components can be recognized.

Fig. 6.24 shows the $\mu+3\sigma$ total τ_{max} response along the base computed using (a) Harichandran's, (b) Abrahamson's, (c) Novak's Case II and (d) Novak's Case I models, respectively. The corresponding $\mu+3\sigma$ static response contours of are shown in Fig. 6.25. Note that the magnitudes and distributions of τ_{max} are significantly different for each case. The contours are not drawn on the same scale because of the large differences in the

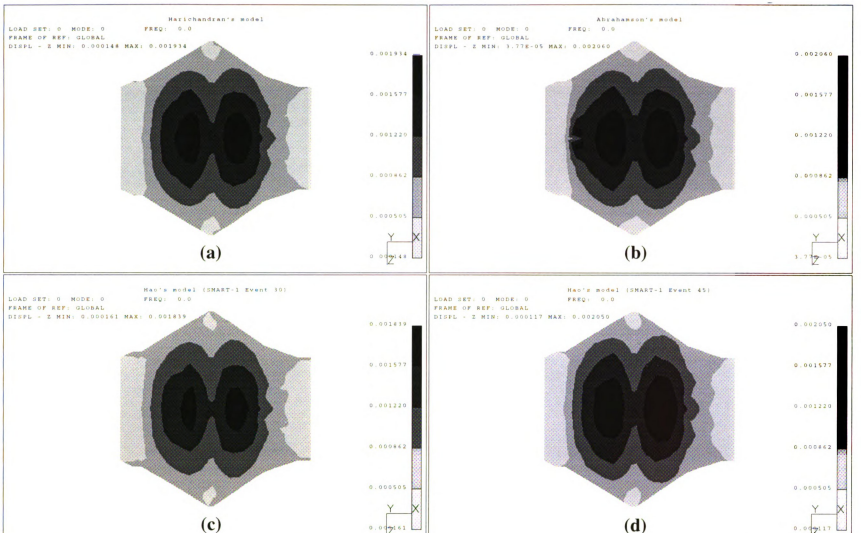

Figure 6.23 $\mu+3\sigma\ \gamma_{max}$ **response using (a) Harichandran's (b) Abrahamson's (c) Hao's (Event 30) and (d) Hao's (Event 45) models**

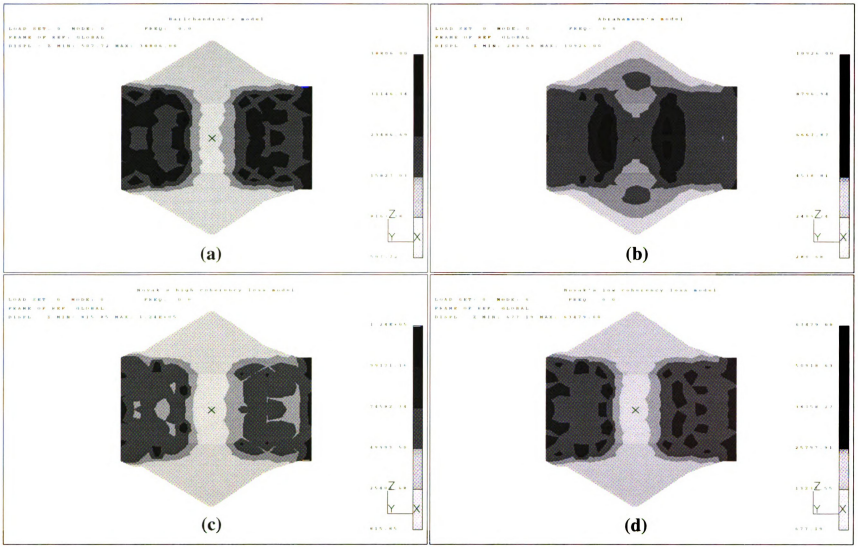

Figure 6.24 $\mu+3\sigma\ \tau_{max}$ **response (lb/ft^2) using (a) Haricharandran's (b) Abrahamson's (c) Novak's Case II and (d) Novak's Case I models**

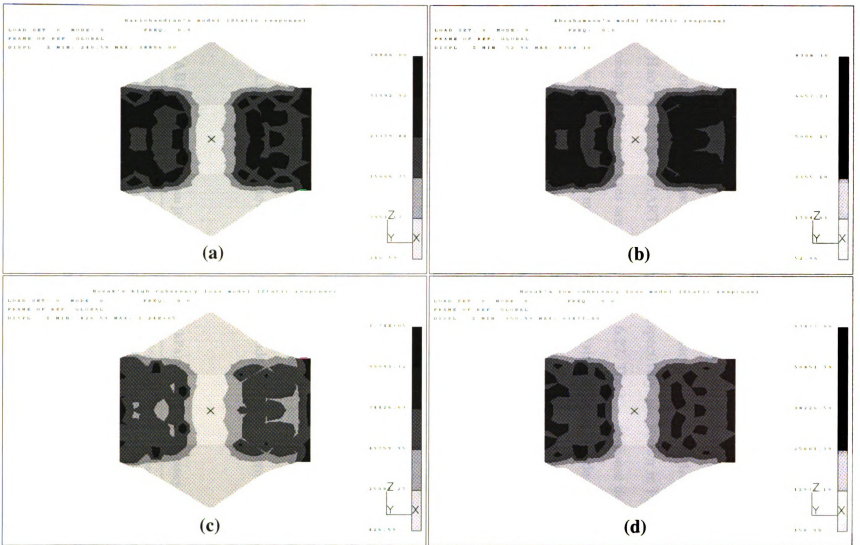

Figure 6.25 $\mu+3\sigma$ Static τ_{max} response (lb/ft^2) using (a) Harichandran's (b) Abrahamson's (c) Novak's Case II and (d) Novak's Case I models

response magnitudes. The total and static τ_{max} responses are quite different for Abrahamson's coherency function, indicating that the static component does not dominate for this low coherency decay model. For the other three high coherency decay functions, however, the static response dominates the total response.

The total $\mu+3\sigma$ τ_{max} response for (a) Luco & Wong's low coherency decay model, (b) Luco & Wong's high coherency decay model, (c) Hao's model for SMART-1 Event 45, and (d) Hao's model for SMART-1 Event 30, respectively, are shown in Fig. 6.26. The corresponding static responses are shown in Fig. 6.27. The τ_{max} response due to Luco & Wong's low coherency decay model (Fig. 6.26(a)) is similar in magnitude and distribution to the response due to Abrahamson's model (Fig. 6.24(a)), and is also not dominated by the static component (see Figs. 6.26(a) and 6.27(a)). The other three responses in Fig. 6.26, however, are dominated by the static component. Note that although the magnitude of the τ_{max} response due to Hao's two models is significantly different, their distributions are similar (see Figs. 6.26(c) and (d)).

Excluding responses around the artificial upstream and downstream boundaries, the maximum $\mu+3\sigma$ total τ_{max} responses are given in Table 6.5 for each coherency function, and the numbers listed in parentheses are the static components. There is a wide variation in the maximum τ_{max} response, with Novak's model (Case II) being ten times higher than that due to Luco and Wong's low coherency decay model. For high coherency decay cases,

TABLE 6.5 **Maximum $\mu+3\sigma$ τ_{max} response (kPa) to different coherency models**

Harichandran's	Abrahamson's	Novak's (case I)	Novak's (case II)
1,670 (1,636)	523 (342)	2,650 (2,639)	4,866 (4,859)

Luco & Wong's (low decay)	Luco & Wong's (high decay)	Hao's (Event 45)	Hao's (Event 30)
476 (231)	1,083 (1,074)	1,368 (1,319)	2,026 (2,000)

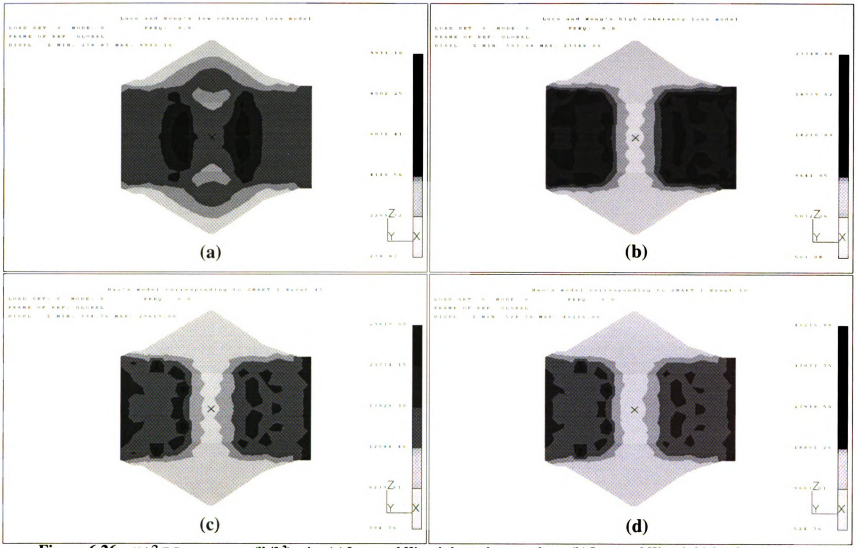

Figure 6.26 $\mu+3\sigma\ \tau_{max}$ **response (lb/ft^2) using (a) Luco and Wong's low coherency decay (b) Luco and Wong's high coherency decay (c) Hao's SMART-1 Event 45 and (d) Hao's SMART-1 Event 30 models**

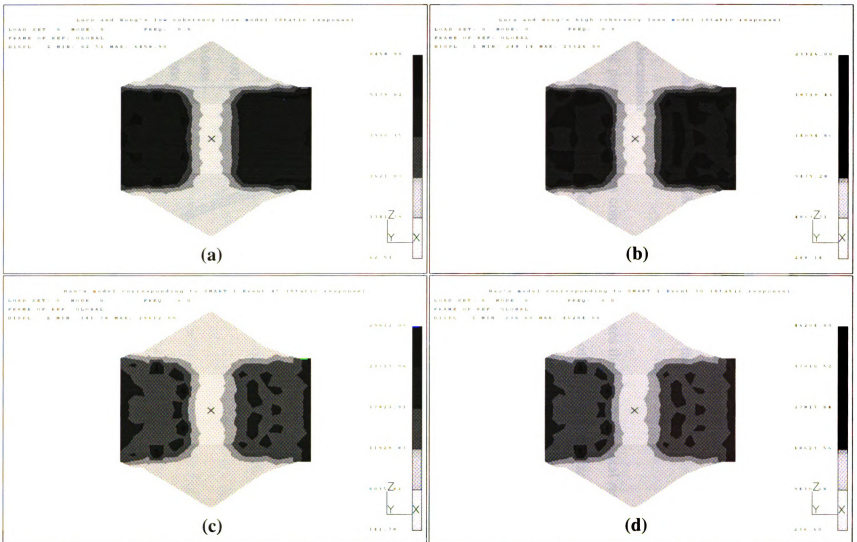

Figure 6.27 $\mu+3\sigma$ Static τ_{max} response (lb/ft^2) using (a) Luco and Wong's low coherency decay (b) Luco and Wong's high coherency decay (c) Hao's SMART-1 Event 45 and (d) Hao's SMART-1 Event 30 models

the static stress component alone is a very good approximation of the total stress response. Surprisingly, the critical τ_{max} responses occur at the same location for all these high coherency decay models (x = -160 ft, y = 0 ft, z = ± 122 ft).

Note that for the low coherency decay models (Abrahamson's and Luco & Wong's), the τ_{max} responses are very similar to that due to identical ground motion (see Fig. 5.11(c)), and hence the effect of SVEGM can be neglected for these cases.

6.3.3 Discussion

The pseudo-static stress component contributes the most to the total responses. This component is based on the calculation of the integral of the ground displacement spectrum as shown in equation (4.42). Fig. 6.28 shows plots of the integrand $S_{\ddot{u}_g}(\omega)\,|\gamma(v, \omega)|/\omega^4$ against frequency for various separations for Harichandran's model, and indicates that only low frequencies up to about 10 rad/s contributes to the area and hence the static stress component. The fact that the curves shown in Fig. 6.28 for different separations are distinct

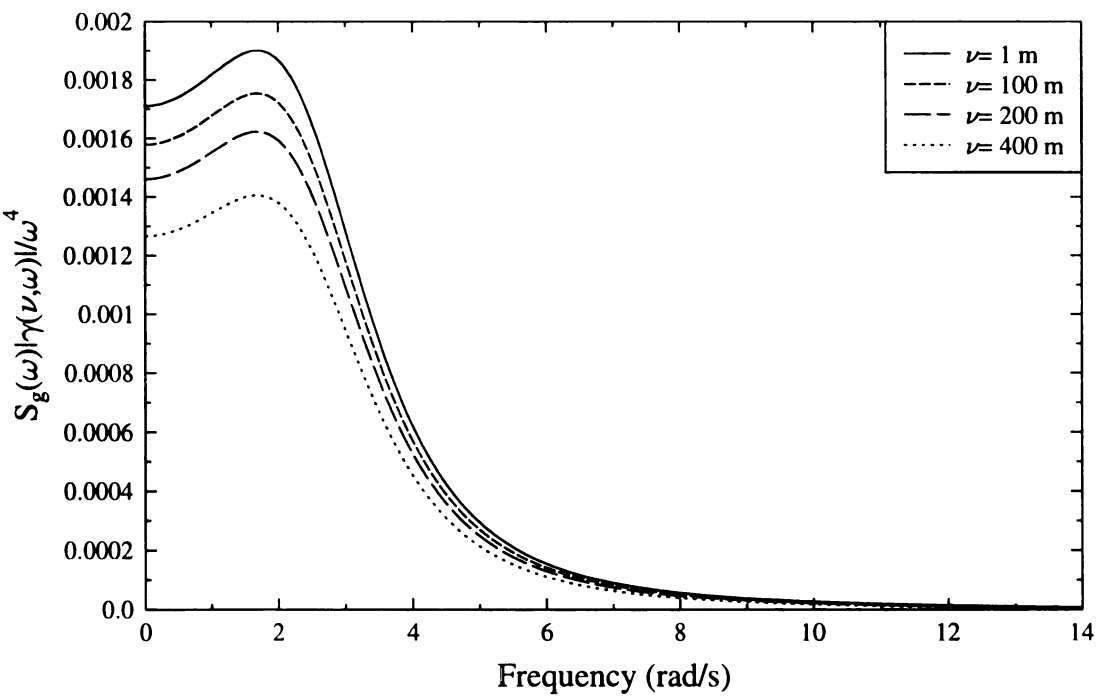

Figure 6.28 **Plot of static response integrand for Harichandran's ground motion model**

implies that the coherency loss is significant at the low frequencies that contribute to the static stresses. Thus, a plot of the static response in integrand, as in Fig. 6.28, can be used to assess whether or not the static stress response will be significant for the coherency model used.

To illustrate this further, the static response integrand is plotted in Figs. 6.29 and 6.30 for Novak's Case I and Case II models, respectively. The integrand values decay much faster than for Harichandran's model, and so it can be concluded that stress responses at the base would be more critical for these models than for Harichandran's model.

Another two coherency models proposed by Hao were developed according to Events 30 and 45 from SMART-1 array. Plots of the pseudo-static response integrand for the coherency models proposed by Hao for the SMART-1 Events 30 and 45 are shown in Figs. 6.31 and 6.32, respectively. Six combinations of the longitudinal and transverse separations are used in these plots. Based on these two figures alone, it can be concluded that the static stress responses at the base will be greater for Event 30 than for Event 45, since the family of curves are more distinct for the former event. A comparison of Harichandran's model used in the study, which corresponds to Event 20 recorded by the SMART-1 array, and Hao's model for Event 30 & 45 reveals that coherency loss and hence the stress response may change significantly from one earthquake ground motion to another.

Finally, according to Abrahamson's coherency model for horizontal ground motions, coherency loss results in only 5% increase of τ_{max}. The curves for the static response integrand at different separations almost overlap each other as shown in Fig. 6.33. Within the dimensions of the Santa Felicia dam, the effect of SVEGM is not significant for Abrahamson's model. One possible reason is that Abrahamson averaged the coherency curves for a number of earthquake events and sites which may have resulted in high coherencies at low frequencies.

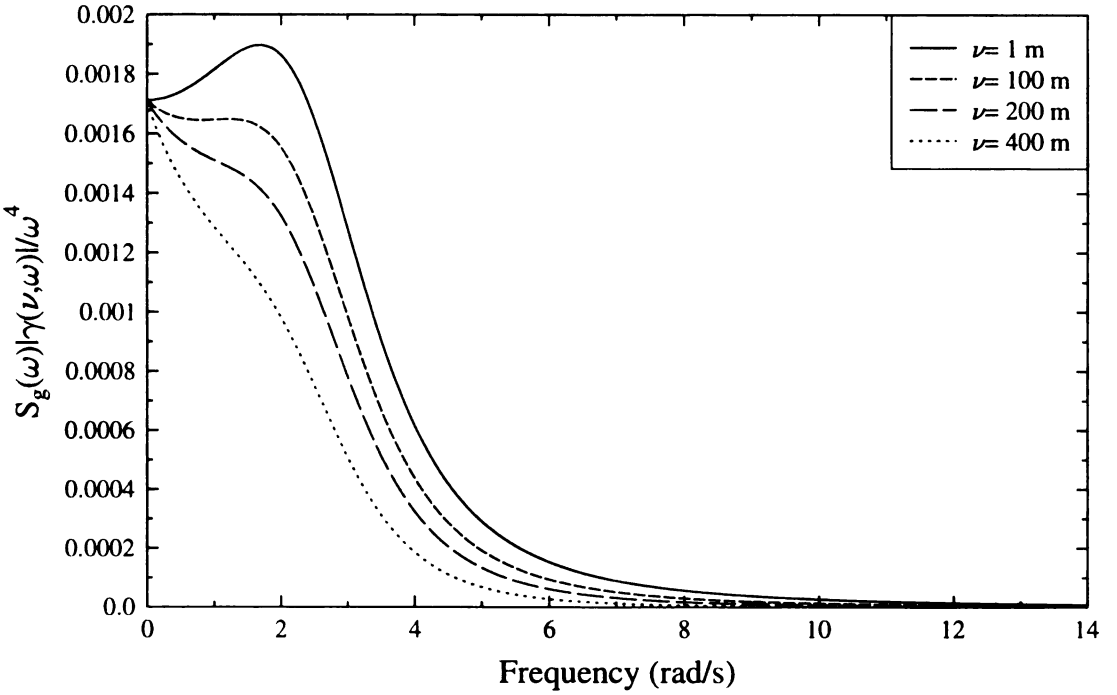

Figure 6.29 **Plot of the static response integrand for Novak's Case I model**

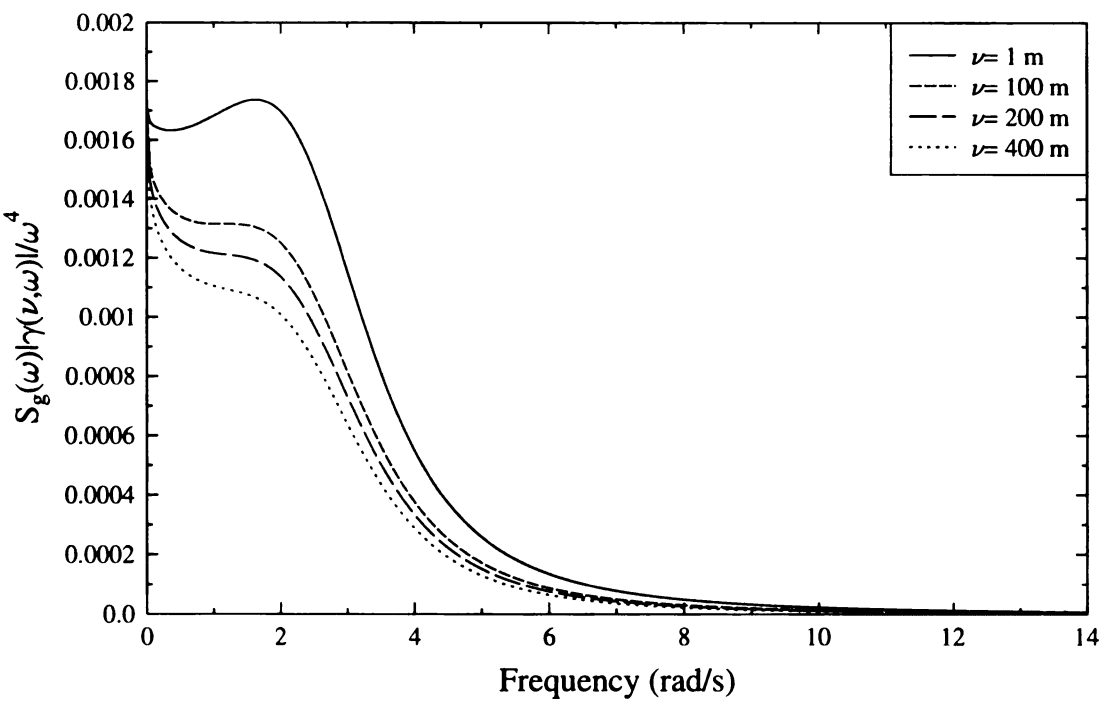

Figure 6.30 **Plot of the static response integrand for Novak's Case II model**

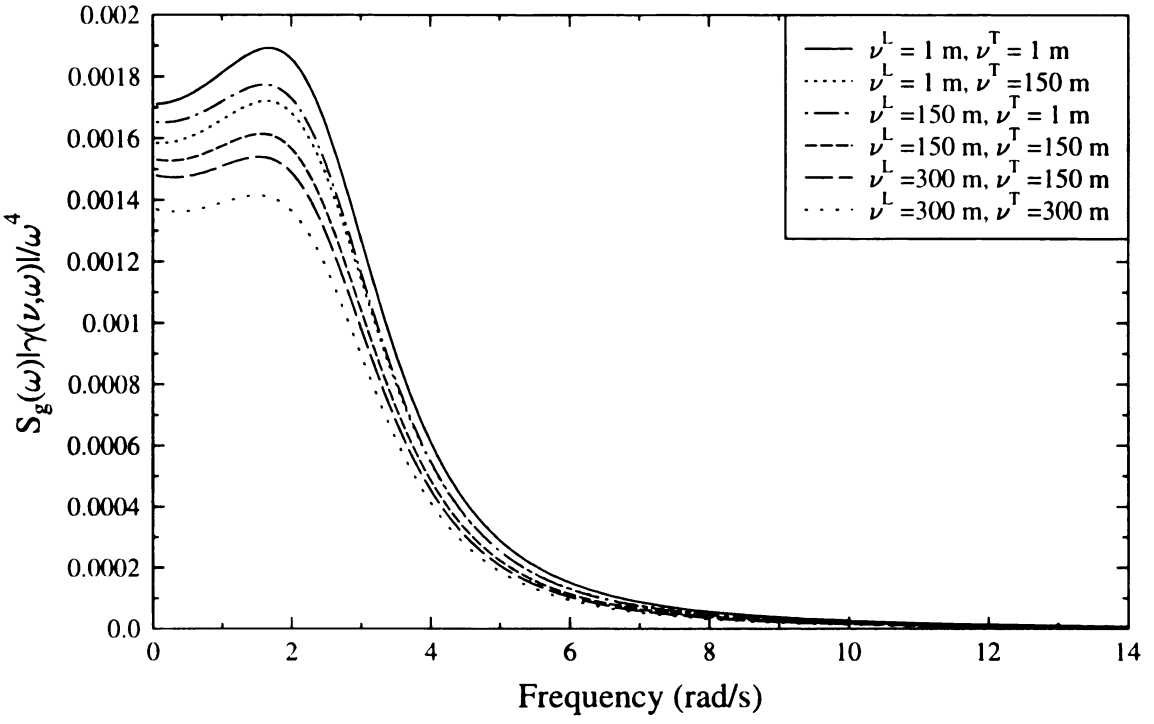

Figure 6.31 **Plot of the static response integrand for Hao's model–Event 30**

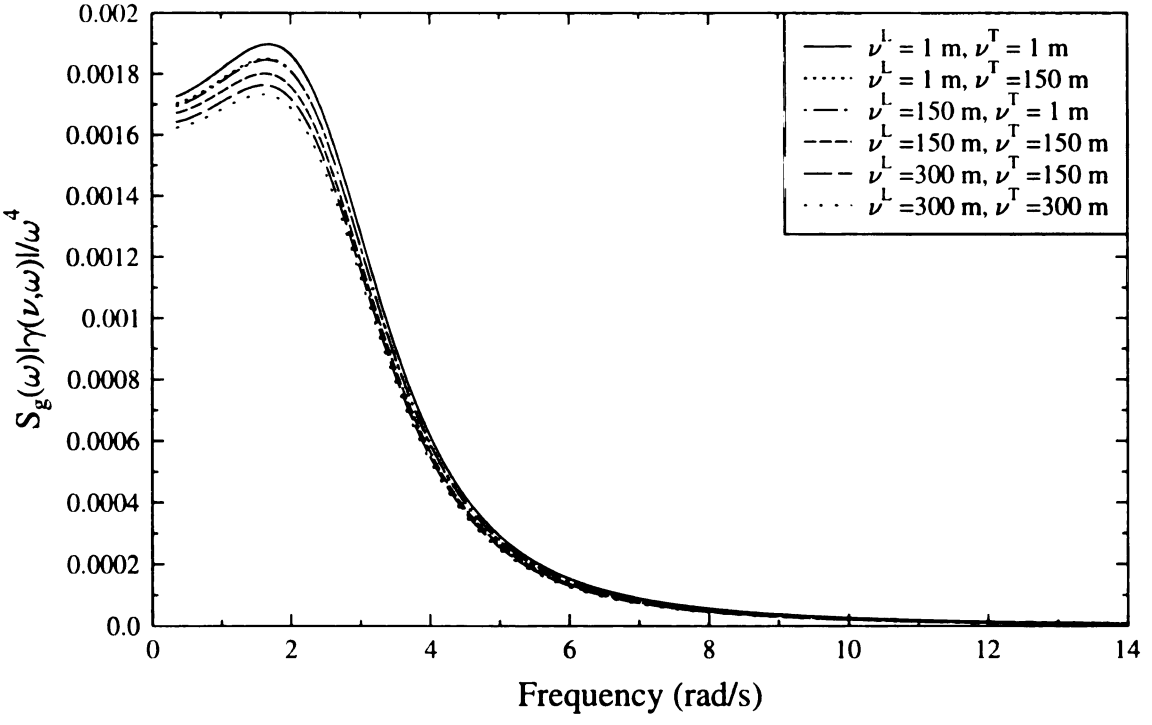

Figure 6.32 **Plot of the static response integrand for Hao's model–Event 45**

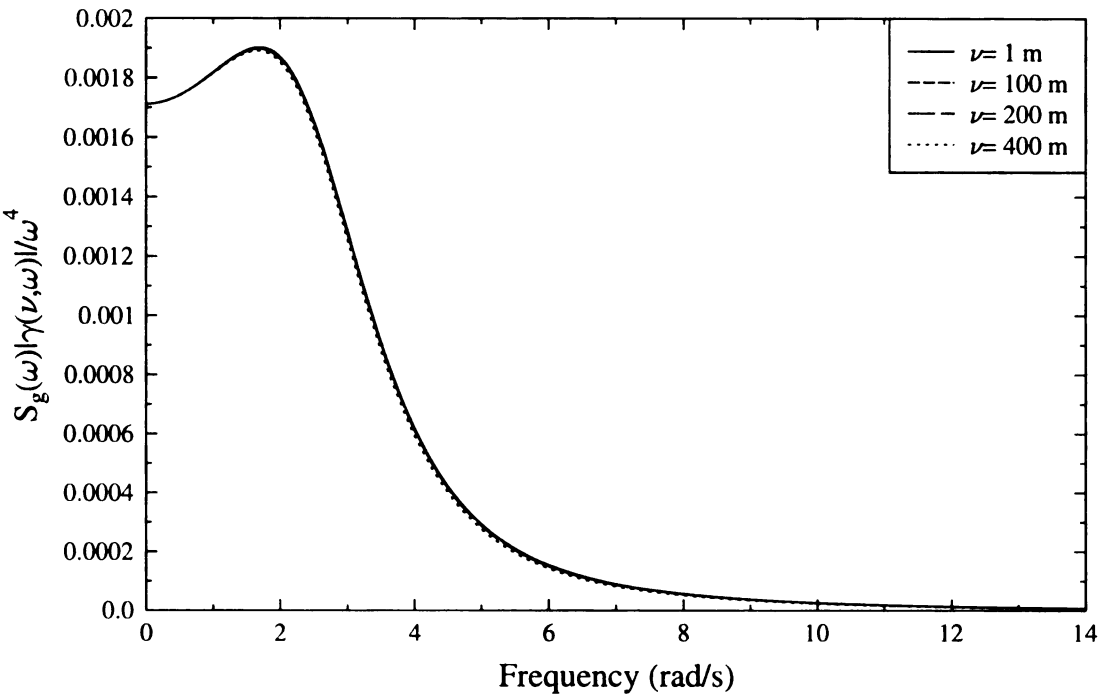

Figure 6.33 **Plot of the static response integrand for Abrahamson's horizontal ground motion**

To sum up, the stress response at the base of earth dams are sensitive to the specific coherency model used. The stress response at the base is governed by low frequency excitations while displacement and strain responses are dominated by medium frequency motions. At frequencies less than 0.5 Hz, Abrahamson's model is essentially unity for most separations as a result of which the stress responses at the base are essentially the same as those due to identical excitation.

In fact, coherencies in the frequency range from 0 to 0.5 Hz cannot be reliably estimated from data. The reason for this is that estimation of the coherency requires adequate smoothing of the auto and cross spectral estimates (Jenkins and Watts 1969). However, smoothing results in a loss of resolution. For limited duration accelerograms (e.g. 10 second long records sampled every 0.01 second), the bandwidth of the smoothing window used in spectral estimation is typically about 0.5 Hz. If at any frequencies the spectra vary very rapidly within the bandwidth of the smoothing window centered at those

frequencies, then the spectral estimates and hence the coherency at those frequencies will be highly biased and unreliable. For frequencies approaching zero, physical considerations require that the auto and cross spectra of accelerograms must rapidly decay to zero. Since this rapid decay usually occurs within the frequency range of 0 to 0.5 Hz (see Fig. 5.1 El Centro spectrum) which corresponds to the bandwidth of the smoothing window, the coherency estimates in this frequency range are unreliable.

Thus, most coherency models that are developed are reliable only for frequencies above 0.5 Hz. The extrapolation of the coherency from 0.5 Hz to 0 Hz is strongly influenced by the functional form chosen for the empirical coherency model, and is somewhat arbitrary. However, since ground displacements are dominated by low frequency components, the coherency in the range of 0 to 0.5 Hz is extremely important for characterizing the correlation between ground displacements at different spatial locations.

Although a few coherency functions have been proposed in the last decade, the investigation of SVEGM is still at an early stage. It has been shown that the coherency models presented in this study are rather inconsistent. It appears important to address this incoherency in future efforts at processing seismograph array data.

7. Simplified Modeling and Analysis Techniques

7.1 Introduction

A finite element-based random vibration analysis of a 3-D earth dam model subjected to earthquake ground motion is time-consuming and costly. From a practical point of view, it is of interest to explore simplified modeling and analysis that may be capable of yielding acceptable results. In other studies, simplified earth dam models such as 2-D shear beam models and plane strain finite element models have been used. As mentioned previously, SVEGM cannot be represented exactly for such models in reduced dimensions. Techniques to simplify the SVEGM at the base, so that a 2-D shear beam model can be used for approximate analysis, are explored in this chapter.

7.2 One-dimensional Excitation Model

For a 2-D shear beam model of an earth dam, as shown in Fig. 7.1, the base consists of a finite number of truncated wedges. The base of each wedge is a strip along the upstream to downstream width of the dam. The strips where ground motion excitation is applied each have a single degree of freedom. As a result, all points within a strip have

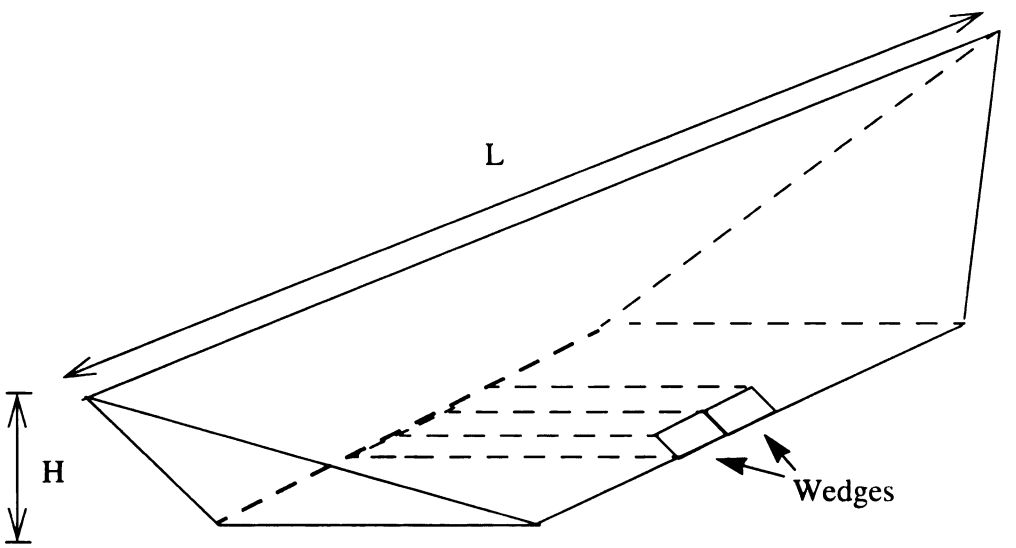

Figure 7.1 **Illustration of truncated wedges in 2-D shear beam model**

identical excitations. However, the ground motion at two points on different strips may be incoherent. One method of obtaining "equivalent" excitations for each strip is to assume that it is the average of the correlated excitations at each point within the strip. The coherency between the equivalent excitations at different strips would then be the coherency between each average excitation. However, the calculations required to obtain the SDFs of the average excitations and the coherency between them is tedious. Therefore, as a first step, the coherency decay along the width of the dam is neglected, and the SDF of the equivalent excitation for each strip is taken to be the point SDF, $S_{\ddot{u}_g}(\omega)$. Further, the coherency between the excitations at two different strips is taken to be the coherency evaluated at the average separation between all pairs of points in the two strips. For any pair of strips i and j as shown in Fig. 7.2, the average separation between a point on strip i and a point on strip j is

$$\gamma_{ij} = \frac{1}{\Delta x_1 \Delta z_1 \Delta x_2 \Delta z_2} \int_{x_1=0}^{\Delta x_1} \int_{z_1=0}^{\Delta z_1} \int_{x_2=L_1}^{L_1+\Delta x_2} \int_{z_2=L_2}^{L_2+\Delta z_2} \sqrt{(x_2-x_1)^2 + (z_2-z_1)^2}\, dx_1 dz_1 dx_2 dz_2 \tag{7.1}$$

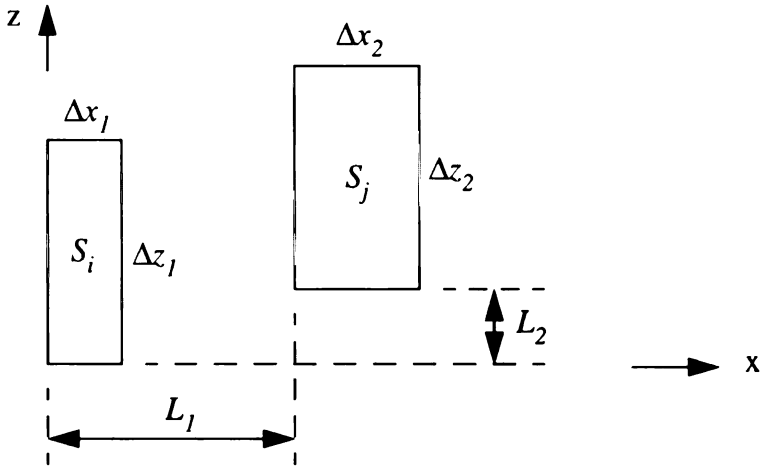

Figure 7.2 **Illustration for calculation of average separation between two rectangular areas**

where Δx_1 and Δz_1 are the width and length of strip i; Δx_2 and Δz_2 are the width and length of strip j; and L_1 and L_2 are separations between the lower left corners of these two strips in the x and z directions, respectively.

The analytical expression in equation (7.1) cannot be evaluated in closed-form. However, $\overline{v}_{ij}$ may be estimated by taking the average separation of a sufficient number of simulated pairs of points on strips i and j. The average separation is used to determine the coherency loss in the simplified excitation model, which is called a 1-D excitation model because only separation in the longitudinal direction of the dam (perpendicular to the length direction of strips) is used to account for the incoherency effect. For the general excitation model, coherency loss in the upstream-downstream direction as well as the longitudinal direction at the base was considered. The base of the dam was divided into 15 strips for the 1-D excitation model. In addition, the effects of using a different number of strips at the base on the earth dam responses were investigated by considering 9 and 21 strips in addition to the 15-strip case.

It should be noted that a 2-D shear beam model of the dam was not actually used. Both the 1-D and general excitation models were used with the 3-D finite element model of the dam. For the 1-D excitation model, all base nodes located within a strip were assumed to have identical excitations. The intent of the analysis was to assess the effect of simplifying the excitation model. If the simplified excitation model is acceptable, then it could be used with a 2-D shear beam model of the dam.

7.2.1 Fifteen strip subdivision of the base

7.2.1.1 Introduction

It is convenient to use a new Cartesian coordinate system as shown in Fig. 7.3. The origin is located on the left-hand side of the base instead of at the middle of the base so that the coordinates of every point of the dam are always positive. In Fig. 7.4, the boundary of the dam was divided into 15 strips. The ith strip is denoted by Si. Each strip has a reference

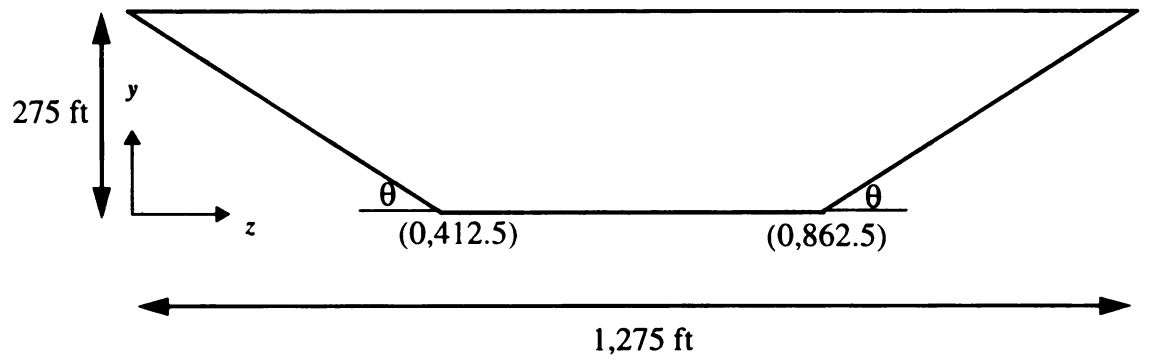

Figure 7.3 YZ Cutting Plane at x=0

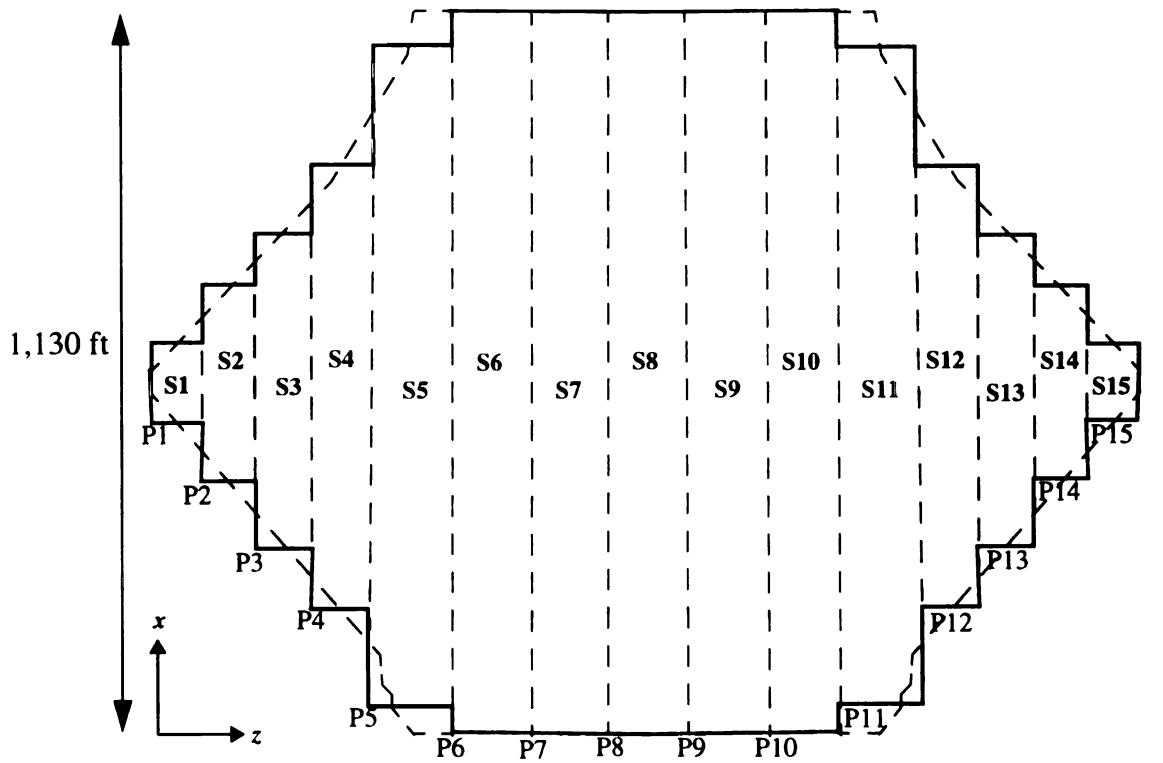

Figure 7.4 Illustration of 15-strip division

point which is denoted by P*i*. The point closest to the origin of each strip was selected to be the reference point. The length Δx and width Δz of each strip and the x and z coordinates of each reference point are given in Table 7.1. Because the length Δx is variable along the width on the inclined boundary, an average value of Δx was adopted as shown in Fig. 7.4.

In order to randomly generate points on strip i, n pairs of independent random numbers were simulated in the range between 0 and 1 using a uniform distribution function U(0,1). If the pairs of random number sequences are denoted by $a_{x_i}(n)$ and $a_{z_i}(n)$, the x and z coordinates for each point at the ith strip can then be determined by

TABLE 7.1 Strip dimensions and reference point coordinates (ft)

Strip Number	Strip Width (Δz)	Strip Length (average Δx)	Reference Point	z	x
S1	75	130	P1	0	472.75
S2	75	330	P2	75	378.25
S3	75	530	P3	150	283.75
S4	75	730	P4	225	189.25
S5	112.5	980	P5	300	71
S6	90	1130	P6	412.5	0
S7	90	1130	P7	502.5	0
S8	90	1130	P8	592.5	0
S9	90	1130	P9	682.5	0
S10	90	1130	P10	772.5	0
S11	112.5	980	P11	862.5	71
S12	75	730	P12	975	189.25
S13	75	530	P13	1050	283.75
S14	75	330	P14	1125	378.25
S15	75	130	P15	1200	472.75

$$\begin{aligned} x_{ni} &= x_{Pi} + \Delta x_{Si} \times a_{x_i}(n) \\ z_{ni} &= z_{Pi} + \Delta z_{Si} \times a_{z_i}(n) \end{aligned} \tag{7.2}$$

The y coordinate has the following relationship with the z coordinate:

$$y_{ni} = \begin{cases} (412.5 - z_{ni}) \tan\theta & \text{if} \quad 0.0 \le z_{ni} < 412.5 \text{ ft} \\ 0 & \text{if} \quad 412.5 \le z_{ni} \le 862.5 \text{ ft} \\ (z_{ni} - 862.5) \tan\theta & \text{if} \quad 862.5 < z_{ni} \le 1275 \text{ ft} \end{cases} \tag{7.3}$$

where θ is the angle of inclination shown in Fig. 7.3 ($\tan\theta = \dfrac{275}{412.5} = 0.66667$).

A total of m points on strip j can be generated in a similar manner using two other pairs of random number sequences $a_{x_i}(m)$ and $a_{z_i}(m)$. Consequently, the average separation between strips i and j can be calculated by

$$\nabla_{ij} = \frac{1}{nm} \sum_{k=1}^{n} \sum_{l=1}^{m} \sqrt{(x_{ki} - x_{lj})^2 + (y_{ki} - y_{lj})^2 + (z_{ki} - z_{lj})^2} \tag{7.4}$$

For the two strips S1 and S11, the average separation corresponding to different numbers of samples are plotted in Fig. 7.5, and the figure indicates that using one hundred samples

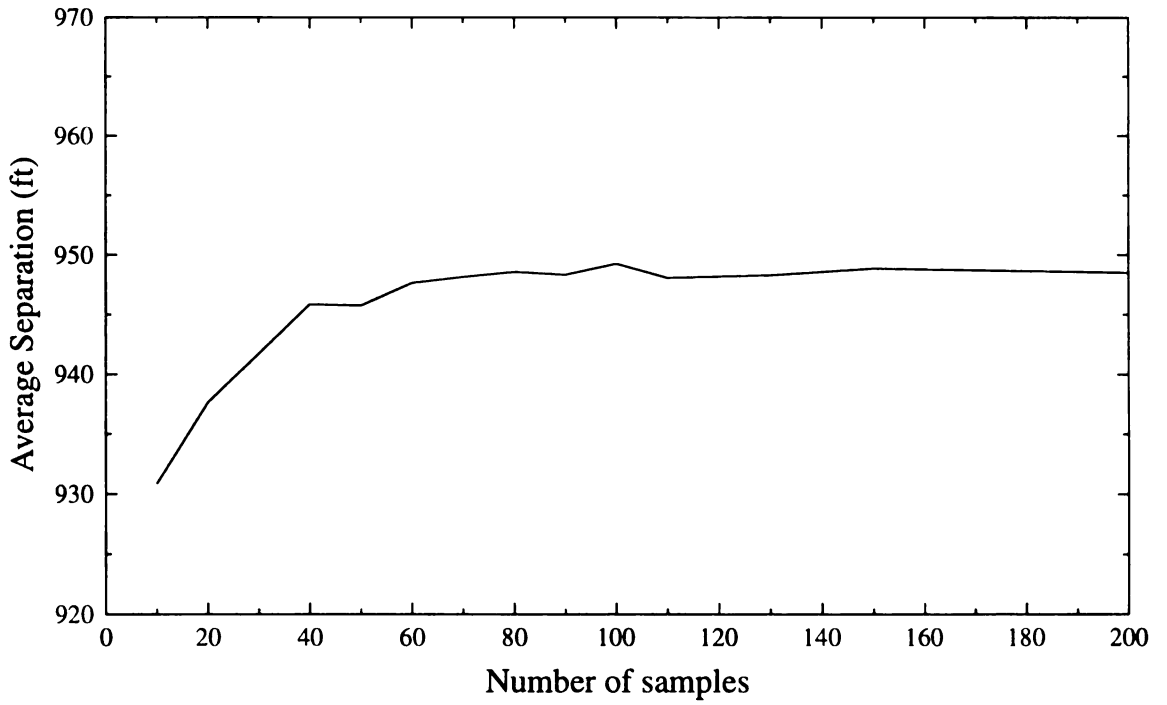

Figure 7.5 **Convergence of average separation between S1 and S11**

is adequate to estimate $\bar{v}$. The average separation between each pair of strips using 100 randomly generated points in each strip is shown in Table 7.2. The responses due to the simplified 1-D earthquake excitation were obtained using these values for $\bar{v}$ in equation (4.3).

7.2.1.2 Displacement and maximum shear strain responses

The 3σ x-displacement responses for the 1-D and general excitation models are shown in Fig. 7.6, in which figures (a) and (b) are plan views of the response contours, and figures (c) and (d) are contours on the XY cutting plane at z = 0. All contours are set to the same scale. It is apparent that x-displacement responses inside the dam as well as on the top surface due to the 1-D excitation model agree well with those due to the general excitation model. Using the 1-D excitation model, the maximum 3σ x-displacement response is only 1.3% higher than that using the general excitation model. Note that the maximum 3σ displacement response due to the identical excitation model is 8.1% larger than that due to the general excitation model.

The $\mu+3\sigma$ maximum shear strain responses using these two excitation models are shown in Fig. 7.7. Figures (a) and (b) are plan views of the γ_{max} contours, and figures (c) and (d) are the γ_{max} contours displayed on the XY cutting plane at z = 0. Although γ_{max} is slightly different near the side boundaries between the two excitation models, the critical response regions are quite similar to each other. The maximum $\mu+3\sigma$ γ_{max} response is about 1.9% larger for the 1-D simplified model compared to the general model. Note that for the identical excitation model, the maximum $\mu+3\sigma$ γ_{max} response is 10.3% higher than that using the general excitation model.

7.2.1.3 Maximum shear stress response

The $\mu+3\sigma$ maximum shear stress responses at the base are shown in Figs. 7.8(a) and (b) for the 1-D and general excitation models, respectively, and these are quite dissimilar. The maximum τ_{max} response is 50% larger for the 1-D excitation model compared to that

TABLE 7.2 **Estimated average separation (ft) between each pair of strips**

Strip	S1	S2	S3	S4	S5	S6	S7	S8	S9	S10	S11	S12	S13	S14	S15
S1	0.														
S2	131.8	0.													
S3	233.3	182.4	0.												
S4	337.4	276.7	238.9	0.											
S5	469.1	402.9	351.1	318.8	0.										
S6	580.0	509.8	450.3	404.6	374.2	0.									
S7	649.0	576.1	512.6	460.8	418.3	388.2	0.								
S8	722.5	647.9	581.5	525.5	474.4	430.0	388.2	0.							
S9	799.3	723.6	655.2	596.0	538.4	484.1	430.0	388.2	0.						
S10	878.5	802.0	732.2	670.6	608.0	546.2	484.1	430.0	388.2	0.					
S11	948.4	871.9	801.8	739.5	675.2	608.8	539.2	475.2	419.1	374.9	0.				
S12	1008.3	932.9	863.8	802.5	739.3	671.0	596.5	526.2	461.6	405.5	319.0	0.			
S13	1066.0	992.0	924.2	864.1	801.9	732.9	656.0	582.5	513.7	451.6	352.0	239.4	0.		
S14	1130.7	1058.3	992.2	933.4	872.3	802.8	724.5	649.1	577.5	511.4	404.2	277.9	183.1	0.	
S15	1201.3	1130.8	1066.3	1008.9	948.8	879.3	800.3	723.7	650.4	581.6	470.6	339.1	234.9	133.1	0.

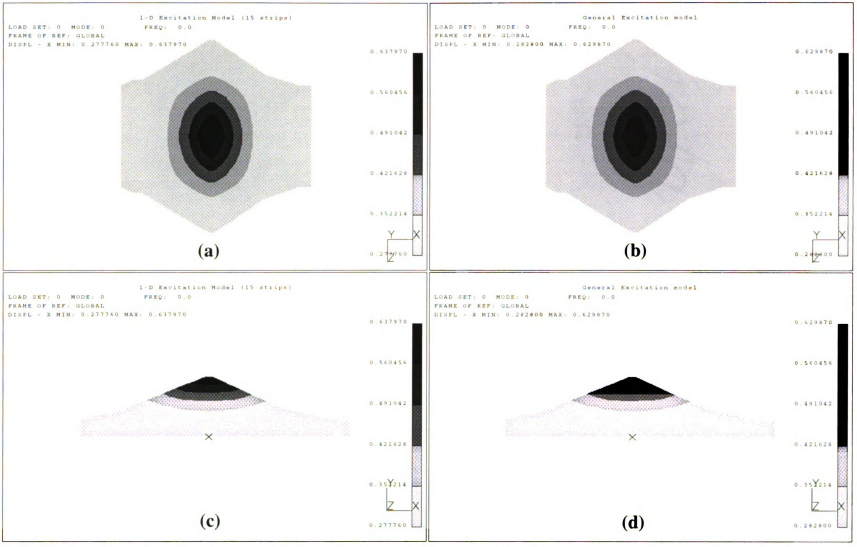

Figure 7.6 Plan and elevation views of the 3σ x-displacement responses (ft) using the 1-D ((a) and (c)) and general ((b) and (d)) excitation models

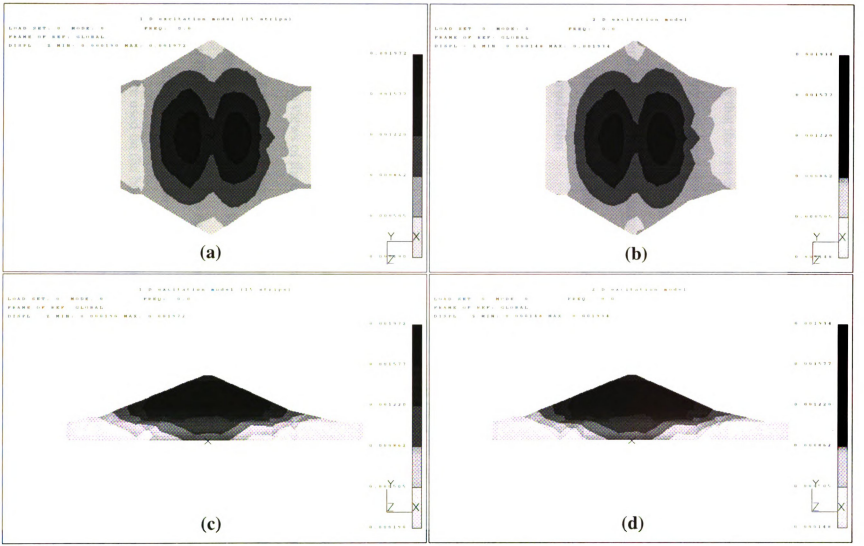

Figure 7.7 Plan and elevation views of the$\mu + 3\sigma$ γ_{max} responses using the 1-D ((a) and (c)) and general ((b) and (d)) excitation models

due to the general model. Figs. 7.8(c) and (d) show the $\mu+3\sigma$ τ_{max} contours on the XY cutting plane at z = 0. Although the 1-D excitation model does not predict τ_{max} well near the base, the predictions at locations away from the boundary are reasonable. Figs. 7.9(a) and (b) display the τ_{max} contours on the horizontal cutting plane at the mid-height of the dam, and show that the two contour patterns match each other very well. The τ_{max} responses in the core clay region are shown in Figs. 7.9(c) and (d) which display the YZ cutting planes at x = 0. The τ_{max} response due to the 1-D simplified excitation is very similar to that due to general excitation over the entire dam except near the base.

7.2.2 Effect of different number of strips on the boundary

7.2.2.1 Introduction

As the number of strips on the base is reduced, the accuracy of the 1-D excitation model would be expected to become poorer. Analyses with 9 and 21 strips on the base were performed to assess this effect. The horizontal and two inclined portions of the base were divided into 3 strips each for the 9-strip case, and 7 strips each for the 21-strip case, respectively.

7.2.2.2 Responses

The 3σ x-displacement response contours are shown in Fig. 7.10, in which figures (a) and (b) are plan views of the contours for the 9- and 21-strip cases, respectively, and figures (c) and (d) show the x-displacements on the XY cutting plane at z = 0 for the 9- and 21-strip cases, respectively. Generally speaking, the displacements do not vary significantly between the 9-, 15- and 21-strip cases. The values of the critical x-displacement response for all excitation cases used in this study are given in Table 7.3, which indicates that as more strips are used on the base, the maximum x-displacement response becomes closer to that due to the general excitation. However, the use of 9 strips, which appears minimal, seems adequate, and the improvement with 15 and 21 strips is marginal. In the limit, as

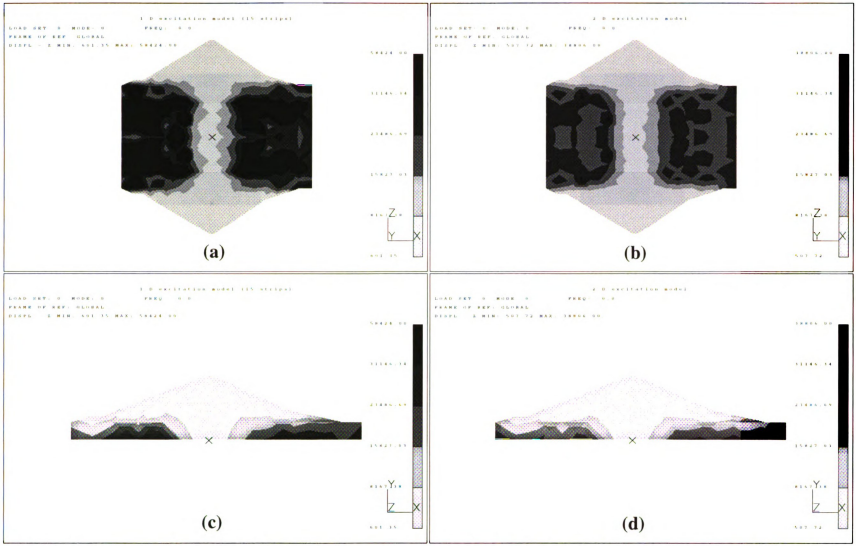

Figure 7.8 Bottom and elevation views of the $\mu + 3\sigma\ \tau_{max}$ responses (lb/ft^2) using the 1-D ((a) and (c)) and general ((b) and (d)) excitation models

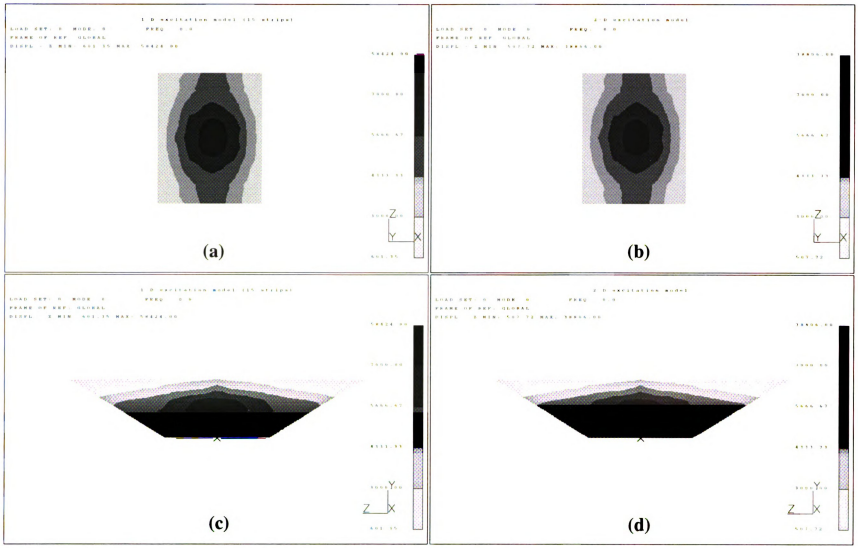

Figure 7.9 $\mu+3\sigma\ \tau_{max}$ **responses (lb/ft²) inside the dam: (a) and (b) are XZ cutting planes at mid-height; (c) and (d) are YZ cutting planes at x = 0**

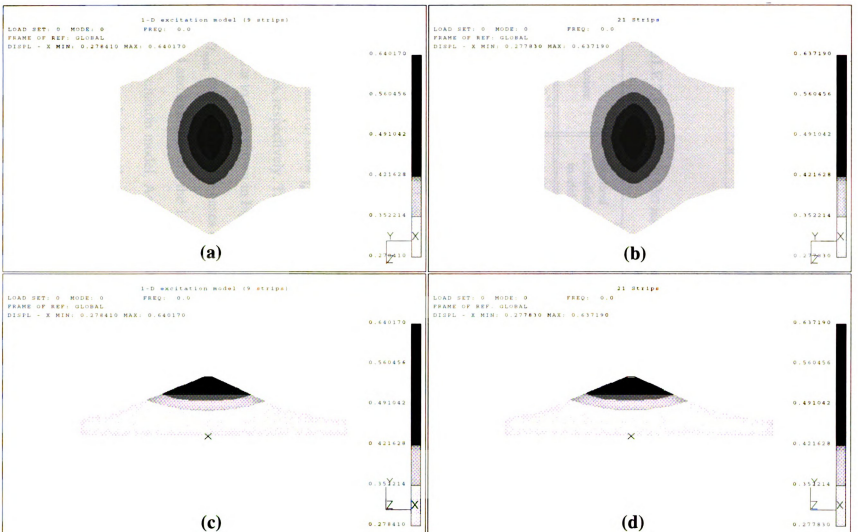

Figure 7.10 **Plan and elevation views of the 3σ x-displacement responses (ft) using the 1-D excitation model with 9 strips ((a) and (c)) and 21 strips ((b) and (d)) at the base.**

TABLE 7.3 Maximum 3σ displacement responses using simplified and general excitation models

Response	Identical excitation model	1-D excitation model			General excitation model
		9 strips	15 strips	21 strips	
x-displacement (mm)	207.4	194.93	194.26	194.02	191.80

TABLE 7.4 Critical μ+3σ maximum shear strain responses using simplified and general excitation models

Response	Identical excitation model	1-D excitation model			General excitation model
		9 strips	15 strips	21 strips	
γ_{max} ($\times 10^{-3}$)	2.133	1.979	1.972	1.970	1.934

fewer and fewer strips are used on the base, the 1-D excitation model approaches the identical excitation model.

The μ+3σ maximum shear strain responses are shown in Fig. 7.11, in which the responses for all cases are set to the same scale. Figs. 7.11(a) and (b) show γ_{max} responses at the top free surface for the 1-D excitation model with 9 and 21 strips, respectively; and Figs. 7.11(c) and (d) show γ_{max} responses on the XY cutting plane at z = 0 for the 9- and 21-strip cases, respectively. The use of 21 strips on the base yields γ_{max} response contours very similar to those shown in Fig. 7.7(b) for the general excitation model. The maximum μ+3σ γ_{max} responses for the cases of identical, 1-D and general excitations are listed in Table 7.4 and indicates that the 1-D excitation model yields better γ_{max} responses than the identical excitation model. As with the displacement response, the accuracy of the 1-D model becomes better as the number of strips is increased, but the improvement beyond 9 strips is marginal.

The μ+3σ maximum shear stress response contours at the base are shown in Figs. 7.12(a) and (b) for the 1-D excitation model with 9 and 21 strips, respectively.

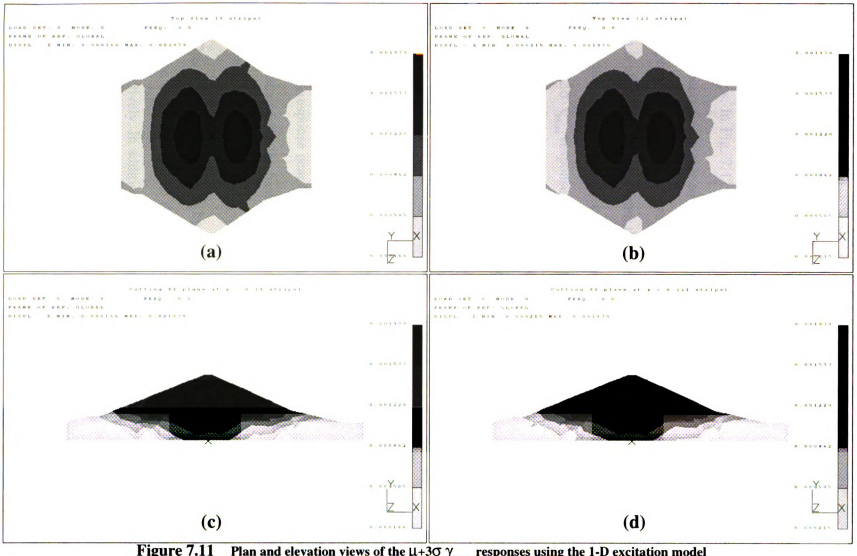

Figure 7.11 Plan and elevation views of the $\mu+3\sigma$ γ_{max} responses using the 1-D excitation model with 9 strips ((a) and (c)) and 21 strips ((b) and (d)) at the base.

Fig. 7.12(a) shows that high stresses occur near the edge of each strip in the gravel material regions due to the relative displacement between adjacent strips. For this 9-strip case, each strip is quite wide and since the excitations at all nodes in a strip are fully-correlated, the τ_{max} responses are small within the strip and are relatively high on the boundary between adjacent strips. In Fig. 7.12(b), even larger τ_{max} values occurs over the gravel region. Instead of becoming closer to the results obtained with the general excitation model the τ_{max} response at the base becomes worse as the number of strips is increased. The contour pattern is also quite different from that due to the general case. However, for the core and shell regions, the 21-strip case is better than the other two. Figs. 7.13 (a), (b), (c) and (d) show the $\mu+3\sigma$ τ_{max} response contours at the base for the shell and core using the general, 9-strip, 15-strip and 21-strip models, respectively. The scale has been adjusted so that details within the core and shell are displayed. The contour pattern for the 21-strip model is similar to that for the general model, except around the central part of the base where the response is overestimated.

In order to assess the stress distribution inside the dam, some cutting planes were taken. Figs. 7.12(c) and (d) show the $\mu+3\sigma$ τ_{max} response on the XY cutting plane at $z = 0$ for the 9- and 21-strip models, respectively. These figures, along with Fig. 7.8(c), indicate that the stress response near the base is sensitive to the number of strips used. However, at locations distant from the base the stress responses is not very sensitive to the number of strips used.

This is investigated further by plotting the contours of τ_{max} response on the horizontal plane at the mid-height (137.5 ft) as shown in Figs. 7.14(a) and (b) for the 9- and 21-strip cases, respectively. In addition, the responses on the YZ cutting plane at $x = 0$ are shown in Figs. 7.14(c) and (d) for the 9- and 21-strip cases, respectively. It is seen that the stress contours on these cutting planes are very similar to each other. The contours on these two cutting planes for the identical excitation case are also shown in Figs. 7.15(a) and (b),

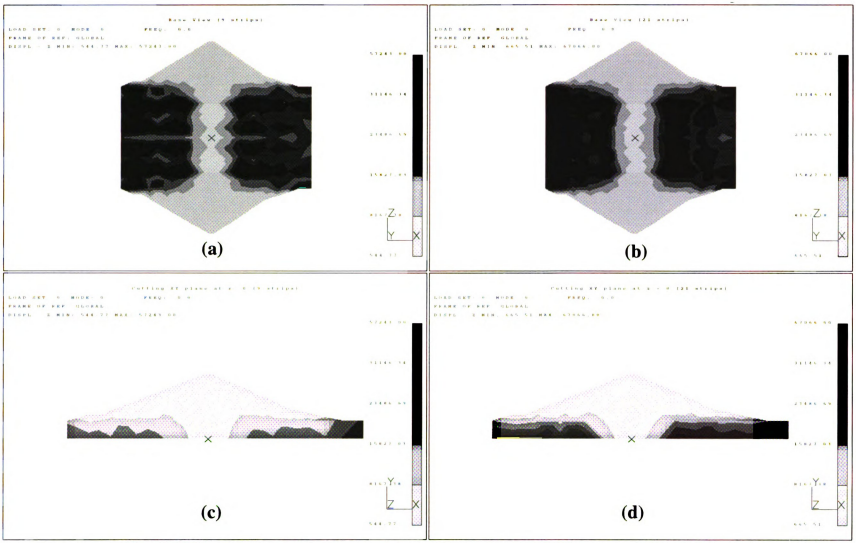

Figure 7.12 Bottom and elevation views of the $\mu + 3\sigma\ \tau_{max}$ responses (lb/ft^2) using the 1-D excitation model with 9 strips ((a) and (c)) and 21 strips ((b) and (d)) on the base.

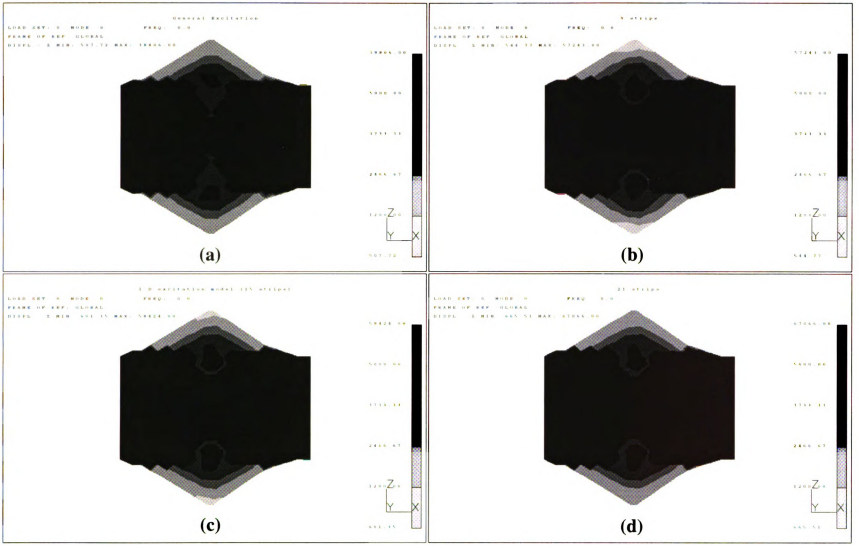

Figure 7.13 $\mu + 3\sigma\ \tau_{max}$ responses (lb/ft^2) in the core and shell for the (a) general (b) 9-strip (c) 15-strip (d) 21-strip excitation cases

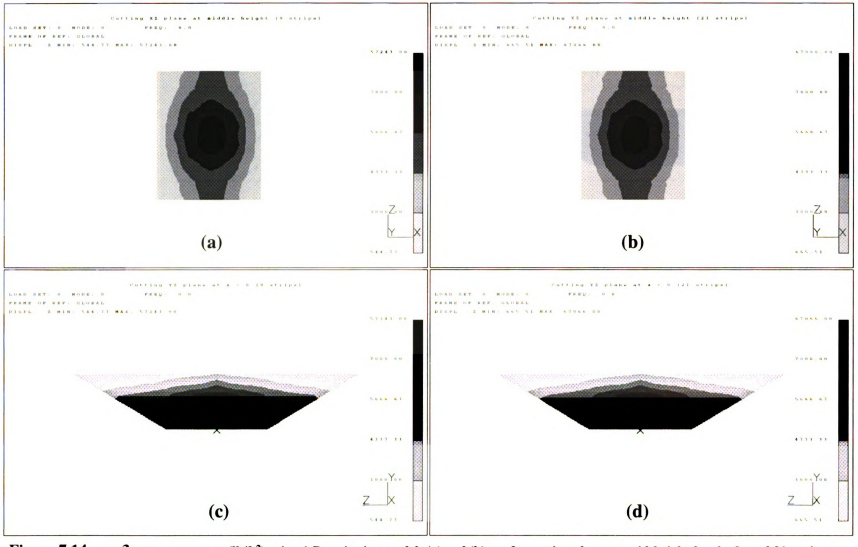

Figure 7.14 $\mu+3\sigma\ \tau_{max}$ **response (lb/ft²) using 1-D excitation model: (a) and (b) are for cutting planes at mid-height for the 9- and 21- strip case; (c) and (d) are for YZ cutting planes at x = 0 for the 9- and 21- strip cases.**

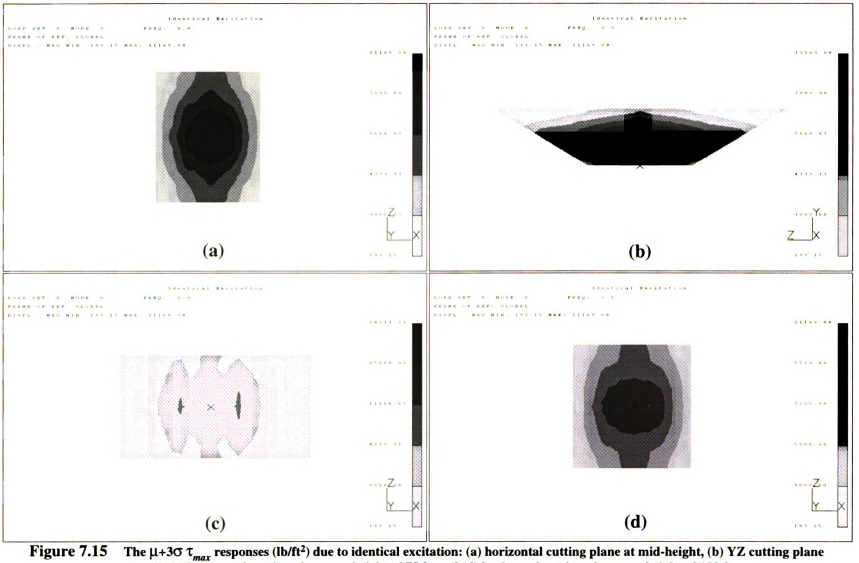

Figure 7.15 The $\mu+3\sigma$ τ_{max} responses (lb/ft^2) due to identical excitation: (a) horizontal cutting plane at mid-height, (b) YZ cutting plane at x = 0, (c) horizontal cutting plane at a height of 75 ft, and (d) horizontal cutting plane at a height of 120 ft.

which indicate that higher τ_{max} responses occur in the core clay region due to identical excitation than for the 1-D and general excitations.

Various horizontal cutting planes were used to assess the minimum height at which stresses due to the simplified 1-D excitation were acceptable, and it was found that this minimum height was about 120 ft, which is just below the mid-height. Figs. 7.16 (c) and (d) show τ_{max} contours at a height of 120 ft, and these are reasonably similar. Figs. 7.16 (a) and (b) show τ_{max} contours at a height of 75 ft, and these are quite dissimilar. Figs. 7.15 (c) and (d) show τ_{max} contours on horizontal cutting planes at 75 ft and 120 ft heights for identical excitation. Clearly at 75 ft, the identical excitation model significantly under-estimates τ_{max} response in the gravel region, while at 120 ft it overestimate τ_{max} in the core.

The maximum τ_{max} responses are given in Table 7.5 for each excitation model. The 1-D excitation model yields stress responses that are only 1.5% to 2% larger than those due to general excitation at the mid-height of the dam, with marginal improvement as the number of strips is increased from 9 to 21. However, stresses predicted at the base using the 1-D excitation model is poor (over-conservative) and becomes worse as more strips are used.

To sum up, for the critical displacement and γ_{max} responses and for the τ_{max} response away from the base, the use of 9 strips is sufficient and little improvement is obtained by

TABLE 7.5 Critical $\mu+3\sigma$ τ_{max} responses (kPa) using simplified and general excitation models

Cutting plane	Identical excitation model	1-D excitation model			General excitation model
		9 strips	15 strips	21 strips	
At the base (excluding response on the artificial boundary)	498	2,607	2,749	3,212	1,670
Horizontal plane at mid-height (same as on YZ cutting plane)	410.57	379.1	378.2	378.0	373.8

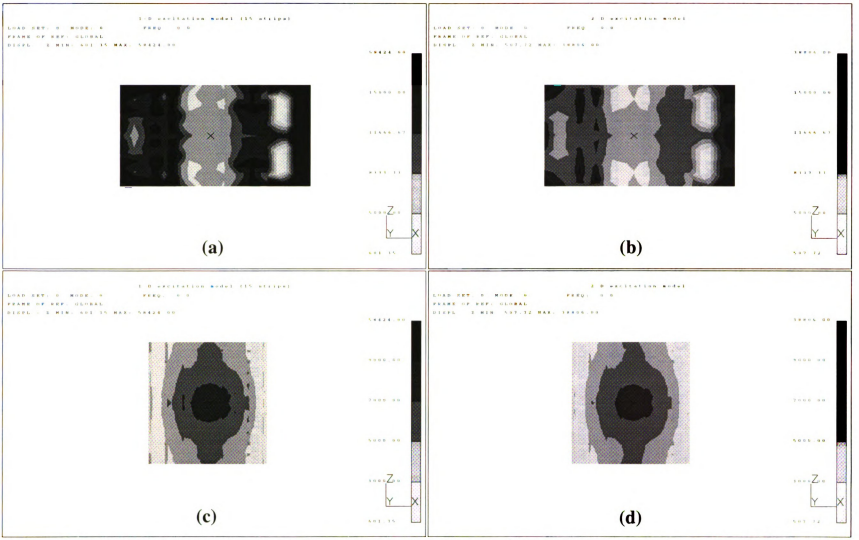

Figure 7.16 $\mu+3\sigma\ \tau_{max}$ **contours (lb/ft²) on horizontal cutting planes at heights of 75 ft ((a) and (b)) and 120 ft ((c) and (d)), (a) and (c) are for 1-D excitation (15 strips), (b) and (d) are for general excitations.**

increasing the number of strips. However, when using a 2-D shear beam model, the number of strips at the base would equal the number of wedge-type finite elements used along the length of the dam, and the analyst may as well consider correlation effects between all such strips.

7.3 Conclusion and Discussion

For the dynamic analysis of earth dams, the 2-D shear beam model exhibits slightly higher natural frequencies and has larger responses than the 3-D model. Similarly, for earthquake ground motion models, using the simplified 1-D excitation model discussed in this chapter gives rise to slightly larger displacement, stress and strain responses than using the general excitation model. As a consequence, the use of the 2-D shear beam model in conjunction with the simplified 1-D excitation model would be expected to yield reasonable and slightly conservative results at locations distant from the base.

For the prediction of stresses in the bottom half of the dam, especially in the stiff gravel, the simplified 1-D excitation significantly overestimates the response and is unacceptable. On the other hand, the use of identical excitation significantly underestimates the stress response when ground displacements are not highly coherent. Therefore, a 3-D model is required in order to predict stresses in the lower half of the dam accurately under SVEGM. However, it was shown in Section 5.3.6.3 that the use of static response component can approximate the stress response in the stiff gravel region well such that the time-consuming 3-D dynamic analysis can be avoided.

8. Conclusions and Recommendations

8.1 Summary and Conclusions

This research was conducted to study the effect of spatially varying earthquake ground motions (SVEGM) on the response of earth dams. The Santa Felicia earth dam was selected for analysis because it has been studied extensively and data was easily available for it. The Santa Felicia earth dam located on southern California is a modern rolled-fill embankment with a central impervious core and pervious shell upstream and downstream resting on a rigid bedrock. The dam is 83.8 m (275 ft) high above its rock foundation, 388.6 m (1,275 ft) long at the crest and 137.2 m (450 ft) long across the valley at the base. A three-dimensional inhomogeneous finite element model consisting of 1,004 nodes and 4,140 tetrahedral elements was used for the dam. The model was assumed to be symmetric about the middle of the dam axis. Shear modulus increasing with depth from the crest was used to account for the effect of confining pressure. A response convergence analysis indicated that eighty vibration modes were required to obtain accurate responses to earthquake excitation. A viscous damping ratio of 0.06 corresponding to low strain deformation was adopted for all modes.

In most cases, the SVEGM model proposed by Harichandran and Vanmarcke (1986), which accounts for both spatial correlation and wave propagation effects, was used to specify the base motions in the upstream/downstream direction. However, the effect of using coherency models proposed by other researchers was also investigated. The auto spectral density function of the ground acceleration estimated from the El Centro record with a root-mean-square intensity of 0.09g was used. The coherency decay was characterized by a double exponential function based on Event 20 recorded by the SMART-1 array in Lotung, Taiwan. An apparent wave velocity of 4,267 m/s corresponding to waves in the bedrock propagating at 2,134 m/s with an incident angle of 60° to the horizontal was assumed in the study. In addition, conventional simplified ground motion

models such as identical excitation and a simple propagating wave were also used so that the effect of SVEGM on earth dam responses could be evaluated. The effects of soil-structure interaction, hydrodynamic impact, radiation damping and topography were neglected in this study.

Stochastic moments of the displacement, stress and strain responses were computed and displayed as shaded image contours over the entire dam. SVEGM, characterized by wave propagation as well as by coherency loss, was found to have a significant impact on the responses of the dam, especially on the maximum shear stress in the stiff gravel in the streambed. A study of the reliability analysis against local failure characterized by the Mohr-Coulomb criterion further highlighted the significance of SVEGM. SVEGM can cause local failure in the granular streambed In addition to the core and shell material, thereby making a larger variety of sliding failure possible. However, the stress response due to SVEGM is very sensitive to the low frequency decay of the coherency used. The coherency model proposed by Abrahamson (1992), which is highly coherent at low frequencies, has very little effect on the stress response. It is therefore imperative that the current discrepancy in the low frequency coherency decay in different coherency models be investigated further and resolved. Finally, method of simplifying SVEGM excitation so that it can be used with a 2-D shear beam model of the dam is described. More detailed summaries are given below. Except for Section 8.1.6, in all other sections the Harichandran and Vanmarcke's coherency model was used to characterize the SVEGM.

8.1.1 Responses

Compared to SVEGM, the identical and delayed (wave propagation only) excitation models both overestimate the maximum three standard deviations (3σ) x-displacement response at the middle of the crest by about 8%. However, the contour patterns of the displacement responses are quite similar to each other for all the excitation cases. The two simplified excitation models both over-predict the critical mean plus three standard

deviations ($\mu+3\sigma$) maximum shear strain (γ_{max}) response by about 10%. As with the displacement response, the contour patterns are similar for all excitation models.

The critical $\mu+3\sigma$ maximum shear stress (τ_{max}) response in the stiff granular material at the base due to SVEGM is about 3.5 times larger than those due to identical and delayed excitations. In addition, the contour pattern of the τ_{max} response due to SVEGM differs greatly from those due to identical and delayed excitations. However, the effect of SVEGM is not very significant on flexible materials such as the core and shell. For these regions, the identical excitation model slightly overestimates the critical τ_{max} response. In addition, the τ_{max} response at the top free surface and the γ_{max} response at the base both are larger due to identical excitation compared to SVEGM. Although higher strains occur in flexible materials at the base, the larger stresses occur in the stiff gravel material because of the much higher shear modulus of the gravel.

8.1.2 Modal contributions

The dynamic response variances consist of individual modal response variances and covariance between pairs of modal responses. The relative modal contributions to the upstream-downstream displacement (x-displacement) at the middle point of the crest were examined. Basically, symmetric vibration modes contribute much more than anti-symmetric modes under SVEGM. Mode 1 dominates the dynamic variances with a contribution of more than 90% for all the critical displacement, stress and strain responses. Identical support motions on the other hand do not excite anti-symmetry modes at all.

8.1.3 Contribution of response components

The variance of the total response consists of three components: the variance of the pseudo-static response, the variance of the dynamic response, and the covariance between the pseudo-static and dynamic responses. For the 15 largest x-displacements, the dynamic response component contributes the most for all the excitation cases: general, identical and delayed excitations, but the other response components are also significant. For the 15

largest γ_{xy} responses which occur at the top free surface, the dynamic response component is dominant for all excitation cases and the pseudo-static and covariance components can be neglected.

The largest variance of τ_{xy} occurs at different locations for different excitation models. For the general excitation, the static component contributes the most to the largest τ_{xy} response. For delayed excitations with an apparent wave speed of 4.27 km/s, the static response is not significant, but the covariance between the static and dynamic responses becomes significant. Note that for identical excitation the static stress component is zero since this consists of a pure rigid body translation of the dam. Consequently, the covariance between the static and dynamic components is also zero, and the total stress response consists of only the dynamic component.

However, for the critical τ_{xy} response in the core region, the dynamic component overwhelms the static component for all excitation cases. On the other hand, for the τ_{max} responses in the base gravel layer due to general excitation, the pseudo-static component is dominant and the other two components can be neglected.

8.1.4 Reliability against local failure

As a simple illustration of the failure analysis of earth dams subjected to a combination of gravity loads and SVEGM, the reliability against local shear failure is assessed. The effective shear strength of soils is determined by the Mohr-Coulomb criterion and the static pore water pressure on the upstream side is accounted for. The reliability index against local failure was computed at each node and shown as shaded image contours over the entire dam for the identical and general excitations. The soils on the upstream and downstream surfaces and at around two-thirds the height of the dam violate the Mohr-Coulomb criterion due to identical excitation having a r.m.s. acceleration of 0.09g. For the SVEGM, the potential failure zones become larger, and include the base gravel material

because higher stresses occur in this region. Reasons why this simplistic illustration is likely to be over-conservative are discussed.

8.1.5 Effect of wave propagation

The wave passage effect is not so significant as coherency decay if the ground motion is significantly incoherent. In general, seismic waves with lower apparent velocities cause smaller displacements but result in larger stresses at the base due to out-of-phase motions. For upstream-downstream excitation, the responses to SV/P waves propagating in the upstream-downstream direction are more critical than for SH waves propagating in the longitudinal direction at the same apparent velocity. However, the critical responses due to these two kinds of waves do not occur at the same locations. SH waves cause the critical response locations to shift in the longitudinal direction. The shift is more significant for responses corresponding to lower SH wave speeds.

Variation of the incidence angle of the seismic waves within realistic limits (30° to 60° to the horizontal) did not significantly affect the responses in this study.

8.1.6 Effect of coherency function

In the last decade, a number of empirical coherency functions have been proposed based on strong motion records. In this study, in addition to Harichandran's model (1986), coherency functions proposed by Abrahamson (1993), Novak (1987), Luco & Wong (1986) and Hao (1989) models were also used to investigate the effect of the different models on the Santa Felicia dam.

The x-displacement response is not very sensitive to the coherency model. Higher coherency decay models give rise to smaller x-displacements. The largest difference between the critical 3σ x-displacements is about 10% (between Abrahamson's and Hao's Event 30 models). For the $\mu+3\sigma$ γ_{max} response, higher coherency decay models result in lower γ_{max}, but the largest difference between the critical $\mu+3\sigma$ γ_{max} values is about 12% (between Abrahamson's and Hao's Event 30 models).

Stress responses are very sensitive to the coherency functions. The τ_{max} response using Novak's model (which was fitted to Harichandran's model in this study) has the largest value among the models investigated. Hao's model calibrated to SMART-1 Events 45 and 30, respectively, yields τ_{max} responses that are closer to Harichandran's model which is calibrated to SMART-1 Event 20. Surprisingly, the τ_{max} response corresponding to Abrahamson's coherency model is very similar to that due to identical excitation. This is because the stress response at the base is dominated by low frequency excitations (i.e., ground displacements) while displacements and strains are governed by medium frequency motions. At frequencies less than 0.5 Hz, Abrahamson's model yields essentially unit coherency for most separations. Consequently, the $\mu+3\sigma$ τ_{max} response at the base are essentially the same as those due to identical excitation. Harichandran's and Hao's models yield significantly lower coherencies at lower frequencies than Abrahamson's model (i.e., ground displacements that are more incoherent), which is why they yield large stresses at the base. However, coherencies in the frequencies range from 0 to 0.5 Hz cannot be reliably estimated from data using conventional spectral analysis, and yet the coherency in this frequency range strongly affects the stresses in stiff material at the base. It is therefore extremely important to focus future research on accurately describing the coherency at low frequencies.

8.1.7 FOSM method for estimating the statistics of the maximum shear stress

The $\mu+3\sigma$ τ_{max} response at each node is non-linearly related to the Cartesian stresses, and its statistics were computed based on 10,000 Monte Carlo simulations. However, for more efficient computation, the first-order second-order (FOSM) method was also employed to approximately estimate the statistics of τ_{max}. The FOSM method using the square of each Cartesian stress component as the basic variable was found to be most suitable. The use of correction factors for the mean and standard deviation of τ_{max} enabled the FOSM estimates to be sufficiently accurate, but the correction factors needed to be calibrated using simulation results, which partially offset the computational saving of the

FOSM approach. Correction factors for the mean and standard deviation of τ_{max} of 1.04 and 0.95, respectively, for general excitation and 0.86 and 0.83, respectively, for identical excitation produced good results, but the optimal correction factors for the general excitation may change for different coherency parameters than the ones used.

8.1.8 Simplified ground motion excitation model

A finite element-based random vibration analysis of a 3-D earth dam model subjected to SVEGM is time-consuming and costly. Therefore, simplified modeling and analysis that is capable of yielding acceptable results were explored.

Attention was focussed on simplifying the excitation for use with a 2-D shear beam model which could at least represent the excitation incoherence along the length of the dam. The base of the dam was divided into several strips along the length of the dam to simulate the bases of truncated wedge elements of the 2-D shear beam model. To be consistent with each wedge element of a 2-D shear beam model having a single DOF, the excitation within each strip along the base was taken to be fully correlated. However, the ground motion between two different strips could be incoherent. The coherency between the excitations at two different strips was taken to be the coherency evaluated at the average separation between all pairs of points in the two strips. Since only separation in the longitudinal direction of the dam (perpendicular to the length direction of strips) was used to account for the incoherency effect, the simplified excitation model is called a 1-D excitation model.

Using the 1-D excitation model, the maximum 3σ x-displacement response is only 1.3% higher than that using the general SVEGM model, while the response due to identical excitation is 7.6% higher than that due to SVEGM. The maximum $\mu+3\sigma$ γ_{max} response is about 1.9% larger for the 1-D simplified model compared to the general model, while it is 10.3% higher for the identical excitation model. Apparently, the improvement on the displacement and γ_{max} responses using the 1-D excitation model is significant.

For the maximum $\mu+3\sigma$ τ_{max} response, the 1-D excitation model does not yield good results in the gravel material since it is very sensitive to the relative displacement between each pair of strips, but the predictions at locations away from the boundary are reasonable. The 1-D excitation model yields critical $\mu+3\sigma$ τ_{max} responses in the core as well as in the shell that are only 2% larger than that due to general excitation. Therefore, the use of a 2-D shear beam model in conjunction with the simplified 1-D excitation model would be expected to yield reasonable and slightly conservative results at locations distant from the base. To predict stress responses at the base in the gravel streambed, the pseudo-static component from a 3-D analysis can be used as long as ground displacements are not highly coherent because this component dominates the total response. As a result, in many cases a costly 3-D dynamic analysis can be avoided.

The effect of using a different number of strips on the base for the 1-D excitation model was evaluated. Models with 9, 15 and 21 strips were used in this study. It was found that the displacement, γ_{max} and τ_{max} responses using the 21-strip model, were all closer to those due to the general excitation than using the 9- and 15-strip models, except for the τ_{max} response in the gravel streambed. However, the improvement in the responses from the 9- to 21-strip models was not very significantly. In general, when using a 2-D shear beam model, accuracy considerations would govern the discretization along the length of the dam and more than 9 elements would be expected at the base.

8.2 Recommendations for future research

8.2.1 Topographic effects

This research is restricted to assessing the effect of spatial variation due to incoherence and global wave propagation effects on earth dam responses. It is well known that SVEGM can also occur due to amplification of ground motions that is dependent on the canyon shape, the relative rigidities of the canyon and the dam, and the type of excitation wave (SH, SV, P, Rayleigh, etc.). In general, intensity and phase variations due

to topographic effects should be combined with the spatial variation due to incoherence effects when specifying the input motions at the base of the dam.

8.2.2 2-D shear beam model and SVEGM

In Chapter 7, techniques to simplify the general SVEGM model to a 1-D excitation model that can be used with a 2-D shear beam model of the dam are proposed. The simplified excitation model was used with the 3-D finite element model of the dam, and the results were found to be slightly conservative but acceptable for most responses. Although the proposed excitation model should be applicable to a 2-D shear beam model, a 2-D shear beam model of the dam was not actually used. The use of 2-D shear beam models for earth dams subjected to conventional excitation models has been found to cause slightly higher natural frequencies and larger responses than 3-D models and hence conservative results are expected. However, this postulate should be verified by investigating the responses of a 2-D shear beam model excited by the simplified 1-D SVEGM model.

8.2.3 Nonlinear analysis

In reality, soil exhibits nonlinear hysteretic behavior. When large responses occur under strong ground motion, linear random vibration analysis might not be adequate for predicting the dam response. The restoring force of a hysteretic system depends not only on the instantaneous displacement but also on its past history. For lightly damped systems, the method of equivalent linearization including the effects of strain-dependent shear modulus may be used for an approximate solution by performing iterative analysis.

8.2.4 Dynamic pore water pressure

Increasing pore water pressure during an earthquake may affect the stability of earth dams significantly. More realistic models of the saturated granular soil, account for the two-phase fluid-solid mixture, can be used to account for the build-up of pore water pressure during the dynamic response. The use of such advanced models with SVEGM input may yield insight into the effect of SVEGM on liquefaction failure.

APPENDICES

APPENDIX A

Outline of the Use of I-DEAS VI.i Computer Software

A.1 Introduction

The I-DEAS families including *Solid_Modeling*, *FE_Modeling_&_Analysis* and *System_Dynamics_Analysis* were used in the modeling and analysis of the Santa Felicia dam. Each one offers a set of interactive, graphically-oriented tasks.

- *Solid_Modeling*: The Solid Modeling application offers a full range of tools needed to develop geometric concepts and detailed mechanical designs for parts, assemblies, and mechanism.
- *FE_Modeling_&_Analysis*: I-DEAS Finite Element Modeling (FEM) is a mechanical design automation tool which can be used to build a complete finite element model, including physical and material properties, loads, and boundary conditions. With FEM, the linear statics and dynamics behavior of mechanical component and structures can be modeled and analyzed.
- *System_Dynamics_Analysis*: The System Dynamics Analysis family is an interactive, graphically-oriented system modeling and analysis module which can be used to simulate the dynamic response of complex mechanical systems. This application evaluates the dynamic performance in terms of modal, frequency, and transient response of interconnected linear systems.

A.2 Finite Element Modeling Procedures

The Santa Felicia earth dam was modeled as a three-dimensional inhomogeneous finite element model using I-DEAS VI.i. The following is a brief description of the modeling procedures:

1. The *Solid_Modeling/Object_Modeling/Create* command was used to generate a block for each material zone, and *Construct/Cut* was used to trim its dimension to

match the geometry of the dam. Twenty-two objects are needed to satisfy the discretization requirement for elements with different material properties. Since the dam is assumed to be symmetric about the mid-plane of the dam axis, only half of the dam is generated as shown in Fig. A.1.

2. The *Solid_Modeling/Assembly_Modeling/Create* command was used to put together parts which were modeled and stored as objects into a system. Because each object was created according to its own coordinate system, some orientations to desired location need to be done in the assemblage of these parts to an entire dam model.

3. The *FE_Modeling_&_Analysis/Geometry_Modeling/Surface/Create* command was used to import the dam system from the solid modeling module to the FE module. In this step, the default for the *Model_file/Tolerances/Point_Coincidence* needed adjustment to avoid dangerously large or unnecessarily tight tolerances.

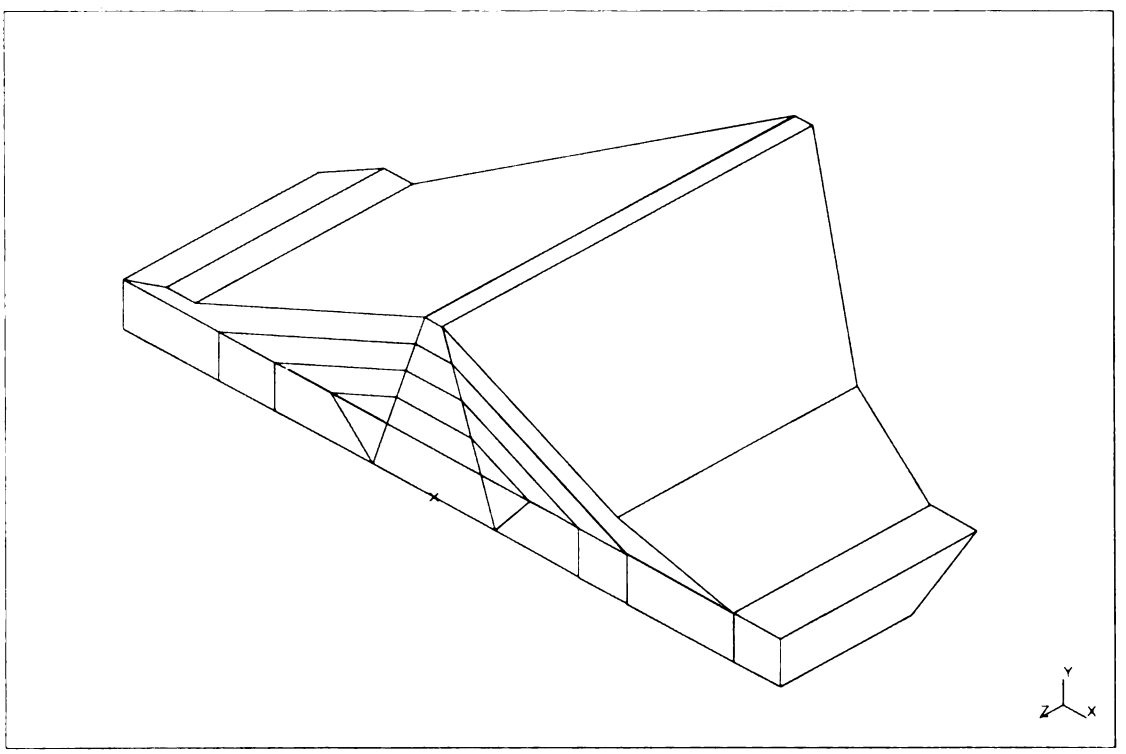

Figure A.1 Display of half of the Santa Felicia dam model consisting of twenty-two objects

4. The *Mesh_Creation/Mesh_Areas* and *Mesh_Creation/Mesh_Volume* commands were used to create mesh areas and mesh volumes, respectively. The *Mesh_Creation* task can automatically apply free meshing to the geometry as it is extracted from solid objects or assemblies. Material properties were defined for each volume at this stage.
5. The *Mesh_Size/Free_Meshing/Settings* command was used to specify global element sizes, and the *Generate_Mesh/Solids* command was used to generate the finite element mesh. Linear tetrahedral solid elements were used throughout.
6. Coincident nodes lying on the interfaces of the various assembled objects were merged to obtain a single monolithic model. Nodes were renumbered for convenience. After these steps it was necessary to reload the graphics database using the *Model_File/Reload_Graphics_Db* command.
7. The *FE_Modeling_&_Analysis/Boundary_Conditions/Restraints* command was used to specify boundary conditions. The nodal degrees of freedom (DOF) for solid elements consist of the three translation components (X, Y and Z translations) and these were all restrained at the nodes on the boundary between the dam and the canyon.

A.3 Steps for Free Vibration Analysis

Free vibration analysis of the Santa Felicia dam model was performed using I-DEAS so that its natural frequencies and vibration modes were obtained. Subsequent to the finite element modeling procedures described in the last section, the following steps were used to perform a free vibration analysis:

1. The *Case_Management/Create* command was used to generate a case set. For free vibration analysis, the case set includes only restraint conditions.
2. The *Model_Solution/Normal_Mode_Dynamics/Case_Set* command was used to specify the case set to be used.

3. The *Method/Simult_Vector_Iterati/Solution_Control* command was used to define the number of flexible modes to be solved.
4. Modes, Stresses and Strains were selected for output. This yielded the stresses and strains corresponding to each mode.

A.4 Deterministic Dynamic Analysis

The steps using I-DEAS VI.i to conduct deterministic dynamic analysis are briefly described below.

1. The *FE_Modeling_&_Analysis/Boundary_Conditions/Restraints* command was to set the upstream-downstream DOF at the nodes on the boundary to be free, and the *Dof_Sets* command was used to define these as kinematic DOF. In I-DEAS VI.i, enforced motion can only be applied along kinematic DOF.
2. The *Solution/Control* command was used to specify the case set to be used and the number of rigid body modes. The *Normal_Mode_Dynamics* command was used to perform modal analysis.
3. The *Component_Definition/Create_Component/Analytical_modal* command in the *System_Dynamics_Analysis* module was used to import analytical modes from the *FE_Modeling_&_Analysis* module. Damping ratios were specified at this step.
4. The *System_Definition/Components/Degrees_of_Freedom/Physical* command was used to restrain all kinematic DOFs.
5. The *System_Solution/Transformation_Method* command was used to solve damped vibration modes.
6. The *Excitation_Definition/Functions* command was used to create an acceleration excitation function at the restrained nodes. The time history of velocity and displacement were obtained from the acceleration function using the *Integrate* command.

7. The *Load_Cases* command was used to combine acceleration, velocity and displacement functions into a load case.
8. The *Response/Modal_Properties/Mode_Shapes* command was used to activate the number of vibration modes used in the enforced motion analysis. The load case in step 7 was set to be active using *Response/Load_Set*.
9. The *Response_DOF_Sets* command was used to select component entities and physical DOF at nodes where responses were to be evaluated.
10. The *Evaluate/Options/Limits/Time* command was used to specify the desired length of the responses. The types of responses were defined using the *Response_Form* command and the analysis was performed using the *Evaluate/Response* command.

A.5 Generating [M] and [A] Matrices

In I-DEAS, the mass matrix $[M_{FF}]$ in equation (4.17) corresponding to DOF is identical to the matrix $[M_{II}]$ corresponding to independent DOF, and $[M_{FR}]$ is identical to $[M_{IS}]$. Program files written in a special language are used in I-DEAS to drive each type of computation. By modifying these program files, intermediate or specialized results can be output. The program files and modification are briefly described below:

1. Copy files nbb42.prg and svi.prg from I-DEAS programs library directory to the directory in which normal mode analysis will be performed.
2. Edit the file nbb42.prg so that it calls the local copy of svi.prg, instead of svnores.prg. Change the lines

```
C : TO RUN A USER DEFINE PROGRAM FILE CHANGE "HMPACK" TO
"MODEL_FILE"
C : IN THE FOLLOWING LINE
K : /HMPACK PROGRAM_FILE RUN
K :                    "SVNORES.PRG"
```

To:

```
K : /MODEL_FILE PROGRAM_FILE RUN
K :                    "SVI.PRG"
```

3. Edit the file svi.prg to write the mass matrix MII immediately after EIGENRAT.PRG is called, because in the process of checking orthogonality ratios and eigenratios MII is deleted. After the first line shown, add the remaining lines that follow in the boxed section below:

```
C : CALCULATE AND LOG ORTHOGONALITY RATIOS AND EIGENRATIOS
    ....
C : ------------------------------------------------
C : WRITE MASS MATRIX MII
C :   TO UNIV FILE MII.UNV
C : ------------------------------------------------
K : /LOG MESSAGE "Writing mass matrix MII to file"
K : /HMPACK UNIVERSAL_FILE WRITE_READABLE MII
K :  " MII.UNV "
```

4. Edit the file svi.prg to write MIS immediately after SREACT.PRG is called. In the process of computing reaction forces, MIS is deleted. After the first line shown, add the remaining lines that follow in the boxed section below:

```
C : CALCULATE REACTION FORCES
    ....
C : ------------------------------------------------
C : WRITE MASS MATRIX MIS
C :   TO UNIV FILE MIS.UNV
C : --------------------------------
K : /LOG MESSAGE "Writing mass matrix MIS to file"
K : /HMPACK UNIVERSAL_FILE WRITE_READABLE MIS
K :  " MIS.UNV "
```

5. Run the normal mode solution. Use the *Execution_Options* command, turn off profile reduction so that the mass matrix components will be sequenced using the

user-specified node numbers. By default I-DEAS internally renumbers nodes to minimize the bandwidth of the stiffness matrix and this shuffles the elements of the mass matrix. Since the mode shape matrix and displacement vector are output according to the user-specified node number sequence, the elements of the mass matrix must be consistent with these.

6. Use the simultaneous vector iteration method and select the *User_Defined* method. The program will prompt for the name of the program file to run. Enter the name given to the copy of nbb42.prg.
7. Use the *Output_Selection* command to select reaction forces as well as vibration modes, because MIS is created only when the reaction forces are selected for output.
8. Watch the solution log to ensure that the proper version of the program runs, and that the mass matrix is written. If the files are edited at the wrong locations, a message saying that the MII and/or MIS matrix does not exist will usually be reported.
9. The universal files MII.UNV and MIS.UNV contain the mass matrices. The format of these files is documented in the *Model Solution Manual*, in the *Open Architecture* section. It should be noted that SI units are used in these files. If the model file is based on other units, appropriate conversion of units is necessary.

The $[A]$ matrix is expressed as $[A] = -[K_{FF}]^{-1}[K_{FR}]$ in equation (4.9). Each column of $[A]$ consists of the deformed shapes of the model subjected to a unit displacement at each restrained node. The $[A]$ matrix can be obtained directly in I-DEAS using static constraint analysis, and hence there is no need to obtain the stiffness matrices and invert $[K_{FF}]$. The following steps are used to obtain the $[A]$ matrix:

1. Since only upstream-downstream excitation (x-direction) is considered, the unit displacements are applied only in this direction at the boundary nodes. All

x-translation DOFs of restrained nodes were set to be active using the *Boundary_Conditions/Dof_Sets* command, and then defined to be connection DOF using the *Case_Management* command. The other two translation components (y and z components) are kept restrained.

2. The *Model_Solution/Constraint_Mode_Dynamics* command was used to select the case set specified in step 1. The other procedures are similar to those in normal mode analysis. Since displacement, stress and strain responses are of interest, all of these were selected for output. It is of interest to note that the stress or strain output file occupied about 500 MB of storage space.
3. Stress and strain constraint modes are computed for each element. The average of the element stresses and strains at nodes from adjacent elements was used to represent the nodal stresses and strains. A computer program was written to extract the nodal values from the I-DEAS output files.
4. It should be noted that the static constraint modes are derived corresponding to a one meter displacement at connection DOF. If the model uses other units, the output should be converted appropriately.

A.6 Techniques to Display Response Contours

The *Manage_Models* command in the I-DEAS *Finite Element Modeling* family can be used to read and write universal files. Universal files provide a means of passing data in and out of I-DEAS model files. An I-DEAS universal file is a sequential formatted file consisting of one or more I-DEAS universal datasets. An universal dataset is a group of records that define the properties of an I-DEAS entity such as a profile or a point. The I-DEAS *Core Utilities User's Guide* documents the record format for each type of universal dataset. In order to display response contours through I-DEAS, the first step is to write nodal response values in the format required for the universal file. Fig. A.2 shows a partial dataset of a typical displacement file.

```
-1
  151
/usr/hpideas_tmp/chenm/con/contour
Santa Felicia Earth Dam
SDRC I-DEAS VI.i: Monitor
05-DEC-94  11:04:49       6       0
Never    Never
SDRC I-DEAS VI.i: FE_Modeling_&_Analysis
05-DEC-94  12:46:50
  -1
  -1
  164
     2British grav             2
 3.28083989501312330E+00 2.24808943099710450E-01 1.80000000000000000E+00
 4.59670000000000000E+02
  -1
  -1
  800
     1
WORKING_SET1
  -1
  -1
  770
     1       0
MAIN
  -1
  -1
  771
     1       1       1
FE MODEL1
  -1
  -1
  55
General Excitation (3SD)
Model Solution
NONE
The time of Analysis was   05-DEC-94      11:33:41
NONE
     1       2       3       8       2       6
     2       3       0       0
 0.00000E+00 3.43029E+08 0.00000E+00
     1
  .28800E+00  .00000E+00  .00000E+00  .00000E+00  .00000E+00  .00000E+00
     2
  .28800E+00  .00000E+00  .00000E+00  .00000E+00  .00000E+00  .00000E+00
     3
  .28800E+00  .00000E+00  .00000E+00  .00000E+00  .00000E+00  .00000E+00
  . . .
```

Figure A.2 Partial dataset of an universal file

The upper part (the first line down to the seventh line from the bottom shown) can be reproduced by copying it from any contour universal file written from within I-DEAS. The remaining part specifies nodal numbers and nodal values, which have been replaced by the values of the mean plus three standard deviations of the displacement, stress or strain responses in order to display contours of these quantities. Using I-DEAS, the modified universal file is read back to create a new analysis dataset. Subsequently, contours of the new data component can be displayed using the *Post_Processing* command. I-DEAS assumes that the values read from the universal file are the six displacements at each node, but this is of no real significance.

A.7 Gravity-induced Stresses

The stresses due to gravity were obtained using the following steps:

1. The finite element model and restraint boundary condition used for the free vibration analysis were used.
2. The *Boundary_Conditions/Structural_Loads/Acceleration_Load/Create* command was used to apply an acceleration vector of $1g$ in the vertical direction. An acceleration vector represents the loading effects from the acceleration on the entire model.
3. The *Case_Management/Modify* command was used to add the acceleration load to the case set.
4. The *Linear_Statics* command was used to solve the static loading problem and the stress response was selected for output.

APPENDIX B

Comparison between Seismograph Records and Computed Responses for the Northridge Earthquake of January 17, 1994

The Northridge earthquake having a magnitude of M = 6.7 occurred at 4:30 am (PST) on January 17, 1994 under the north-western end of the San Fernando Valley, Los Angeles. The epicenter location determined by the U.S. Geological Survey is 34.213 N and 118.537 W, with a focal depth of 18.4 km. The Northridge earthquake was recorded by two seismographs located on the Santa Felicia dam; one on the downstream abutment and the other on the crest of the dam (Stewart et al. 1994). Fig. B.1 shows the location of the seismographs and directions in which the ground accelerations were recorded. The instrument and baseline-corrected acceleration, velocity and displacement in the upstream-downstream (U-D) direction at the downstream station are shown in Figs B.2, B.3 and B.4, respectively. The peak U-D acceleration is 0.27g.

The U-D ground motion recorded at the downstream station was used as input to the 3-D finite element model of the dam and the response at the node (x = 15 ft, y = 275 ft, z = -71 ft) closet to the crest station was computed. Fig. B.5 shows the recorded and computed displacement responses due to U-D excitation only. The station at the crest triggered 1.18 seconds before the downstream station, and hence the recorded motions were translated to the left by 1.18 seconds. Although the peak displacements are in reasonable agreement, the computed response has many more oscillations than the recorded response indicating that the assumed modal damping ratio of 0.06 is too low.

In reality, the Northridge earthquake ground motion contains three components in the upstream-downstream, vertical and longitudinal directions. To examine the adequacy of the earth dam model, all three recorded components at the downstream station were applied as excitations at those nodes on the boundary between the dam and the bedrock. Fig. B.6

Lake Piru - Santa Felicia Dam
(CSMIP Station No. 24280)

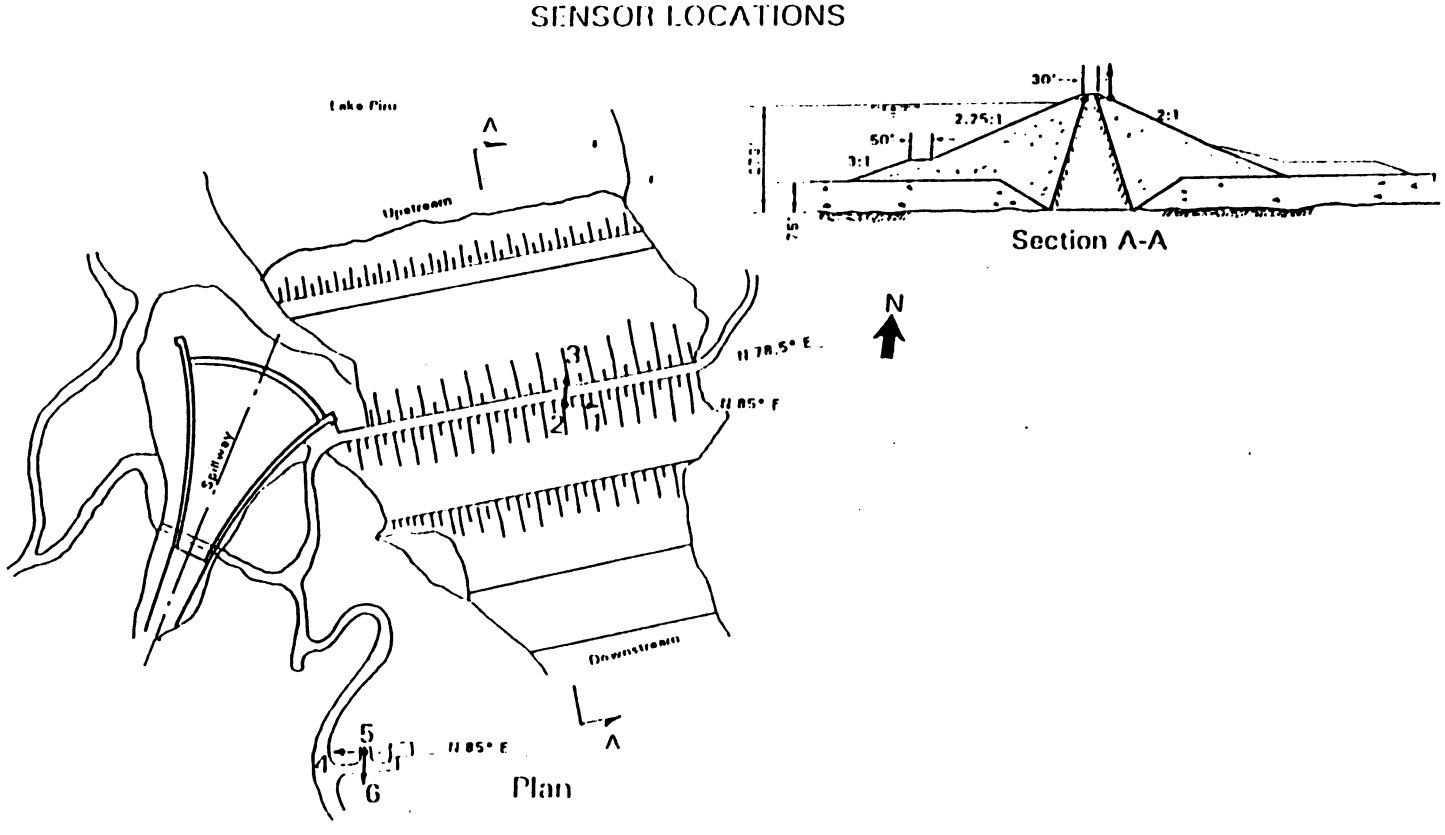

Figure B.1 Locations of the recorders on the Santa Felicia dam

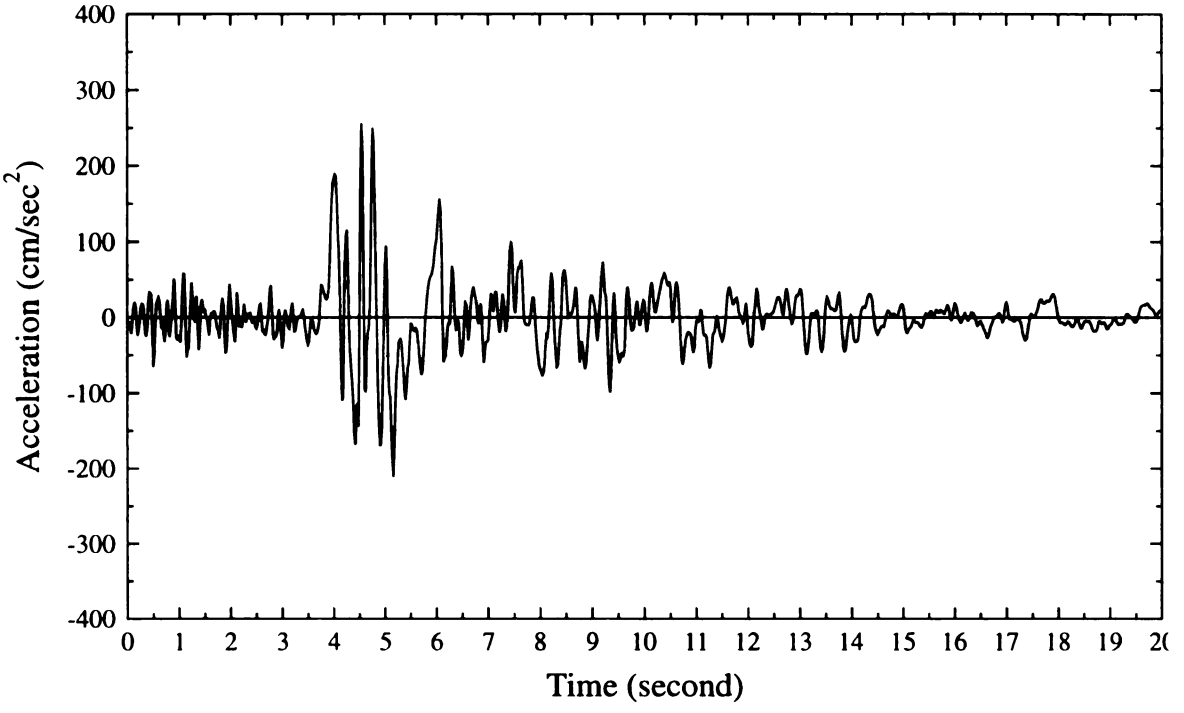

Figure B.2 Ground accelerations of Northridge earthquake in the upstream-downstream direction

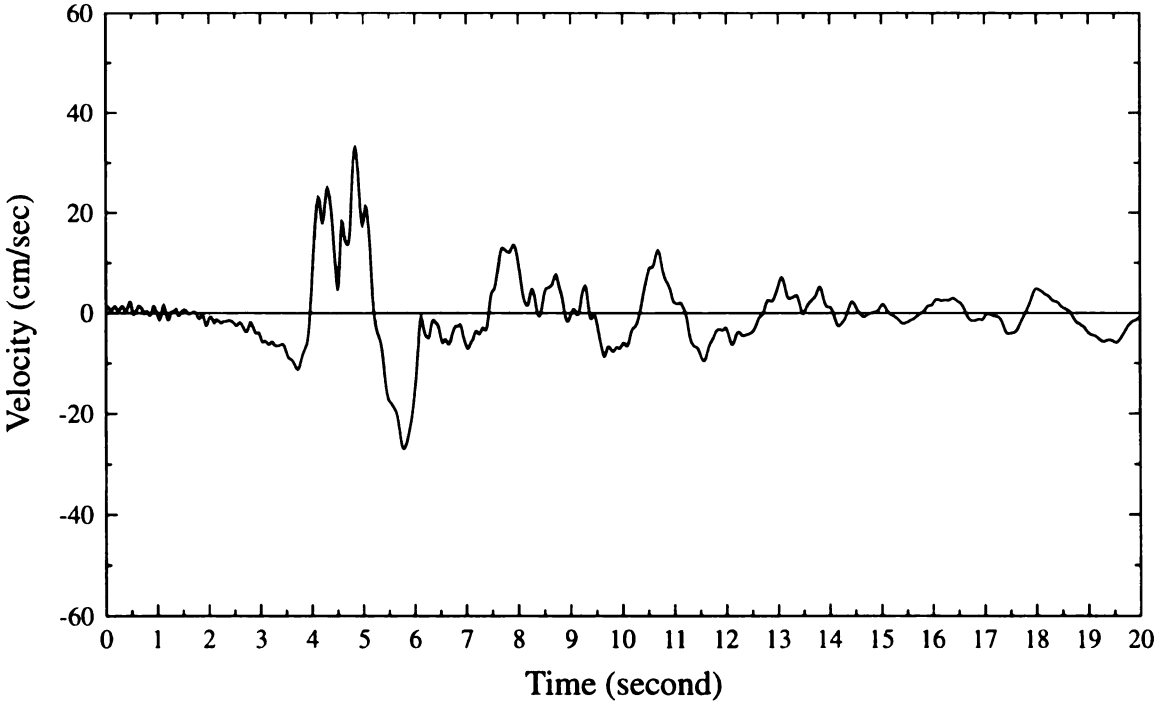

Figure B.3 Ground velocities of Northridge earthquake in the upstream-downstream direction

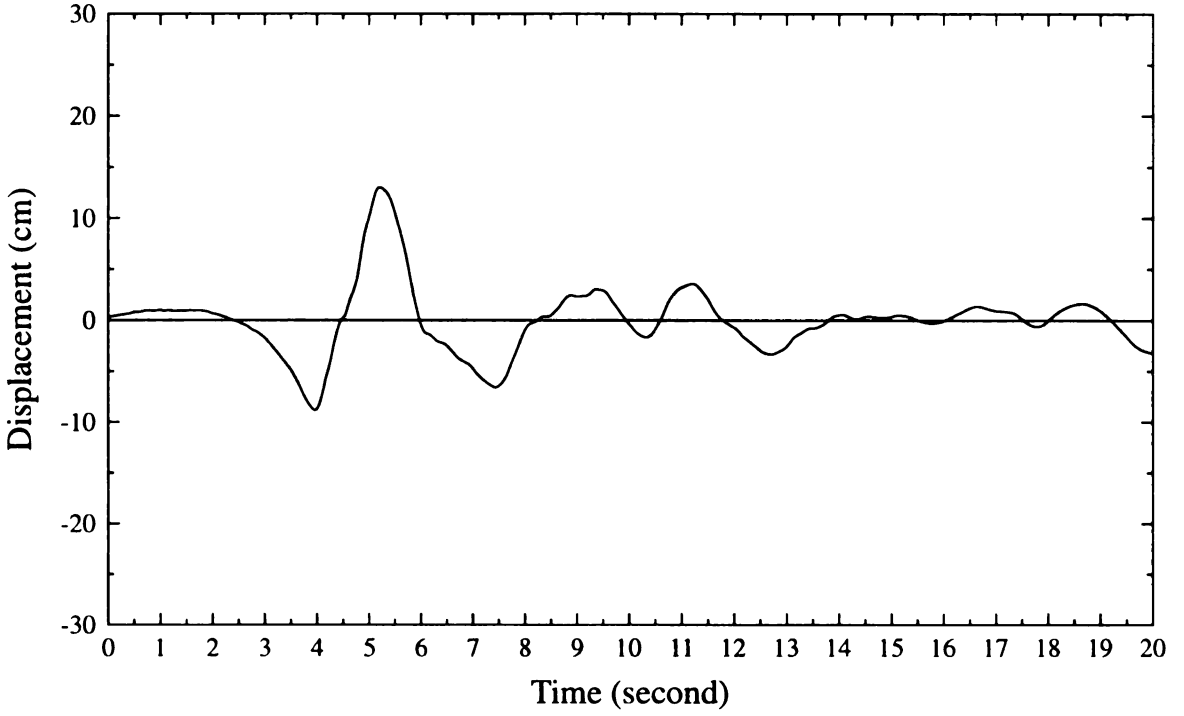

Figure B.4 Ground displacements of Northridge earthquake in the upstream-downstream direction

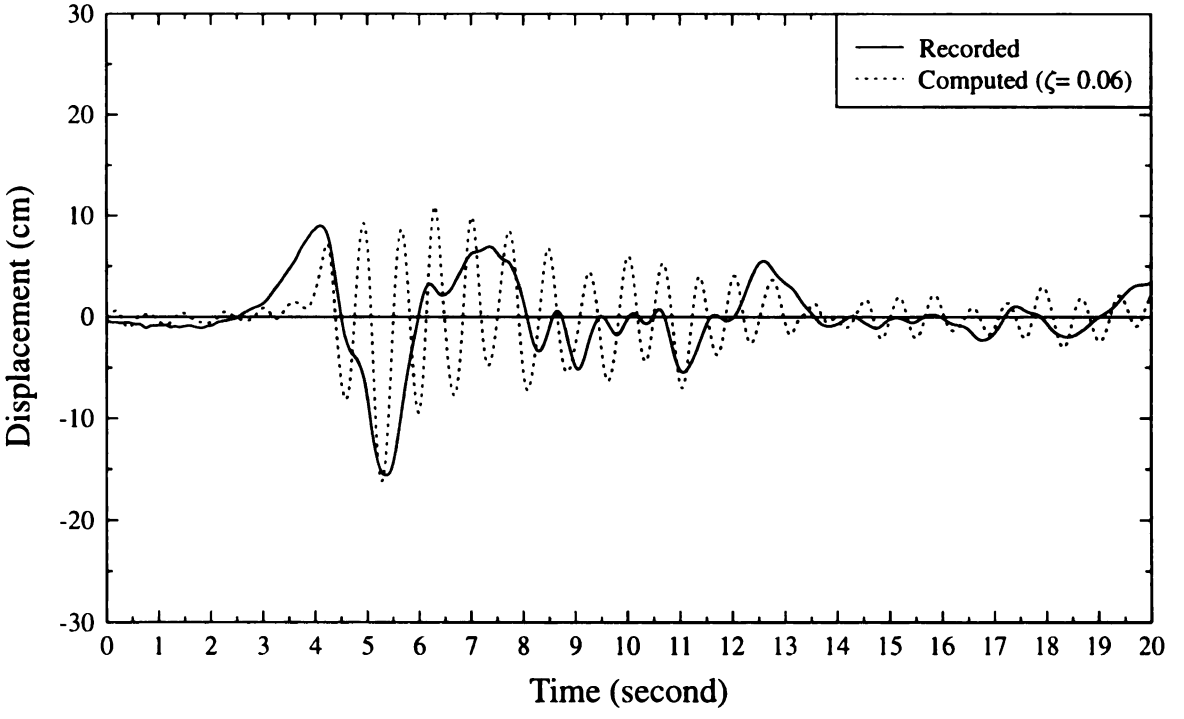

Figure B.5 Comparison of upstream-downstream displacement records at the crest with computed response due to upstream-downstream excitation

shows the time history of computed U-D displacement at the crest corresponding to modal damping ratios of 0.06 and 0.25. It is seen that the displacement corresponding to a damping ratio of 0.06 is higher for each vibration cycle than that corresponding to a damping ratio of 0.25, and both responses are higher than the recorded response shown in Fig. B.5. Fig. B.7 shows the response computed using a modal damping ratio of 0.45 as well as the recorded displacement, and the two are in reasonable agreement although the computed peak response is a little higher. Figs. B.8 and B.9 show the computed and recorded velocity and acceleration traces, which also agree reasonably well. It appears therefore that a modal damping ratio of 0.45 is more appropriate for the level of excitation imparted by the Northridge earthquake. The Northridge data became available after most of the research described in this study (which is based on a modal damping ratio of 0.06) was completed.

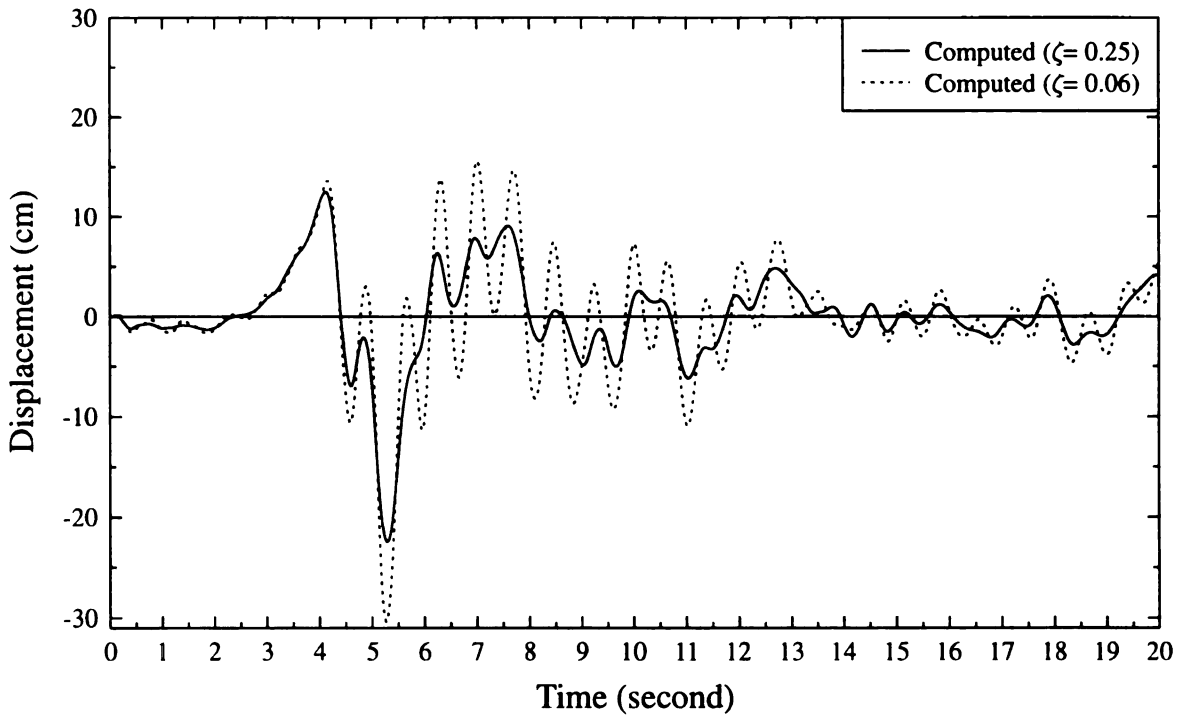

Figure B.6 Comparison between the computed upstream-downstream displacement responses at the crest of the dam having damping ratios of 0.25 and 0.06.

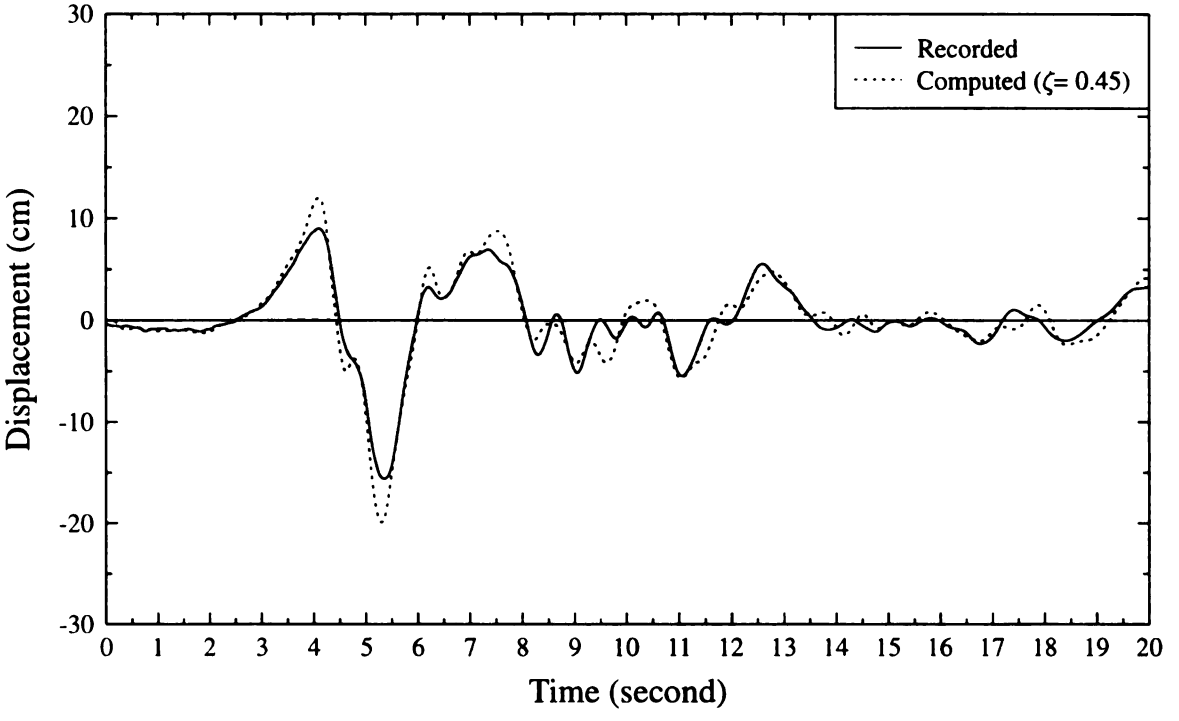

Figure B.7 Comparison between computed displacement response of Santa Felicia dam with a damping ratio of 0.45 and seismograph records

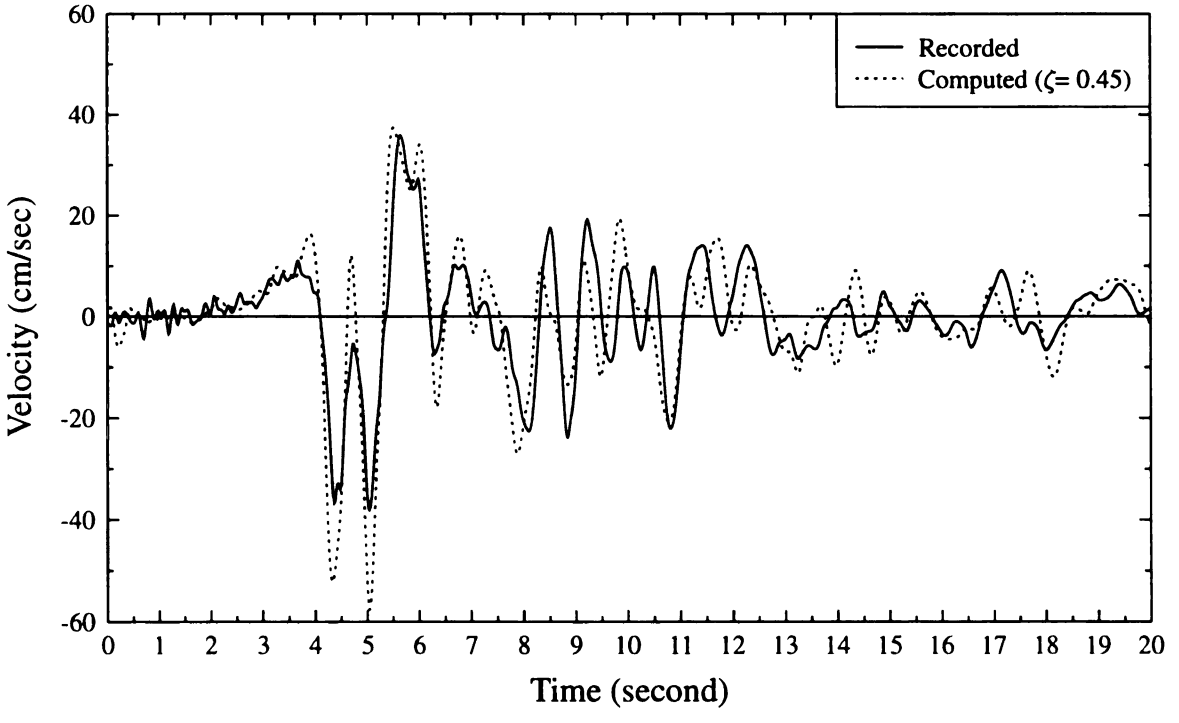

Figure B.8 Comparison between computed velocity response of Santa Felicia dam with a damping ratio of 0.45 and seismograph records

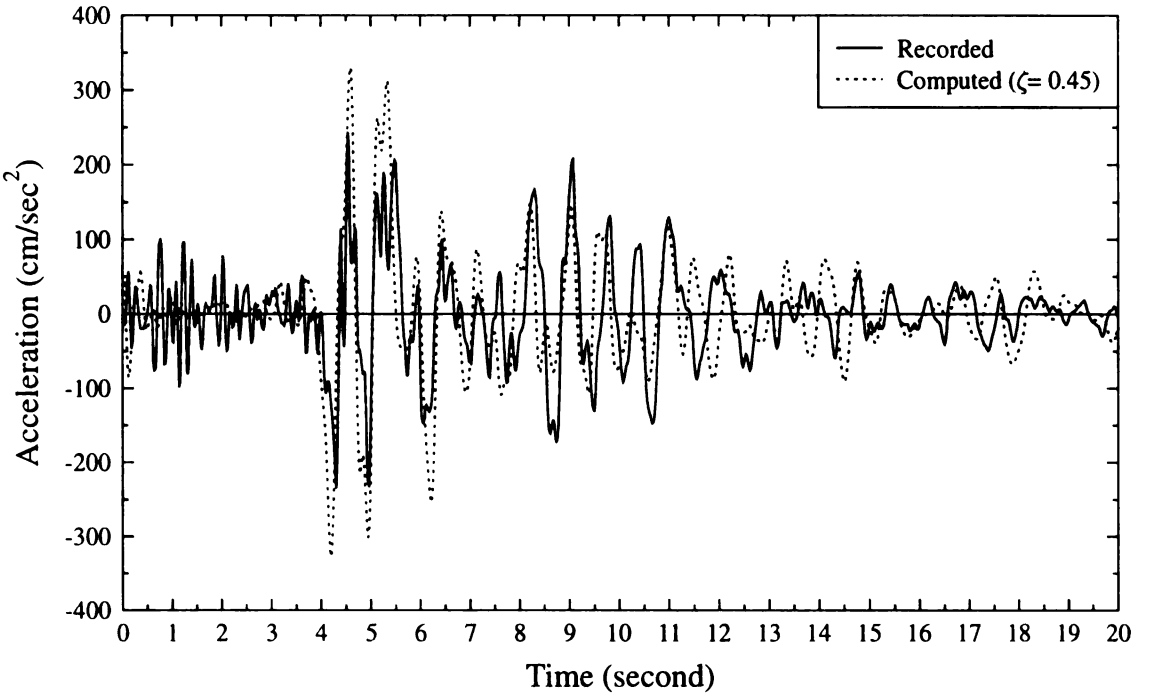

Figure B.9 Comparison between computed displacement response of Santa Felicia dam with a damping ratio of 0.45 and seismograph records

The maximum U-D displacement, velocity and acceleration for all the cases investigated in this study are given in Table B.1. The best agreement is obtained for the three-component excitation and a modal damping ratio of 0.45.

TABLE B.1 Critical computed and recorded responses of the Santa Felicia dam at the crest to the Northridge earthquake

Response type (Upstream/ downstream)	Upstream/ downstream excitation only (ζ =0.06)	Three-component excitations			Recorded
		ζ = 0.06	ζ = 0.25	ζ = 0.45	
Displacement (cm)	16.2	30.4	22.6	19.8	15.6
Velocity (cm/sec)	125	155	82.3	57.9	38.1
Acceleration (cm/sec^2)	1024	1039	485	326	243.8

BIBLIOGRAPHY

BIBLIOGRAPHY

Abdel-Ghaffar, A. M. and Scott, R. F. (1979a). "Analysis of Earth Dam Response to Earthquake," *Journal of the Geotechnical Engineering Division, ASCE*, 105 (12), 1379-1404.

Abdel-Ghaffar, A. M. and Scott, R. F. (1979b). "Shear Moduli and Damping Factors of an Earth Dam," *Journal of the Geotechnical Engineering Division, ASCE*, 105 (12), 1405-1426.

Abdel-Ghaffar, A. M. and Scott, R. F. (1981a). "Vibration Test of Full-scale Earth Dam," *Journal of the Geotechnical Engineering Division, ASCE*, 107(3), 241-286.

Abdel-Ghaffar, A. M. and Scott, R. F. (1981b). "Comparative Study of Dynamic Response of Earth Dams," *Journal of the Geotechnical Engineering Division, ASCE*, 107(3),271-286.

Abdel-Ghaffar, A. M. and Koh, A. S. (1982). "Three-dimensional Dynamic Analysis of Non-homogeneous Earth Dams," *Soil Dynamic and Earthquake Engineering*, 1, 136-144.

Abdel-Ghaffar, A. M. and Elgamal, A. M. (1987). "Elasto-plastic Seismic Response of 3-D Earthdam:Theory," *Journal of the Geotechnical Engineering Division*, 113 (11), 1293-1308.

Abrahamson, N. A., Schneider, J. F. and Step, J. C. (1990). "Spatial Variation of Strong Ground Motion for Use in Soil-structure Interaction Analyses," *Proceedings of the Fourth National Conference on Earthquake Engineering*, May 20-24, Palm Springs, California, 317-326.

Abrahamson, N. A. (1992). "Spatial Variation of Earthquake Ground Motion for Application to Soil-Structure Interaction," Electric Power Research Institute, TR 100463.

Abrahamson, N. A. (1993). "Spatial Variation of Multiple Support Inputs," *Proceedings of the first U.S. Seminar*, Seismic Evaluation and Retrofit of Steel Bridges, University of California at Berkeley, Department of Civil Engineering and California Department of Transportation, Division of Structures, San Francisco.

Ambraseys, N. N. and Sarma, S. K. (1967). "The Response of Earth Dams to Strong Earthquakes," *Geotechnique*, 17(3), 181-213.

Chopra, A. K. (1967). "Earthquake Response of Earth Dam," *Journal of the Soil Mechanics and Foundation Division, ASCE*, 93, SM2.

Chopra, A.K. and Gupta, S. (1981). "Hydrodynamic and Foundation Interaction Effects in Earthquake Response of a Concrete Gravity Dam," *Journal of Structural Division, ASCE*, Vol 107, 1399-1412.

Chopra, A. K. and Perumalswami, P. R. (1969). "Dam-foundation Interaction during Earthquake," *Proc. 4th World Conf. on Earthq. Engrg.*, Santiago.

Clough, R.W. and Chopra, A. K. (1966). "Earthquake Stress Analysis in Earth Dams," *Journal of the Engineering Mechanics Division, ASCE*, 92(EM2).

Clough, R. W. and Penzien, J. (1975). *Dynamics of Structure*, McGraw-Hill, New York.

Commission on Engineering and Technical Systems - Committee on Earthquake Engineering (1985). "Liquefaction of Soils during Earthquakes," *National Academy Press*, Washington, D.C.

Das, B. (1993). *Principles of Soil Dynamics*, PWS-KENT publishing company, Boston.

Dakoulas, P. and Gazetas, G. (1985). "A Class of Inhomogeneous Shear Models for Seismic Response of Dams and Embankments," *Soil Dynamics and Earthquake Engineering*, 4(4), 166-182.

Dakoulas, P. and Hashmi, H. (1992). "Wave Passage Effect on the Response of Earth Dams," *Soils and Foundations*, 32(2), 97-110.

Der Kiareghian, A. (1980). "Structural Response to Stationary Excitation," *Journal of Engineering Mechanics, ASCE*, 106(6), 1195-1213.

Desai, C. S. and Abel, J. F. (1972). *Introduction to the Finite Element Method*, Van Nostrand Reinhold Company, New York.

Dibaj, M. and Penzien, J. (1969). "Response of Earth Dams to Travelling Seismic Waves," *J. Soil Mech. and Found. Div., ASCE*, 95, SM2.

Dunlop, P. and Duncan, J. M. (1970). "Development of Failure around Excavated Slopes," *Proc. ASCE, Journal of Soil Mechanics and Foundation Division*, Vol. 96, SM2.

Elgamal, A.-W. M., Abdel-Ghaffar, A. M. and Prevost, J. H. (1984). "Nonlinear Earthquake Response Analysis of Earth Dams," Princeton Univ. *Research Report.*

Elgamal, A.-W. M. and Abdel-Ghaffar, A. M. (1987). "Elasto-plastic Seismic Response of 3-D Earthdam:Application," *Journal of the Geotechnical Engineering Division*, 113 (11), 1309-1325.

Ernesto Motta, M. M. and Zeng. (1993). "The Effect of Travelling Seismic Waves on the Dynamic Response of Earth Dams," *Soil Dynamics and Earthquake Engineering*, 12, 61-72.

Farmer, I. W. (1968). *Engineering Properties of Rocks*, E. & F. N. Spon L.T.D., London.

Gasparini, D. A. and Sun, W. J. (1982). "Random Vibration Analysis for the Seismic Response of Earth Dams," *Soil Dynamic and Earthquake Engineering*, Cakmak, A. S. et al. (eds.).

Gazetas, G. (1980). "2-Dimensional Lateral and Longitudinal Seismic Stability of Earth and Rockfill Dams," *Proc. 7th World Conf. Earthq. Engrg.*, Instanbul, 1980, 8, 109-116.

Gazetas, G. (1981). "Longitudinal Vibration of Embankment Dams," *Journal of the Geotechnical Engineering Division, ASCE*, 107(GT1), 21-40.

Gazetas, G., Debchaudhury, A. and Gaspirani, D. A. (1981). "Random Vibration Analysis for the Seismic Response of Earth Dams," *Geotechnique*, 1(2), 261-277.

Gazetas, G., Debchaudhury, A. and Gaspirani, D. A. (1982). "Stochastic Estimation of Nonlinear Response of Earth Dams to Strong Earthquakes," *Soil Dynamic and Earthquake Engineering*, 1(1), 39-46.

Gazetas, G. (1987). "Seismic Response of Earth Dams: Some Recent Developments," *Soil Dynamics and Earthquake Engineering*, 6(1), 2-47.

Ghaboussi, J. and Wilson, E. (1973). "Seismic Analysis of Earth Dam-reservoir Systems," *Journal of the Soil Mechanics and Foundation Division, ASCE*, 99,SM10, 849-862

Hao, H. (1993). "Arch Responses to Correlated Multiple Excitations," *Earthquake Engineering and Structural Dynamics*, 22, 389-404.

Hao, H., Oliveira, C. S. and Penzien, J. (1989). "Multiple-station Ground Motion Processing and Simulation based on SMART-1 array data," *Nuclear Eng. Design*, 111, 293-310.

Harichandran, R. S. and Vanmarcke, E. H. (1986). "Stochastic Variation of Earthquake Ground Motion in Space and Time," *Journal of the Engineering Mechanics, ASCE*, 154-174.

Harichandran, R. S. (1987). "Stochastic Analysis of Rigid Foundation Filtering," *Earthquake Engineering and Structural Dynamics*, 15(7), 889-899.

Harichandran, R. S. and Wang, W. (1990). "Response of Indeterminate Two-span Beam to Spatially Varying Seismic Excitation," *Earthquake Engineering and Structural Dynamics*, 19(2), 173-187.

Harichandran, R. S. (1991). "Closed-form solutions for random vibration under propagating excitation," *Earthquake Engineering and Structural Dynamics*, 15(7), 889-899.

Haroun, M. A. and Abdel-Hafiz E. A. (1987). "Seismic Response Analysis of Earth Dams Under Differential Ground Motion," *Bulletin of the Seismological Society of American*, Vol 77, No 5, 1514-1529.

Hatanaka, M. (1952). "3-Dimensional Consideration on the Vibration of Earth Dams," *Journal of Japanese Society of Civil Engineering*, 37, 10.

Hindy A. and Novak M. (1980). "Pipeline Response to Random Ground Motion," *Journal of the Engineering Mechanics Division, ASCE*, 339-359.

Idriss, I. M., Mathur, G. M. and Seed, H. B. (1974). "Earth Dams Foundation Interaction during Earthquake," *Earthquake Engineering and Structural Dynamics*, 2, 313-323.

Jennings, P. C., Housner, G. W. and Tsai, N. C. (1968). "Simulated Earthquake Motions," Earthquake Engineering Research Laboratory, California Institute of Technology, Pasadena, California.

Johnson, S. J. (1975). "Analysis and Design Relating to Embankment: a State-of-the-art Review," *U.S. Army Engineer Waterways Experiment Station Report*, Vicksburg, Miss.

Keightley, W. O. (1966). "Vibration Characteristics of an Earth Dam," *Bulletin of the Seismological Society of America*, 56(6), 1207-1226.

Kuhlemeyer, R. L. and Lysmer J. (1973). "Finite Element Accuracy for Wave Propagation Problems (Technical note)." *J. Soil Mech. Foun. Div., Proc. ASCE*, 99, SM5, 421-427.

Lacy, S. J. and Prevost, J. H. (1987). "Non-linear Seismic Response Analysis of Earth Dams," *Soil Dynamics and Earthquake Engineering*, 6(1), 48-63.

Loh, C. H. (1985). "Analysis of the Spatial Variation of Seismic Waves and Ground Movements from Smart-1 Array Data," *Earthquake Engineering and Structural Dynamics*, Vol. 13, 561-581.

Loh, C. H. and Yeh, Y. T. (1988). "Spatial Variation and Stochastic Modeling of Seismic Differential Ground Movement," *Earthquake Engineering and Structural Dynamics*, Vol.16, 583-596.

Lowe, J. (1967). "Stability Analysis of Embankment," *Journal of the Soil Mechanics and Foundations Division, Proceeding of ASCE*, Vol. 93, NO. SM4.

Luco, J. E. and Wong, H. L. (1986). "Response of a Rigid Foundation to a Spatially Random Ground Motion," *Earthquake Engineering and Structural Dynamics*, 14, 891-908.

Madsen, H. O., Krenk, S. and Lind, N. C. (1986). *Method of Structural Safety*, Prentice-Hall, Englewood Cliffs, NJ.

Makdisi, F. I. and Seed, H. B. (1978). "Simplified Procedure for Estimating Dam and Embankment Earthquake Induced Deformation," *Journal of the Geotechnical Engineering Division*,104(7), 849-867.

Makdisi, F. I. and Seed, H. B. (1979). "Simplified Procedure for Evaluating Embankment Response," *Journal of the Geotechnical Engineering Division, ASCE*, 105 (12), 1427-1434.

Makdisi, F. I., Kagawa, T. and Seed, H. B. (1982). "Seismic Response of Earth Dams in Triangular Canyons," *Journal of the Geotechnical Engineering, ASCE*,108(10), 1328-1338.

Mansouri, T. A., Nelson, J. D. and Thompson, E. G. (1983). "Dynamic Response and Liquefaction of Earth Dams," *Journal of the Geotechnical Engineering*, 109(1), 89-100.

Martin, G. R. (1965). "The Response of Earth Dams to Earthquakes," Ph.D. Thesis, Univ. of Calif., Berkeley.

Martinez, B. and Bielak, J. (1980). "On the Three-dimensional Seismic Response of Earth Structures," *Proc. 7th World Conf. Earthq. Engrg.*, Instanbul, 8, 523-528.

Mejia, L. H., Seed, H. B. and Lysmer, J. (1982). "Dynamic Analysis of Earth Dams in 3-D," *Journal of the Geotechnical Engineering Division, ASCE*, 108(GT12), 1586-1604.

Mejia, L. H. and Seed, H. B. (1983). "Comparison of 2D and 3D Dynamic Analysis of Earth Dam," *Journal of the Geotechnical Engineering Division, ASCE*, 109(11), 1383-1398.

Mononobe, N., Takata, A. and Matumura, M. (1936). "Seismic Stability of the Earth Dam," *Transactions*, Vol. 4, 2nd Congress on Large Dams, washington, D.C.

Newmark, N. M. (1965), "Effects of Earthquakes on Dams and Embankments," *Geotechnique*, 15(2), 139-160.

Newland, D. E. (1984), *Random Vibrations and Spectral Analysis*, 2nd edition, John Wiley & Sons, Inc., New York.

Novak, M. and Suen, E. (1987). "Dam-foundation Interaction under Spatially Correlated Random Ground Motion," *Proceedings of the 3rd International Conference on Soil Dynamics and Earthquake Engineering*, Developments in Geotechnical Engineering, Vol. 43: Soil-Structural Interaction, Elsevier, 25-39.

NSWC (1993). "Library of Mathematics Subroutines," Naval Surface Warfare Center, Dahlgren, Virginia.

Ohmachi, T. (1981). "Analysis of Dynamic Shear Strain Distributed in 3-D Earth Dams," *Proc. Inc. Conf. on Recent Advances in Geotech. Earthq. Engrg. and Soil Dyn.*, St. Louis, 1, 459-464.

Okamoto, S. et al. (1969), "On the Dynamical Behavior of an Earth Dam during Earthquakes," *Proc. 4th World Conf. Earthquake Engineering*, Santiago.

Okamoto, S. (1984). *Introduction to Earthquake Engineering*, University of Toyko Press, Japan.

Oner, M. (1984). "Shear Vibration of Inhomogeneous Earth Dams in Rectangular Canyons," *Soil Dynamic and Earthquake Engineering*, 3(1), 19-26.

Papoulis, A. (1991). *Probability, Random Vibration and Stochastic Process*, 3rd edition, McGraw Hill, New York.

Paskalov, T. A. (1985). "Earthquake Induced Deformations on Earth-fill and Rock-fill Dams," *Soil Dynamics and Earthquake Engineering*, 4(1), 35-42.

Peakcock, W. H. and Seed, H. B. (1968). "Sand Liquefaction under Cyclic Loading Simple Shear Condition," *Proc. ASCE, Journal of Soil Mechanics and Foundation Division*, Vol. 94, No. SM3, 689-708.

Petrovski, J., Paskalov, T. and Jurukovski (1974). "Dynamic Full-scale Test of an Earthfill Dam," *Geotechnique*, 24(2), 193-206.

Prato, C. A. and Delmastro E. (1987). "1-D Seismic Analysis of Embankments Dams," *Journal of Geotechnical Engineering*, Vol 113, No 8, 904-909.

Prevost, J. H., Abdel-Ghaffar, A. M. and Lacy, S. J. (1985). "Non-linear Dynamic Analysis of an Earth Dam," *Journal of the Geotechnical Engineering Division, ASCE*, 111(7), 882-897.

Price, W. M. P., Jr. (1956). "Technical Record of Design and Construction, Santa Felicia Dam," United Water Conservation District of Ventura County, California UWCD, Santa Paula, Calif.

Ramadan, O. and Novak, M. (1993). "Simulation of Spatially Incoherent Random Ground Motions," *Journal of Engineering Mechanics*, 19(5), 997-1015.

Sarma, S. K. (1975). "Seismic Stability of Earth Dams and Embankments," *Geotechnique*, 25(4), 743-761.

Sawada, Y. and Takahashi, T. (1975). "Study on the Material Properties and the Earthquake Behaviors of Rockfill Dams," *Proc. of 4-NSEE.*

Schneider, J. F., Abrahamson, N. A., et. al. (1990). "Spatial Variation of Strong Ground Motion from EPRI's Dense Accelerograph Array at Parkfield, California," *Proceedings of the Fourth National Conference on Earthquake Engineering*, Palm Springs, California.

SDRC (1987). "Integrated Design Engineering Analysis Software (I-DEAS)," Structural Dynamics Research Corporation, Milford, Ohio.

Seed, H. B. (1979). "Considerations in the Earthquake Design of Earth and Rockfill Dams," *Geotechnique*, 29(3), 215-263.

Seed, H. B., Lee, K. L. and Idriss, I. M. (1973). "Analysis of Sheffield Dam Failure," *Proc. of ASCE.*, Vol. 95, No. SM6.

Seed, H. B., Lee, K. L., Idriss, I. M. and Makdisi, F. I. (1973). "Analysis of the Slides in the San Fernando Dams during the Earthquake of Feb. 9, 1971," *Report* No. EERC 73-2. Univ. of Cali., Berkeley.

Seed, H. B., Lysmer, J. and Hwang, R. (1975). "Soil-Structure Interaction Analyses for Seismic Response," *Journal of the Geotechnical Engineering Division, ASCE*, Vol 101, 439-457.

Seed, H. B., Makdisi, F. I. and Dealba, P. (1978). "Performance of Earth Dams during Earthquakes," *Journal of the Geotechnical Engineering Division,* 104(7), 967-994.

Seed, H. B. and Martin, G. R. (1966). "The Seismic Coefficient of Earth Dam Design," *Journal of the Soil Mechanics and Foundation Division, ASCE*, Vol. 92, No. SM3, 25-58.

Severn, R. J., Jeary, A. P., Ellis, B. R. and Dungar, R. (1979). "Prototype Dynamic Studies on a Rockfill Dam and on a Buttress Dam," *Trans.* of 8th ICOLD.

Sherard, J. L., Woodward, R. J., Gizienski, S. F. and Clevenger, W. A. (1963). *Earth and Earth-Rock Dams*, John Wiley and Sons, Inc.

Soong, T. T. and Grigoriu, M. (1993). *Random Vibration of Mechanical and Structural Systems*, P T R Prentice-Hall, Inc., New Jersey.

Stewart, J. P., Bray, J. D., Seed, R. B. and Sitar, N. (1994). "Preliminary Report on the Principal Geotechnical Aspects of the January 17, 1994 Northridge Earthquake," editors, Report No. UCB/EERC-94/08, Earthquake Engineering Research Center, University of California at Berkeley.

Sweidan, B. N. (1990). "Stochastic Response of Deck and Arch Bridges to Correlated Support Excitations," *Ph.D. Thesis*, Dept. of Civil and Environmental Engineering, Michigan State University, East Lansing, Michigan.

Tsiatas, G. and Gazetas, G. (1982). "Plane-strain and Shear Beam Free Vibration of Earth Dam," *Soil Dynamic and Earthquake Engineering*, 1(4), 150-161.

Uscinski, B. J. (1977). *The Elements of Wave Propagation in Random Media*, McGraw-Hill, New York.

Zerva, A., Ang, A. H-S and Wen, Y. K. (1988). "Lifeline Response to Spatially Variable Ground Motions," *Earthquake Engineering and Structural Dynamics*, 16, 361-379.